

**Advances in Non-Heme Diiron Modeling Chemistry:
Developing Functional Protein Mimics Through Ligand Design
and Understanding Dioxygen Activation**

by

Loi Hung Do

B.S., Chemistry/Biochemistry
University of California, San Diego, 2006

Submitted to the Department of Chemistry in Partial Fulfillment
of the Requirements for the degree of

DOCTOR OF PHILOSOPHY IN CHEMISTRY

at the
Massachusetts Institute of Technology

May 2011

© Massachusetts Institute of Technology, 2011

All rights reserved

Signature of Author:

Department of Chemistry
May 02, 2011

Certified by:

Stephen J. Lippard
Arthur Amos Noyes Professor of Chemistry
Thesis Supervisor

Accepted by:

Robert W. Field
Professor of Chemistry
Chairman, Departmental Committee on Graduate Students

This doctoral thesis has been examined by a committee of the Department of Chemistry as follows:

Richard R. Schrock
Frederick G. Keyes Professor of Chemistry
Committee Chairman

Stephen J. Lippard
Arthur Amos Noyes Professor of Chemistry
Thesis Supervisor

Daniel G. Nocera
Henry Dreyfus Professor of Energy and Professor of Chemistry

**Advances in Non-Heme Diiron Modeling Chemistry:
Developing Functional Protein Mimics Through Ligand Design
and Understanding Dioxygen Activation**

by

Loi Hung Do

Submitted to the Department of Chemistry
in Partial Fulfillment of the Requirements for
the Degree of Doctor of Philosophy in Chemistry

ABSTRACT

Chapter 1

A comprehensive review of diiron modeling in the Lippard group over the past thirty years is presented. This account describes the different strategies employed to prepare biomimetic complexes of non-heme diiron protein active sites, highlighting the accomplishments of the past as well as the challenges for the future. Studies of various model systems have led to a more profound understanding of the fundamental properties of carboxylate-bridged diiron units and their reactivity toward molecular oxygen and organic substrates. The key principles and lessons that have emerged from these studies have been an inspiration for the original work presented in this thesis.

Chapter 2

A series of phenoxyipyridyl and phenoxyimine ligands, $H_2L^{R,R'}$ (compounds derived from bis(phenoxyipyridyl)diethynylbenzene, where $R = H, Me, \text{ or } t\text{-Bu}$, and $R' = H, \text{ or } Ph$) and $H_2BIPS^{Me,Ph}$ (bis((phenylphenoxy)iminephenyl)sulfone) were synthesized as platforms for non-

heme diiron(II) protein model complexes. UV-vis spectrophotometric studies and preparative-scale reactions of $[L^{R,R'}]^{2-}$ or $[BIPS^{Me,Ph}]^{2-}$, where $[L^{R,R'}]^{2-}$ and $[BIPS^{Me,Ph}]^{2-}$ are the deprotonated forms of $H_2L^{R,R'}$ and $H_2BIPS^{Me,Ph}$, respectively, with Fe(II) revealed that the presence of sterically protective ortho phenol substituents is necessary to obtain discrete dinuclear species. Reaction of $[L^{Me,Ph}]^{2-}$ with Fe(II) in THF afforded the doubly-bridged compound $[Fe_2(L^{Me,Ph})_2(THF)_3]$ (**1**), which was characterized in the solid state by X-ray crystallography. A large internal cavity in this complex facilitates its rapid reaction with dioxygen, even at $-50\text{ }^\circ\text{C}$, to produce the thermodynamically stable $[Fe_2(\mu-O)(L^{Me,Ph})_2]$ (**2**) species. Reaction of $^{18}\text{O}_2$ instead of $^{16}\text{O}_2$ with **1** led to a shift in the Fe–O–Fe vibrational frequency from 833 cm^{-1} to 798 cm^{-1} , confirming the presence of the μ -oxodiiron(III) core and molecular oxygen as the source of the bridging oxo group. The $[L^{Me,Ph}]^{2-}$ ligand is robust toward oxidative decomposition and does not display any reversible redox activity.

Chapter 3

A dinucleating macrocycle, H_2PIM , containing phenoxyimine metal-binding units has been prepared. Reaction of H_2PIM with $[Fe_2(Mes)_4]$ ($Mes = 2,4,6\text{-trimethylphenyl}$) and sterically hindered carboxylic acids, Ph_3CCO_2H or $Ar^{Tol}CO_2H$ ($2,6\text{-bis}(p\text{-tolyl})\text{benzoic acid}$), afforded complexes $[Fe_2(PIM)(Ph_3CCO_2)_2]$ (**1**) and $[Fe_2(PIM)(Ar^{Tol}CO_2)_2]$ (**2**), respectively. X-ray diffraction studies revealed that these diiron(II) complexes closely mimic the active site structures of the hydroxylase components of bacterial multi-component monooxygenases (BMMs), particularly the syn disposition of the nitrogen donor atoms and the bridging $\mu\text{-}\eta^1\eta^2$ and $\mu\text{-}\eta^1\eta^1$ modes of the carboxylate ligands at the diiron(II) centers. Cyclic voltammograms of **1** and **2** displayed quasi-reversible redox couples at $+16$ and $+108\text{ mV}$ vs. ferrocene/ferrocenium, respectively, assigned to metal-centered oxidations. Treatment of **2** with silver perchlorate

afforded a silver(I)/diiron(III) heterotrimetallic complex, $[\text{Fe}_2(\mu\text{-OH})_2(\text{ClO}_4)_2(\text{PIM})(\text{Ar}^{\text{Tol}}\text{CO}_2)\text{Ag}]$ (**3**), which was structurally and spectroscopically characterized. Complexes **1** and **2** both react rapidly with dioxygen. Oxygenation of **1** afforded a (μ -hydroxo)diiron(III) complex $[\text{Fe}_2(\mu\text{-OH})(\text{PIM})(\text{Ph}_3\text{CCO}_2)_3]$ (**4**), a hexa(μ -hydroxo)tetrairon(III) complex $[\text{Fe}_4(\mu\text{-OH})_6(\text{PIM})_2(\text{Ph}_3\text{CCO}_2)_2]$ (**5**), and an unidentified iron(III) species. Oxygenation of **2** exclusively formed di(carboxylato)diiron(III) products. X-ray crystallographic and ^{57}Fe Mössbauer spectroscopic investigations indicated that **2** reacts with dioxygen to give a mixture of (μ -oxo)diiron(III) $[\text{Fe}_2(\mu\text{-O})(\text{PIM})(\text{Ar}^{\text{Tol}}\text{CO}_2)_2]$ (**6**) and di(μ -hydroxo)diiron(III) $[\text{Fe}_2(\mu\text{-OH})_2(\text{PIM})(\text{Ar}^{\text{Tol}}\text{CO}_2)_2]$ (**7**) complexes in the same crystal lattice. Compounds **6** and **7** spontaneously convert to a tetrairon(III) complex, $[\text{Fe}_4(\mu\text{-OH})_6(\text{PIM})_2(\text{Ar}^{\text{Tol}}\text{CO}_2)_2]$ (**8**), when treated with excess H_2O . The possible biological implications of these findings are discussed.

Chapter 4

To investigate how protons may be involved in the dioxygen activation pathway of non-heme diiron enzymes, the reaction of H^+ with a synthetic (μ -1,2-peroxo)(carboxylato)diiron(III) complex was explored. Addition of an H^+ donor to $[\text{Fe}_2(\text{O}_2)(N\text{-EtHPTB})(\text{PhCO}_2)]^{2+}$ ($\mathbf{1}\cdot\text{O}_2$, where $N\text{-EtHPTB}$ = anion of N,N,N',N' -tetrakis(2-benzimidazolylmethyl)-2-hydroxy-1,3-diaminopropane) resulted in protonation of the carboxylate rather than the peroxo ligand. Mössbauer and resonance Raman spectroscopic measurements indicate that the $\text{Fe}_2(\text{O}_2)$ core of the protonated complex $[\mathbf{1}\cdot\text{O}_2]\text{H}^+$ is identical to that of $\mathbf{1}\cdot\text{O}_2$. In contrast, the benzoate ligand of $[\mathbf{1}\cdot\text{O}_2]\text{H}^+$ displays significantly different IR and NMR spectral features relative to those of the starting complex. The $[\mathbf{1}\cdot\text{O}_2]\text{H}^+$ species can be converted back to $\mathbf{1}\cdot\text{O}_2$ upon treatment with base, indicating that protonation of the carboxylate is reversible. These findings suggest that in the reaction cycle of soluble methane monooxygenases and related diiron proteins, protons may

induce a carboxylate shift to enable substrate access to the diiron core and/or increase the electrophilicity of the oxygenated complex.

Chapter 5

To explore additional methods to interrogate the properties of diiron protein intermediates, studies of the vibrational profiles of (μ -1,2-peroxo)diiron(III) species were pursued using nuclear resonance vibrational spectroscopy (NRVS). Comparison of the NRVS of $[\text{Fe}_2(\text{O}_2)(N\text{-EtHPTB})(\text{PhCO}_2)]^{2+}$ ($\mathbf{1}\cdot\text{O}_2$) to that of the diiron(II) starting material $[\text{Fe}_2(N\text{-EtHPTB})(\text{PhCO}_2)]^{2+}$ ($\mathbf{1}$) revealed that the oxygenated complex displays new frequencies above 350 cm^{-1} , which are attributed to the Fe–O–O–Fe core vibrations based on $^{18}\text{O}_2/^{16}\text{O}_2$ isotopic labeling studies. The peak at 338 cm^{-1} has not been previously observed by resonance Raman spectroscopy. Empirical normal mode analysis provides a qualitative description of these isotopic sensitive modes. The NRVS of $[\text{Fe}_2(\mu\text{-O}_2)(\text{HB}(^{iPr}\text{pz})_3)_2(\text{PhCH}_2\text{CO}_2)_2]$ ($\mathbf{4}\cdot\text{O}_2$, where $\text{HB}(^{iPr}\text{pz})_3 = \text{tris}(3,5\text{-diisopropylpyrazoyl})\text{hydroborate}$) was also measured and shows several $\text{Fe}_2(\text{O}_2)$ modes between $350\text{--}500\text{ cm}^{-1}$.

Appendix A

Attempts to prepare a diiron(IV) complex described in the literature led to several unexpected discoveries. Reaction of tris((3,5-dimethyl-4-methoxy)pyridyl-2-methyl)amine (R_3TPA) with iron(III) perchlorate decahydrate and sodium hydroxide afforded a (μ -oxo)(μ -hydroxo)diiron(III) $[\text{Fe}_2(\mu\text{-O})(\mu\text{-OH})(\text{R}_3\text{TPA})_2](\text{ClO}_4)_3$ complex ($\mathbf{1}$), rather than $[\text{Fe}_2(\mu\text{-O})(\text{OH})(\text{H}_2\text{O})(\text{R}_3\text{TPA})_2](\text{ClO}_4)_3$ (\mathbf{B}) as previously reported. The putative diiron(III) starting material \mathbf{B} is formed only at low temperature when excess water is present. Compound $\mathbf{1}$ hydrolyzes acetonitrile to acetate under ambient conditions. The acetate-bridged diiron compound, $[\text{Fe}_2(\mu\text{-O})(\mu\text{-CH}_3\text{CO}_2)(\text{R}_3\text{TPA})_2](\text{ClO}_4)_3$ ($\mathbf{4A}$), was characterized by X-ray crystallography as well as

various spectroscopic methods and elemental analysis. The identity of the acetate bridged complex was confirmed by comparing the structural and spectroscopic characteristics of **4A** to those of an independently prepared sample of $[\text{Fe}_2(\mu\text{-O})(\mu\text{-CH}_3\text{CO}_2)(\text{R}_3\text{TPA})_2](\text{ClO}_4)_3$.

Thesis Supervisor: Stephen J. Lippard
Title: Arthur Amos Noyes Professor of Chemistry

Preface

The goal of synthetic modeling is to illuminate the underlying inorganic chemistry adopted by nature to achieve specific and complex transformations. A family of metalloenzymes that catalyzes the regio- and stereoselective oxidation of hydrocarbons using the earth abundant molecule O_2 is the bacterial multi-component monooxygenases (BMMs). The BMMs are sophisticated biological machineries that require several protein components to function, including a hydroxylase that contains a diiron active site, a reductase that shuttles electrons from nicotinamide adenine dinucleotide (NADH) to the hydroxylase, and a regulatory protein that controls electron transfer and substrate oxidation. In addition to studying the biomolecules directly, our laboratory has employed a complementary approach using synthetic modeling to interrogate the structure and reactivity of the carboxylate-bridged diiron unit of the BMM active sites.

To place the work in this thesis into context, a chronological review of diiron modeling in the Lippard laboratory is presented in Chapter 1. This account highlights the various strategies utilized to prepare mimics of non-heme diiron protein active sites, with particular emphasis on rational ligand design. Despite the advances that have been made since the early 1980s, developing a functional protein mimic is still a significant challenge. To obtain a scaffold that can support a diiron core having the same coordination environment/geometry as that in the protein, a series of syn *N*-donor ligands were prepared. The diiron complexes assembled using these ligands, however, were too substitutionally labile to be useful as model compounds. Chapter 2 describes our attempt to prepare a more kinetically stabilizing ligand framework; the bis(phenoxy)pyridine and bis(phenoxy)imine ligands are anionic when deprotonated and form six-membered chelate rings upon complexation with iron. These ligands, however, spontaneously form bis(syn *N*-donor)diiron units when treated with iron(II) salts. To prevent undesired association of two syn *N*-donor ligands in a diiron complex, the two phenyl groups of the bis(phenoxy)imine compound were linked to afford a macrocycle, PIM²⁻. Chapter 3 reports the synthesis and characterization of di(μ -carboxylato)(PIM)diiron(II) complexes that are excellent structural models of the BMM active sites in their reduced state. The [Fe₂PIM] unit is stable under oxidizing conditions and accommodates changes in the binding mode of the carboxylate moieties upon reaction with O_2 . Although further modifications to the aryl groups of PIM²⁻ are necessary to prevent formation of tetranuclear species, the macrocyclic framework is an important breakthrough in our goal to access more advanced diiron protein models.

To gain insight into the O_2 reaction pathway, another research objective was to examine the characteristics of well-defined diiron complexes that mimic the oxygenated intermediates formed during the BMM catalytic cycle. Extensive biochemical studies revealed that the generation and activation of [Fe₂(O₂)] units in the BMMs occur through proton dependent processes. To interrogate the possible role of protons in the biological O_2 reduction mechanism, the study presented in Chapter 4 explores the effect of H⁺ on the stability of a synthetic (μ -1,2-peroxo)(carboxylato)diiron(III) model compound. Resonance Raman (RR), infrared (IR), nuclear magnetic resonance (NMR), and Mössbauer spectroscopic studies indicate that the carboxylate is protonated rather than the dioxygen moiety upon treating the synthetic [Fe₂(O₂)] complex with H⁺. These results suggest that during O_2 activation in the catalytic cycle of the BMMs, protons might induce a carboxylate shift in the diiron core, possibly increasing the electrophilicity of the [Fe₂(O₂)] unit or facilitating substrate access to the active site.

Inspired by nuclear resonance vibrational spectroscopic (NRVS) studies of mononuclear iron complexes, we initiated a project to evaluate the feasibility of applying this technique to probe the vibrational profile of diiron protein intermediates. As described in Chapter 5, to obtain spectroscopic benchmarks for possible $[\text{Fe}_2(\text{O}_2)]$ species that occur during the BMM reaction cycle, the vibrational spectra of two (peroxo)diiron(III) model compounds were recorded using the synchrotron facility at SPring8, Japan. For one of the compounds, $^{16}\text{O}_2/^{18}\text{O}_2$ studies revealed three isotopic sensitive peaks in the NRVS, one of which was not previously detected by RR spectroscopy. Normal coordinate analyses provide a qualitative description of the modes that involve vibrations of the $[\text{Fe}_2(\text{O}_2)]$ core. These results suggest that NRVS may be a useful tool for studying diiron protein samples if an appropriate set of conditions can be met.

As a spectroscopic standard of an $[\text{Fe}^{\text{IV}}_2(\text{O})_2]$ unit for the NRVS studies described above, attempts were made to prepare a di(μ -oxo)bis(tris(pyridyl-2-methyl)amine)diiron(IV) complex that was reported in the literature. As summarized in Appendix A, our efforts led to several unexpected observations that prompted a re-evaluation of the identity of the diiron(III) precursor. Our data suggest that the (μ -oxo)(hydroxo)(aquo)diiron(III) compound reported is only present in sufficient amounts in wet solvent at low temperature. Furthermore, the diiron(III) complex mediates hydrolysis of acetonitrile to acetate when H_2O is present. These findings raise some concerns regarding the purported generation of high-valent diiron(IV) species derived from the mischaracterized diiron(III) starting material.

Diiron modeling has been at the heart of our research program for many years and will continue to be a vital research area for many more. The sophistication of today's chemical toolbox should enable synthetic chemists to overcome the obstacles that have previously limited significant advances in biomimetic chemistry.

TABLE OF CONTENTS

	Page
Title Page	1
Signature Page	2
Abstract	3
Preface	9
Table of Contents	11
List of Figures	14
List of Charts	16
List of Schemes	17
List of Tables	18
List of Abbreviations	19
List of Compound Identifiers	23
Chapter 1. Rationally Designed Synthetic Mimics of Diiron Protein Active Sites: A Chronological Perspective	27
1.1. Introduction	28
1.2. Non-Heme Diiron Proteins	29
1.3. Mononucleating <i>N</i> -Heterocyclic Ligands	31
1.4. Dicarboxylate Ligands	34
1.5. Terphenylcarboxylate Ligands	38
1.6. Dinucleating Polynitrogen Ligands	43
1.7. Syn <i>N</i> -Donor Ligands	45
1.8. Macrocyclic Ligands	48
1.9. Concluding Remarks	49
1.10. References	52
Chapter 2. Kinetic Stabilization of Diiron Complexes Using Phenoxyipyridine and Phenoxyimine Syn <i>N</i>-Donor Ligands	61
2.1. Introduction	62
2.2. Experimental	64
Synthesis	66
UV-vis Spectrophotometric Studies	81
2.3. Results and Discussion	82
Ligand Design and Synthesis	82
UV-vis Spectrophotometric Studies	87
Isolation and Characterization of Iron Complexes	91

Reaction of Complex 1 with Dioxygen	99
2.4. Conclusion	104
2.5. References	105
Chapter 3. Redox Behavior and Dioxygen Reactivity of a Macrocyclic Carboxylate-Bridged Diiron(II) Mimic of Bacterial Monooxygenase Active Sites	111
3.1. Introduction	112
3.2. Experimental	114
Synthesis	117
3.3. Results	126
Ligand Design and Synthesis	126
Assembly of Diiron(II) Complexes	127
Redox Chemistry	136
Reactivity with O ₂	141
3.4. Discussion	154
Macrocyclic Ligands for Constructing Biomimetic Carboxylate-Bridged Diiron Models	154
Reactivity of Diiron(II) Mimics and Their Biological Implications	156
3.5. Conclusion	159
3.6. References	159
Chapter 4. Carboxylate as the Protonation Site in (Peroxo)diiron(III) Model Complexes of Soluble Methane Monooxygenase and Related Diiron Proteins	165
4.1. Introduction	166
4.2. Experimental	169
Synthesis	170
Spectroscopic Studies	173
4.3. Results and Discussion	175
Mössbauer and Resonance Raman Spectroscopy	176
Infrared Spectroscopy	180
NMR Spectroscopy	183
4.4. Conclusion	186
4.5. References	186
Chapter 5. Characterization of Synthetic (μ-1,2-Peroxo)diiron(III) Complexes by Nuclear Resonance Vibrational Spectroscopy	191
5.1. Introduction	192
5.2. Experimental	194

Synthesis	195
NRVS Sample Preparation	196
Nuclear Resonance Vibrational Spectroscopy (NRVS)	197
Empirical Force Field Normal Mode Analysis	197
5.3. Results and Discussion	198
NRVS of Diiron <i>N</i> -EtHPTB Complexes	198
NRVS of Iron HB(^{<i>iPr</i>} pZ ₃) ⁻ Complexes	200
Empirical Normal Coordinate Analysis	202
5.4. Conclusion	205
5.5. References	205
Appendix A. Evaluating the Identity of an Electron Rich Bis(tris(pyridyl-2-methyl)amine)diiron(III) Complex and Its Involvement in the Hydrolysis of Acetonitrile	211
A.1. Introduction	212
A.2. Experimental	214
Synthesis	217
A.3. Results and Discussion	218
Characterization of Diiron(III) Complexes	218
Effect of Solvent, Water, and Temperature on the Stability of 1	230
Hydrolysis of Acetonitrile to Acetate	232
Validity of the Reported Results	234
A.4. Conclusion	235
A.5. References	235
Biographical Sketch	239
Curriculum Vitae	240
Acknowledgements	243

LIST OF FIGURES

	Page
Chapter 2	
Figure 2.1. Absorption spectra of $\text{Fe}^{\text{II}}/\text{Na}_2\text{L}^{\text{H,H}}$, $\text{Fe}^{\text{II}}/\text{Na}_2\text{L}^{\text{H,Ph}}$, and $\text{Fe}^{\text{II}}/\text{Na}_2\text{L}^{\text{H,Ph}}$ + sodium triphenylacetate.	88
Figure 2.2. Single wavelength plots of the optical changes associated with addition of $\text{Fe}(\text{II})$ to $\text{Na}_2\text{L}^{\text{H,H}}$, $\text{Na}_2\text{L}^{\text{H,Ph}}$, $\text{Na}_2\text{L}^{\text{tBu,Ph}}$, and $\text{Na}_2\text{BIPS}^{\text{Me,Ph}}$.	90
Figure 2.3. Absorption spectra of $\text{Fe}^{\text{II}}/\text{Na}_2\text{L}^{\text{tBu,Ph}}$ and $\text{Fe}^{\text{II}}/\text{Na}_2\text{BIPS}^{\text{Me,Ph}}$.	90
Figure 2.4. Thermal ellipsoid (50%) diagram of the X-ray structure of 1 .	94
Figure 2.5. Electronic spectra of 1 and 2 in THF.	95
Figure 2.6. ^1H NMR spectra of 1 and 2 in $\text{THF-}d_8$.	96
Figure 2.7. Zero-field ^{57}Fe Mössbauer spectra of polycrystalline 1 and 2 at 90 K.	96
Figure 2.8. Cyclic and differential pulse voltammograms of 1 and 2 .	98
Figure 2.9. Absorption spectra of 1 and ferrocenium in THF.	99
Figure 2.10. Stick figure diagram of the X-ray structure of 2 .	100
Figure 2.11. Cyclic voltammograms of 2 in THF.	102
Figure 2.12. Stopped-flow absorption spectra of the reaction of 1 with O_2 .	103
Chapter 3	
Figure 3.1. Absorption spectra of $\text{Fe}^{\text{II}}/\text{PIM}^{2-}$ and $\text{Fe}^{\text{II}}/\text{PIM}^{2-}/\text{Ph}_3\text{CCO}_2\text{Na}$.	128
Figure 3.2. Thermal ellipsoid (50%) diagram of the X-ray structure of 1 .	129
Figure 3.3. Thermal ellipsoid (50%) diagram of the X-ray structure of 2 .	130
Figure 3.4. Absorption spectra of 1 and 2 in CH_2Cl_2 .	133
Figure 3.5. Zero-field ^{57}Fe Mössbauer spectrum of polycrystalline 1 at 80 K.	133
Figure 3.6. EPR spectrum of 1 in 2-MeTHF at 5K.	134
Figure 3.7. ^1H NMR spectra of 1 and 2 at RT.	135
Figure 3.8. Cyclic voltammograms of 1 and 2 in CH_2Cl_2 at RT.	136
Figure 3.9. Absorption spectra of 3 and 2 / AgSbF_6 in CH_2Cl_2 .	138
Figure 3.10. Thermal ellipsoid (50%) diagram of the X-ray structure of 3 .	140
Figure 3.11. Absorption spectra of 1 / O_2 , 4 , and 5 in CH_2Cl_2 .	141
Figure 3.12. ^1H NMR spectra of 1 / O_2 , 4 , and 5 at RT.	142
Figure 3.13. Thermal ellipsoid (50%) diagram of the X-ray structure of 4 .	143
Figure 3.14. Thermal ellipsoid (50%) diagram of the X-ray structure of 5 .	144
Figure 3.15. Zero-field ^{57}Fe Mössbauer spectrum of polycrystalline 4 and 5 at 80 K.	146
Figure 3.16. Zero-field ^{57}Fe Mössbauer spectrum of 1 / O_2 in benzene- d_6 at 80 K.	148
Figure 3.17. Absorption spectra of 2 / O_2 and 2 / O_2 + H_2O in CH_2Cl_2 .	149
Figure 3.18. ^1H NMR spectrum of 2 / O_2 in CD_2Cl_2 .	149
Figure 3.19. Thermal ellipsoid (50%) diagram of the X-ray structure of 6 .	150

Figure 3.20. Hybrid stick and space-filling diagram of the X-ray structures of 4 and 6 .	150
Figure 3.21. Zero-field ^{57}Fe Mössbauer spectra of 2 , 2 / O_2 , and 2 / O_2 + H_2O .	153
Figure 3.22. Comparison of the diiron cores of sMMOH and the synthetic models.	155
Chapter 4	
Figure 4.1. Absorption spectra of 1a · O_2 with protons and base in CH_3CN .	176
Figure 4.2. Absorption spectra of 2 · O_2 with protons in CH_3CN .	177
Figure 4.3. Zero-field ^{57}Fe Mössbauer spectra of 1a · O_2 , [1a · O_2] H^+ , 2 · O_2 , and [2 · O_2] H^+ in CH_3CN at 80 K.	178
Figure 4.4. Resonance Raman spectra of 1a · O_2 , [1a · O_2] H^+ , 1b · O_2 , and [1b · O_2] H^+ in CH_3CN .	179
Figure 4.5. Resonance Raman spectra of 2 · O_2 and [2 · O_2] H^+ in CH_3CN .	179
Figure 4.6. IR spectra of 1a and 1b in the solid-state and in solution.	181
Figure 4.7. Solution IR spectra of 1a · O_2 , 1b · O_2 , [1a · O_2] H^+ , and [1b · O_2] H^+ .	182
Figure 4.8. Solution IR spectra of 2 · O_2 and [2 · O_2] H^+ .	183
Figure 4.9. ^1H NMR spectra of 1a · O_2 , [1a · O_2] H^+ , 2 · O_2 and [2 · O_2] H^+ in CH_3CN .	184
Figure 4.10. ^{19}F NMR spectra of 2 · O_2 and [2 · O_2] H^+ in CH_3CN and CH_2Cl_2 .	185
Chapter 5	
Figure 5.1. NRVS of polycrystalline 1 at ~ 10 K.	199
Figure 5.2. NRVS of frozen THF solutions of 1 · $^{16}\text{O}_2$ and 1 · $^{18}\text{O}_2$ at ~ 10 K.	200
Figure 5.3. Resonance Raman spectra of 1 · $^{16}\text{O}_2$ and 1 · $^{18}\text{O}_2$ in CH_3CN .	201
Figure 5.4. NRVS of 4 , 4 / $^{16}\text{O}_2$, and 4 / $^{18}\text{O}_2$ at ~ 10 K.	202
Figure 5.5. Normal coordinate calculations for 1 · O_2 of modes involving vibrations of the $\text{Fe}_2(\text{O}_2)$ core.	204
Appendix A	
Figure A.1. Zero-field Mössbauer spectra of the crude reaction material, 1 , 4A , and 4B at 80 K.	219
Figure A.2. IR spectra of $\text{Fe}^{\text{III}}/\text{R}_3\text{TPA}/\text{OH}^-$, 1 , 4A , and 4B and their difference plots.	221
Figure A.3. Thermal ellipsoid (50%) diagram of the X-ray structure of 1 .	222
Figure A.4. Thermal ellipsoid (50%) diagram of the X-ray structure of 4A .	225
Figure A.5. Absorption spectra of 1 , 4A , and 4B in CH_2Cl_2 .	227
Figure A.6. ^1H NMR spectra of 1 , 4A , and 4B in CD_2Cl_2 .	228
Figure A.7. Thermal ellipsoid (50%) diagram of the X-ray structure of 4B .	229
Figure A.8. Absorption spectra of 1 in CH_2Cl_2 , CH_3CN , and $\text{CH}_2\text{Cl}_2/\text{MeOH}$.	231
Figure A.9. Optical changes of 1 in CH_3CN at various temperatures and in the presence of water.	232
Figure A.10. Decay of 1 monitored by stopped-flow UV-vis spectroscopy.	234

LIST OF CHARTS

	Page
Chapter 1	
Chart 1.1. The tethered substrates that were successfully oxidized by reaction with O ₂ when integrated into a diiron(II) complex.	41
Chart 1.2. Examples of crystallographically characterized [Fe ₂ (syn <i>N</i> -donor) ₂] complexes.	47
Chapter 2	
Chart 2.1. The active site structure of sMMOH _{red} and a proposed synthetic mimic.	63
Chart 2.2. The series of phenoxyipyridyl and phenoxyimine dinucleating ligands synthesized.	84
Chapter 3	
Chart 3.1. Syn <i>N</i> -donor ligands containing mixed <i>N,O</i> metal binding units.	113
Chapter 4	
Chart 4.1. Depiction of the (peroxo)diiron(III) complexes that have been structurally determined by X-ray crystallography.	167
Chapter 5	
Chart 5.1. Possible geometries of the (μ -peroxo)diiron(III) unit.	193
Chart 5.2. Structural depiction of compounds 1 ·O ₂ , 2 ·O ₂ , 3 ·O ₂ , and 4 ·O ₂ .	194
Appendix A	
Chart A.1. Structural depiction of the diiron TPA complexes A and B .	212

LIST OF SCHEMES

	Page
Chapter 1	
Scheme 1.1. Dioxygen reactivity of Hr, RNR, and sMMOH.	30
Scheme 1.2. Proposed mechanism for the reaction of $[\text{Fe}_2(\mu\text{-Ar}^{\text{Tol}}\text{CO}_2)_4(4\text{-}^t\text{Bupy})_2]$ with dioxygen.	40
Scheme 1.3. Proposed reaction of O_2 with a sterically-hindered PIM^{2-} variant.	49
Chapter 2	
Scheme 2.1. Synthesis of $\text{H}_2\text{LV}^{\text{H,H}}$ and $\text{H}_2\text{L}^{\text{H,H}}$.	85
Scheme 2.2. Synthesis of $\text{H}_2\text{L}^{\text{H,Ph}}$, $\text{H}_2\text{L}^{\text{Me,Ph}}$, and $\text{H}_2\text{L}^{\text{tBu,Ph}}$.	86
Scheme 2.3. Synthesis of $\text{H}_2\text{BIPS}^{\text{Me,Ph}}$.	86
Scheme 2.4. Reaction of $\text{H}_2\text{L}^{\text{H,H}}$ and $\text{H}_2\text{L}^{\text{Me,Ph}}$ with iron(II).	92
Chapter 3	
Scheme 3.1. Reaction of sMMOH with dioxygen.	112
Scheme 3.2. Synthesis of H_2PIM .	126
Scheme 3.3. Reaction of 1 and 2 with dioxygen and silver perchlorate.	157
Chapter 4	
Scheme 4.1. Proposed catalytic cycle of sMMOH.	167
Scheme 4.2. Reaction of 1a with dioxygen and protons.	169
Appendix A	
Scheme A.1. Reaction of B leading to formation of high-valent diiron species.	213
Scheme A.2. Propose reaction pathway for the formation of 4A from 1 .	232

LIST OF TABLES

	Page
Chapter 1	
Table 1.1. Various ligands employed to prepare diiron protein model complexes.	32
Chapter 2	
Table 2.1. X-ray crystallographic data and refinement for 1 .	93
Chapter 3	
Table 3.1. X-ray crystallographic data and refinement for 1 , 2 , and 3 .	131
Table 3.2. Spectroscopic data for 1-8 .	132
Table 3.3. Bond valence sum analysis for 3 , 6 , and 7 .	139
Table 3.4. X-ray crystallographic data and refinement for 4 , 5 , and 6/7 .	145
Chapter 4	
Table 4.1. Spectroscopic data for 1a ·O ₂ , [1a ·O ₂]H ⁺ , 2 ·O ₂ , and [2 ·O ₂]H ⁺ .	178
Appendix A	
Table A.1. Summary of spectroscopic data for Fe ^{III} /R ₃ TPA/OH ⁻ , 1 , 4A , and 4B .	220
Table A.2. X-ray crystallographic data and refinement for 1 , 4A , and 4B .	223
Table A.3. Select structural parameters of 1 and two structurally related diiron TPA complexes.	224
Table A.4. Select structural parameters of 4A and 4B .	226

LIST OF ABBREVIATIONS

2-Ph ₂ P(O)py	2-pyridyldiphenylphosphine oxide
2-Ph ₂ Py	2-pyridyldiphenylphosphine
3-Fpy	3-fluoropyridine
4- ^t Bupy	4- <i>tert</i> -butylpyridine
4-CNpy	4-cyanopyridine
5-Et ₃ -TPA	tris((5-ethylpyridyl)-2-methyl)amine
6Me ₂ -BPP	bis((6-methylpyridyl)-2-methyl)propionate amine
6-Me ₃ TPA	tris((6-methylpyridyl)-2-methyl)amine
[BIPS ^{Me,Ph}] ²⁻	anion of bis((phenylphenoxy)iminophenyl)sulfone
[G3]CO ₂ ⁻	third generation dendrimer appended terphenylcarboxylate
[L ^{H,H}] ²⁻	anion of bis(phenoxy)pyridyl)diethynylbenzene
[L ^{H,Ph}] ²⁻	anion of bis((phenylphenoxy)pyridyl)diethynylbenzene
[L ^{Me,Ph}] ²⁻	anion of bis(phenyl(<i>p</i> -cresol)pyridyl)diethynylbenzene
[L ^{tBu,Ph}] ²⁻	anion of bis(<i>o</i> -phenyl- <i>p</i> - <i>tert</i> -butylphenoxy)pyridyl)diethynylbenzene
[LV ^{H,H}] ²⁻	anion of bis(phenoxy)pyridyl)diethynylveratrole
Abs	absorption
AMO	alkene monooxygenase
APD	avalanche photodiode detector
Ar ^{4-FPh} CO ₂ ⁻	2,6-bis(<i>p</i> -fluorophenyl)benzoate
Ar ^{tBu} CO ₂ ⁻	2,6-bis(<i>p</i> -(<i>tert</i> -butyl)phenyl)benzoate
Ar ^{Tol} CO ₂ ⁻	2,6-bis(<i>p</i> -tolyl)benzoate
Asp	aspartate
bdptz	1,4-bis(2,2'-dipyridylmethyl)phthalazine
BEPEAN	2,7-bis(bis(2-(2-(5-ethyl)pyridyl)ethyl)aminomethyl)-1,8-naphthyridine
BIPhMe	bis(1-methylimidazol-2-yl)phenylmethoxymethane
BMMs	bacterial multi-component monooxygenases
BPEAN	2,7-bis(bis(2-(2-(5-methyl)pyridyl)ethyl)aminomethyl)-1,8-naphthyridine
BPMAN	2,7-bis(bis(2-pyridylmethyl)aminomethyl)-1,8-naphthyridine
bpy	2,2'-bipyridine
BVS	bond valence sum
BXDK ²⁻	benzyl substituted variant of XDK ²⁻
Cp	cyclopentadienyl
CV	cyclic voltammetry
deoxyHr	reduced form of hemerythrin, with no dioxygen bound

DAFA ²⁻	1,8-bis(dimethylaminomethylethynyl)-3,6-di(<i>tert</i> -butyl)fluorine-9-yl-acetate
DFT	density functional theory
DMF	dimethylformamide
DMSO	dimethyl sulfoxide
DNA	deoxyribonucleic acid
DPV	differential pulse voltammetry
EPR	electron paramagnetic resonance
E _{1/2}	average of anodic and cathodic redox potential
ET	electron transfer
Et ₂ BCQEB ^{Et}	1,2-bis(3-ethynyl-8-carboxylatequinoline)-4,5-diethynylbenzene methyl ester
EXAFS	extended X-ray absorption fine structure
Fc	ferrocene
Fc ⁺	ferrocenium
FTIR	fourier transform infrared
GC-MS	gas chromatography-mass spectrometry
Glu	glutamate
H[BAr ^F ₄]	bis(diethyl ether)hydronium tetrakis((3,5-trifluoromethyl)phenyl)borate
His	histidine
HMDS	hexamethyldisilazide
H _{mv}	mixed-valent diiron(II,III) state of soluble methane monooxygenase
Hr	hemerythrin
Im ₂ DET	bis(<i>N</i> -methylimidazole)diethynyltripitycene
<i>i</i> PrCO ₂ ⁻	isobutyrate
IR	infrared
<i>k</i>	kinetic rate constant
<i>K</i> _{com}	comproportionation constant
Lut	2,6-lutidine
MAr ^{Tol} CO ₂ ²⁻	1,3-bis(aminomethyl)-4,6-diisopropylbenzene linked bis(terphenylcarboxylate)
<i>Mc</i>	<i>Methylococcus capsulatus</i>
Mes	2,4,6-trimethylphenyl
metHr	the oxidized inactive form of hemerythrin
MPDP ²⁻	<i>m</i> -phenylenedipropionate
NADH	the reduced form of nicotinamide adenine dinucleotide
<i>N</i> -EtHPTB	anion of <i>N,N,N',N'</i> -tetrakis(<i>N</i> -ethylbenzimidazolyl)methyl)-2-hydroxy-

	1,3-diaminopropane
<i>N</i> -MeIm	<i>N</i> -methylimidazole
NMR	nuclear magnetic resonance
<i>N,N</i> -Bn ₂ en	<i>N,N</i> -dibenzylethylenediamine
NRVS	nuclear resonance vibrational spectroscopy
<i>N</i> - <i>t</i> BuIm	<i>N</i> - <i>tert</i> -butylimidazole
oxyHr	dioxygen-bound form of hemerythrin
PDK ⁴⁻	anion of α,α -5,15-bis(α - <i>N</i> -(Kemp's triacid imido)- <i>o</i> -tolyl)-2,8,12,18-tetraethyl-3,7,13,17-tetramethylporphyrin
PIC ₂ DET	bis(picolinic methyl ester)diethynyltriptycene
PIM ²⁻	dibenzylether linked bis(3-(methylphenoxyimine)phenyl)sulfone
PH	phenol hydroxylase
Ph ₄ DBA ²⁻	dibenzofuran-4,6-bis(diphenylacetate)
PhCO ₂ ⁻	benzoate
PhCyCO ₂ ⁻	1-phenylcyclohexylcarboxylate
Ph-bimp	2,6-bis(bis(2-(1-methyl-4,5-diphenylimidazolyl)methyl)aminomethyl)-4-methylphenolate
<i>pK_a</i>	acid dissociation constant, log scale
PXDK ²⁻	propyl substituted variant of XDK ²⁻
py	pyridine
R2	ribonucleotide reductase subunit containing the diiron active site
R ₃ TPA	tris((3,5-dimethyl-4-methoxypyridyl)-2-methyl)amine
RNR	ribonucleotide reductase
RR	resonance Raman
RT	room temperature
sMMO	soluble methane monooxygenase
sMMOH	soluble methane monooxygenase hydroxylase
sMMOH _{red}	the active form of soluble methane monooxygenase hydroxylase
sMMOH _{ox}	the resting state of soluble methane monooxygenase hydroxylase
sMMOR	soluble methane monooxygenase reductase
<i>t</i> -BuCH ₂ CO ₂ ⁻	1- <i>tert</i> -butylacetate
<i>t</i> -BuCO ₂ ⁻	pivalate
T4MoH	toluene 4-monooxygenase hydroxylase
THF	tetrahydrofuran
TMEDA	<i>N,N,N',N'</i> -tetramethylethylenediamine
ToMO	toluene/ <i>o</i> -xylene monooxygenase

TP ⁻	tris(pyrazolyl)borate
TPA	tris(pyridyl-2-methyl)amine
TrpCO ₂ ⁻	triptycenecarboxlate
UV-vis	ultraviolet-visible
XDK ²⁻	anion of <i>m</i> -xylenediamine bis(Kemp's triacid)imide
δ	isomer shift
ΔE _Q	quadrupole splitting
Γ	linewidth

LIST OF COMPOUND IDENTIFIERS

Chapter 1

- 1 $[\text{Fe}^{\text{III}}_2(\mu\text{-O})(\mu\text{-CH}_3\text{CO}_2)_2(\text{TP})_2]$
- 2 $[\text{Fe}^{\text{III}}_2(\mu\text{-OH})(\mu\text{-CH}_3\text{CO}_2)_2(\text{TP})_2]^+$
- 3 $[\text{Fe}^{\text{II}}_2(\mu\text{-HCO}_2)_3(\text{HCO}_2)(\text{BIPhMe})_2]$
- 4 $[\text{Fe}^{\text{III}}_2(\mu\text{-O})(\mu\text{-HCO}_2)_2(\text{HCO}_2)_2(\text{BIPhMe})_2]$
- 5 $[\text{Fe}^{\text{III}}_2(\mu\text{-O})(\text{MPDP})(\text{bpy})_2\text{Cl}_2]$
- 6 $[\text{Fe}^{\text{III}}_2(\mu\text{-O})(\text{MPDP})(\text{BIPhMe})_2\text{Cl}_2]$
- 7 $[\text{Fe}^{\text{III}}_2(\mu\text{-O})(\text{MPDP})(\text{TP})_2]$
- 8 $[\text{Fe}^{\text{III}}_2(\mu\text{-O})(\text{XDK})(\text{CH}_3\text{OH})_5(\text{H}_2\text{O})]^{2+}$
- 9 $[\text{Fe}^{\text{II}}_2(\text{XDK})(\mu\text{-PhCyCO}_2)(\text{PhCyCO}_2)(\text{py})_2]$
- 10 $[\text{Fe}^{\text{II}}_2(\mu\text{-OH})(\text{Ph}_4\text{DBA})(\text{TMEDA})_2(\text{CH}_3\text{CN})]^+$
- 11 oxygenated species of $[\text{Fe}^{\text{II}}_2(\mu\text{-OH})(\text{Ph}_4\text{DBA})(\text{TMEDA})_2(\text{CH}_3\text{CN})]^+$
- 12 $[\text{Fe}^{\text{II}}_3(\text{PDK})(\text{Lut})(\text{Br})_2(\text{HBr})]$
- 13 $[\text{Fe}^{\text{II}}_2(\mu\text{-Ar}^{\text{Tol}}\text{CO}_2)_2(\text{Ar}^{\text{Tol}}\text{CO}_2)_2(\text{THF})_2]$
- 14A quadruply-bridged form of $[\text{Fe}^{\text{II}}_2(\text{Ar}^{\text{Tol}}\text{CO}_2)_4(4\text{-}^t\text{Bupy})_2]$
- 14B triply-bridged form of $[\text{Fe}^{\text{II}}_2(\text{Ar}^{\text{Tol}}\text{CO}_2)_4(4\text{-}^t\text{Bupy})_2]$
- 14C doubly-bridged form of $[\text{Fe}^{\text{II}}_2(\text{Ar}^{\text{Tol}}\text{CO}_2)_4(4\text{-}^t\text{Bupy})_2]$
- 15 $[\text{Fe}^{\text{II}}\text{Fe}^{\text{III}}(\text{Ar}^{\text{Tol}}\text{CO}_2)_4(4\text{-}^t\text{Bupy})_2]^+$
- 16 putative $[\text{Fe}^{\text{III}}\text{Fe}^{\text{IV}}(\mu\text{-O})_2]$ species
- 17 $[\text{Fe}^{\text{III}}_2(\mu\text{-OH})_2(\mu\text{-Ar}^{\text{Tol}}\text{CO}_2)_2(\text{Ar}^{\text{Tol}}\text{CO}_2)_2(4\text{-}^t\text{Bupy})_2]$
- 18 $[\text{Fe}^{\text{II}}_2(\mu\text{-Ar}^{\text{Tol}}\text{CO}_2)_2(\text{Ar}^{\text{Tol}}\text{CO}_2)_2(\text{N,N-Bn}_2\text{en})_2]$
- 19 $[\text{Fe}^{\text{III}}_2(\mu\text{-OH})_2(\mu\text{-Ar}^{\text{Tol}}\text{CO}_2)(\text{Ar}^{\text{Tol}}\text{CO}_2)_3(\text{N-Bnen})(\text{N,N-Bn}_2\text{en})]$
- 20 $[\text{Fe}^{\text{II}}_2([\text{G3}]\text{-CO}_2)_4(4\text{-CNpy})_2]$
- 21 $[\text{Fe}^{\text{II}}_2(\mu\text{-H}_2\text{O})_2(\mu\text{-Ar}^{\text{Tol}}\text{CO}_2)_2(\text{Ar}^{\text{Tol}}\text{CO}_2)_2(4\text{-}^t\text{Bupy})_2]$
- 22 $[\text{Fe}^{\text{II}}_2(\mu\text{-H}_2\text{O})_2(\mu\text{-Ar}^{4\text{-FPh}}\text{CO}_2)_2(\text{Ar}^{4\text{-FPh}}\text{CO}_2)_2(\text{THF})_2(\text{H}_2\text{O})]$
- 23 $[\text{Fe}^{\text{II}}_2(\mu\text{-Ar}^{\text{Tol}}\text{CO}_2)_4(4\text{-CNpy})_2]$
- 24 $[\text{Fe}^{\text{II}}_2(\mu\text{-OH})(\text{BPEAN})(\text{SO}_3\text{CF}_3)]^{2+}$
- 25 $[\text{Fe}^{\text{II}}_2(\mu\text{-OH})(\text{BEPEAN})(\text{SO}_3\text{CF}_3)]^{2+}$
- 26 putative $[\text{Fe}^{\text{III}}_2(\text{OOH})]$ species
- 27 $[\text{Fe}^{\text{II}}_2(\text{BPMAN})(\mu\text{-PhCyCO}_2)_2]^{2+}$
- 28 $[\text{Fe}^{\text{II}}_2(\mu\text{-OH})(\mu\text{-Ar}^{\text{Tol}}\text{CO}_2)(\text{bdptz})(\text{CH}_3\text{CN})(\text{SO}_3\text{CF}_3)]^+$
- 29 $[\text{Fe}^{\text{III}}_2(\mu\text{-O})(\mu\text{-Ar}^{\text{Tol}}\text{CO}_2)(\text{bdptz})(\text{acetone})(\text{SO}_3\text{CF}_3)]^{2+}$
- 30 $[\text{Fe}^{\text{II}}_2(\text{Et}_2\text{BCQEB}^{\text{Et}})(\mu\text{-Ar}^{\text{Tol}}\text{CO}_2)_3]^+$
- 31 $[\text{Fe}^{\text{II}}\text{Na}(\text{PIC}_2\text{DET})(\mu\text{-TrpCO}_2)_3]$

- 32 $[\text{Fe}^{\text{II}}_2(\text{L}^{\text{Me,Ph}})_2(\text{THF})_2]$
 33 $[\text{Fe}^{\text{III}}_2(\mu\text{-O})(\text{L}^{\text{Me,Ph}})_2]$
 34 $[\text{Fe}^{\text{II}}_2(\mu\text{-Ar}^{\text{Tol}}\text{CO}_2)_2(\text{PIM})]$
 35 $[\text{Fe}^{\text{II}}_2(\mu\text{-Ph}_3\text{CCO}_2)_2(\text{PIM})]$
 36 $[\text{Fe}^{\text{III}}_2(\mu\text{-O})(\text{Ar}^{\text{Tol}}\text{CO}_2)_2(\text{PIM})]$
 37 $[\text{Fe}^{\text{III}}_2(\mu\text{-OH})_2(\text{Ar}^{\text{Tol}}\text{CO}_2)_2(\text{PIM})]$
 38 $[\text{Fe}^{\text{III}}_4(\mu\text{-OH})_6(\text{PIM})_2(\text{Ar}^{\text{Tol}}\text{CO}_2)_2]$
 39 $[\text{Fe}^{\text{II}}_2(\mu\text{-RCO}_2)_2(\text{bulky PIM})]$
 40 $[\text{Fe}^{\text{III}}_2(\mu\text{-OH})_2(\text{RCO}_2)_2(\text{L})(\text{bulky PIM})]$
 41 $[\text{Fe}^{\text{III}}_4(\mu\text{-OH})_6(\text{bulky PIM})_2(\text{RCO}_2)_2]$

Chapter 2

- A 1-Benzyloxy-2-iodobenzene
 B 2-(2-Benzyloxyphenyl)-5-bromopyridine
 C 5-Bromo-2-(2-methoxyphenyl)pyridine
 D 2-Phenylanisole
 E 2-Bromo-6-phenylanisole
 F 5-Bromo-2-(2-methoxybiphenyl-3-yl)pyridine
 G 1-Benzyloxy-2,6-dibromo-4-methylbenzene
 H 1-Benzyloxy-2,6-dibromo-4-*tert*-butylbenzene
 I 1-Benzyloxy-2-bromo-4-methyl-6-phenylbenzene
 J 1-Benzyloxy-2-bromo-6-phenyl-4-*tert*-butylbenzene
 K 5-Bromo-2-(2-benzyloxy-5-methylbiphenyl-3-yl)pyridine
 L 5-Bromo-2-(2-benzyloxy-5-*tert*-butylbiphenyl-3-yl)pyridine
 M 2-(5-Methylbiphenyl-2-yloxy)tetrahydro-2*H*-pyran
 N 3-Bromo-5-methylbiphenyl-2-ol
 O 1-Benzyloxy-2,6-dibromo-4-methyl-benzene
 P 2-Benzyloxy-3-bromo-5-methylbenzaldehyde
 Q 2-Benzyloxy-5-methyl-3-phenylbenzaldehyde
 R 2-Hydroxy-5-methyl-3-phenylbenzaldehyde
 1 $[\text{Fe}^{\text{II}}_2(\text{L}^{\text{Me,Ph}})_2(\text{THF})_2]$
 2 $[\text{Fe}^{\text{III}}_2(\mu\text{-O})(\text{L}^{\text{Me,Ph}})_2]$

Chapter 3

- A 3,3'-[Oxybis(methylene)]bis(bromobenzene)

B	2,2'-[(Oxybis(methylene))bis(5-methyl-[1,1'-biphenyl]-3',2'-diyl)]bis(oxy)bis(tetrahydro-2H-pyran)
C	Bis(3-(2-hydroxy-5-methylphenyl)benzyl)ether
D	Bis(3-(2-hydroxy-5-methylphenyl-3-carbaldehyde)benzyl)ether
1	$[\text{Fe}^{\text{II}}_2(\text{PIM})(\text{Ph}_3\text{CCO}_2)_2]$
2	$[\text{Fe}^{\text{II}}_2(\text{PIM})(\text{Ar}^{\text{Tot}}\text{CO}_2)_2]$
3	$[\text{Fe}^{\text{III}}_2(\mu\text{-OH})_2(\text{ClO}_4)_2(\text{PIM})(\text{Ar}^{\text{Tot}}\text{CO}_2)\text{Ag}]$
4	$[\text{Fe}^{\text{III}}_2(\mu\text{-OH})(\text{PIM})(\text{Ph}_3\text{CCO}_2)_3]$
5	$[\text{Fe}^{\text{III}}_4(\mu\text{-OH})_6(\text{PIM})_2(\text{Ph}_3\text{CCO}_2)_2]$
6	$[\text{Fe}^{\text{III}}_2(\mu\text{-O})(\text{PIM})(\text{Ar}^{\text{Tot}}\text{CO}_2)_2]$
7	$[\text{Fe}^{\text{III}}_2(\mu\text{-OH})_2(\text{PIM})(\text{Ar}^{\text{Tot}}\text{CO}_2)_2]$
8	$[\text{Fe}^{\text{III}}_4(\mu\text{-OH})_6(\text{PIM})_2(\text{Ar}^{\text{Tot}}\text{CO}_2)_2]$

Chapter 4

1a	$[\text{Fe}^{\text{II}}_2(\text{N-EtHPTB})(\text{Ph}^{12}\text{CO}_2)]^{2+}$
1b	$[\text{Fe}^{\text{II}}_2(\text{N-EtHPTB})(\text{Ph}^{13}\text{CO}_2)]^{2+}$
1a · ¹⁶ O ₂	$[\text{Fe}^{\text{III}}_2(\mu\text{-}^{16}\text{O}_2)(\text{N-EtHPTB})(\text{Ph}^{12}\text{CO}_2)]^{2+}$
1a · ¹⁸ O ₂	$[\text{Fe}^{\text{III}}_2(\mu\text{-}^{18}\text{O}_2)(\text{N-EtHPTB})(\text{Ph}^{12}\text{CO}_2)]^{2+}$
1b · ¹⁶ O ₂	$[\text{Fe}^{\text{III}}_2(\mu\text{-}^{16}\text{O}_2)(\text{N-EtHPTB})(\text{Ph}^{13}\text{CO}_2)]^{2+}$
1b · ¹⁸ O ₂	$[\text{Fe}^{\text{III}}_2(\mu\text{-}^{18}\text{O}_2)(\text{N-EtHPTB})(\text{Ph}^{13}\text{CO}_2)]^{2+}$
[1a · ¹⁶ O ₂] ⁺ H ⁺	$[\text{Fe}^{\text{III}}_2(\mu\text{-}^{16}\text{O}_2)(\text{N-EtHPTB})(\text{Ph}^{12}\text{CO}_2\text{H})]^{3+}$
[1a · ¹⁸ O ₂] ⁺ H ⁺	$[\text{Fe}^{\text{III}}_2(\mu\text{-}^{18}\text{O}_2)(\text{N-EtHPTB})(\text{Ph}^{12}\text{CO}_2\text{H})]^{3+}$
[1b · ¹⁶ O ₂] ⁺ H ⁺	$[\text{Fe}^{\text{III}}_2(\mu\text{-}^{16}\text{O}_2)(\text{N-EtHPTB})(\text{Ph}^{13}\text{CO}_2\text{H})]^{3+}$
[1b · ¹⁸ O ₂] ⁺ H ⁺	$[\text{Fe}^{\text{III}}_2(\mu\text{-}^{18}\text{O}_2)(\text{N-EtHPTB})(\text{Ph}^{13}\text{CO}_2\text{H})]^{3+}$
2	$[\text{Fe}^{\text{II}}_2(\text{N-EtHPTB})(\text{C}_6\text{F}_5\text{CO}_2)]^{2+}$
2 · ¹⁶ O ₂	$[\text{Fe}^{\text{III}}_2(\mu\text{-}^{16}\text{O}_2)(\text{N-EtHPTB})(\text{C}_6\text{F}_5\text{CO}_2)]^{2+}$
2 · ¹⁸ O ₂	$[\text{Fe}^{\text{III}}_2(\mu\text{-}^{18}\text{O}_2)(\text{N-EtHPTB})(\text{C}_6\text{F}_5\text{CO}_2)]^{2+}$
[2 · ¹⁶ O ₂] ⁺ H ⁺	$[\text{Fe}^{\text{III}}_2(\mu\text{-}^{16}\text{O}_2)(\text{N-EtHPTB})(\text{C}_6\text{F}_5\text{CO}_2\text{H})]^{3+}$
[2 · ¹⁸ O ₂] ⁺ H ⁺	$[\text{Fe}^{\text{III}}_2(\mu\text{-}^{18}\text{O}_2)(\text{N-EtHPTB})(\text{C}_6\text{F}_5\text{CO}_2\text{H})]^{3+}$

Chapter 5

1	$[\text{Fe}^{\text{II}}_2(\text{N-EtHPTB})(\text{PhCO}_2)]^{2+}$
1 · ¹⁶ O ₂	$[\text{Fe}^{\text{III}}_2(\mu\text{-}^{16}\text{O}_2)(\text{N-EtHPTB})(\text{PhCO}_2)]^{2+}$
1 · ¹⁸ O ₂	$[\text{Fe}^{\text{III}}_2(\mu\text{-}^{18}\text{O}_2)(\text{N-EtHPTB})(\text{PhCO}_2)]^{2+}$
2 ·O ₂	$[\text{Fe}^{\text{III}}_2(\mu\text{-O}_2)(\text{N-EtHPTB})(\text{OPh}_3)_2]^{3+}$
3 ·O ₂	$[\text{Fe}^{\text{III}}_2(\mu\text{-O}_2)(\text{Ph-bimp})(\text{PhCO}_2)]^{2+}$

4-Br	$[\text{Fe}^{\text{II}}(\text{HB}(iPr)\text{pz})_3\text{Br}]$
4	$[\text{Fe}^{\text{II}}(\text{HB}(iPr)\text{pz})_3(\text{PhCH}_2\text{CO}_2)]$
4-¹⁶O₂	$[\text{Fe}^{\text{III}}_2(\mu\text{-}^{16}\text{O}_2)(\text{HB}(iPr)\text{pz})_2(\text{PhCH}_2\text{CO}_2)_2]$
4-¹⁸O₂	$[\text{Fe}^{\text{III}}_2(\mu\text{-}^{18}\text{O}_2)(\text{HB}(iPr)\text{pz})_2(\text{PhCH}_2\text{CO}_2)_2]$

Appendix A

A	$[\text{Fe}^{\text{III}}\text{Fe}^{\text{IV}}(\mu\text{-O})_2(5\text{-Et-TPA})_2]^{3+}$
B	$[\text{Fe}^{\text{III}}_2(\mu\text{-O})(\text{OH})(\text{H}_2\text{O})(\text{R}_3\text{TPA})_2]^{3+}$
C	$[\text{Fe}^{\text{III}}_2(\mu\text{-O})(\text{OOH})(\text{R}_3\text{TPA})_2]^{3+}$
D	$[\text{Fe}^{\text{IV}}_2(\mu\text{-O})(\text{OH})(\text{O})(\text{R}_3\text{TPA})_2]^{3+}$
E	$[\text{Fe}^{\text{III}}\text{Fe}^{\text{IV}}(\mu\text{-O})(\text{OH})(\text{O})(\text{R}_3\text{TPA})_2]^{2+}$
F	$[\text{Fe}^{\text{III}}\text{Fe}^{\text{IV}}(\text{O})_2(\text{R}_3\text{TPA})_2]^{3+}$
G	$[\text{Fe}^{\text{IV}}_2(\text{O})_2(\text{R}_3\text{TPA})_2]^{4+}$
1	$[\text{Fe}^{\text{III}}_2(\mu\text{-O})(\mu\text{-OH})(\text{R}_3\text{TPA})_2]^{3+}$
2	$[\text{Fe}^{\text{III}}_2(\mu\text{-O})(\text{OH})(\text{CH}_3\text{CN})(\text{R}_3\text{TPA})_2]^{3+}$
3	$[\text{Fe}^{\text{III}}_2(\mu\text{-O})(\mu\text{-CH}_3\text{CONH})(\text{R}_3\text{TPA})_2]^{3+}$
4A	$[\text{Fe}^{\text{III}}_2(\mu\text{-O})(\mu\text{-CH}_3\text{CO}_2)(\text{R}_3\text{TPA})_2](\text{ClO}_4)_3 \cdot (\text{CH}_3\text{CN})_3$
4B	$[\text{Fe}^{\text{III}}_2(\mu\text{-O})(\mu\text{-CH}_3\text{CO}_2)(\text{R}_3\text{TPA})_2](\text{ClO}_4)_3 \cdot (\text{CH}_3\text{CN})_{2.5}(\text{Et}_2\text{O})_{0.5}$

Chapter 1

Rationally Designed Synthetic Mimics of Diiron Protein Active Sites: A Chronological Perspective

1.1. Introduction

Understanding the role of metal ions in dictating protein structure and function is a central theme in bioinorganic research.¹⁻⁴ In addition to the arsenal of modern physical techniques and instrumentation available for studies of biomolecules,⁵ synthetic modeling has been pursued as a complementary tool to interrogate complex biological systems.⁶ It provides a convenient simplification of elaborate macromolecules in a real, rather than a virtual (e.g. computational),⁷ platform. By reducing a metalloprotein to its functional core, it is possible to gain insight into whether the chemistry that occurs at the metal center is predominantly a result of the inorganic component alone or a consequence of the protein complex as a whole. Synthetic modeling also provides an opportunity to access chemistry that has not yet been achieved artificially using simple biological building blocks under ambient conditions. Some of the most remarkable transformations in nature, such as nitrogen fixation,⁸⁻¹¹ water splitting,¹² and hydrogen production,¹³ are performed by metalloenzymes. Reproducing such chemical reactivity in an efficient manner would not only revolutionize the chemical industry but also provide new sustainable sources of energy.¹⁴ Finally, the synthetic challenges of modeling chemistry will push the limits of current synthetic methodologies. Although natural product synthesis has been largely aided by an understanding of organic chemistry,¹⁵ inorganic synthesis is not governed by the same set of well-defined rules.¹⁶ Controlling the nuclearity and kinetic stability of metal clusters or components using organic ligands is still a significant challenge.

Small-molecule metalloprotein mimics are prepared using one of two design strategies.⁴ The *biomimetic* approach seeks to duplicate the active site structure as faithfully as possible, particularly in matching the identity and geometric arrangement of ligands in the primary coordination sphere. The *bio-inspired* approach, on the other hand, only requires that the

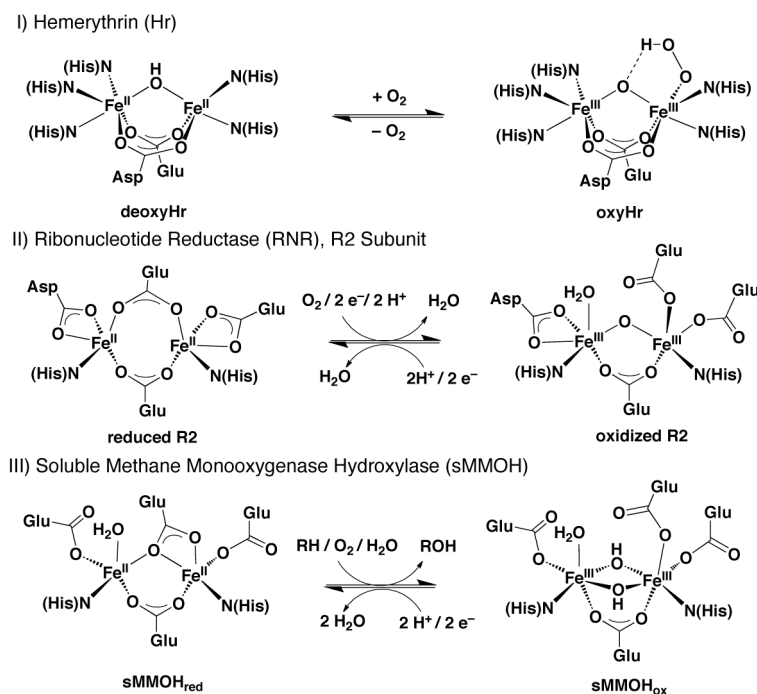
synthetic model shares some common features with those of the protein core, unrestricted by the type or position of ligands coordinated to the metal center. For modeling studies, the former is preferred over the latter because biomimetic complexes more accurately reproduce the characteristics of the biological center under investigation.

The following is a chronological account of the strategies and tactics employed in the Lippard group to prepare structural and functional mimics of diiron protein active sites. This work will describe the rational basis for ligand design and selection as well as the notable findings that resulted from studies of the various model systems. The reader is referred elsewhere for more general reviews of synthetic diiron modeling.¹⁷⁻²²

1.2. Non-Heme Diiron Proteins

Non-heme carboxylate-bridged diiron proteins are involved in essential physiological processes.^{23,24} Although their roles vary, the first step in their respective reaction mechanisms involves binding and activation of dioxygen. In hemerythrin (Hr),²⁵ the O₂ molecule coordinates to a single iron site and acquires two electrons and a proton to generate a (hydroperoxo)diiron(III) unit (Scheme 1.1, top). This process is reversible and is the basis for O₂ transport in some marine invertebrates. Unlike hemerythrin, ribonucleotide reductase (RNR)²⁶ and bacterial multi-component monooxygenases (BMMs)²⁷ consume dioxygen to perform catalytic reactions (Scheme 1.1, middle and bottom, respectively). Activation of O₂ by these enzymes leads to formation of (peroxo)diiron(III) or di(μ -oxo)diiron(IV) complexes that are capable of oxidizing organic moieties.²⁸⁻³² The high-valent diiron intermediate in the R2 subunit of RNR generates a tyrosyl radical that initiates the first step in DNA biosynthesis, whereas that in the hydroxylase component of the BMMs is responsible for inserting an oxygen atom into the

C–H bond of hydrocarbon substrates. The most well-studied member of the BMM family is soluble methane monooxygenase (sMMO),³³ which is unique for its ability to hydroxylate methane to methanol. Recent studies have revealed that other classes of enzymes containing carboxylate-bridged diiron motifs also exist in biology.³⁴⁻³⁶



Scheme 1.1. Dioxygen reactivity of hemerythrin (Hr, top), ribonucleotide reductase (RNR, middle), and soluble methane monooxygenase hydroxylase (sMMOH, bottom). The active site structures of the proteins in various redox states are depicted.

These diiron proteins contain two iron atoms that are coordinated by imidazole and carboxylate residues, where at least one of the carboxylate groups bridges the two metal centers.²³ The structural similarities between the active sites of this protein family indicate that their functional differences are derived from variations in their Asp/Glu/His amino acid combinations and/or careful tuning of their tertiary and quaternary protein structures. Discerning

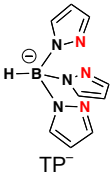
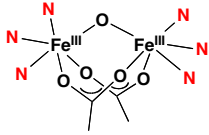
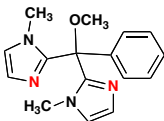
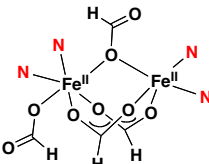
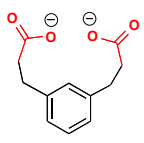
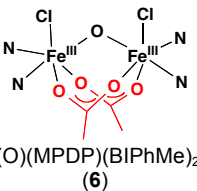
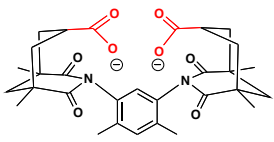
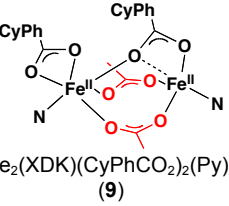
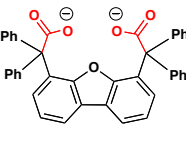
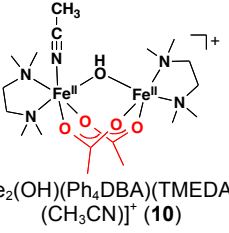
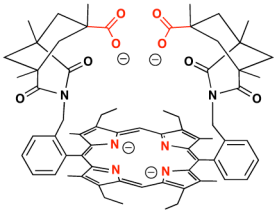
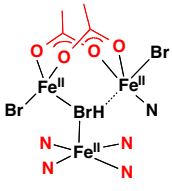
the factors that contribute to their mechanism of action is an important goal in synthetic model studies.^{19,20}

1.3. Mononucleating *N*-Heterocyclic Ligands

The first successful attempt to prepare a mimic of the Hr core was achieved using tris(pyrazolyl)borate (TP⁻) (Table 1.1),^{37,38} a tripodal ligand commonly employed in inorganic coordination chemistry. Reaction of TP⁻, iron(III), and acetate led to the spontaneous self-assembly of [Fe^{III}₂(μ-O)(μ-CH₃CO₂)₂(TP)₂] (**1**), the structure of which closely matches that of metHr, the inactive form of Hr.²⁵ Reaction of **1** with an H⁺ donor led to formation of [Fe^{III}₂(μ-OH)(μ-CH₃CO₂)₂(TP)₂]⁺ (**2**), a stable protonated analogue of **1**.³⁹ Spectroscopic and magnetic measurements of the (μ-oxo)di(μ-carboxylato)diiron(III) and (μ-hydroxo)di(μ-carboxylato)diiron(III) compounds provided, for the first time, benchmarks for identifying such units in biology.^{40,41} When **1** was exposed to H₂¹⁸O, the ¹⁶O bridge was readily exchanged for ¹⁸O, indicating that a lack of exchange with water in the protein is due to inaccessibility of H₂O to the diiron core rather than an intrinsic property of the [Fe^{III}₂O] unit. An undesirable feature of **1** and **2** is that the facial capping nature of the TP⁻ ligands blocks having open sites for binding of O₂. Furthermore, reduction of the diiron(III) species resulted in irreversible dissociation to monoiron complexes.³⁸

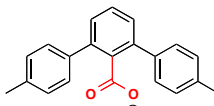
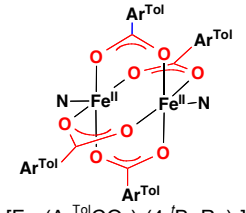
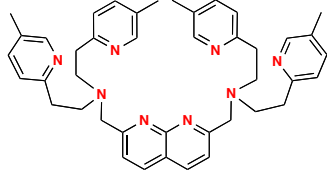
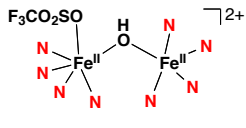
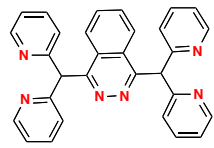
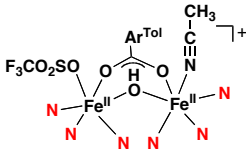
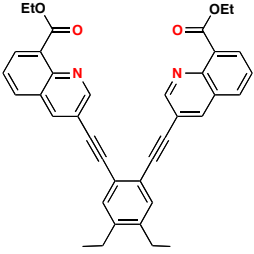
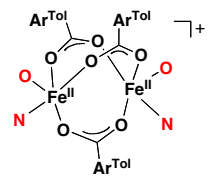
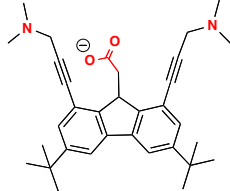
To access the asymmetric iron centers in Hr, the denticity of the capping ligand was reduced from three to two, using bis(1-methylimidazol-2-yl)phenylmethoxymethane (BIPhMe) (Table 1.1).^{42,43} Stirring iron(II) formate with BIPhMe in a methanol solution provided [Fe^{II}₂(μ-HCO₂)₃(HCO₂)(BIPhMe)₂] (**3**). X-ray crystallography revealed a dinuclear structure with both five- and six-coordinate iron sites, in which each metal ion is bound by a BIPhMe ligand and bridged by three formate groups. A terminal acetate group completes the coordination sphere of

Table 1.1. Various Ligands Employed to Prepare Diiron Protein Model Complexes.

Ligand/ Example of Iron Complex*	Desirable Characteristics	Undesirable Characteristics	Reference No.
Mononucleating N-Heterocyclic Ligands			
 <p>TP⁻</p>	 <p>[Fe₂(O)(CH₃CO₂)₂(TP)₂] (1)</p>	<ul style="list-style-type: none"> • Forms stable tripodal chelate with iron • N-donors similar to histidine residues • Easy to synthesize 	<ul style="list-style-type: none"> • Capping unit restricts binding to the metal center • Does not enforce dinuclearity <p>37-39, 41</p>
 <p>BIPhMe</p>	 <p>[Fe₂(HCO₂)₄(BIPhMe)₂] (3)</p>	<ul style="list-style-type: none"> • Contains biomimetic imidazole groups • Bidentate chelate allows assembly of asymmetric diiron unit with open sites • Easy to synthesize 	<ul style="list-style-type: none"> • Does not enforce dinuclearity <p>42, 43</p>
Dicarboxylate Ligands			
 <p>MPDP²⁻</p>	 <p>[Fe₂(O)(MPDP)(BIPhMe)₂Cl₂] (6)</p>	<ul style="list-style-type: none"> • Enables assembly of [Fe^{III}₂O] units that could not be accessed using simple carboxylates 	<ul style="list-style-type: none"> • Does not enforce dinuclearity <p>44, 45</p>
 <p>XDK²⁻</p>	 <p>[Fe₂(XDK)(CyPhCO₂)₂(Py)₂] (9)</p>	<ul style="list-style-type: none"> • Supports a diiron core with open sites for substitution with external bases • Maintains a dinuclear structure upon reaction with dioxygen 	<ul style="list-style-type: none"> • Endo positioning of carboxylates may be too geometrically restrictive • Does not prevent polynuclear aggregation <p>49-57</p>
 <p>Ph₄DBA²⁻</p>	 <p>[Fe₂(OH)(Ph₄DBA)(TMEDA)₂(CH₃CN)]⁺ (10)</p>	<ul style="list-style-type: none"> • Supports an [Fe^{II}₂(OH)] core with an open metal binding site • Stabilizes an oxygenated adduct to the diiron center 	<ul style="list-style-type: none"> • Does not prevent formation of tetranuclear complexes <p>60, 61</p>
 <p>PDK⁴⁻</p>	 <p>[Fe₃(PDK)(Lut)(Br)₂(HBr)] (12)</p>	<ul style="list-style-type: none"> • Provides both a porphyrin and non-porphyrin binding sites 	<ul style="list-style-type: none"> • Does not prevent formation of polyiron clusters • Difficult to prepare in gram quantities <p>62-64</p>

* The donor atoms highlighted in red in the iron complexes (second column) are derived from the donor groups, also shown in red, of the featured ligand (first column).

Table 1.1. (Continued)

Ligand/ Example of Iron Complex*	Desirable Characteristics	Undesirable Characteristics	Reference No.	
Terphenylcarboxylate Ligands				
 $\text{Ar}^{\text{Tol}}\text{CO}_2^-$	 $[\text{Fe}_2(\text{Ar}^{\text{Tol}}\text{CO}_2)_4(4\text{-BuPy})_2]$ (14A)	<ul style="list-style-type: none"> • Forms diiron complexes in the presence of Fe(II) salts and an appropriate base • Stabilizes high-valent iron species • Easy to synthesize 	<ul style="list-style-type: none"> • The steric encumbrance of the 2,6-aryl groups restricts access to the diiron core. • Does not prevent formation of polyiron species 	69-72, 74-90
Dinucleating Polynitrogen Ligands				
 BPEAN	 $[\text{Fe}_2(\text{OH})(\text{BPEAN})(\text{SO}_3\text{CF}_3)]^{2+}$ (24)	<ul style="list-style-type: none"> • Contains a "masked carboxylate" to bridge two metal centers • Stabilizes diiron species in multiple oxidation states 	<ul style="list-style-type: none"> • Nitrogen-rich, rather than carboxylate-rich 	95-98
 bdptz	 $[\text{Fe}_2(\text{OH})(\text{bdptz})(\text{Ar}^{\text{Tol}}\text{CO}_2)(\text{SO}_3\text{CF}_3)(\text{CH}_3\text{CN})]^+$ (28)	<ul style="list-style-type: none"> • Forms very stable bimetallic compounds 	<ul style="list-style-type: none"> • Nitrogen-rich, rather than carboxylate-rich 	99, 100
syn N-Donor Ligands				
 $\text{Et}_2\text{BCQEB}^{\text{Et}}$	 $[\text{Fe}_2(\text{Ar}^{\text{Tol}}\text{CO}_2)_3(\text{Et}_2\text{BCQEB}^{\text{Et}})]^+$ (30)	<ul style="list-style-type: none"> • Enforces the syn stereochemistry of nitrogen donors relative to the Fe-Fe vector • Accommodates binding of external carboxylates to the diiron core 	<ul style="list-style-type: none"> • Neutral oxygen donors, rather than anionic • Quinoline ester groups do not sufficiently stabilize the iron centers 	101, 102-108
 DAFA^-	N.A.	<ul style="list-style-type: none"> • Contains a bridging carboxylate unit in addition to two adjacent amine groups 	<ul style="list-style-type: none"> • Not sufficiently pre-organized, could not metallate with iron • No clear advantage over $\text{Et}_2\text{BCQEB}^{\text{Et}}$ design 	109

* The donor atoms highlighted in red in the iron complexes (second column) are derived from the donor groups, also shown in red, of the featured ligand (first column).

Table 1.1. (Continued)

Ligand/ Example of Iron Complex*	Desirable Characteristics	Undesirable Characteristics	Reference No.	
Macrocyclic Ligands				
<p>MAr^{Tol}CO₂²⁻</p>	N.A.	<ul style="list-style-type: none"> • May help control the nuclearity of the resulting iron complex 	113	
<p>PIM²⁻</p>	<p>[Fe₂(Ar^{Tol}CO₂)₂(PIM)] (34)</p>	<ul style="list-style-type: none"> • Supports a carboxylate-bridged diiron(II) unit • Maintains a dinuclear core upon reaction with O₂ • Can be sterically tuned without obstructing access to the metal binding pocket. 	<ul style="list-style-type: none"> • Does not prevent formation of tetrairon species • Phenolate and imine donors are not biomimetic 	114

* The donor atoms highlighted in red in the iron complexes (second column) are derived from the donor groups, also shown in red, of the featured ligand (first column).

the octahedral iron atom. Complex **3** reacts instantaneously with dioxygen to give [Fe^{III}₂(μ-O)(μ-HCO₂)₂(HCO₂)₂(BIPhMe)₂] (**4**), with no detectable intermediates. Manometric measurements indicated that 0.5 equiv of O₂ was consumed per diiron(II) complex, suggesting that **4** is formed through a tetranuclear dioxygen species. Unfortunately, the behavior of **3** toward dioxygen is markedly different than that of deoxyHr, which binds O₂ reversibly (Scheme 1.1, top).²⁵

1.4. Dicarboxylate Ligands

To increase the structural integrity of the model compounds, several dicarboxylate ligands were explored as dinucleating platforms. The first of these is *m*-phenylenedipropionate (MPDP²⁻, Table 1.1),^{44,45} which was selected because the distance between its β-methylene carbon atoms matches the 6 Å separation between the acetate methyl carbons in [Fe^{III}₂(μ-O)(μ-CH₃CO₂)₂(TP)₂] (**1**).³⁷ The use of MPDP²⁻ facilitated synthesis of [Fe^{III}₂(μ-O)(MPDP)(bpy)₂Cl₂]

(**5**) (bpy = 2,2'-bipyridine) and $[\text{Fe}^{\text{III}}_2(\mu\text{-O})(\text{MPDP})(\text{BIPhMe})_2\text{Cl}_2]$ (**6**, Table 1.1), complexes that could not be obtained from self-assembly with simple monocarboxylate anions. The cyclic voltammogram of $[\text{Fe}^{\text{III}}_2(\mu\text{-O})(\text{MPDP})(\text{TP})_2]$ (**7**), an analogue of **1**, showed that mononuclear $[\text{Fe}^{\text{II}}(\text{TP})_2]$ and $[\text{Fe}^{\text{III}}(\text{TP})_2]^+$ species were generated upon electrochemical reduction and oxidation, respectively. These results demonstrated that linking the carboxylate groups using MPDP^{2-} does not impart additional stability to the diiron models.

To obtain a more stable bridging framework, *m*-xylenediamine bis(Kemp's triacid)imide (H_2XDK , Table 1.1), a compound developed from studies of molecular recognition in organic chemistry,^{46,47} was employed. The rigid conformation of the carboxylate units in XDK^{2-} provides a well-defined cleft for assembly of homo- and heterodimetallic complexes.⁴⁸⁻⁵¹ A diiron(III) compound, $[\text{Fe}^{\text{III}}_2(\mu\text{-O})(\text{XDK})(\text{CH}_3\text{OH})_5(\text{H}_2\text{O})](\text{NO}_3)_2$ (**8**), was readily prepared from iron(III) nitrate and XDK^{2-} .⁵² Kinetic studies of the substitution of 2,2'-bipyridine or *N*-methylimidazole with the coordinated solvents in **8** suggested that anion binding and exchange at the active site of hemerythrin proceed with rates similar to those exhibited by small-molecules; thus, the protein scaffold of Hr does not alter the intrinsic rate of terminal ligand exchange at the diiron center. Preparation of a series of pseudohalide bound diiron(III) compounds, with the formula $[\text{Fe}^{\text{III}}_2(\mu\text{-O})(\text{XDK})(\text{bpy})_2(\text{X})_2]$ (where $\text{X} = \text{NCS}^-$, NCSe^- , or N_3^-), allowed detailed studies of the spectroscopic signatures of molecules with terminal ligation to carboxylate-bridged diiron units.⁵³ A notable discovery is that the appearance of only one asymmetric $^{15}\text{NNN}^-$ stretch is not sufficient to discount the possibility of a terminally coordinated azide group, for isotopically shifted peaks may occur too close to one another in energy to be resolved.

The XDK^{2-} ligand also supports carboxylate-bridged diiron(II) units with the general composition $[\text{Fe}^{\text{II}}_2(\text{XDK})(\mu\text{-RCO}_2)(\text{RCO}_2)(\text{N-donor})_2]$, where $\text{R} = t\text{-Bu-}$ (pivalate), PhCy- (1-

phenylcyclohexylcarboxylate), Ph- (benzoate), *i*Pr- (isobutyrate), or *t*BuCH₂- (1-*tert*-butylacetate); *N*-donor = py (pyridine), 3-Fpy (3-fluoropyridine), *N*-MeIm (*N*-methylimidazole), or *N*-*t*BuIm (*N*-*tert*-butylimidazole).⁵⁴⁻⁵⁶ More sterically-protecting XDK²⁻ variants, containing either propyl (PXDK²⁻) or benzyl (BXDK²⁻) substituents in place of the methyl groups on the Kemp's triacid moiety, were also successfully employed to assemble similar diiron(II) compounds. The asymmetric bridging mode of the ancillary carboxylate to the diiron(II) core is determined by both steric and electronic factors.⁵⁶ X-ray structural studies suggested that greater steric repulsion, between XDK²⁻ and the external carboxylate, and more basic *N*-donors favor a *syn,syn*-bidentate bridging mode of the ancillary carboxylate rather than a *syn,anti*-monodentate one. For complexes that have sufficiently bulky groups, such as [Fe^{II}₂(XDK)(μ -PhCyCO₂)(PhCyCO₂)(py)₂] (**9**, Table 1.1), exposure to O₂ led to formation of stable peroxo adducts at low temperature.⁵⁶ Although these (peroxo)diiron(III) species could not be crystallized for X-ray diffraction analysis, resonance Raman measurements indicate that the dioxygen molecule is bound in a μ -1,2 fashion. Reactivity studies of the [Fe^{III}₂(O₂)] units revealed that they are nucleophilic,⁵⁷ rather than electrophilic like the oxygenated intermediates in the BMMs.^{58,59} When warmed above -65°C, the [Fe^{III}₂(O₂)] species rapidly decayed, initiating a radical chain pathway that oxidized solvents with weak to intermediate C–H bond strengths. Despite having the same ligand stoichiometry as that of the (peroxo)diiron(III) species in sMMOH (H_{peroxo}) and related enzymes,³³ the synthetic analogues do not reproduce the substrate scope, product selectivity, or reaction mechanism of the diiron monooxygenases. It is possible that the doubly-bridging XDK²⁻ ligand is too rigid in the synthetic models to achieve an H_{peroxo}-like structure, a prerequisite that may be necessary to attain the high oxidizing power of the oxygenated diiron protein intermediates.

The search for a ligand that is sufficiently pre-organized yet structurally flexible led to examination of other dicarboxylate motifs. One potential candidate was the compound dibenzofuran-4,6-bis(diphenylacetate) ($\text{Ph}_4\text{DBA}^{2-}$, Table 1.1).^{60,61} Similar to XDK^{2-} , $\text{Ph}_4\text{DBA}^{2-}$ has two orthogonal carboxylate groups that can support an $\{\text{Fe}^{\text{III}}_2\text{O}\}^{4+}$ core. The $\text{Ph}_4\text{DBA}^{2-}$ ligand, however, has more conformational freedom because the C–C bond between its carboxylate groups and the dibenzofuran linker can rotate freely. The compound $[\text{Fe}^{\text{II}}_2(\mu\text{-OH})(\text{Ph}_4\text{DBA})(\text{TMEDA})_2(\text{CH}_3\text{CN})]^{+}$ (**10**, Table 1.1), where TMEDA = *N,N,N',N'*-tetramethylethylenediamine, was prepared from $\text{Ph}_4\text{DBA}^{2-}$, triethylamine, TMEDA, and iron(II) triflate. The structure of **10** is unique because it is the first synthetic complex to reproduce the (μ -hydroxo)di(μ -carboxylato)diiron(II) core of deoxyHr²⁵ with an open coordination site for binding of a terminal ligand. When **10** was treated with dioxygen at $-78\text{ }^\circ\text{C}$ in the presence of 3 equiv of *N*-MeIm in CH_2Cl_2 or in neat EtCN, a red-orange species (**11**) appeared that decayed after ~ 10 min. The UV-vis, Mössbauer, resonance Raman, and EXAFS spectra of the transient intermediate closely match those of oxyHr (Scheme 1.1, top), strongly suggesting that **11** contains a (hydroperoxo)(μ -oxo)diiron(III) unit. Unfortunately, oxygenation of **10** is irreversible and led to decomposition to a tetrairon(III) cluster.

A fourth dicarboxylate ligand, α,α -5,15-bis(α -*N*-(Kemp's triacid imido)-*o*-tolyl)-2,8,12,18-tetraethyl-3,7,13,17-tetramethylporphyrin (H_4PDK , Table 1.1), was prepared by replacing the *m*-xylenediamine linker of XDK^{2-} with a porphyrin unit.⁶² The construct was designed so that activation of O_2 within a trimetallic cavity would offer the possibility of supplying additional electrons to the carboxylate-bridged diiron centers, much like the reductase component of sMMO.³³ A triiron(II) compound, $[\text{Fe}^{\text{II}}_3(\text{PDK})(\text{Lut})(\text{Br})_2(\text{HBr})]$ (**12**, where Lut = 2,6-lutidine, Table 1.1), was successfully prepared from metallation with iron(II) bromide.⁶³

When iron(II) chloride was used instead of iron(II) bromide in the preparation, a mixed-valent heptairon chloride cluster was isolated.⁶⁴ Due to the complicated nature of the iron complexes of PDK⁴⁻, no further studies were pursued using this ligand.

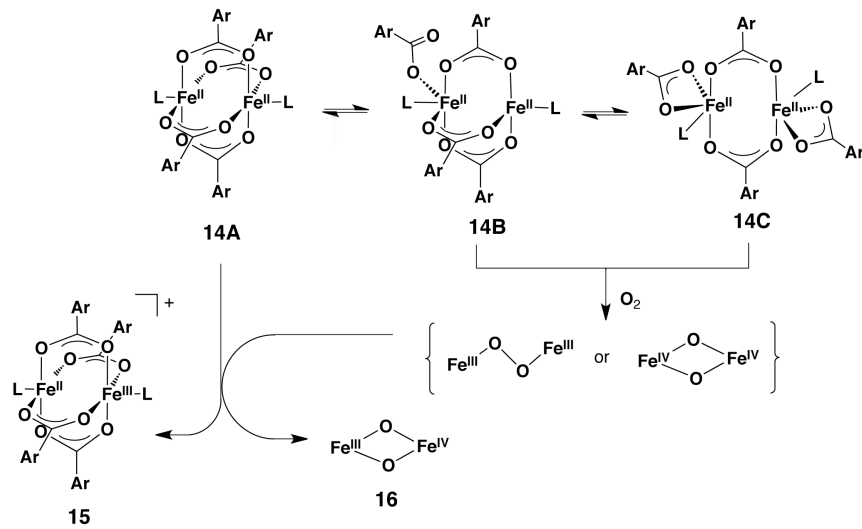
The more pre-organized dicarboxylate ligands XDK²⁻ and Ph₄DBA²⁻ impart enhanced stability to their respective diiron complexes and allow detection of O₂ adducts at low temperature. A common problem with the dicarboxylate ligands, however, is that they do not prevent aggregation of the diiron compounds into oligo- and polynuclear clusters,⁶⁵ an undesired reaction that is detrimental to the synthesis of accurate models. Furthermore, the conformationally rigid ligand framework may be a liability in terms of accessing oxygenated diiron species that could further react with external substrates.

1.5. Terphenylcarboxylate Ligands

To reduce the geometric constraints of the ligand platform, bulky terphenylcarboxylates were employed. Unlike simple benzoates that form polynuclear clusters with iron,⁶⁶⁻⁶⁸ the sterically-hindered 2,6-bis(*p*-tolyl)benzoate (Ar^{Tol}CO₂⁻, Table 1.1) and 2,6-bis(*p*-fluorophenyl)benzoate (Ar^{4-FPh}CO₂⁻) self-assemble into discrete diiron compounds in the presence of iron salts and an appropriate base.^{69,70} The first iron complex synthesized in this series is [Fe^{II}₂(μ-Ar^{Tol}CO₂)₂(Ar^{Tol}CO₂)₂(THF)₂] (**13**), which adopts a windmill structure with two *syn,syn*-bridging carboxylates and two bidentate terminal carboxylates in the solid-state. The coordinated THF molecules in **13** can be readily substituted with *N*-donors to afford the corresponding [Fe^{II}₂(Ar^{Tol}CO₂)₄(*N*-donor)₂] complex. Use of 4-*tert*-butylpyridine (4-^tBuPy) as the ancillary base provided a quadruply-bridged [Fe^{II}₂(Ar^{Tol}CO₂)₄(4-^tBuPy)₂] (**14A**, Table 1.1) paddlewheel compound. Interconversion between the windmill and paddlewheel structures in

solution was demonstrated by variable temperature NMR spectroscopy.⁷⁰ Oxygenation of **14A** at -78°C resulted in irreversible formation of a deep green intermediate that decayed to a $[\text{Fe}^{\text{III}}_2(\mu\text{-OH})_2(\mu\text{-Ar}^{\text{Tol}}\text{CO}_2)_2(\text{Ar}^{\text{Tol}}\text{CO}_2)_2(4\text{-}^t\text{Bupy})_2]$ (**17**) product.^{71,72} The di(μ -hydroxo)diiron(III) unit of **17** closely resembles that of the oxidized core of sMMOH.⁷³ Characterization of the green intermediate revealed two mixed-valent complexes, a diiron(II,III) (**15**) and a diiron(III,IV) (**16**) species, that are present in equal amounts. EPR and magnetic Mössbauer measurements indicated that **15** and **16** have spin states of 9/2 and 1/2, respectively. The assignment of **15** as a diiron(II,III) compound was confirmed by comparing its spectroscopic properties to those of a crystallographically characterized $[\text{Fe}^{\text{II}}\text{Fe}^{\text{III}}(\text{Ar}^{\text{Tol}}\text{CO}_2)_4(4\text{-}^t\text{Bupy})_2]$ complex.^{74,75} As shown in the proposed mechanism in Scheme 1.2, reaction of **14A** with dioxygen proceeds through a carboxylate shift, in which either one or two of the bridging $\text{Ar}^{\text{Tol}}\text{CO}_2^-$ groups rearrange to adopt terminal positions, providing an open site for O_2 . Binding of dioxygen to **14B** or **14C** affords a (μ -peroxo)diiron(III) or a di(μ -oxo)diiron(IV) intermediate that further reacts with **14A**, giving an equal mixture of **15** and **16**. This reaction is noteworthy because it is the first synthetic example in which treatment of a diiron(II) precursor with O_2 resulted in formation of an iron(IV) species, a process that parallels the chemistry of several non-heme diiron enzymes.²³

Although the steric hindrance provided by the terphenylcarboxylates could suppress undesired reactions involving bond-making processes, it could not eliminate deleterious intermolecular electron transfer (ET) reactions.^{71,72} To prevent the paddlewheel diiron(II) complex from quenching the oxygenated intermediates, bidentate ancillary ligands were used to favor the assembly of windmill rather than paddlewheel species. The doubly-bridged $[\text{Fe}^{\text{II}}_2(\mu\text{-Ar}^{\text{Tol}}\text{CO}_2)_2(\text{Ar}^{\text{Tol}}\text{CO}_2)_2(N,N\text{-Bn}_2\text{en})_2]$ (**18**) complex, where $N,N\text{-Bn}_2\text{en} = N,N\text{-dibenzylethylenediamine}$, was successfully prepared to test this strategy.^{76,77} Compound **18**



Scheme 1.2. A proposed mechanism for the reaction of $[\text{Fe}^{\text{II}}_2(\mu\text{-Ar}^{\text{Tol}}\text{CO}_2)_4(4\text{-}^t\text{Bupy})_2]$ (**14A**) with O₂.^{71,72}

reacted with dioxygen, but instead of producing a green intermediate, *N*-dealkylation occurred affording $[\text{Fe}^{\text{III}}_2(\mu\text{-OH})_2(\mu\text{-Ar}^{\text{Tol}}\text{CO}_2)(\text{Ar}^{\text{Tol}}\text{CO}_2)_3(\text{N-Bnen})(\text{N,N-Bn}_2\text{en})]$ (**19**) (where *N*-Bnen = *N*-benzylethylenediamine) and benzaldehyde. Isotopic labeling with ¹⁸O₂ demonstrated that the oxygen atom in benzaldehyde was derived from dioxygen. When a non-coordinating *N,N*-Bn₂en analogue, such as *N,N*-dibenzylpropylamine, was treated with O₂ in the presence of either mononuclear or dinuclear iron(II) complexes, the yield of benzaldehyde was significantly reduced. Detailed mechanistic studies suggested that oxidative *N*-dealkylation of **18** involved single electron transfer, proton abstraction, and rearrangement.^{78,79} The fortuitous discovery that high-valent diiron terphenylcarboxylate complexes could be intercepted by *tethered substrates* enabled studies of the reactivity of oxygenated intermediates toward organic moieties. Attachment of benzyl,^{80,81} ethyl,⁸¹ ethynyl,⁸² phenoxy,⁸³ phosphido,^{80,84} or sulfido^{84,85} units to an amine or pyridine ligand afforded a series of tethered substrates that could be easily incorporated into **13**, giving the corresponding diiron(II) compounds. After exposing the substrate/diiron(II)

complex to O₂, the reaction products were analyzed by gas chromatography-mass spectrometry (GC-MS). Chart 1.1 depicts the substrates that were successfully oxidized by this method. When 2-pyridyldiphenylphosphine (2-Ph₂Ppy) was employed in excess, catalytic oxidation to 2-pyridyldiphenylphosphine oxide (2-Ph₂P(O)py) was observed.^{80,84} Because external non-coordinating substrates cannot be oxidized by [Fe₂(Ar^{Tol}CO₂)₄(THF)₂]/O₂, these results suggest that intramolecular reactions are preferred over intermolecular ones in the terphenylcarboxylate diiron complexes. This behavior is most likely due to reaction of the active diiron oxidant with solvent or adventitious reductants before it can be intercepted by the desired external substrates.

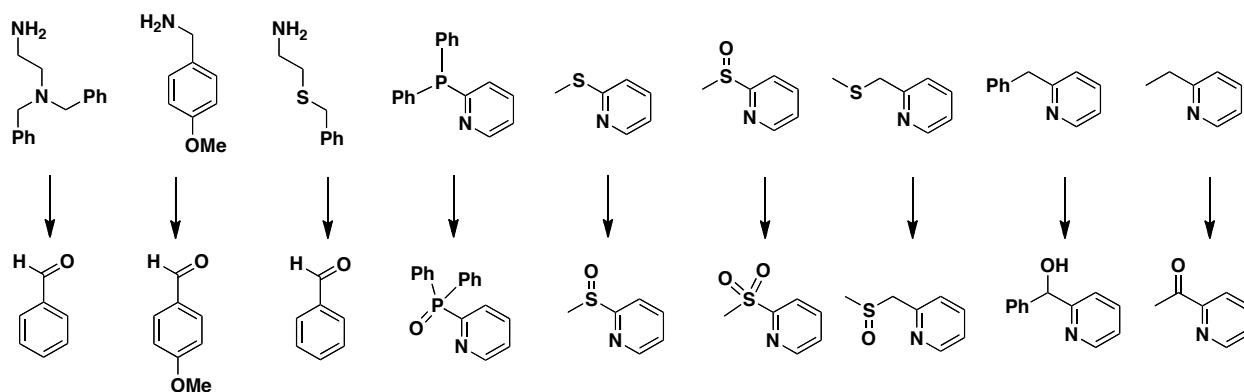


Chart 1.1. The tethered substrates that were successfully oxidized with O₂ when integrated into a diiron(II) terphenylcarboxylate complex. The starting substrate is depicted on top and the product isolated after oxygenation is shown directly below.

One strategy to prevent premature deactivation of the oxygenated diiron intermediate was to attach dendritic groups to the terphenylcarboxylate ligand that would shield the diiron core from participating in intermolecular ET reactions.⁸⁶ The complex [Fe^{II}₂([G-3]CO₂)₄(4-CNpy)₂] (**20**) (where [G-3]CO₂⁻ = third-generation dendrimer-appended terphenylcarboxylate and 4-CNpy = 4-cyanopyridine) was synthesized in a manner analogous to that for the simpler diiron(II) compounds. Treatment of **20** with dioxygen resulted in formation of a diiron(II,III)

intermediate that was postulated to have a superoxo moiety. This colored intermediate is capable of oxidizing dihydroanthracene, albeit in only modest yields.

The influence of water on the structure and reactivity of the diiron(II) terphenylcarboxylate compounds was also examined. Treatment of **14A** with excess water afforded a diaqua-bridged diiron(II) species, $[\text{Fe}^{\text{II}}_2(\mu\text{-H}_2\text{O})_2(\mu\text{-Ar}^{\text{Tol}}\text{CO}_2)_2(\text{Ar}^{\text{Tol}}\text{CO}_2)_2(4\text{-}t\text{Bupy})_2]$ (**21**), in which the terminal carboxylates exhibit strong hydrogen-bonding interactions with the bridging waters.⁸⁷ In addition to having a diaqua bridge, a third H₂O molecule occupies a terminal position in $[\text{Fe}^{\text{II}}_2(\mu\text{-H}_2\text{O})_2(\mu\text{-Ar}^{4\text{-FPh}}\text{CO}_2)(\text{Ar}^{4\text{-FPh}}\text{CO}_2)_3(\text{THF})_2(\text{H}_2\text{O})]$ (**22**).⁸⁸ When a large excess of water was added to **22** complete dissolution occurred, giving the fully aquated $[\text{Fe}^{\text{II}}(\text{H}_2\text{O})_2]^{2+}$ cation. These observations suggest that the accessibility of water within diiron enzyme active sites may be a control element for achieving different functions using a common structural motif. Furthermore, the presence of excess amounts of water may be destructive to the integrity of the carboxylate-bridged diiron core. Stopped-flow kinetic studies using $[\text{Fe}^{\text{II}}_2(\mu\text{-Ar}^{\text{Tol}}\text{CO}_2)_4(4\text{-CNpy})_2]$ (**23**) showed that it reacts with H₂O ~1000 times faster than with O₂ and that aquated **23** reacts with O₂ ~10 times faster than anhydrous **23**.^{89,90} Coordination of water to **23** most likely induces rearrangement from a paddlewheel to a windmill complex, facilitating more rapid binding of dioxygen to the diiron centers.

The iron chemistry of a variety of other monocarboxylate ligands was evaluated. When the steric bulk of the terphenylcarboxylate was increased using 2,6-bis(*p*-*tert*-butyl)phenyl)benzoate ($\text{Ar}^{\text{tBu}}\text{CO}_2^-$), reaction with iron(II) salts afforded a tetrairon cluster.⁹¹ When the steric demand of the carboxylate was reduced using 2-biphenylcarboxylate, an assortment of di-, tri-, and tetranuclear species was obtained.⁹² Replacing the

terphenylcarboxylate with 9-triptycenecarboxylate resulted in diiron paddlewheel complexes that could not convert to the more reactive windmill structure.⁹³

Terphenylcarboxylate ligands are a simple alternative to the conformationally restricting dicarboxylate compounds. Diiron complexes derived from $\text{Ar}^{\text{Tol}}\text{CO}_2^-$ or $\text{Ar}^{4\text{-FPh}}\text{CO}_2^-$ can access high valent iron(IV) species from O_2 , which are capable of hydroxylating hydrocarbons, a first for synthetic modeling studies. Although the 2,6-aryl substituents of $\text{Ar}^{\text{Tol}}\text{CO}_2^-$ and $\text{Ar}^{4\text{-FPh}}\text{CO}_2^-$ are effective in shielding against metal cluster assembly, they also contribute to excessive steric crowding at the diiron core that prevent facile entry of external guest molecules.

1.6. Dinucleating Polynitrogen Ligands

Polydentate nitrogen donors are commonly utilized as ligands in synthetic modeling studies.^{19,94} Although these compounds provide a nitrogen-rich, rather than a carboxylate-rich, coordination environment they are well suited for stabilizing kinetically labile first row transition metal ions. Efforts to mimic the *syn, syn* coordination of the bridging carboxylate in the active site of diiron enzymes led to use of a naphthyridine framework as a “masked carboxylate.”⁹⁵ Several 1,8-substituted naphthyridine compounds were prepared and successfully employed to assemble dicopper(II), dizinc(II), dinickel(II), and diiron(II) complexes.⁹⁶ The most notable of these are $[\text{Fe}^{\text{II}}_2(\mu\text{-OH})(\text{BPEAN})(\text{SO}_3\text{CF}_3)]^{2+}$ (**24**, where BPEAN = 2,7-bis(bis(2-(2-(5-methyl)pyridyl)ethyl)aminomethyl)-1,8-naphthyridine, Table 1.1) and $[\text{Fe}^{\text{II}}_2(\mu\text{-OH})(\text{BEPEAN})(\text{SO}_3\text{CF}_3)]^{2+}$ (**25**, where BEPEAN = 2,7-bis(bis(2-(2-(5-ethyl)pyridyl)ethyl)aminomethyl)-1,8-naphthyridine).⁹⁷ Exposing either **24** or **25** to O_2 at room temperature resulted in rapid decomposition without any detectable intermediates. When the more sterically-hindered **25** was treated with excess hydrogen peroxide at $-30\text{ }^\circ\text{C}$ a red-brown species (**26**) appeared, which

decayed upon warming to room temperature. Spectroscopic characterization of **26** suggested that it is a (hydroperoxo)diiron(III) species. The decay of **26** is accompanied by O₂ evolution and formation of a diiron(II) unit, the identity of which is different from that of **25**. Although the mechanism of this reaction is uncertain, the release of O₂ from **26** may mimic a process similar to that in hemerythrin.

The stability of the diiron(II) naphthyridine compounds afforded an opportunity to investigate how the redox properties of the model complexes vary depending on their composition and structure. Because activation of O₂ in the diiron enzymes invariably results in oxidation of the metal center, knowledge of the redox potential of the diiron(II) models may help explain their dioxygen reactivity. The cyclic voltammogram of [Fe^{II}₂(BPMAN)(μ-PhCyCO₂)₂]²⁺ (**27**, where BPMAN = 2,7-bis(bis(2-pyridylmethyl)aminomethyl)-1,8-naphthyridine) displayed two reversible redox waves at +296 and +681 mV (vs. ferrocene/ferrocenium) that have been attributed to two one-electron oxidation processes, of diiron(II,II) to diiron(II,III) and diiron(II,III) to diiron(III,III), respectively.⁹⁸ The presence of two reversible metal-centered redox couples is unprecedented for diiron(II) compounds having no single atom bridge. Comparing the first oxidation potential of **27** to that of [Fe^{II}₂(Ar^{Tol}CO₂)₄(4-^tBupy)₂] (**14A**) (E_{1/2} = -216 mV) revealed that addition of each anionic carboxylate group *lowers* the redox potential of the diiron center by ~ 250 mV. These results also suggested that diiron(II) sites bridged only by Asp and Glu residues in biology could supply up to two electrons without significant change in geometry.

Another polynitrogen donor compound, 1,4-bis(2,2'-dipyridylmethyl)phthalazine (bdptz, Table 1.1) was explored as a potential dinucleating platform.⁹⁹ Reaction of bdptz with iron(II) triflate and Ar^{Tol}CO₂⁻ afforded a stable diiron(II) complex, [Fe^{II}₂(μ-OH)(μ-

$\text{Ar}^{\text{Tol}}\text{CO}_2)(\text{bdptz})(\text{CH}_3\text{CN})(\text{SO}_3\text{CF}_3)](\text{SO}_3\text{CF}_3)$ (**28**, Table 1.1). Treatment of **28** with dioxygen instantaneously led to formation of a (μ -oxo)diiron(III) product, $[\text{Fe}^{\text{III}}_2(\mu\text{-O})(\mu\text{-Ar}^{\text{Tol}}\text{CO}_2)(\text{bdptz})(\text{acetone})(\text{SO}_3\text{CF}_3)](\text{SO}_3\text{CF}_3)_2$ (**29**) with no detectable intermediates. A bulkier derivative of bdptz was prepared to block the possible formation of tetranuclear species, but no remarkable oxygenation chemistry was observed with the diiron complex of this compound.¹⁰⁰

Although the naphthyridine and phthalazine bridged diiron model complexes are structurally robust, they do not exhibit the same O_2 reactivity observed in the diiron proteins. Perhaps polydentate ligands with internal bridging units are too rigid to accommodate binding of O_2 to the diiron center.

1.7. Syn *N*-Donor Ligands

An important structural feature that has been difficult to reproduce in carboxylate-bridged diiron model complexes is the syn coordination of nitrogen donors relative to the iron-iron vector.¹⁹ Despite the different arrangement of carboxylate ligands within the active sites of the BMMs, RNR, and related enzymes, ligation of the two histidine residues always occurs with syn stereochemistry.²³ To enforce the syn arrangement of nitrogen donors within a single ligand framework, two quinoline ester moieties were covalently attached using a diethynylbenzene linker, giving 1,2-bis(3-ethynyl-8-carboxylatequinoline)-4,5-diethynylbenzene ethyl ester ($\text{Et}_2\text{BCQEB}^{\text{Et}}$, Table 1.1).¹⁰¹ Metallation of $\text{Et}_2\text{BCQEB}^{\text{Et}}$ using iron(II) trilate and $\text{Ar}^{\text{Tol}}\text{CO}_2^-$ afforded the compound $[\text{Fe}^{\text{II}}_2(\text{Et}_2\text{BCQEB}^{\text{Et}})(\mu\text{-Ar}^{\text{Tol}}\text{CO}_2)_3]^+$ (**30**, Table 1.1). X-ray structural analysis of **30** revealed a diiron complex with three bridging carboxylates and syn binding of the quinoline moieties. Although **30** is a close structural mimic of $\text{sMMOH}_{\text{red}}$ (Scheme 1.1, bottom),⁷³ exposing the compound to dioxygen resulted in unidentified iron products. Other

neutral derivatives of Et₂BCQEB^{Et} were synthesized and examined as *syn N*-donor ligands.¹⁰² The compound bis(picolinic methyl ester)diethynyltritycene (PIC₂DET) containing pyridine methyl ester groups afforded a heterometallic [Fe^{II}Na(PIC₂DET)(μ -TrpCO₂)₃] (**31**) complex that could exchange sodium for iron; the resulting diiron(II) compound could not be structurally characterized, however.¹⁰³ Two *syn N*-donor ligands can also bridge two iron(II) centers, giving [Fe^{II}₂(*syn N*-donor)₂] species.¹⁰⁴⁻¹⁰⁶ Several examples are shown in Chart 1.2. Such undesired [Fe^{II}₂(*syn N*-donor)₂] species were avoided by the use of ligands bearing polydentate nitrogen-rich metal binding groups.¹⁰⁷ Only diiron(III) complexes, however, could be prepared from these ligands.

To obtain a kinetically more stabilizing platform, 2-phenoxy pyridine groups were attached to a 1,2-diethynylbenzene backbone.¹⁰⁸ Reaction of bis(phenyl(*p*-cresol)pyridyl)-diethynylbenzene ([L^{Me,Ph}]²⁻, Chart 1.2) with iron(II) in tetrahydrofuran (THF) led to spontaneous formation of [Fe^{II}₂(L^{Me,Ph})₂(THF)₂] (**32**). Once again, rotation about the C–C bond of the ethynyl arms allowed association of two *syn N*-donor ligands. Unlike complex **30**, however, reaction of **32** with dioxygen resulted in the formation of a (μ -oxo)diiron(III) [Fe^{III}₂(μ -O)(L^{Me,Ph})₂] (**33**) product. No intermediates were detected during the oxygenation reaction.

Several other ligand designs based on the *syn N*-donor concept were also explored. An attempt was made to incorporate both a bridging carboxylate and adjacent amino moieties into a dinucleating platform using 1,8-bis(dimethylaminomethylethynyl)-3,6-di(*tert*-butyl)fluorene-9-yl-acetate (DAFA²⁻, Table 1.1).¹⁰⁹ Efforts to metallate DAFA²⁻ with iron(II) were unsuccessful, possibly due to a lack of pre-organization among the amino and carboxylate donor groups of the ligand. A two-component system was also proposed as a method to assemble diiron(II) model

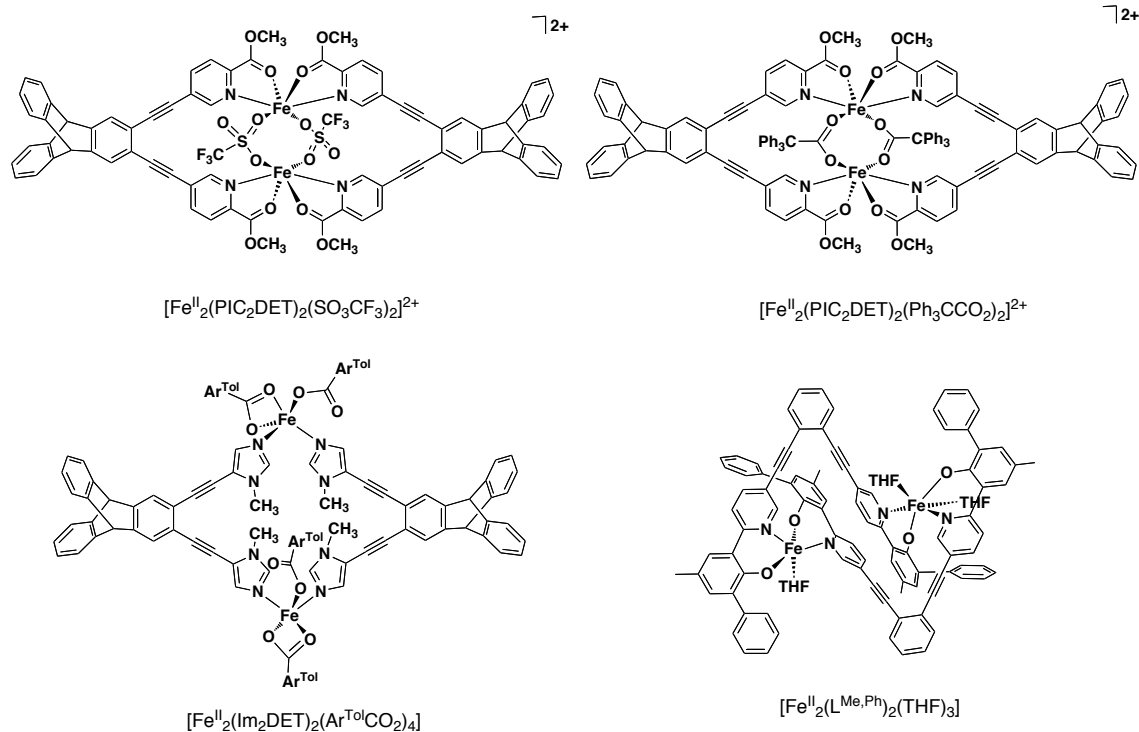


Chart 1.2. Examples of crystallographically characterized $[\text{Fe}^{\text{II}}_2(\text{syn } N\text{-donor})_2]$ species isolated from reaction of iron(II) salts and the corresponding *syn N*-donor ligand. Additional external carboxylate ligands were used in the preparation in some cases. PIC₂DET = bis(picolinic methyl ester)diethynyltritycene;¹⁰² Im₂DET = bis(*N*-methylimidazole)diethynyltritycene;¹⁰² $[\text{L}^{\text{Me,Ph}}]^{2-}$ = bis(phenyl(*p*-cresol)pyridyl)diethynylbenzene;¹⁰⁸ Ar^{Tol}CO₂⁻ = 2,6-(*p*-tolyl)benzoate.

complexes. In addition to a *syn N*-donor, a “C-clamp” ligand with two *endo*-oriented dicarboxylate groups may enforce a doubly-bridging motif and form a hydrophobic pocket around the diiron center.¹¹⁰ Complexation reactions with a C-clamp and *syn N*-donor ligands have not yet afforded the desired $[\text{Fe}^{\text{II}}_2(\text{syn } N\text{-donor})(\text{C-clamp})]$ unit, however.

Linking two *N*-heterocycles with a 1,2-diethynylarene spacer effectively enforces the *syn* coordination of nitrogen donors in a diiron complex. Because the compounds do not have an internal bridging group to link the two metal ions like other dinucleating ligands, their terminal metal-binding units must be sufficiently stabilizing to prevent dissociation of the dinuclear core.

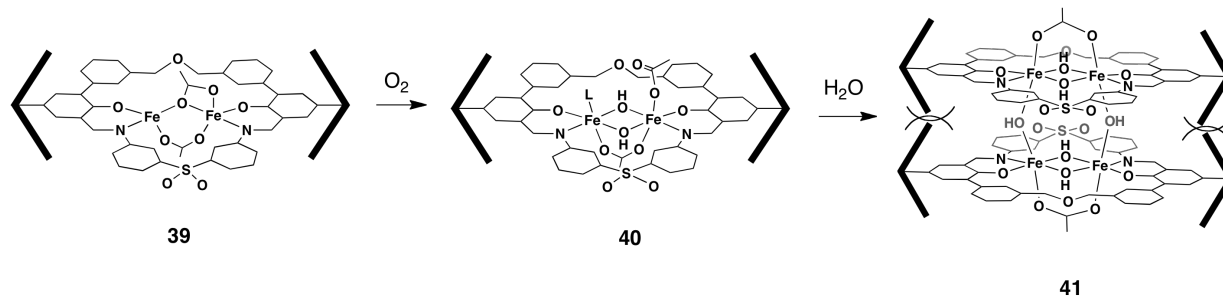
Additional ligand modifications are needed to eliminate the possibility of forming $[\text{Fe}^{\text{II}}_2(\text{syn } N\text{-donor})_2]$ species.

1.8. Macrocyclic Ligands

Macrocyclic ligands are excellent hosts for transition metal ions, as evident from examples in biology^{3,4} as well as synthetic coordination chemistry.^{111,112} Initial efforts to prepare a dinucleating macrocycle led to synthesis of a bis(terphenylcarboxylate) compound linked by 1,3-bis(aminomethyl)-4,6-diisopropylbenzene ($\text{MAr}^{\text{Tol}}\text{CO}_2^{2-}$, Table 1.1).¹¹³ The *endo*-carboxylate groups in $\text{MAr}^{\text{Tol}}\text{CO}_2^{2-}$ were designed to bridge two iron atoms to form a pre-organized platform for binding of additional external ligands. Failure to complex $\text{MAr}^{\text{Tol}}\text{CO}_2^{2-}$ with iron, however, was attributed to either the flexibility of the ligand architecture or an improper spacing provided by the phenylene linker.

An improved macrocyclic design was obtained with the compound PIM^{2-} (Table 1.1), which contains two phenoxyimine metal binding units linked by diphenylsulfone and dibenzylether moieties.¹¹⁴ Reaction of H_2PIM , the protonated form of PIM^{2-} , with $[\text{Fe}^{\text{II}}_2(2,4,6\text{-trimethylphenyl})_4]$ and sterically-hindered carboxylic acid afforded di(μ -carboxylato)diiron(II) complexes in good yield. Use of terphenylcarboxylic acid and triphenylacetic acid gave $[\text{Fe}^{\text{II}}_2(\mu\text{-Ar}^{\text{Tol}}\text{CO}_2)_2(\text{PIM})]$ (**34**, Table 1.1) and $[\text{Fe}^{\text{II}}_2(\mu\text{-Ph}_3\text{CCO}_2)_2(\text{PIM})]$ (**35**), respectively. X-ray structural analysis revealed that both compounds accurately mimic the active site structure of $\text{sMMOH}_{\text{red}}$ (Scheme 1.1, bottom),⁷³ including the asymmetric $\mu\text{-}\eta^1, \eta^1$ and $\mu\text{-}\eta^1, \eta^2$ binding mode of carboxylates as well as the *syn* stereochemistry of nitrogen donors. When **34** was exposed to dioxygen, a mixture of (μ -oxo)diiron(III) $[\text{Fe}^{\text{III}}_2(\mu\text{-O})(\text{Ar}^{\text{Tol}}\text{CO}_2)_2(\text{PIM})]$ (**36**) and di(μ -hydroxo)diiron(III) $[\text{Fe}^{\text{III}}_2(\mu\text{-OH})_2(\text{Ar}^{\text{Tol}}\text{CO}_2)_2(\text{PIM})]$ (**37**) species was isolated. Further treatment

of **36** and **37** with excess water resulted in dimerization of the complexes to form tetranuclear $[\text{Fe}^{\text{III}}_4(\mu\text{-OH})_6(\text{PIM})_2(\text{Ar}^{\text{Tol}}\text{CO}_2)_2]$ (**38**) species. To eliminate this decomposition pathway, the PIM^{2-} ligand could be modified with sterically more hindering groups at the para position of the phenolate (Scheme 1.3). Having a more bulky platform would also allow smaller carboxylate ligands to be employed, which may facilitate dioxygen binding or substrate access to the diiron center. Unlike other platforms that have been investigated to date, the planar nature of the macrocycle allows for steric tuning of the diiron complex without obstructing access to the dimetallic center.



Scheme 1.3. A cartoon depiction of a diiron(II) model complex (**39**) containing a more sterically-hindering PIM^{2-} ligand, where the dark wedges represent a bulky organic substituent. Reaction of **39** with dioxygen may lead to a carboxylate shift and formation of a di(μ -hydroxo)diiron(III) product (**40**). The steric repulsion between the bulky PIM^{2-} substituents should prevent undesired formation of $[\text{Fe}^{\text{III}}_4(\mu\text{-OH})_6(\text{bulky PIM})_2(\text{RCO}_2)_2]$ (**41**) complexes.

1.9. Concluding Remarks

The early years of synthetic modeling in the Lippard group were characterized by use of simple chelating ligands to prepare structural mimics of diiron protein active sites. Efforts to replicate the functional aspects of these proteins, however, required that more elaborately designed ligands be employed. The search for an ideal synthetic platform is complicated by a number of factors, such as constructing ligands that can complex with iron to afford the desired coordination geometry, tuning of ligand steric properties to prevent unproductive decomposition of reactive oxygenated species, and developing short and convenient routes to obtain the target

compounds. Although there is no substitute for direct studies of biomolecules, the work described in this account illustrates that investigations using synthetic mimics can provide insight into metallobiochemistry in ways that could not be achieved through other means.

Synthetic diiron modeling still offers many unexplored frontiers. One area of interest is understanding the chemical nature as well as the requirements for generating highly oxidizing diiron(IV) units. One strategy to access such chemically reactive species is to prepare diiron complexes that have optimally positioned functional groups to stabilize key transition states along the O₂ reaction pathway. Identifying which transition state structures to target can be aided by the use of quantum mechanical calculations.^{115,116} This concept has been successfully demonstrated in de novo protein design,¹¹⁷⁻¹¹⁹ but has not yet been seriously applied to construct small-molecule protein models. Another avenue of research that would help advance diiron modeling chemistry is to establish a clear structure-function relationship between the model compounds and their oxygenation behavior.¹²⁰ For example, although it has been shown that exposing dioxygen to a synthetic diiron(II) complex can lead to formation of a (peroxo)diiron(III) species, this reactivity is not general to all diiron(II) model compounds. In many cases, it is unclear whether the oxygenated diiron units are not observed because they are rapidly quenched by external reactants, do not form under the experimental conditions employed, or the starting complexes are too sterically hindered to bind O₂. To evaluate the various factors that contribute to the dioxygen reactivity in a synthetic model, it is necessary to study the effects of introducing systematic structural and electronic modifications to the complex. Unfortunately, most model systems are not amenable to such investigations because the integrity of the complexes may be comprised upon introducing such changes. Because PIM²⁻ is a remarkably

robust dinucleating platform and has many potential sites for derivatization, it is an excellent framework for such studies.

Although this review has focused exclusively on diiron modeling chemistry in our laboratory, many other research groups have made significant contributions to the development of carboxylate-bridged diiron protein model complexes and the investigation of their chemical and physical characteristics. A large number of synthetic platforms have been devised for the assembly of non-heme diiron model complexes, ranging from simple carboxylate/pyridine donors¹²¹ to tailored-made dinucleating ligands^{19,122} and synthetic peptides.^{123,124} Although many of the diiron model compounds reported are structurally robust,^{19,122} they do not capture the unique coordination sphere of the bioinorganic unit of interest. Perhaps as a consequence of the incomplete match, the synthetic complexes do not typically exhibit the same reactivity profile as that of the diiron proteins.^{21,125} It is unlikely that every element of a protein active site, including especially the second coordination sphere, can be reproduced in a single model system. But given the extent of the synthetic methodologies available today, it should be possible to overcome many of the obstacles that have impeded the development of more sophisticated diiron protein mimics.²⁰

Extensive reactivity studies utilizing molecular oxygen, hydrogen peroxide, alkyl peroxides, and oxygen atom transfer reagents with diiron model compounds have led to a much improved understanding of the oxidation chemistry that takes place in the active sites of non-heme diiron proteins.^{17,22} For example, characterization of diiron(III,IV) and diiron(IV,IV) species in synthetic models¹²⁶⁻¹²⁹ has shed some light on similar high-valent states that are accessible within the diiron protein cores. These achievements help us to formulate possible reaction schemes that reconcile the biochemical data^{23,24} with the proposed biological

mechanisms suggested by theory.¹³⁰⁻¹³³ Beyond the O₂ activation step, some synthetic systems are even able to perform *catalytic* hydrocarbon oxidation.^{18,134,135} Although these reactions are typically not as efficient as those catalyzed by the bacterial monooxygenases, they represent a good start. The current challenge in diiron model chemistry is to achieve regio- and stereospecific oxidation of external substrates by non-“free radical” reaction pathways. Use of the earth-abundant molecule dioxygen, rather than other more reactive but environmentally less friendly chemical oxidants, to facilitate this chemistry is the ultimate goal. The tasks set forth for future researchers in biomimetic modeling are numerous and complex, but the advances that have been made over the past thirty years promise a future that is full of many exciting discoveries.

1.10. References

- (1) Williams, R. J. P. *Coord. Chem. Rev.* **1990**, *100*, 573-610.
- (2) Holm, R. H.; Kennepohl, P.; Solomon, E. I. *Chem. Rev.* **1996**, *96*, 2239-2314.
- (3) Bertini, I.; Gray, H. B.; Lippard, S. J.; Valentine, J. S., *Bioinorganic Chemistry*. Mill Valley: University Science Books; 1994.
- (4) Lippard, S. J.; Berg, J. M., *Principles of Bioinorganic Chemistry*. Mill Valley: University Science Books; 1994.
- (5) Que, L., Jr.; *Physical Methods in Bioinorganic Chemistry: Spectroscopy and Magnetism*; University Science Books: Sausalito, CA, 2000.
- (6) Vilar, R. *Annu. Rep. Sect. A* **2009**, *105*, 477-504.
- (7) Kirchner, B.; Wennmohs, F.; Ye, S.; Neese, F. *Curr. Opin. Chem. Biol.* **2007**, *11*, 134-141.

- (8) Chatt, J.; Dilworth, J. R.; Richards, R. L. *Chem. Rev.* **1978**, *78*, 589-625.
- (9) Howard, J. B.; Rees, D. C. *Chem. Rev.* **1996**, *96*, 2965-2982.
- (10) Dance, I. *Dalton Trans.* **2010**, *39*, 2972-2983.
- (11) Schrock, R. R. *Acc. Chem. Res.* **2005**, *38*, 955-962.
- (12) Williamson, A.; Conlan, B.; Hillier, W.; Wydrzynski, T. *Photosyn. Res.* **2011**, *107*, 71-86.
- (13) Gordon, J. C.; Kubas, G. J. *Organometallics* **2010**, *29*, 4682-4701.
- (14) Lewis, N. S.; Nocera, D. G. *Proc. Natl. Acad. Sci. U.S.A.* **2006**, *103*, 15729-15735.
- (15) Nicolaou, K. C.; Vourloumis, D.; Winssinger, N.; Baran, P. S. *Angew. Chem., Int. Ed.* **2000**, *39*, 44-122.
- (16) Lippard, S. J. *Nature* **2002**, *416*, 587.
- (17) Que, L., Jr. *Dalton Trans.* **1997**, 3933-3940.
- (18) Fontecave, M.; Ménage, S.; Duboc-Toia, C. *Coord. Chem. Rev.* **1998**, *178-180*, 1555-1572.
- (19) Tshuva, E. Y.; Lippard, S. J. *Chem. Rev.* **2004**, *104*, 987-1012.
- (20) Que, L., Jr.; Tolman, W. B. *Nature* **2008**, *455*, 333-340.
- (21) Friedle, S.; Reisner, E.; Lippard, S. J. *Chem. Soc. Rev.* **2010**, *39*, 2768-2779.
- (22) Du Bois, J.; Mizoguchi, T. J.; Lippard, S. J. *Coord. Chem. Rev.* **2000**, *200-202*, 443-485.
- (23) Feig, A. L.; Lippard, S. J. *Chem. Rev.* **1994**, *94*, 759-805.
- (24) Wallar, B. J.; Lipscomb, J. D. *Chem. Rev.* **1996**, *96*, 2625-2658.
- (25) Stenkamp, R. E. *Chem. Rev.* **1994**, *94*, 715-726.
- (26) Nordlund, P.; Reichard, P. *Annu. Rev. Biochem.* **2006**, *75*, 681-706.
- (27) Leahy, J. G.; Batchelor, P. J.; Morcomb, S. M. *FEMS Microbiol. Rev.* **2003**, *27*, 449-479.

- (28) Liu, K. E.; Valentine, A. M.; Wang, D.; Huynh, B. H.; Edmondson, D. E.; Salifoglou, A.; Lippard, S. J. *J. Am. Chem. Soc.* **1995**, *117*, 10174-10185.
- (29) Moënné-Loccoz, P.; Baldwin, J.; Ley, B. A.; Loehr, T. M.; Bollinger, J. M., Jr. *Biochemistry* **1998**, *37*, 14659-14663.
- (30) Brazeau, B. J.; Lipscomb, J. D. *Biochemistry* **2000**, *39*, 13503-13515.
- (31) Murray, L. J.; Naik, S. G.; Ortillo, D. O.; García-Serres, R.; Lee, J. K.; Huynh, B. H.; Lippard, S. J. *J. Am. Chem. Soc.* **2007**, *129*, 14500-14510.
- (32) Shu, L.; Nesheim, J. C.; Kauffmann, K.; Münck, E.; Lipscomb, J. D.; Que, L., Jr. *Science* **1997**, *275*, 515-518.
- (33) Merckx, M.; Kopp, D. A.; Sazinsky, M. H.; Blazyk, J. L.; Müller, J.; Lippard, S. J. *Angew. Chem., Int. Ed.* **2001**, *40*, 2782-2807.
- (34) Korboukh, V. K.; Li, N.; Barr, E. W.; Bollinger, J. M., Jr.; Krebs, C. *J. Am. Chem. Soc.* **2009**, *131*, 13608-13609.
- (35) Vu, V. V.; Emerson, J. P.; Martinho, M.; Kim, Y. S.; Münck, E.; Park, M. H.; Que, L., Jr. *Proc. Natl. Acad. Sci. U.S.A.* **2009**, *106*, 14814-14819.
- (36) Behan, R. K.; Lippard, S. J. *Biochemistry* **2010**, *49*, 9679-9681.
- (37) Armstrong, W. H.; Lippard, S. J. *J. Am. Chem. Soc.* **1983**, *105*, 4837-4838.
- (38) Armstrong, W. H.; Spool, A.; Papaefthymiou, G. C.; Frankel, R. B.; Lippard, S. J. *J. Am. Chem. Soc.* **1984**, *106*, 3653-3667.
- (39) Armstrong, W. H.; Lippard, S. J. *J. Am. Chem. Soc.* **1984**, *106*, 4632-4633.
- (40) Spool, A.; Williams, I. D.; Lippard, S. J. *Inorg. Chem.* **1985**, *24*, 2156-2162.
- (41) Hedman, B.; Co, M. S.; Armstrong, W. H.; Hodgson, K. O.; Lippard, S. J. *Inorg. Chem.* **1986**, *25*, 3708-3711.

- (42) Tolman, W. B.; Bino, A.; Lippard, S. J. *J. Am. Chem. Soc.* **1989**, *111*, 8522-8523.
- (43) Tolman, W. B.; Liu, S.; Bentsen, J. G.; Lippard, S. J. *J. Am. Chem. Soc.* **1991**, *113*, 152-164.
- (44) Beer, R. H.; Tolman, W. B.; Bott, S. G.; Lippard, S. J. *Inorg. Chem.* **1989**, *28*, 4557-4558.
- (45) Beer, R. H.; Tolman, W. B.; Bott, S. G.; Lippard, S. J. *Inorg. Chem.* **1991**, *30*, 2082-2092.
- (46) Rebek, J., Jr.; Marshall, L.; Wolak, R.; Parris, K.; Killoran, M.; Askew, B.; Nemeth, D.; Islam, N. *J. Am. Chem. Soc.* **1985**, *107*, 7476-7481.
- (47) Marshall, L.; Parris, K.; Rebek, J., Jr.; Luis, S. V.; Burguete, M. I. *J. Am. Chem. Soc.* **1988**, *110*, 5192-5193.
- (48) Hagen, K. S.; Lachicotte, R.; Kitaygorodskiy, A.; Elbouadili, A. *Angew. Chem., Int. Ed.* **1993**, *32*, 1321-1324.
- (49) Goldberg, D. P.; Watton, S. P.; Masschelein, A.; Wimmer, L.; Lippard, S. J. *J. Am. Chem. Soc.* **1993**, *115*, 5346-5347.
- (50) Goldberg, D. P.; Koulougliotis, D.; Brudvig, G. W.; Lippard, S. J. *J. Am. Chem. Soc.* **1995**, *117*, 3134-3144.
- (51) Tanase, T.; Watton, S. P.; Lippard, S. J. *J. Am. Chem. Soc.* **1994**, *116*, 9401-9402.
- (52) Watton, S. P.; Masschelein, A.; Rebek, J., Jr.; Lippard, S. J. *J. Am. Chem. Soc.* **1994**, *116*, 5196-5205.
- (53) Mizoguchi, T. J.; Lippard, S. J. *Inorg. Chem.* **1997**, *36*, 4526-4533.
- (54) Herold, S.; Pence, L. E.; Lippard, S. J. *J. Am. Chem. Soc.* **1995**, *117*, 6134-6135.
- (55) Herold, S.; Lippard, S. J. *J. Am. Chem. Soc.* **1997**, *119*, 145-156.

- (56) LeCloux, D. D.; Barrios, A. M.; Mizoguchi, T. J.; Lippard, S. J. *J. Am. Chem. Soc.* **1998**, *120*, 9001-9014.
- (57) LeCloux, D. D.; Barrios, A. M.; Lippard, S. J. *Bioorg. Med. Chem.* **1999**, *7*, 763-772.
- (58) Beauvais, L. G.; Lippard, S. J. *J. Am. Chem. Soc.* **2005**, *127*, 7370-7378.
- (59) Beauvais, L. G.; Lippard, S. J. *Biochem. Biophys. Res. Commun.* **2005**, *338*, 262-266.
- (60) Mizoguchi, T. J.; Lippard, S. J. *J. Am. Chem. Soc.* **1998**, *120*, 11022-11023.
- (61) Mizoguchi, T. J.; Kuzelka, J.; Spingler, B.; DuBois, J. L.; Davydov, R. M.; Hedman, B.; Hodgson, K. O.; Lippard, S. J. *Inorg. Chem.* **2001**, *40*, 4662-4673.
- (62) Zhang, X.-X.; Lippard, S. J. *J. Org. Chem.* **2000**, *65*, 5298-5305.
- (63) Zhang, X.-X.; Fuhrmann, P.; Lippard, S. J. *J. Am. Chem. Soc.* **1998**, *120*, 10260-10261.
- (64) Zhang, X.-X.; Lippard, S. J. *Inorg. Chem.* **2000**, *39*, 4388-4389.
- (65) Watton, S. P.; Fuhrmann, P.; Pence, L. E.; Caneschi, A.; Cornia, A.; Abbati, G. L.; Lippard, S. J. *Angew. Chem., Int. Ed.* **1997**, *36*, 2774-2776.
- (66) Micklitz, W.; Lippard, S. J. *Inorg. Chem.* **1988**, *27*, 3067-3069.
- (67) Micklitz, W.; McKee, V.; Rardin, R. L.; Pence, L. E.; Papaefthymiou, G. C.; Bott, S. G.; Lippard, S. J. *J. Am. Chem. Soc.* **1994**, *116*, 8061-8069.
- (68) Ammala, P.; Cashion, J. D.; Kepert, C. M.; Moubaraki, B.; Murray, K. S.; Spiccia, L.; West, B. O. *Angew. Chem., Int. Ed.* **2000**, *39*, 1688-1690.
- (69) Lee, D.; Lippard, S. J. *J. Am. Chem. Soc.* **1998**, *120*, 12153-12154.
- (70) Lee, D.; Lippard, S. J. *Inorg. Chem.* **2002**, *41*, 2704-2719.
- (71) Lee, D.; Du Bois, J.; Petasis, D.; Hendrich, M. P.; Krebs, C.; Huynh, B. H.; Lippard, S. J. *J. Am. Chem. Soc.* **1999**, *121*, 9893-9894.

- (72) Lee, D.; Pierce, B.; Krebs, C.; Hendrich, M. P.; Huynh, B. H.; Lippard, S. J. *J. Am. Chem. Soc.* **2002**, *124*, 3993-4007.
- (73) Rosenzweig, A. C.; Nordlund, P.; Takahara, P. M.; Frederick, C. A.; Lippard, S. J. *Chem. Biol.* **1995**, *2*, 409-418.
- (74) Lee, D.; Krebs, C.; Huynh, B. H.; Hendrich, M. P.; Lippard, S. J. *J. Am. Chem. Soc.* **2000**, *122*, 5000-5001.
- (75) Lee, D.; DuBois, J. L.; Pierce, B.; Hedman, B.; Hodgson, K. O.; Hendrich, M. P.; Lippard, S. J. *Inorg. Chem.* **2002**, *41*, 3172-3182.
- (76) Lee, D.; Lippard, S. J. *J. Am. Chem. Soc.* **2001**, *123*, 4611-4612.
- (77) Lee, D.; Lippard, S. J. *Inorg. Chem.* **2002**, *41*, 827-837.
- (78) Yoon, S.; Lippard, S. J. *Inorg. Chem.* **2003**, *42*, 8606-8608.
- (79) Yoon, S.; Lippard, S. J. *Inorg. Chem.* **2006**, *45*, 5438-5446.
- (80) Carson, E. C.; Lippard, S. J. *J. Am. Chem. Soc.* **2004**, *126*, 3412-3413.
- (81) Carson, E. C.; Lippard, S. J. *Inorg. Chem.* **2006**, *45*, 828-836.
- (82) Carson, E. C.; Lippard, S. J. *J. Inorg. Biochem.* **2006**, *100*, 1109-1117.
- (83) Friedle, S.; Lippard, S. J. *Eur. J. Inorg. Chem.* **2009**, 5506-5515.
- (84) Carson, E. C.; Lippard, S. J. *Inorg. Chem.* **2006**, *45*, 837-848.
- (85) Reisner, E.; Abikoff, T. C.; Lippard, S. J. *Inorg. Chem.* **2007**, *46*, 10229-10240.
- (86) Zhao, M.; Helms, B.; Slonkina, E.; Friedle, S.; Lee, D.; DuBois, J.; Hedman, B.; Hodgson, K. O.; Fréchet, J. M.; Lippard, S. J. *J. Am. Chem. Soc.* **2008**, *130*, 4352-4363.
- (87) Yoon, S.; Kelly, A. E.; Lippard, S. J. *Polyhedron* **2004**, *23*, 2805-2812.
- (88) Yoon, S.; Lippard, S. J. *J. Am. Chem. Soc.* **2004**, *126*, 16692-16693.
- (89) Yoon, S.; Lippard, S. J. *J. Am. Chem. Soc.* **2005**, *127*, 8386-8397.

- (90) Zhao, M.; Song, D.; Lippard, S. J. *Inorg. Chem.* **2006**, *45*, 6323-6330.
- (91) Lee, D.; Sorace, L.; Caneschi, A.; Lippard, S. J. *Inorg. Chem.* **2001**, *40*, 6774-6781.
- (92) Reisner, E.; Telser, J.; Lippard, S. J. *Inorg. Chem.* **2007**, *46*, 10754-10770.
- (93) Friedle, S.; Kodanko, J. J.; Fornace, K. L.; Lippard, S. J. *J. Mol. Struct.* **2008**, *890*, 317-327.
- (94) Lewis, E. A.; Tolman, W. B. *Chem. Rev.* **2004**, *104*, 1047-1076.
- (95) He, C.; Lippard, S. J. *Tetrahedron* **2000**, *56*, 8245-8252.
- (96) He, C.; Lippard, S. J. *J. Am. Chem. Soc.* **2000**, *122*, 184-185.
- (97) He, C.; Barrios, A. M.; Lee, D.; Kuzelka, J.; Davydov, R. M.; Lippard, S. J. *J. Am. Chem. Soc.* **2000**, *122*, 12683-12690.
- (98) He, C.; Lippard, S. J. *Inorg. Chem.* **2001**, *40*, 1414-1420.
- (99) Barrios, A. M.; Lippard, S. J. *Inorg. Chem.* **2001**, *40*, 1060-1064.
- (100) Kuzelka, J.; Spingler, B.; Lippard, S. J. *Inorg. Chim. Acta* **2002**, *337*, 212-222.
- (101) Kuzelka, J.; Farrell, J. R.; Lippard, S. J. *Inorg. Chem.* **2003**, *42*, 8652-8662.
- (102) Kodanko, J. J.; Morys, A. J.; Lippard, S. J. *Org. Lett.* **2005**, *7*, 4585-4588.
- (103) Kodanko, J. J.; Xu, D.; Song, D.; Lippard, S. J. *J. Am. Chem. Soc.* **2005**, *127*, 16004-16005.
- (104) Kodanko, J. J.; Lippard, S. J. *Inorg. Chim. Acta* **2008**, *361*, 894-900.
- (105) Friedle, S.; Lippard, S. J. **2005**, *Unpublished results*.
- (106) Do, L. H.; Lippard, S. J. **2006**, *Unpublished results*.
- (107) Friedle, S.; Kodanko, J. J.; Morys, A. J.; Hayashi, T.; Moënne-Loccoz, P.; Lippard, S. J. *J. Am. Chem. Soc.* **2009**, *131*, 14508-14520.
- (108) Do, L. H.; Lippard, S. J. *Inorg. Chem.* **2009**, *48*, 10708-10719.

- (109) Burdinski, D.; Cheng, K.; Lippard, S. J. *Tetrahedron* **2005**, *61*, 1587-1594.
- (110) Reisner, E.; Lippard, S. J. *Eur. J. Org. Chem.* **2008**, 156-163.
- (111) Archibald, S. J. *Annu. Rep. Sect. A* **2007**, *103*, 264-286.
- (112) Busch, D. H. *Acc. Chem. Res.* **1978**, *11*, 392-400.
- (113) Farrell, J. R.; Stiles, D.; Bu, W.; Lippard, S. J. *Tetrahedron* **2003**, *59*, 2463-2469.
- (114) Do, L. H., Ph.D. Dissertation: Chapter 3, Massachusetts Institute of Technology, **2011**.
- (115) Tantillo, D. J.; Jiangang, C.; Houk, K. N. *Curr. Opin. Chem. Biol.* **1998**, *2*, 743-750.
- (116) Zhang, X.; DeChancie, J.; Gunaydin, H.; Chowdry, A. B.; Clemente, F. R.; Smith, A. J. T.; Handel, T. M.; Houk, K. N. *J. Org. Chem.* **2008**, *73*, 889-899.
- (117) DeGrado, W. F.; Summa, C. M.; Pavone, V.; Nastri, F.; Lombardi, A. *Annu. Rev. Biochem.* **1999**, *68*, 779-819.
- (118) Floudas, C. A.; Fung, H. K.; McAllister, S. R.; Mönnigmann, M.; Rajgaria, R. *Chem. Eng. Sci.* **2006**, *61*, 966-988.
- (119) Kiss, G.; Röthlisberger, D.; Baker, D.; Houk, K. N. *Protein Sci.* **2010**, *19*, 1760-1773.
- (120) Solomon, E. I.; Brunold, T. C.; Davis, M. I.; Kemsley, J. N.; Lee, S.-K.; Lehnert, N.; Neese, F.; Skulan, A. J.; Yang, Y.-S.; Zhou, J. *Chem. Rev.* **1999**, *100*, 235-350.
- (121) Reynolds, R. A., III; Dunham, W. R.; Coucouvanis, D. *Inorg. Chem.* **1998**, *37*, 1232-1241.
- (122) Gavrilova, A. L.; Bosnich, B. *Chem. Rev.* **2004**, *104*, 349-384.
- (123) Hill, R. B.; Raleigh, D. P.; Lombardi, A.; DeGrado, W. F. *Acc. Chem. Res.* **2000**, *33*, 745-754.
- (124) Lombardi, A.; Summa, C. M.; Geremia, S.; Randaccio, L.; Pavone, V.; DeGrado, W. F. *Proc. Natl. Acad. Sci. U.S.A.* **2000**, *97*, 6298-6305.

- (125) Siewert, I.; Limberg, C. *Chem. Eur. J.* **2009**, *15*, 10316-10328.
- (126) Wang, D.; Farquhar, E. R.; Stubna, A.; Münck, E.; Que, L., Jr. *Nature Chem.* **2009**, *1*, 145-150.
- (127) Martinho, M.; Xue, G.; Fiedler, A. T.; Que, L., Jr.; Bominaar, E. L.; Münck, E. *J. Am. Chem. Soc.* **2009**, *131*, 5823-5830.
- (128) Xue, G.; Wang, D.; De Hont, R.; Fiedler, A. T.; Shan, X.; Münck, E.; Que, L., Jr. *Proc. Natl. Acad. Sci. U.S.A.* **2007**, *104*, 20713-20718.
- (129) Stassinopoulos, A.; Caradonna, J. P. *J. Am. Chem. Soc.* **1990**, *112*, 7071-7073.
- (130) Dunietz, B. D.; Beachy, M. D.; Cao, Y.; Whittington, D. A.; Lippard, S. J.; Friesner, R. A. *J. Am. Chem. Soc.* **2000**, *122*, 2828-2839.
- (131) Baik, M.-H.; Gherman, B. F.; Friesner, R. A.; Lippard, S. J. *J. Am. Chem. Soc.* **2002**, *124*, 14608-14615.
- (132) Rinaldo, D.; Philipp, D. M.; Lippard, S. J.; Friesner, R. A. *J. Am. Chem. Soc.* **2007**, *129*, 3135-3147.
- (133) Jensen, K. P.; Bell, C. B., III; Clay, M. D.; Solomon, E. I. *J. Am. Chem. Soc.* **2009**, *131*, 12155-12171.
- (134) Costas, M.; Chen, K.; Que, L., Jr. *Coord. Chem. Rev.* **2000**, *200-202*, 517-544.
- (135) Mukerjee, S.; Stassinopoulos, A.; Caradonna, J. P. *J. Am. Chem. Soc.* **1997**, *119*, 8097-8098.

Chapter 2

Kinetic Stabilization of Diiron Complexes Using Phenoxyipyridine and Phenoxyimine Syn *N*-Donor Ligands

Portions of this chapter have appeared in print:

Loi H. Do, Stephen J. Lippard. “2-Phenoxyipyridyl Dinucleating Ligands for Assembly of Diiron(II) Complexes; Efficient Reactivity with O₂ to Form μ -Oxodiiron(III) units.” *Inorg. Chem.*, **2009**, 48(22), 10708–10719.

2.1. Introduction

Our recent synthetic efforts have been largely inspired by the bacterial multi-component monooxygenase (BMM) family of enzymes.¹⁻³ These multi-component systems, which include soluble methane monooxygenase (sMMO),¹ phenol hydroxylase (PH),⁴ and toluene/*o*-xylene monooxygenase (ToMO),^{4,5} perform oxygen-atom transfer reactions in aerobic environments under mild conditions. Although substrate oxidation is believed to occur at the diiron centers of the hydroxylase component, the BMM machinery also requires both reductase and regulatory proteins to function efficiently. Attempts to mimic monooxygenase activity in synthetic systems by our group, as discussed in Chapter 1, as well as others have led to the preparation of a rich assortment of diiron compounds that display structural, spectroscopic, and/or functional features similar to those of the protein active sites.⁶⁻⁹ To date, however, no diiron model complexes have been able to match the biological systems in terms of catalytic efficiency, chemoselectivity, and oxygenation ability.¹⁰⁻¹²

To overcome the shortcomings of existing model designs, our strategy has been to construct diiron compounds with organic ligands that more accurately resemble the primary coordination spheres of the BMM hydroxylase active sites. The structure of each diiron protein core comprises four carboxylate amino acid side chains, two histidine imidazole groups syn to the Fe–Fe vector, and an internal O₂-binding cavity.¹³⁻¹⁵ A representative view of the reduced form of soluble methane monooxygenase hydroxylase (sMMOH_{red}) is provided in Chart 2.1 (left). To achieve such an architecture in a small-molecule host, we have synthesized dinucleating ligands derived from 1,2- diethynylbenzene.^{16,17} Our studies with this class of ligands have resulted in the preparation of several dinuclear compounds, most notably with 8-carboxylquinoline ester¹⁶ and 2-carboxylpyridyl ester¹⁸ metal-binding groups. These dimetallic

complexes, however, are substitutionally labile and readily dissociate upon exposure to dioxygen. To obtain a more kinetically stable platform, we introduced 2-phenoxy-pyridine moieties into the 1,2-diethynylbenzene backbone. Although the diiron sites in the BMM hydroxylases do not contain phenolate donors, iron-bound tyrosinate ligands occur in the O₂-activating enzymes intradiol dioxygenases^{19,20} and the phosphate ester hydrolyzing proteins mammalian purple acid phosphatases.²¹ Incorporating phenol rings into the ligand design also facilitates synthetic modifications, such as appending bulky moieties for steric protection or introducing electron-donating/or -withdrawing groups for electronic tuning. Our initial synthetic target based on the 2-phenoxy-pyridine motif is shown in Chart 2.1 (right). In this design, the exogenous carboxylates are unrestrained so that the diiron complex could accommodate structural rearrangements upon reaction with dioxygen.

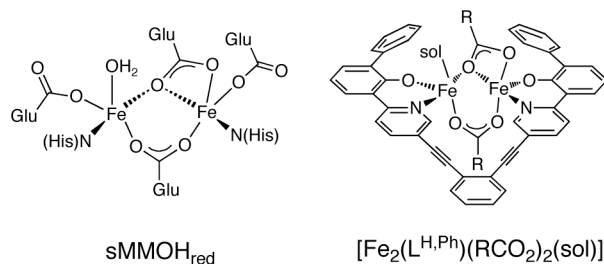


Chart 2.1. Active site structure of reduced soluble methane monooxygenase hydroxylase (sMMOH_{red}, left) and a proposed synthetic analog with a dinucleating ligand, [L^{H,Ph}]²⁻ (right), containing 2-phenoxy-pyridine metal binding groups. Sol = solvent molecule.

In the present chapter, we report a systematic study of the coordination chemistry of phenoxy-pyridine- and phenoxy-imine-appended ligands with iron(II). The importance of incorporating sterically protecting groups to the ligand periphery and its implication for future ligand designs is discussed. This work led to the synthesis of a diiron(II) complex that reacted

rapidly with dioxygen and demonstrated the ability to perform *O*-atom transfer to phosphines, although it did not yield the target structure in Chart 2.1.

2.2. Experimental

Materials and Methods. Reagents were obtained from Strem, Aldrich Chemical Co., and Alfa Aesar and used as received. The iron(II) starting material [Fe₂(Mes)₄] (where Mes = 2,4,6-trimethylphenyl) was prepared according to a literature procedure.²² Air-sensitive manipulations were performed using standard Schlenk techniques or under a nitrogen atmosphere inside a MBraun drybox. All solvents were saturated with argon and purified by passage through two columns of activated Al₂O₃. Labeled dioxygen (~98% ¹⁸O₂) was obtained from Isotech and used without further purification.

General Physical Methods. NMR spectra were recorded on a 500 MHz Varian Mercury spectrometer and chemical shifts for ¹H and ¹³C spectra were referenced to residual solvent peaks. IR spectra were recorded on a ThermoNicolet Avatar 360 spectrophotometer with the OMNIC software. Absorption spectra were recorded on a Cary 50 spectrophotometer using 6Q Spectrosil quartz cuvettes (Starna) with 1 cm path lengths. Cyclic voltammetry and differential pulse voltammetry measurements were made using a VersaSTAT3 potentiostat from Princeton Applied Research using the V3 Studio software. Electrospray ionization mass spectra were acquired on an Agilent Technologies 1100 Series LC-MSD Trap. Gas-chromatographic mass spectra were obtained using an Agilent Technologies 6890 N GC system equipped with a 5973N mass selective detector (MSD) unit.

X-ray Collection and Data Refinement. Single crystals were mounted in Paratone oil on a cryo-loop and frozen under a 110 K KRYO-FLEX nitrogen cold stream. Data were collected on a Bruker APEX CCD X-ray diffractometer with Mo K α radiation ($\lambda = 0.71073 \text{ \AA}$) controlled by the SMART software package.²³ Empirical absorption corrections were applied using SADABS.²⁴ The structures were solved by Patterson methods with refinement by full-matrix least squares based on F^2 using the SHELXTL-97 software package.²⁵ All non-hydrogen atoms were located and refined anisotropically. Hydrogen atoms were assigned idealized positions based on a riding model. X-ray refinement data for complex **1** is given in Table 2.1

⁵⁷Fe Mössbauer Spectroscopy. Mössbauer spectra were recorded on a MSI spectrometer (WEB Research Company) with a ⁵⁷Co source in a Rh matrix maintained at room temperature. Polycrystalline samples were prepared by suspending in Apiezon M grease and placed in a nylon sample holder. Data were acquired at 90 K, and the isomer shift (δ) values are reported with respect to metallic iron that was used for velocity calibration at room temperature. The spectra were fit to Lorentzian lines using the WMOSS plot and fit program (WEB Research, Minneapolis).

Stopped-flow UV-visible Spectrophotometry. Ambient-pressure kinetic studies were performed using a Canterbury SF-41 stopped-flow instrument (Hi-Tech) and a fused-silica fiber optics spectrometer (Oriel Corp.). Data were acquired using a KinetAsyst v.3.16 software (TgK Scientific Limited) at a sampling rate of 300 scans in 30 s. To remove moisture and air, the stainless-steel lines were washed with dioxygen-free anhydrous THF before loading the sample syringes. The mixing cell was maintained at $-50.0 \pm 0.1 \text{ }^\circ\text{C}$. Before mixing, the concentration of complex **1** was 26 μM in THF and that of the dioxygen solution was assumed to be 10 mM.²⁶

Synthesis

1-Benzyloxy-2,6-dibromo-4-*tert*-butylbenzene (H). Solid 2,6-dibromo-4-*tert*-butylphenol (10.0 g, 32.5 mmol), K₂CO₃ (6.7 g, 48.8 mmol), and benzyl bromide (4.7 mL, 39.0 mmol) were combined in 300 mL of CH₃CN and refluxed for 3 h. Water was added to the reaction mixture and the organic phase was extracted with CH₂Cl₂ (3 x 200 mL). The organic layer was separated, dried over Na₂SO₄, and evaporated to dryness. Purification of the crude material by silica gel column chromatography (5:95 EtOAc/hexanes) gave a yellow oil (5.54 g, 42%). ¹H NMR (CDCl₃, 500 MHz): δ 7.64 (d, *J* = 7.0 Hz, 2H), 7.55 (s, 2H), 7.44 (t, *J* = 7.0 Hz, 2H), 7.40 (d, *J* = 7.0 Hz, 1H), 5.03 (s, 2H), 1.32 (s, 9H). ¹³C NMR (CDCl₃, 125 MHz): δ 150.55, 150.35, 136.63, 130.14, 128.68, 128.66, 128.54, 118.23, 74.78, 34.84, 31.37. GC-MS = 398 [M]⁺ (Calcd = 398 [M]⁺).

3-Bromo-5-methylbiphenyl-2-ol (N). The tetrahydropyran protected 2-(5-methylbiphenyl-2-yloxy)tetrahydro-2*H*-pyran (**M**)²⁷ (20.0 g, 74.6 mmol) was dissolved in 100 mL of CH₃OH/CH₃CN (1:1). The mixture was treated with conc. HCl (10 mL), refluxed for 1 h, and concentrated by evaporation. About 200 mL of H₂O was added and the product was extracted with CH₂Cl₂ (3x 100 mL). The organic layer was dried over Na₂SO₄, filtered, and evaporated to afford a white solid. The resulting 5-methylbiphenyl-2-ol was re-dissolved in CH₂Cl₂ (100 mL) and cooled to 0 °C. Liquid bromine (3.8 mL, 74.6 mmol) was added dropwise to the reaction flask. The reaction mixture was stirred for 1 h, washed with sat. Na₂SO₂ (aq), dried over Na₂SO₄, and evaporated to yield a pale brown oil (18.8 g, 96%). ¹H NMR (CDCl₃, 500 MHz): δ 7.58 (d, *J* = 9 Hz, 2H), 7.50 (t, *J* = 8 Hz, 2H), 7.42 (t, *J* = 8 Hz, 1H), 7.35 (s, 1H), 7.11 (s, 1H), 5.59 (s, 1H), 2.36 (s, 3H). ¹³C NMR (CDCl₃, 125 MHz): δ 147.10, 137.50, 131.73, 131.29, 130.96, 129.31, 129.26, 128.63, 127.81, 110.78, 20.42. GC-MS = 262 [M]⁺ (Calcd = 262 [M]⁺).

1-Benzyloxy-2-bromo-4-methyl-6-phenylbenzene (I). Method A: Solid 1-benzyloxy-2,6-dibromo-4-methylbenzene (**G**)²⁸ (12.0 g, 33.7 mmol), phenyl boronic acid (4.11 g, 33.7 mmol), and [Pd(PPh₃)₄] (1.94 g, 1.68 mmol) were combined in 100 mL of THF and 100 mL of 1.0 M aqueous Na₂CO₃ in a 500 mL Schlenk flask. The mixture was degassed with nitrogen for 30 min and then refluxed for 20 h. The organic phase was then extracted with CH₂Cl₂ (3 x 150 mL), dried over Na₂SO₄, and evaporated to dryness. Purification of the crude material by silica gel column chromatography (5:95 EtOAc/hexanes) gave a colorless oil (10.12 g) that contained a mixture of 1-benzyloxy-2,6-dibromo-4-methylbenzene (929 mg, 7%), 1-benzyloxy-2,6-diphenyl-4-methylbenzene (1.83 g, 15%) and 1-benzyloxy-2-bromo-4-methyl-6-phenylbenzene (7.26 g, 62%). The three compounds could not be separated; therefore, the mixture was used in the next step. GC-MS = 356 [1-benzyloxy-2,6-dibromo-4-methylbenzene]⁺ (Calcd = 356 [M]⁺), 350 [1-benzyloxy-2,6-diphenyl-4-methylbenzene]⁺ (Calcd = 350 [M]⁺), and 352 [1-benzyloxy-2-bromo-4-methyl-6-phenylbenzene]⁺ (Calcd = 352 [M]⁺). **Method B:** Solid 3-bromo-5-methylbiphenyl-2-ol (**N**) (18.8 g, 71.5 mmol) and benzyl bromide (9.3 mL, 78.6 mmol) were dissolved in CH₃CN (400 mL). The solution was refluxed for 4 h, evaporated to dryness, and the residue was re-dissolved in CH₂Cl₂ (300 mL). The organic phase was washed with H₂O (3 x 100 mL), dried over Na₂SO₄, filtered, and evaporated to give an oil. The crude material was purified by silica gel column chromatography (5:95 EtOAc/ hexanes) and re-crystallized from hot hexanes to give a white solid (16.0 g, 72%). ¹H NMR (CDCl₃, 125 MHz): δ 7.62 (m, 2H), 7.48-7.43 (m, 4H), 7.32 (m 3H), 7.22 (m, 2H), 7.18 (s, 1H), 4.55(s, 2 H), 2.40 (s, 3H). ¹³C NMR (CDCl₃, 500 MHz): δ 150.89, 137.99, 137.00, 136.61, 135.57, 132.98, 131.06, 129.46, 128.90, 128.42, 128.39, 128.24, 127.76, 118.29, 74.95, 20.78. GC-MS: m/z = 352 [M]⁺ (Calcd = 352 [M]⁺). Mp = 64-65 °C.

1-Benzyloxy-2-bromo-6-phenyl-4-*tert*-butylbenzene (J). The same procedure was employed as described for the synthesis of 1-benzyloxy-2-bromo-4-methyl-6-phenylbenzene (**I**) (Method A), except that 1-benzyloxy-2,6-dibromo-4-*tert*-butylbenzene (**H**) was used in place of 1-benzyloxy-2,6-dibromo-4-methylbenzene (**G**). The reaction was performed with the following reagents: 1-benzyloxy-2,6-dibromo-4-*tert*-butylbenzene (1.0 g, 2.51 mmol), phenyl boronic acid (306 mg, 2.51 mmol), [Pd(PPh₃)₄] (146 mg, 0.126 mmol), and 1.0 M Na₂CO₃ (20 mL, H₂O/THF). Purification of the crude material by silica gel column chromatography (2:1 hexanes/CH₂Cl₂) gave a colorless oil (997 mg) that contained a mixture of 1-benzyloxy-2,6-dibromo-4-*tert*-butylbenzene (170 mg, 17%), 1-benzyloxy-2,6-diphenyl-4-*tert*-butylbenzene (257 mg, 26%), and 1-benzyloxy-2-bromo-6-phenyl-4-*tert*-butylbenzene (576 mg, 57%). The three compounds could not be separated so the mixture was used in the next step. GC-MS = 398 [1-benzyloxy-2,6-dibromo-4-*tert*-butylbenzene]⁺ (Calcd = 398 [M]⁺), 392 [1-benzyloxy-2,6-diphenyl-4-*tert*-butylbenzene]⁺ (Calcd = 392 [M]⁺), and 394 [1-benzyloxy-2-bromo-6-phenyl-4-*tert*-butylbenzene]⁺ (Calcd = 394 [M]⁺).

2-(2-Benzyloxyphenyl)-5-bromopyridine (B). The compound 1-benzyloxy-2-iodobenzene (1.00 g, 3.22 mmol) was dissolved in 15 mL of dry THF in a 50 mL Schlenk flask and the mixture was cooled to -78 °C. A 1.6 M hexanes solution of *n*-butyllithium (2.0 mL, 3.22 mmol) was added slowly to the reaction flask. The mixture was stirred at -78 °C for 30 min. Solid anhydrous ZnCl₂ (351 mg, 3.22 mmol) was added and the mixture was stirred at RT for 30 min. The reaction flask was brought inside a drybox and charged with 2,5-dibromopyridine (694 mg, 2.93 mmol) and [Pd(PPh₃)₄] (169 mg, 0.146 mmol). The resulting solution was transferred to a sealed reaction vessel and stirred at 80 °C for 15 h. Water was added to the reaction mixture and the organic phase was extracted with dichloromethane (3x15 mL). The organic layer was

separated, dried over Na₂SO₄, and evaporated to dryness. The crude material was purified by silica gel column chromatography (5:95 EtOAc/hexanes) to afford a white solid (368 mg, 37%). ¹H NMR (CDCl₃, 500 MHz): δ 8.77 (d, *J* = 2.00 Hz, 1H), 7.86 (m, 2H), 7.78 (dd, *J* = 11.0, 2.5 Hz, 1H), 7.40-7.33 (m, 6H), 7.12 (t, *J* = 8.0 Hz, 1H), 7.07 (d, *J* = 8.5 Hz, 1H), 5.15 (s, 2H). ¹³C NMR (CDCl₃, 125 MHz): δ 156.19, 154.44, 150.48, 138.34, 136.87, 131.27, 130.55, 128.74, 128.35, 128.09, 127.29, 126.61, 121.72, 119.01, 113.25, 70.77. GC-MS: *m/z* = 339 [M]⁺ (Calcd = 339 [M]⁺). Mp = 69-70 °C.

5-Bromo-2-(2-methoxyphenyl)pyridine (C). The same procedure was employed as for the synthesis of 2-(2-benzyloxyphenyl)-5-bromopyridine (**B**), except that 2-bromoanisole was used in place of 1-benzyloxy-2-iodobenzene. The reaction was performed with the following reagents: 2-bromoanisole (2.97 g, 15.9 mmol), 1.6 M *n*-butyllithium in hexanes (10 mL, 15.9 mmol), anhydrous ZnCl₂ (1.73 g, 15.9 mmol), [Pd(PPh₃)₄] (873 mg, 0.755 mmol), and 2,5-dibromopyridine (3.58 g, 15.1 mmol). Purification of the crude material by silica gel column chromatography (5:95 EtOAc/hexanes) gave a light yellow oil (2.29 g, 57%). ¹H NMR (CDCl₃, 500 MHz): δ 8.75 (d, *J* = 2.5 Hz, 1H), 7.81-7.75 (m, 3H), 7.38 (t, *J* = 1.0 Hz, 1H), 7.08 (t, *J* = 1.0 Hz, 1H), 6.99 (d, *J* = 10 Hz, 1H), 3.85 (s, 3H). ¹³C NMR (CDCl₃, 125 MHz): δ 156.94, 154.53, 150.40, 138.32, 131.03, 130.46, 127.86, 126.40, 121.19, 118.88, 111.47, 55.65. GC-MS = 263 [M]⁺ (Calcd = 263 [M]⁺).

5-Bromo-2-(2-methoxybiphenyl-3-yl)pyridine (F). The same procedure was employed as for the synthesis of 2-(2-benzyloxyphenyl)-5-bromopyridine (**B**), except that 2-bromo-6-phenylanisole (**E**) was used in place of 1-benzyloxy-2-iodobenzene (**A**). The reaction was performed with the following reagents: 2-bromo-6-phenylanisole (1.16 g, 4.43 mmol), 1.6 M *n*-butyllithium in hexanes (2.8 mL, 4.43 mmol), anhydrous ZnCl₂ (483 mg, 4.43 mmol),

[Pd(PPh₃)₄] (243 mg, 0.211 mmol), and 2,5-dibromopyridine (1.00 g, 4.22 mmol). Purification of the crude material by silica gel column chromatography (5:95 EtOAc/hexanes) gave a white crystalline solid (868 mg, 57%). ¹H NMR (CDCl₃, 500 MHz): δ 8.80 (s, 1H), 7.87 (s, 2H), 7.74 (dd, *J* = 9.5, 2.0 Hz, 1H), 7.62 (d, *J* = 10 Hz, 2H), 7.47-7.42 (m, 3H), 7.39 (t, *J* = 7.5 Hz, 1H), 7.30 (t, *J* = 7.5 Hz, 1H). ¹³C NMR (CDCl₃, 125 MHz): δ 155.49, 154.91, 150.66, 138.82, 138.44, 136.03, 133.20, 132.26, 130.43, 129.40, 128.44, 127.46, 126.25, 124.79, 119.41, 61.11. GC-MS = 339 [M]⁺ (Calcd = 339 [M]⁺). Mp = 88-89 °C.

5-Bromo-2-(2-benzyloxy-5-methylbiphenyl-3-yl)pyridine (K). The same procedure was employed as for the synthesis of 2-(2-benzyloxyphenyl)-5-bromopyridine (**B**), except that 1-benzyloxy-2-bromo-4-methyl-6-phenylbenzene (**I**) was used in place of 1-benzyloxy-2-iodobenzene (**A**). The reaction was performed with the following reagents: 1-benzyloxy-2-bromo-4-methyl-6-phenylbenzene (~60% purity, 6.00 g, ~10.2 mmol), 1.6 M *n*-butyllithium in hexanes (10 mL, 16.3 mmol), anhydrous ZnCl₂ (1.78 g, 16.3 mmol), [Pd(PPh₃)₄] (751 mg, 0.65 mmol), and 2,5-dibromopyridine (3.06 g, 12.9 mmol). Purification of the crude material by silica gel column chromatography (10:90 EtOAc/hexanes) gave a white solid (2.47 g, ~ 60%). ¹H NMR (CDCl₃, 500 MHz): δ 8.77 (d, *J* = 2.0 Hz, 1H), 7.85 (d, *J* = 8.5 Hz, 1H), 7.78 (dd, *J* = 12, 2.5 Hz, 1H), 7.65 (d, *J* = 8.5 Hz, 2H), 7.56 (d, *J* = 1.5 Hz, 1H), 7.46 (t, *J* = 7.5 Hz, 2H), 7.41 (d, *J* = 7.5 Hz, 1H), 7.28 (d, *J* = 2.0 Hz, 1H), 7.20 (d, *J* = 7.0 Hz, 1H), 7.16 (t, *J* = 7.5 Hz, 2H), 6.75 (d, *J* = 8.0 Hz, 2H). 4.24 (s, 2H). 2.44 (s, 3H). ¹³C NMR (CDCl₃, 125 MHz): δ 155.05, 151.72, 138.62, 138.46, 136.48, 136.38, 134.57, 133.50, 132.84, 130.65, 129.76, 128.82, 128.41, 128.27, 128.12, 127.50, 126.86, 119.30, 75.91, 21.08. ESI-MS = 430.3 [M+H]⁺ (Calcd = 430.1 [M+H]⁺). Mp = 93-95 °C.

5-Bromo-2-(2-benzyloxy-5-*tert*-butylbiphenyl-3-yl)pyridine (L). The same procedure was employed as for the synthesis of 2-(2-benzyloxyphenyl)-5-bromopyridine (**B**), except that 1-benzyloxy-2-bromo-6-phenyl-4-*tert*-butylbenzene (**J**) was used in place of 1-benzyloxy-2-iodobenzene (**A**). The reaction was performed with the following reagents: 1-benzyloxy-2-bromo-6-phenyl-4-*tert*-butylbenzene (~60% purity, 3.26 g, ~8.25 mmol), 1.6 M *n*-butyllithium in hexanes (5.9 mL, 9.43 mmol), anhydrous ZnCl₂ (1.03 g, 9.43 mmol), [Pd(PPh₃)₄] (454 mg, 0.393 mmol), and 2,5-dibromopyridine (1.86 g, 7.86 mmol). Purification of the crude material by silica gel column chromatography (5:95 EtOAc/hexanes) gave a white solid (909 mg, 39%). ¹H NMR (CDCl₃, 500 MHz): δ 8.83 (s, 1H), 7.89 (d, *J* = 8.0 Hz, 1H), 7.81 (s, 2H), 7.70 (d, *J* = 7.0 Hz, 2H), 7.52-7.44 (m, 4H), 7.24-7.20 (m, 3H), 6.80 (d, *J* = 7.0 Hz, 2H), 4.29 (s, 2H), 1.45 (s, 9H). ¹³C NMR (CDCl₃, 125 MHz): δ 155.40, 151.76, 150.58, 147.69, 139.03, 138.39, 136.63, 135.96, 133.05, 129.84, 129.45, 128.70, 128.39, 128.26, 128.06, 127.44, 127.22, 126.87, 119.27, 75.87, 34.82, 31.66. ESI-MS = 472.2 [M+H]⁺ (Calcd = 472.1 [M+H]⁺). Mp = 164-166 °C.

Benz₂LV^{H,H} (5,5'-(4,5-dimethoxy-1,2-phenylene)bis(ethyne-2,1-diyl)bis(2-(2-(benzyloxy)phenyl)-pyridine). Solid 2-(2-benzyloxyphenyl)-5-bromopyridine (**B**) (600 mg, 1.76 mmol), 4,5-diethynylveratrole (149 mg, 0.802 mmol), [Pd(PPh₃)₄] (93 mg, 80.2 μmol), and triethylamine (0.28 mL, 2.00 mmol) were combined with 20 mL of dry THF in a sealed reaction vessel. The reaction was stirred at 80 °C for 3 d. A 20 mL solution of dichloromethane was added and the mixture was washed with H₂O (2 x 50 mL). The organic layer was separated, dried over Na₂SO₄, and evaporated to dryness. The crude material was purified by silica gel column chromatography (20:80 EtOAc/hexanes) to afford a beige solid (381 mg, 67%). ¹H NMR (CDCl₃, 500 MHz): δ 8.91 (d, *J* = 1.5 Hz, 2H), 7.96 (d, *J* = 8.0 Hz, 2H), 7.91 (dd, *J* = 9.0, 1.5 Hz, 2H), 7.80 (dd, *J* = 10.5, 2.0 Hz, 2H), 7.38-7.31 (m, 8H), 7.25 (d, *J* = 7.5 Hz, 2H), 7.13-7.05 (m, 8H), 5.14 (s, 4H),

3.96 (s, 6H). ^{13}C NMR (CDCl_3 , 125 MHz): δ 156.38, 154.94, 151.82, 149.55, 137.98, 136.96, 131.46, 130.50, 128.93, 128.70, 128.00, 127.21, 124.85, 121.70, 118.57, 118.34, 114.27, 113.32, 91.57, 89.76, 70.79, 56.28. ESI-MS = 705.6 $[\text{M}+\text{H}]^+$ (Calcd = 705.3 $[\text{M}+\text{H}]^+$). Mp = 51-54 °C.

$\text{Me}_2\text{L}^{\text{H,H}}$ (1,2-bis((6-(2-methoxyphenyl)pyridin-3-yl)ethynyl)benzene). The same procedure was employed as for the synthesis of $\text{Benz}_2\text{LV}^{\text{H,H}}$, except that 5-bromo-2-(2-methoxyphenyl)pyridine (**C**) was used instead of 2-(2-benzyloxyphenyl)-5-bromopyridine (**B**), and 1,2-diethynylbenzene was used instead of 4,5-diethynylveratrole. The reaction was performed with the following reagents: 1,2-diethynylbenzene (331 mg, 2.63 mmol), 5-bromo-2-(2-methoxyphenyl)pyridine (2.00 g, 5.78 mmol), $[\text{Pd}(\text{PPh}_3)_4]$ (304 mg, 0.263 mmol), and triethylamine (0.92 mL, 6.58 mmol). Purification of the crude material by silica gel column chromatography (20:80 EtOAc/hexanes) gave a light yellow solid (341 mg, 26%). ^1H NMR (CDCl_3 , 500 MHz): δ 8.91 (d, $J = 3.0$ Hz, 2H), 7.92-7.86 (m, 6H), 7.63 (m, 2H), 7.42-7.37 (m, 4H), 7.11 (t, $J = 7.5$ Hz, 2H), 7.02 (2, $J = 8.0$ Hz, 2H), 3.89 (s, 6H). ^{13}C NMR (CDCl_3 , 125 MHz): δ 157.32, 155.33, 151.98, 138.42, 132.34, 131.41, 130.67, 128.72, 128.43, 125.57, 124.83, 121.36, 118.26, 111.63, 91.44, 91.08, 55.84. ESI-MS = 493.3 $[\text{M}+\text{H}]^+$ (Calcd = 493.2 $[\text{M}+\text{H}]^+$). Mp = 150-151 °C.

$\text{Me}_2\text{L}^{\text{H,Ph}}$ (1,2-bis((6-(2-methoxybiphenyl-3-yl)pyridin-3-yl)ethynyl)benzene). The same procedure was employed as for the synthesis of $\text{Benz}_2\text{LV}^{\text{H,H}}$, except that 5-bromo-2-(2-methoxybiphenyl-3-yl)pyridine (**F**) was used instead of 2-(2-benzyloxyphenyl)-5-bromopyridine (**B**), and 1,2-diethynylbenzene was used instead of 4,5-diethynylveratrole. The reaction was performed with the following reagents: 1,2-diethynylbenzene (529 mg, 4.20 mmol), 5-bromo-2-(2-methoxybiphenyl-3-yl)pyridine (3.0 g, 8.82 mmol), $[\text{Pd}(\text{PPh}_3)_4]$ (486 mg, 0.420 mmol), and triethylamine (1.5 mL, 10.5 mmol). Purification of the crude material by silica gel column

chromatography (CH₂Cl₂) gave a light yellow solid (1.84 g, 68%). ¹H NMR (CDCl₃, 500 MHz): δ 8.96 (d, *J* = 1.0 Hz, 2H), 8.00 (d, *J* = 8.5 Hz, 2H), 7.92 (dd, *J* = 10.5, 1.5 Hz, 2H), 7.81 (dd, *J* = 9.0, 1.5 Hz, 2H), 7.66-7.62 (m, 6H), 7.47-7.38 (m, 10H), 7.31 (t, *J* = 8.0 Hz, 2H), 3.26 (s, 6H). ¹³C NMR (CDCl₃, 125 MHz): δ 155.70, 155.63, 152.08, 138.61, 138.54, 136.02, 133.63, 132.28, 130.65, 129.45, 128.73, 128.42, 127.42, 125.44, 124.76, 124.47, 118.53, 91.65, 90.84, 61.15. ESI-MS = 645.5 [M+H]⁺ (Calcd = 645.2 [M+H]⁺). Mp = 128-130 °C.

Benz₂L^{Me,Ph} (1,2-bis((6-(2-(benzyloxy)-5-methylbiphenyl-3-yl)pyridin-3-yl)ethynyl)benzene).

Method A: The same procedure was employed as for the synthesis of Benz₂LV^{H,H}, except that 5-bromo-2-(2-benzyloxy-5-methylbiphenyl-3-yl)pyridine (**K**) was used instead of 2-(2-benzyloxyphenyl)-5-bromopyridine (**B**), and 1,2-diethynylbenzene was used instead of 4,5-diethynylveratrole. The reaction was performed with the following reagents: 1,2-diethynylbenzene (345 mg, 2.74 mmol), 5-bromo-2-(2-benzyloxy-5-methylbiphenyl-3-yl)pyridine (2.47 g, 5.74 mmol), [Pd(PPh₃)₄] (317 mg, 0.274 mmol), and triethylamine (1 mL, 6.85 mmol). Purification of the crude material by silica gel column chromatography (10:90 EtOAc/hexanes) gave a light yellow solid (1.26 g, 56%). **Method B:** Solid 1,2-bis((trimethylsilyl)ethynyl)benzene (1.31 g, 4.85 mmol) was dissolved in THF (50 mL) and treated with a 1.0 M solution of NBu₄F (10.2 mL in THF, 10.2 mmol). The mixture was stirred for 4.5 h and then charged with 5-bromo-2-(2-benzyloxy-5-methylbiphenyl-3-yl)pyridine (**K**) (5.21 g, 12.1 mmol), [Pd(PPh₃)₄] (560 mg, 0.485 mmol), and NEt₃ (2.0 mL, 14.6 mmol). The reaction was stirred at 70 °C for 2 d. The workup and purification procedure was identical to method A. The product was obtained in 45% yield (1.80 g). ¹H NMR (CDCl₃, 500 MHz): δ 8.96 (d, *J* = 1.5 Hz, 2H), 8.02 (d, *J* = 8.5 Hz, 2H), 7.86 (dd, *J* = 10.5, 2.0 Hz, 2H), 7.69-7.67 (m, 8H), 7.47 (t, *J* = 7.0 Hz, 4H), 7.42-7.41 (m, 4H), 7.29 (d, *J* = 2.0 Hz, 2H), 7.17-7.14 (m, 6H), 6.78 (dd,

$J = 9.0, 1.5$ Hz, 4H), 4.27 (s, 4H), 2.46 (s, 6H). ^{13}C NMR (CDCl_3 , 125 MHz): δ 155.82, 152.07, 151.99, 138.79, 138.40, 136.58, 136.48, 134.62, 133.93, 132.97, 132.41, 131.03, 129.90, 128.96, 128.87, 128.48, 128.36, 128.20, 127.55, 125.54, 125.20, 118.52, 91.71, 91.05, 76.02, 21.18. ESI-MS = 825.8 $[\text{M}+\text{H}]^+$ (Calcd = 825.3 $[\text{M}+\text{H}]^+$). Mp = 111-114 °C.

Benz₂L^{tBu,Ph} (1,2-bis((6-(2-(benzyloxy)-5-*tert*-butylbiphenyl-3-yl)pyridin-3-yl)ethynyl)-benzene). The same procedure was employed as for the synthesis of Benz₂L^{H,H}, except that 5-bromo-2-(2-benzyloxy-5-*tert*-butylbiphenyl-3-yl)pyridine (**L**) was used instead of 2-(2-benzyloxyphenyl)-5-bromopyridine (**B**), and 1,2-diethynylbenzene was used instead of 4,5-diethynylveratrole. The reaction was performed with the following reagents: 1,2-diethynylbenzene (64 mg, 0.508 mmol), 5-bromo-2-(2-benzyloxy-5-*tert*-butylbiphenyl-3-yl)pyridine (576 mg, 1.22 mmol), $[\text{Pd}(\text{PPh}_3)_4]$ (59 mg, 0.051 mmol), and triethylamine (0.2 mL, 1.27 mmol). Purification of the crude material by silica gel column chromatography (5:95 to 10:90 EtOAc/hexanes) gave a yellow solid (260 mg, 56%). ^1H NMR (CDCl_3 , 500 MHz): δ 8.97 (d, $J = 1.5$ Hz, 2H), 7.99 (d, $J = 8.0$ Hz, 2H), 7.86-7.83 (m, 4H), 7.69-7.67 (m, 6H), 7.49-7.46 (m, 6H), 7.43-7.41 (m, 4H), 7.15-7.14 (m, 6H), 6.78-6.76 (m, 4H), 4.26 (s, 4H), 1.42 (s, 18H). ESI-MS = 909.9 $[\text{M}+\text{H}]^+$ (Calcd = 909.4 $[\text{M}+\text{H}]^+$). Mp = 176-177 °C.

2-Benzyloxy-3-bromo-5-methylbenzaldehyde (P). Solid 1-benzyloxy-2,6-dibromo-4-methylbenzene (**O**) (27.7 g, 77.8 mmol) was dissolved in 500 mL of dry toluene and cooled to -78 °C. A 1.6 M *n*-butyllithium solution in hexanes (58 mL, 93.4 mmol) was added slowly to the reaction mixture and stirred for 1.5 h. The mixture was then treated with anhydrous DMF (9.0 mL, 117 mmol) and continued to stir at -78 °C for 10 h. Once the reaction was complete, formation of a white precipitate was observed. The reaction mixture was washed with H₂O (3x200 mL), dried over Na₂SO₄, and evaporated to dryness. The resulting oil was dissolved in

MeOH (200 mL) and cooled to -25 °C to induce crystallization. After 4 h, the material was isolated by filtration to give a white solid (15.5 g, 65%). ¹H NMR (CDCl₃, 125 MHz): δ 10.09 (s, 1H), 7.67 (d, *J* = 2.5 Hz, 1H), 7.57 (d, *J* = 2.0 Hz, 1H), 7.47-7.39 (m, 5H), 5.09 (s, 2H), 2.35 (s, 3H). ¹³C NMR (CDCl₃, 500 MHz): δ 189.18, 156.28, 140.06, 136.08, 135.44, 130.96, 128.8, 127.85, 118.08, 77.85, 20.57. GC-MS = 304 [M]⁺ (Calcd = 304 [M]⁺). Mp = 53-55 °C.

2-Benzyloxy-5-methyl-3-phenylbenzaldehyde (Q). Solid 2-Benzyloxy-3-bromo-5-methylbenzaldehyde (**P**) (5.26 g, 17.2 mmol), phenyl boronic acid (3.16 g, 25.9 mmol), Pd(PPh₃)₄ (0.99 g, 0.86 mmol), and NaCO₃ (3.65 g, 34.4 mmol) were combined with 100 mL of H₂O/THF (1:1) and degassed with N₂ for 30 min. The reaction mixture was stirred vigorously and refluxed for 12 h. Dichloromethane (200 mL) was added and the organic phase was separated from the aqueous layer. The organic mixture was dried over Na₂SO₄ and evaporated to yield an oil. The crude material was purified by silica gel column chromatography (5:95 EtOAc/hexanes) and the desired product was further crystallized from hot hexanes to afford a white solid (3.92 g, 76 %). ¹H NMR (CDCl₃, 500 MHz): δ 10.32 (s, 1H), 7.64 (m, 3H), 7.50-7.43 (m, 4H), 7.30-7.27 (m, 3H), 7.08-7.06 (m, 2H), 4.53 (s, 2H), 2.42 (s, 3H). ¹³C NMR (CDCl₃, 125 MHz): δ 190.22, 157.07, 138.05, 137.30, 136.04, 135.66, 134.27, 129.78, 129.12, 128.73, 128.57, 128.44, 127.80, 127.34, 77.06, 20.71. GC-MS = 302 [M]⁺ (Calcd = 302 [M]⁺). Mp = 98-99 °C.

2-Hydroxy-5-methyl-3-phenylbenzaldehyde (R). The 2-benzyloxy-5-methyl-3-phenylbenzaldehyde compound (**Q**) (3.92 g, 13 mmol) was dissolved in 50 mL of dry CH₂Cl₂ and cooled to 0 °C. A 1.0 M boron tribromide solution in CH₂Cl₂ (26 mL, 26 mmol) was added slowly to the reaction flask and the solution immediately became a dark red-orange color. The reaction was stirred for 2 h and then quenched with H₂O (50 mL). The organic layer was

separated, dried over Na₂SO₄ and evaporated to dryness. The crude material was purified by silica gel column chromatography (5:95 EtOAc/hexanes) to give the desired product as a yellow oil (3.92 g, 76%). ¹H NMR (CDCl₃, 500 MHz): δ 11.40 (s, 1H), 9.90 (s, 1H), 7.62 (d, *J* = 8 Hz, 2H), 7.49-7.45 (m, 3 H), 7.39 (m, 1H), 7.34 (s, 1H), 7.40 (s, 3H). ¹³C NMR (CDCl₃, 125 MHz): δ 197.56, 157.52, 139.64, 137.17, 133.78, 130.90, 129.99, 129.88, 129.01, 126.33, 121.35, 21.06. GC-MS = 212 [M]⁺ (Calcd = 212 [M]⁺).

H₂L^{H,H} (2,2'-(5,5'-(4,5-dimethoxy-1,2-phenylene)bis(ethyne-2,1-diyl)bis(pyridine-5,2-diyl)) di-phenol) . Solid Benz₂L^{H,H} (5,5'-(4,5-dimethoxy-1,2-phenylene)bis(ethyne-2,1-diyl)bis(2-(2-(benzyloxy)phenyl)pyridine)) (46.0 mg, 65.3 μmol) and iodotrimethylsilane (0.02 mL, 163 μmol) were combined in 2 mL of dry CH₂Cl₂ in a 10 mL Schlenk flask. The reaction mixture was stirred at RT for 22 h. A diluted solution of HCl(aq) was added and the organic phase was extracted with CH₂Cl₂. The organic layer was separated, dried over Na₂SO₄, filtered, and evaporated to dryness. The crude material was purified by silica gel column chromatography (CH₂Cl₂) to afford a yellow solid (10 mg, 29%). ¹H NMR (CDCl₃, 500 MHz): δ 8.70 (s, 2H), 7.95 (d, *J* = 2.0 Hz, 4H), 7.80 (dd, *J* = 9.5, 1.5 Hz, 2H), 7.34 (t, *J* = 8.5 Hz, 2H), 7.08-7.04 (m, 4H), 6.93 (t, *J* = 8.5 Hz, 2H), 3.98 (s, 6H). ESI-MS = 525.3 [M+H]⁺ (Calcd = 525.2 [M+H]⁺). Mp = 166-167 °C.

H₂L^{H,H} (2,2'-(5,5'-(1,2-phenylenebis(ethyne-2,1-diyl))bis(pyridine-5,2-diyl))diphenol). Solid Me₂L^{H,H} (1,2-bis((6-(2-methoxyphenyl)pyridin-3-yl)ethynyl)benzene) (340 mg, 0.690 mmol) was dissolved in 15 mL of dry CH₂Cl₂ and cooled to -78 °C. A 1.0 M CH₂Cl₂ solution of BBr₃ (3.4 mL, 3.45 mmol) was added slowly to the reaction mixture and stirred for 6 h at 0 °C. The reaction was quenched with trifluoroacetic acid (2 mL) and washed with K₂CO₃ (aq). The

organic layer was separated, dried over Na₂SO₄, filtered, and evaporated to dryness. Purification of the crude material by silica gel column chromatography (20:80 EtOAc/Hexanes) gave a yellow solid (122 mg, 38%). ¹H NMR (CDCl₃, 500 MHz): δ 11.74 (bs, 2H), 8.73 (s, 2H), 8.10-8.01 (m, 4H), 7.86 (d, *J* = 8.0 Hz, 2H), 7.60 (s, 2H), 7.38 (s, 2H), 7.21 (t, *J* = 7.0 Hz, 2H), 6.87-6.81 (m, 4H). ¹³C NMR (CDCl₃, 125 MHz): δ 161.47, 158.28, 149.50, 141.05, 133.09, 132.72, 129.84, 127.62, 126.02, 120.01, 119.57, 119.44, 119.39, 118.72, 92.52, 90.93. ESI-MS = 465.3 [M+H]⁺ (Calcd = 465.2 [M+H]⁺). Mp = 141-145 °C.

H₂L^{H,Ph} (3,3'-(5,5'-(1,2-phenylenebis(ethyne-2,1-diyl))bis(pyridine-5,2-diyl))dibiphenyl-2-ol). The foregoing procedure was employed except that Me₂L^{H,Ph} (1,2-bis((6-(2-methoxybiphenyl-3-yl)pyridin-3-yl)ethynyl)benzene) was used in place of Me₂L^{H,H}. The reaction was performed using Me₂L^{H,Ph} (1.50 g, 2.32 mmol) and 1.0 M BBr₃ in CH₂Cl₂ (12 mL, 12 mmol). Purification of the crude material by silica gel column chromatography (20:80 THF/hexanes) gave a yellow solid (393 mg, 27%). ¹H NMR (CDCl₃, 500 MHz): δ 14.50 (bs, 2H), 8.66 (s, 2H), 8.00-7.95 (m, 4H), 7.82 (d, *J* = 8.0 Hz, 2H), 7.66-7.61 (m, 6H), 7.47-7.34 (m, 10H), 7.00 (t, *J* = 8.0 Hz, 2H). ¹³C NMR (CDCl₃, 125 MHz): δ 157.60, 157.22, 148.33, 140.07, 138.57, 133.35, 132.34, 131.57, 129.69, 129.03, 128.25, 127.23, 126.06, 125.19, 119.31, 119.06, 118.68, 118.10, 92.33, 90.04. ESI-MS = 617.4 [M+H]⁺ (Calcd = 617.2 [M+H]⁺). Mp = 104-106 °C.

H₂L^{Me,Ph} (3,3'-(5,5'-(1,2-phenylenebis(ethyne-2,1-diyl))bis(pyridine-5,2-diyl))bis(5-methylbiphenyl-2-ol). **Method A:** Solid Benz₂L^{Me,Ph} (1,2-bis((6-(2-(benzyloxy)-5-methylbiphenyl-3-yl)pyridin-3-yl)ethynyl)benzene) (1.20 g, 1.45 mmol) and iodotrimethylsilane (2.1 mL, 14.9 mmol) were combined in 50 mL of dry toluene and stirred in a sealed reaction vessel at 130 °C for 3 d. Dilute HCl (aq) was added to quench the reaction and the organic phase was extracted

into CH₂Cl₂ (3 x 30 mL). The organic layer was separated, dried over Na₂SO₄, filtered, and evaporated to dryness. Purification of the crude material by silica gel column chromatography (50:50 hexanes/CH₂Cl₂) gave a yellow solid (630 mg, 67%). **Method B:** Solid Benz₂L^{Me,Ph} (1.65 g, 2.00 mmol) was dissolved in CH₂Cl₂ (75 mL) and cooled to -78°C. A 1.0 M BBr₃ solution in CH₂Cl₂ (4.40 mL, 4.40 mmol) was added dropwise into the reaction flask. After stirring for 2 h, the mixture was quenched with H₂O (100 mL). The organic product was extracted with CH₂Cl₂ (3 x 50 mL), dried over Na₂SO₄, filtered, and evaporated to afford an oil. About 50 mL of CH₃OH was added to the residue and a large amount of yellow solid appeared after 1 h. The product was isolated by filtration and re-crystallized from hot CH₂Cl₂/CH₃OH to give the desired material (0.99 g, 78 %). ¹H NMR (CDCl₃, 500 MHz): δ 14.38 (bs, 2H), 8.64 (s, 2H), 7.95 (dd, *J* = 8.5 Hz, 4H), 7.68-7.61 (m, 8H), 7.48-7.35 (m, 8H), 7.35 (s, 2H), 2.40 (d, 6H). ¹³C NMR (CDCl₃, 125 MHz): δ 155.31, 148.30, 139.94, 138.65, 134.28, 132.28, 131.23, 129.64, 128.96, 128.21, 127.89, 127.15, 126.20, 125.15, 119.24, 118.30, 117.89, 92.26, 90.09, 20.96. ESI-MS = 645.4 [M+H]⁺ (Calcd = 645.2 [M+H]⁺). Mp = 137-140 °C.

H₂L^{tBu,Ph} (3,3'-(5,5'-(1,2-phenylenebis(ethyne-2,1-diyl))bis(pyridine-5,2-diyl))bis(5-tert-butylbiphenyl-2-ol)). The same procedure was employed as for the synthesis of H₂L^{Me,Ph} (Method A), except that Benz₂L^{tBu,Ph} (1,2-bis((6-(2-(benzyloxy)-5-tert-butylbiphenyl-3-yl)pyridin-3-yl)ethynyl)benzene) was used instead of Benz₂L^{Me,Ph}. The reaction was performed with Benz₂L^{tBu,Ph} (260 mg, 0.286 mmol) and iodotrimethylsilane (0.4 mL, 2.86 mmol). Purification of the crude material by silica gel column chromatography (50:50 CH₂Cl₂/Hexanes) gave a yellow solid (43 mg, 21%). ¹H NMR (CDCl₃, 500 MHz): δ 14.39 (bs, 2H), 8.68 (d, 2.5 Hz, 2H), 8.93 (d, *J* = 8.5 Hz, 2H), 7.97 (dd, *J* = 10.5, 2.0 Hz, 2H), 7.83 (d, *J* = 2.5 Hz, 2H), 7.69-7.68 (m, 4H), 7.65-7.63 (m, 2H), 7.50-7.47 (m, 6H), 7.41-7.37 (m, 4H), 1.42 (s, 18H). ¹³C NMR

(CDCl₃, 125 MHz): δ 157.54, 155.28, 148.46, 141.42, 139.93, 139.07, 132.35, 131.08, 130.98, 129.73, 128.98, 128.24, 127.14, 125.14, 122.39, 119.21, 117.86, 117.85, 92.21, 90.12, 34.49, 21.77. ESI-MS = 729.5 [M+H]⁺ (Calcd = 729.3 [M+H]⁺). Mp = 125-128 °C.

H₂BIPS^{Me,Ph} (3,3'-(1*E*,1'*E*)-(3,3'-sulfonylbis(3,1-phenylene)bis(azan-1-yl-1-ylidene))bis(methan-1-yl-1-ylidene)bis(5-methylbiphenyl-2-ol)). In a 100 mL round-bottom flask, 2-hydroxy-5-methyl-3-phenylbenzaldehyde (**R**) (2.60 g, 12.3 mmol) and 3,3'-diaminodiphenylsulfone (1.38 g, 5.56 mmol) were dissolved in 50 mL of MeOH. The mixture was treated with formic acid (0.46 mL, 12.3 mmol) and stirred at room temperature for 5 h. The resulting bright orange precipitate was isolated by filtration and washed with MeOH. Purification of the reaction product by silica gel column chromatography (CH₂Cl₂ → 15:85 EtOAc/CH₂Cl₂) gave the desired product (2.1 g, 48 %). A small amount of the starting aldehyde and singly condensed product (< 2 %) were still present in the purified material, presumably due to hydrolysis of H₂BIPS^{Me,Ph}. ¹H NMR (CDCl₃, 500 MHz): δ 13.19 (s, 2H), 8.59 (s, 2H), 7.88 (m, 2H), 7.61-7.57 (m, 6H), 7.47-7.44 (m, 4H), 7.38-7.24 (m, 6 H), 2.38 (s, 6H). ¹³C NMR (CDCl₃, 125 MHz): δ 164.97, 156.52, 149.62, 142.86, 137.58, 136.23, 132.41, 130.84, 130.18, 129.47, 126.68, 128.37, 127.48, 126.99, 125.88, 119.99, 118.88, 20.61. ESI-MS = 637.2 [M+H]⁺ (Calcd = 637.2 [M+H]⁺). Mp = 141-145 °C.

[Fe₂(L^{Me, Ph})₂(THF)₃] (1). Inside a drybox, solid H₂L^{Me,Ph} (200 mg, 310 μ mol) and [Fe₂(Mes)₄] (91.3 mg, 155 μ mol) were dissolved in 10 mL of THF in a 25 mL flask to give a dark red solution. The mixture was stirred at RT for 10 min and the solvent was removed *in vacuo*. A solution of Et₂O (10 mL) was added and the resulting suspension was stirred for 10 min. The solid material was isolated by filtration and crystallized by layering pentane (2 mL) over a solution of the compound in THF (10 mL). The crystals were isolated by filtration and dried

under vacuum to give a red-brown powder (116 mg, 46%). Crystals suitable for X-ray diffraction studies were obtained by vapor diffusion of pentane into a solution of the complex in THF. ^1H NMR (THF- d_8 , 500 MHz): δ = 44.45 (bs), 42.20 (bs), 38.08 (bs), 36.30 (bs), 34.14 (bs, methyl), 11.01 (bs), 6.84 (bs), 6.25 (bs), 5.61 (bs), 4.61 (bs). IR (KBr): ν = 3442, 2918, 2851, 1595, 1555, 1495, 1453, 1420, 1368, 1292, 1250, 1222, 1045, 840, 821, 757, 698 cm^{-1} . λ_{max} = 395 (ϵ = 5130 $\text{M}^{-1} \text{cm}^{-1}$), 332 (ϵ = 63,300 $\text{M}^{-1} \text{cm}^{-1}$), 306 (ϵ = 94100 $\text{M}^{-1} \text{cm}^{-1}$), 235 (ϵ = 137000 $\text{M}^{-1} \text{cm}^{-1}$) nm. ^{57}Fe Mössbauer (90 K): δ = 1.13 mm/s, ΔE_Q = 1.88 mm/s, $\Gamma_{\text{L/R}}$ = 0.47 mm/s. Mp > 400 °C. Anal. Calc. for **1**, $\text{Fe}_2\text{C}_{104}\text{H}_{84}\text{N}_4\text{O}_7$: C, 77.42; H, 5.25; N, 3.47. Found: C, 76.66, 76.91; H, 4.50, 4.22; N, 4.16, 4.65. Drying of the samples under vacuum at 80 °C and repeated measurements of independently prepared material gave similar results. Deviations between calculated and observed values are ascribed to residual solvent molecules and possibly partial oxidation to form **2** since **1** is quite air-sensitive. Because we have crystal structure information on **1**, which has disordered THF and pentane in the crystal lattice, and the crystalline samples looked identical with copious amounts of material, there is no doubt about the composition of **1**.

[Fe₂(μ -O)(L^{Me, Ph})₂] (2). Method A. The $[\text{Fe}_2(\text{L}^{\text{Me, Ph}})_2(\text{THF})_3]$ complex (50 mg, 31 μmol) was dissolved in THF (2 mL) in a 5 mL Schlenk flask under a nitrogen atmosphere. An excess amount of dry O₂ gas was introduced and the reaction was stirred for 5 min. The solvent mixture was evaporated to dryness and the resulting dark red residue was extracted into dry toluene (2 mL). The desired material was crystallized from vapor diffusion of pentane into a solution of the complex in toluene to give a dark red material (35 mg, 80%). **Method B.** The dinucleating ligand H₂L^{Me, Ph} (137 mg, 213 μmol) and NaHMDS (82 mg, 447 μmol) were dissolved in THF (3 mL) to give a bright orange solution. A solution of (NEt₄)₂[Fe₂OCl₆]²⁹ (141 mg, 234 μmol) in CH₃CN (0.5 mL) was added and the dark red mixture was stirred for 15 min. The solvent was removed *in*

vacuo and the resulting product was extracted into toluene. Evaporation of the toluene solution gave the desired complex as a red solid (70 mg, 47 %). Crystals suitable for X-ray diffraction studies were obtained by vapor diffusion of pentane into a solution of the complex in THF. ^1H NMR (THF- d_8 , 500 MHz): δ = 16.42 (bs), 13.90 (bs), 11.75 (bs), 8.56 (bs), 8.25 (bs), 7.59 (bs), 7.52 (bs), 6.96 (bs), 6.60 (bs). IR (KBr): ν = 3431, 3030, 2917, 2851, 1598, 1493, 1418, 1367, 1290, 1250, 1225, 833, 758, 697 cm^{-1} . λ_{max} = 390 (sh, ϵ = 37,500 $\text{M}^{-1} \text{cm}^{-1}$), 312 (ϵ = 108,000 $\text{M}^{-1} \text{cm}^{-1}$) nm. ^{57}Fe Mössbauer (90K): δ = 0.43 mm/s, ΔE_{Q} = 1.35 mm/s, $\Gamma_{\text{L/R}}$ = 0.42 mm/s. Mp = 335 °C (decomposition). Anal. Calc. for $2 \cdot (\text{THF})_4$, $\text{Fe}_2\text{C}_{108}\text{H}_{92}\text{N}_4\text{O}_9$: C, 76.96; H, 5.50; N, 3.33. Found: C, 76.23; H, 5.45; N, 3.29. This result is consistent with the four THF molecules found in a low-resolution X-ray crystal structure of **2**.

UV-Vis Spectrophotometric Studies

Reaction of $\text{Na}_2\text{L}^{\text{R,R}'}$ or $\text{Na}_2\text{BIPS}^{\text{Me,Ph}}$ with Fe(II) in THF. Inside a nitrogen drybox, stock solutions of either $\text{Na}_2\text{L}^{\text{R,R}'}$ or $\text{Na}_2\text{BIPS}^{\text{Me,Ph}}$ were prepared by dissolving the $\text{H}_2\text{L}^{\text{R,R}'}$ or $\text{H}_2\text{BIPS}^{\text{Me,Ph}}$ ligand in THF containing two equiv of NaHMDS, giving a concentration of ~ 20 μM . A 3.0 mL portion of either the $\text{Na}_2\text{L}^{\text{R,R}'}$ or $\text{Na}_2\text{BIPS}^{\text{Me,Ph}}$ stock solution was added via a septum to a sealed UV-vis quartz cuvette and brought outside of the drybox. An anaerobic CH_3CN solution of $\text{Fe}(\text{OSO}_2\text{CF}_3)_2$ (~ 3 mM) was loaded into a 25 μL gas-tight syringe. Small aliquots (~ 5 μL , 0.25 equiv relative to $\text{Na}_2\text{L}^{\text{R,R}'}$ or $\text{Na}_2\text{BIPS}^{\text{Me,Ph}}$) of the $\text{Fe}(\text{OSO}_2\text{CF}_3)_2$ solution were added to the sample in the cuvette and the absorption spectra were recorded.

Reaction of 2 Fe(II) and $\text{Na}_2\text{L}^{\text{H,Ph}}$ with $\text{Ph}_3\text{CCO}_2\text{Na}$ in THF. Inside a nitrogen drybox, a THF solution containing $\text{Fe}(\text{OSO}_2\text{CF}_3)_2$ (60 μM) and $\text{Na}_2\text{L}^{\text{H,Ph}}$ (30 μM) was prepared in a 25 mL volumetric flask. A 4.0 mL portion of the iron-ligand mixture was added into a septum-sealed UV-vis quartz cuvette and brought outside of the drybox. A 250 μL air-tight syringe was loaded

with a degassed THF solution containing $\text{Ph}_3\text{CCO}_2\text{Na}$ (13 mM). Aliquots of the carboxylate solution ($\sim 10 \mu\text{L}$, 1.0 equiv relative to $\text{Na}_2\text{L}^{\text{H,Ph}}$) were added to the UV-vis cell and the absorption spectra were recorded.

Reaction of $[\text{Fe}_2(\text{L}^{\text{Me, Ph}})_2(\text{THF})_3]$ (1) with $[\text{FeCp}_2](\text{BF}_4)$ (Cp = cyclopentadiene) in THF.

Inside a nitrogen drybox, a stock solution of $[\text{Fe}_2(\text{L}^{\text{Me, Ph}})_2(\text{THF})_3]$ (13 μM) in THF was prepared using a 25 mL volumetric flask. A 3.0 mL portion of the $[\text{Fe}_2(\text{L}^{\text{Me, Ph}})_2(\text{THF})_3]$ solution was added to a septum-sealed UV-vis quartz cuvette and brought outside of the drybox. Small aliquots of an anaerobic CH_2Cl_2 solution of $[\text{FeCp}_2](\text{BF}_4)$ ($\sim 10 \mu\text{L}$, which equals 0.5 equiv relative to $[\text{Fe}_2(\text{L}^{\text{Me, Ph}})_2(\text{THF})_3]$) were added into the UV-vis cell and the absorption spectra were recorded.

2.3. Results and Discussion

Ligand Design and Synthesis. Controlling the coordination chemistry of kinetically labile iron complexes is a formidable challenge.^{30,31} Reaction of iron salts with simple ligands, such as alkoxides or carboxylates, typically results in formation of oligo- or polymeric metal clusters.³¹⁻³⁵ In contrast, when the ligands are too sterically hindered, mononuclear iron species are obtained.^{36,37} To construct functional protein models using carboxylate-bridged diiron assemblies, certain design elements must be considered. First, the diiron framework should be sufficiently stable towards changes of the metal oxidation state. Reaction of the reduced diiron(II) form of sMMOH with dioxygen generates transient diiron(III) and diiron(IV) intermediates.^{1,38} To access such species outside of the protein environment, the ligand must be able to stabilize iron in the +2, +3, and +4 oxidation states. Second, the diiron assembly should be structurally flexible to allow for geometric reorganization. In the biological systems, changes

in ligation of a glutamate side chain to the diiron center occur concomitantly with changes in its redox states. Such carboxylate shifts are believed to be functionally important during dioxygen activation. Third, the ligand scaffold should provide an open site for dioxygen binding between the two iron atoms. To obtain a quadrilateral core, such as the proposed di(μ -oxo)diiron(IV) structure of intermediate Q in sMMOH,³⁹ the diiron unit should be coordinatively unsaturated or have bridging ligands that could be displaced readily. Finally, the ligand framework should be amenable to synthetic modifications. This feature is important because it allows tuning of the geometric and electronic properties of a given construct using the fewest synthetic steps.

Based on the above prerequisites, we designed a series of dinucleating ligands that share a common “V-shaped” architecture (Chart 2.2). These compounds can bind two metal ions, forming stable six-membered ring chelates, and enforce a planar arrangement of O₂N₂ donor atoms. We envisioned that the planar nature of the ligand would allow for axial coordination of external carboxylates, which would match the arrangement of aspartate and glutamate side chains that are bound to the diiron protein active sites (Chart 2.1). The unique “V-shaped” ligand motif also provides an internal pocket for binding of a small molecule, such as dioxygen. Five of these compounds are derived from phenoxyipyridyl binding units tethered to a 1,2-diethynylbenzene linker. The protonated forms of these ligands are designated as H₂L^{R,R'}, where R = H, Me, or *t*-Bu and R' = H or Ph. The steric constraints of H₂L^{R,R'} are adjusted by appending alkyl or phenyl moieties to either the ortho or para positions of the phenol ring. A sixth ligand, H₂BIP^{Me,Ph}, was also synthesized using a different covalent bridge. Replacement of the diethynylbenzene unit in H₂L^{R,R'} with a bis(iminephenyl)sulfone linker alters the rotational freedom of the ligand framework. The parent bis-(3-(2-hydroxybenzylideneamino)phenyl)sulfone compound was synthesized as a ligand for preparing dinuclear copper complexes.⁴⁰

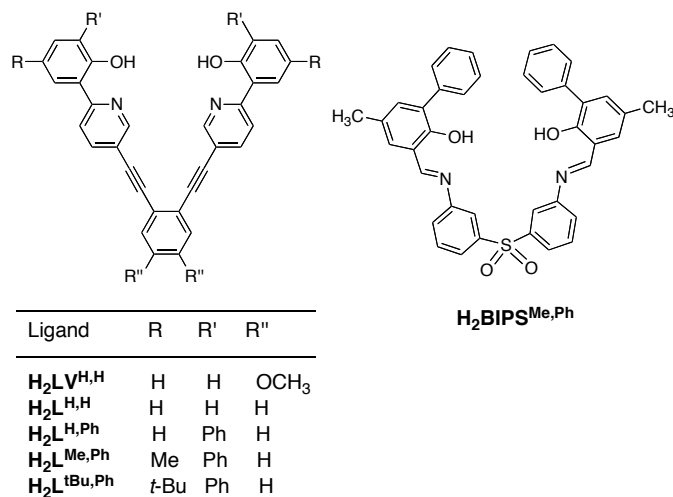
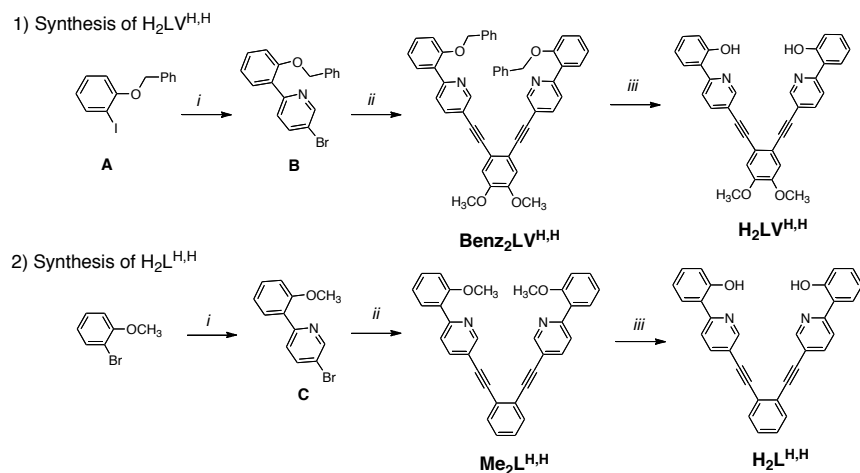


Chart 2.2. The series of phenoxy-pyridyl- (left) and phenoxy-imine- (right) dinucleating ligands synthesized.

Several routes were explored to obtain $H_2L^{R,R'}$. The synthetic routes for $H_2LV^{H,H}$, $H_2L^{H,H}$, $H_2L^{H,Ph}$, and $H_2L^{tBu,Ph}$ are provided in Schemes 2.1 and 2.2. The most efficient synthetic strategy is illustrated for the preparation of $H_2L^{Me,Ph}$ in Scheme 2.3. As described previously,²⁷ protection of the commercially available 2-bromo-4-methylphenol with tetrahydro-2*H*-pyran, followed by a Suzuki cross-coupling reaction with phenylboronic acid, gave **M** as a colorless oil. Deprotection with aqueous HCl, followed by bromination with Br₂, afforded **N** in quantitative yield. Compound **N** was subjected to a second protection procedure with benzyl bromide and isolated, after purification, as a colorless material. Negishi coupling of **I** with 2,5-dibromopyridine gave **K** as a white solid. A Sonogashira procedure was employed to couple **K** and 1,2-diethynylbenzene. Solid 1,2-diethynylbenzene is susceptible to decomposition upon storage; therefore, it was generated *in situ* from 1,2-bis((trimethylsilyl)ethynyl)benzene⁴¹ and tetrabutylammonium fluoride before use in the cross-coupling reaction. This procedure afforded the benzyl-protected

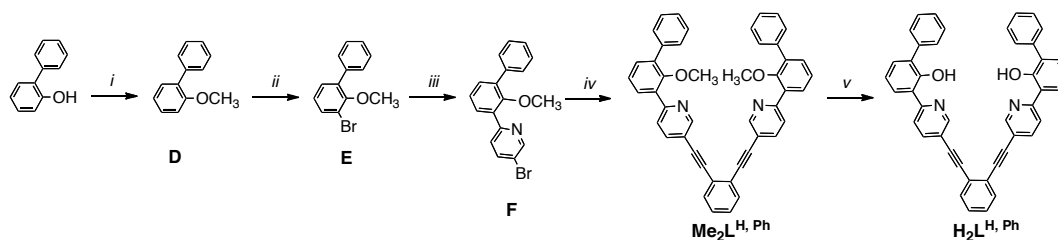
ligand $\text{Benz}_2\text{L}^{\text{Me,Ph}}$ in moderate yield after purification. Finally, the desired $\text{H}_2\text{L}^{\text{Me,Ph}}$ compound was obtained by treatment of $\text{Benz}_2\text{L}^{\text{Me,Ph}}$ with boron tribromide in CH_2Cl_2 and crystallization from $\text{CH}_2\text{Cl}_2/\text{MeOH}$. The $\text{H}_2\text{L}^{\text{Me,Ph}}$ ligand was isolated as a yellow solid.



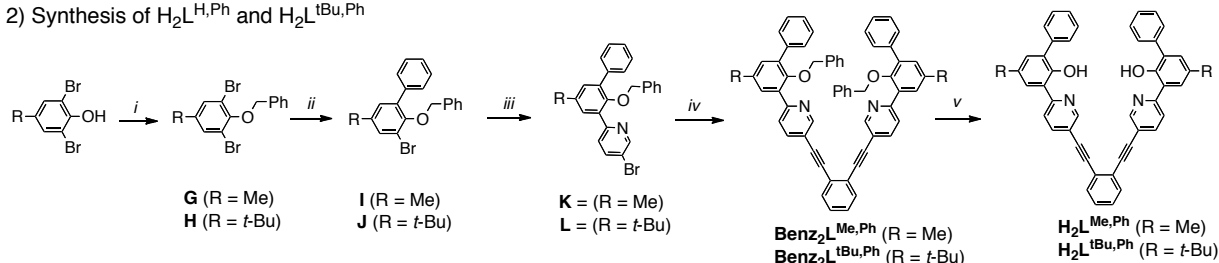
Scheme 2.1. Part 1: *i*) *a.* *n*-BuLi, THF, -78°C , *b.* ZnCl_2 , *c.* 2,5-dibromopyridine, $[\text{Pd}(\text{PPh}_3)_4]$; *ii*) 4,5-diethynylveratrole, $[\text{Pd}(\text{PPh}_3)_4]$, NEt_3 , THF, reflux; *iii*) TMSI, CH_2Cl_2 . Part 2: *i*) *a.* *n*-BuLi, THF, -78°C , *b.* ZnCl_2 , *c.* 2,5-dibromopyridine, $[\text{Pd}(\text{PPh}_3)_4]$; *ii*) 1,2-diethynylbenzene, $[\text{Pd}(\text{PPh}_3)_4]$, NEt_3 , THF, reflux; *iii*) *a.* BBr_3 , CH_2Cl_2 , *b.* $\text{CF}_3\text{CO}_2\text{H}$.

The sulfone bridged compound $\text{H}_2\text{BIPS}^{\text{Me,Ph}}$ was synthesized according to Scheme 2.3. Benzylation of 2,6-dibromo-4-methylphenol with benzyl bromide provided **O** as a colorless crystalline solid. To introduce an aldehyde functionality, **O** was treated with *n*-butyllithium and quenched with dimethylformamide to give **P**. This precursor was coupled to phenylboronic acid to provide **Q** in good yield. Cleavage of the benzyl protecting group by boron tribromide in CH_2Cl_2 cleanly gave **R** as a yellow oil. The final product was obtained by an acid-catalyzed condensation reaction between **R** and the commercially available 3,3'-diaminodiphenyl sulfone in MeOH. The desired bright orange solid, $\text{H}_2\text{BIP}^{\text{Me,Ph}}$, readily precipitated from the reaction mixture and was isolated in moderate yield.

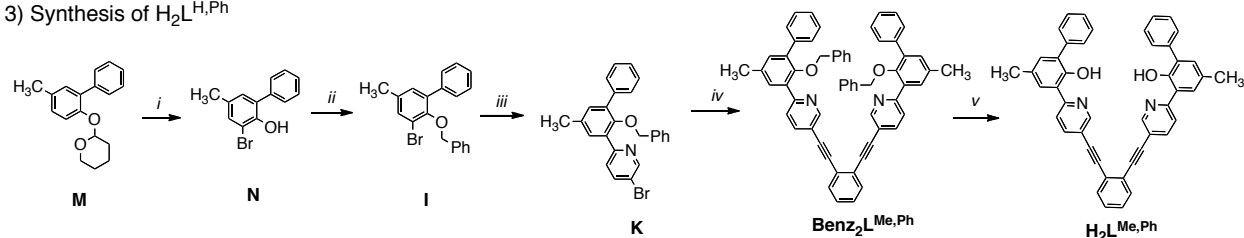
1) Synthesis of $H_2L^{H,Ph}$



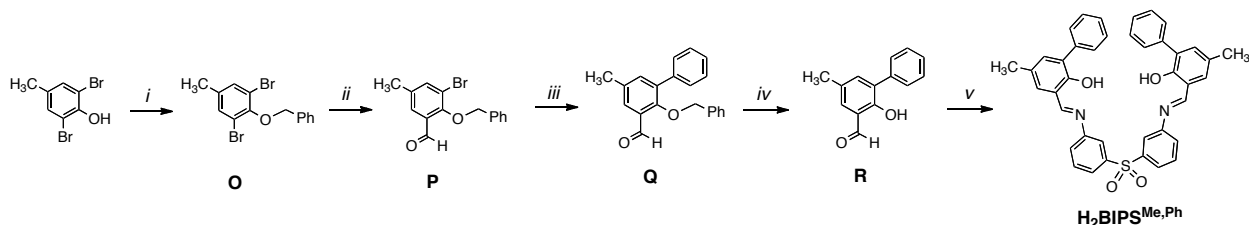
2) Synthesis of $H_2L^{H,Ph}$ and $H_2L^{tBu,Ph}$



3) Synthesis of $H_2L^{H,Ph}$



Scheme 2.2. Part 1: *i*) a. NaH, THF, 0°C , b. CH_3I , reflux; *ii*) a. TMEDA, Et_2O , b. Br_2 ; *iii*) a. *n*-BuLi, THF, -78°C . b. ZnCl_2 , c. 2,5-dibromopyridine, $[\text{Pd}(\text{PPh}_3)_4]$; *iv*) 1,2-diethynylbenzene, $[\text{Pd}(\text{PPh}_3)_4]$, NEt_3 , THF, reflux; *v*) BBr_3 , CH_2Cl_2 , 0°C . Part 2: *i*) benzyl bromide, K_2CO_3 , CH_3CN , reflux; *ii*) phenylboronic acid, $[\text{Pd}(\text{PPh}_3)_4]$, $\text{Na}_2\text{CO}_3(\text{aq})$, THF, reflux; *iii*) a. *n*-BuLi, THF, -78°C , b. ZnCl_2 , c. 2,5-dibromopyridine, $[\text{Pd}(\text{PPh}_3)_4]$; *iv*) 1,2-diethynylbenzene, $[\text{Pd}(\text{PPh}_3)_4]$, NEt_3 , THF, reflux; *v*) TMSI, toluene, reflux. Part 3: *i*) a. $\text{HCl}(\text{aq})$, b. Br_2 , CH_2Cl_2 ; *ii*) benzyl bromide, K_2CO_3 , CH_3CN ; *iii*) a. *n*-BuLi, THF, -78°C , b. ZnCl_2 , c. 2,5-dibromopyridine, $[\text{Pd}(\text{PPh}_3)_4]$; *iv*) a. 1,2-bis(trimethylsilylacetylene)benzene, NBu_4F , THF, b. $[\text{Pd}(\text{PPh}_3)_4]$, NEt_3 ; *v*) BBr_3 , CH_2Cl_2 .



Scheme 2.3. *i*) benzyl bromide, K_2CO_3 , CH_3CN ; *ii*) a. *n*-BuLi, toluene, -78°C , b. anhydrous DMF; *iii*) phenylboronic acid, $[\text{Pd}(\text{PPh}_3)_4]$, Na_2CO_3 THF/ H_2O ; *iv*) BBr_3 , CH_2Cl_2 ; *v*) 3,3'-bis(aminophenyl)sulfone, $\text{CF}_3\text{CO}_2\text{H}$, MeOH

Gram quantities of the final ligands, $H_2L^{Me,Ph}$ and $H_2BIP^{Me,Ph}$, were obtained. These synthetic routes facilitate systematic modification of ligand substituents without significant changes to the overall synthetic strategy.

UV-Vis Spectrophotometric Studies. For systems that display strong optical features, a convenient method to examine metal-ligand binding is to conduct UV-vis spectrophotometric titrations.⁴²⁻⁴⁴ If $[L^{R,R'}]^{2-}$ or $[BIPS^{Me,Ph}]^{2-}$ (where $[L^{R,R'}]^{2-}$ and $[BIPS^{Me,Ph}]^{2-}$ are the doubly deprotonated forms of $H_2L^{R,R'}$ and $H_2BIPS^{Me,Ph}$, respectively) are capable of serving as dinucleating hosts, addition of iron(II) salts to the apo-ligands should yield a 2:1 metal-to-ligand stoichiometry.

Titration experiments were first performed with the parent $H_2L^{H,H}$ compound (Figure 2.1A). Deprotonation of $H_2L^{H,H}$ with 2.0 equiv of sodium hexamethyldisilazide (NaHMDS) in THF afforded $Na_2L^{H,H}$, which displays an intense absorption at 415 nm (dotted trace). When the $Na_2L^{H,H}$ solution was treated with various aliquots of $Fe(OSO_2CF_3)_2$, formation of two sequential isosbestic points were observed, at 392 and 365 nm. This data suggest an $A \rightarrow B \rightarrow C$ reaction scheme, which would be consistent with the binding of a single iron atom followed by binding of a second iron atom to $Na_2L^{H,H}$. A plot of the absorbance change at 350 nm versus equiv of Fe(II) added (relative to $Na_2L^{H,H}$) is shown in Figure 2.2A. A gradual increase in the optical feature at 350 nm upon successive additions of iron(II) indicates that $Na_2L^{H,H}$ is capable of coordinating at least two iron atoms. Saturation behavior was not observed when ≥ 2.0 equiv of Fe(II) were added.

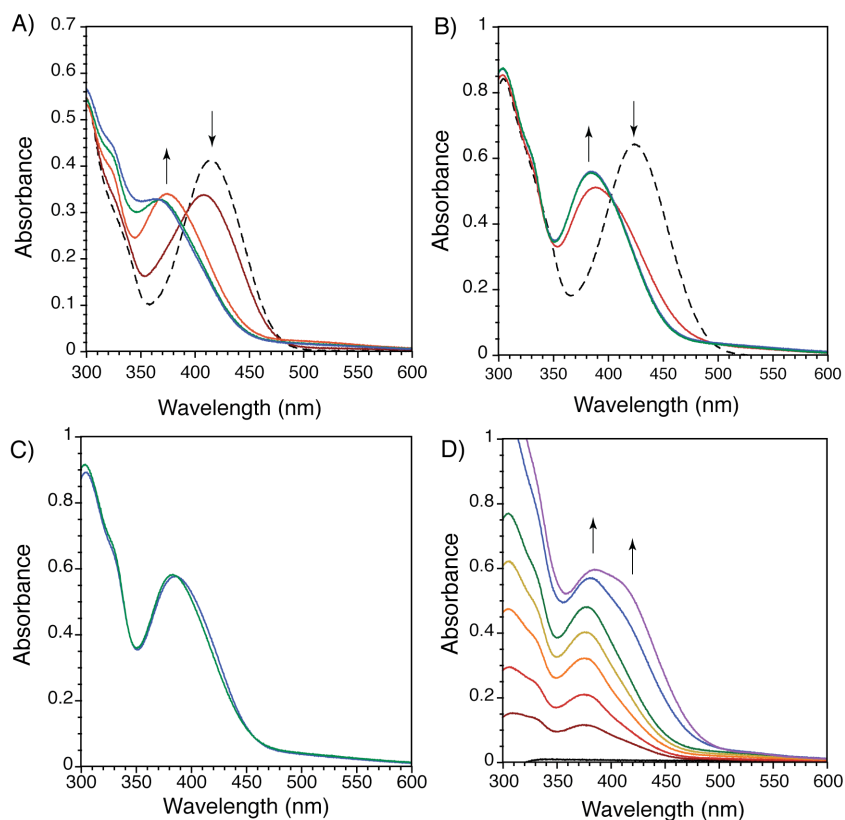


Figure 2.1. Absorption spectra of A) addition of Fe(II) to a solution containing $\text{Na}_2\text{L}^{\text{H,H}}$, B) addition of Fe(II) to a solution containing $\text{Na}_2\text{L}^{\text{H,Ph}}$, C) addition of sodium triphenylacetate to a solution containing Fe(II) and $\text{Na}_2\text{L}^{\text{H,Ph}}$, and D) addition of $\text{Na}_2\text{L}^{\text{H,Ph}}$ to a solution containing Fe(II) and sodium triphenylacetate. For A and B, the equiv of Fe(II) added is relative to the amount of the ligand. For C, the equiv of triphenylacetate added is relative to the amount of $\text{Na}_2\text{L}^{\text{H,Ph}}$. For D, the equiv of $\text{Na}_2\text{L}^{\text{H,Ph}}$ added is relative to the amount of Fe(II). All experiments were performed in tetrahydrofuran at RT. Panel A: black dotted line = $\text{Na}_2\text{L}^{\text{H,H}}$, solid lines = spectra after addition of up to 2.0 equiv of Fe(II). Panel B: black dotted line = $\text{Na}_2\text{L}^{\text{H,Ph}}$, solid lines = spectra after addition of up to 2.0 equiv of Fe(II). Panel C: blue line = $\text{Na}_2\text{L}^{\text{H,Ph}}/2$ Fe(II), green line = spectrum after addition of 20 equiv of $\text{NaO}_2\text{CCPh}_3$. Panel D: black line = Fe(II)/ 20 equiv of $\text{NaO}_2\text{CCPh}_3$, colored lines = spectra after addition of up to 2.0 equiv of $\text{Na}_2\text{L}^{\text{H,Ph}}$.

For comparison to $\text{Na}_2\text{L}^{\text{H,H}}$, reaction of the ortho substituted derivative $\text{Na}_2\text{L}^{\text{H,Ph}}$ to Fe(II) was examined. Treatment of $\text{H}_2\text{L}^{\text{H,Ph}}$ with NaHMDS in THF gave $\text{Na}_2\text{L}^{\text{H,Ph}}$, as indicated by the formation of a prominent absorption band at 424 nm (Figure 2.1B). When aliquots of $\text{Fe}(\text{OSO}_2\text{CF}_3)_2$ were added to $\text{Na}_2\text{L}^{\text{H,Ph}}$, a hypsochromic shift of the feature at 424 nm to 382 nm occurred. The optical spectra were unchanged after ≥ 1.0 equiv of Fe(II) was introduced (relative

to $\text{Na}_2\text{L}^{\text{H,Ph}}$ (Figure 2.2B). This result suggests that in the presence of Fe(II), $\text{Na}_2\text{L}^{\text{H,Ph}}$ forms a complex having a 1:1 metal-to-ligand stoichiometry. To test the stability of this new species, increasing amounts of sodium triphenylacetate were added to the $\text{Fe}^{\text{II}}/\text{Na}_2\text{L}^{\text{H,Ph}}$ mixture and the reaction was followed by UV-vis spectroscopy (Figure 2.1C). The absorbance spectrum did not change after the addition of 20 equiv of triphenylacetate (relative to $\text{Na}_2\text{L}^{\text{H,Ph}}$). If coordination of the carboxylate to the iron centers resulted in significant structural rearrangement, such a change would be reflected in the absorption spectrum. Because no optical changes were observed, it was concluded that the 1:1 Fe(II)-to- $[\text{L}^{\text{H,Ph}}]^{2-}$ species is too stable to be disrupted by triphenylacetate. When the reaction order was reversed, adding $\text{Na}_2\text{L}^{\text{H,Ph}}$ to a THF solution containing 1.0 equiv of Fe(II) and 20.0 equiv of triphenylacetate, a band at 382 nm also appeared (Figure 2.1D). Once again, formation of the 1:1 Fe(II) to $[\text{L}^{\text{H,Ph}}]^{2-}$ species was preferred. We assigned this optical spectrum to the diiron(II) $[\text{Fe}_2(\text{L}^{\text{H,Ph}})_2]$ complex (vide infra).

To investigate the effect of bulkier ligand substituents on the iron binding of $[\text{L}^{\text{R,R'}}]^{2-}$, titration studies were also carried out with $\text{Na}_2\text{L}^{\text{tBu,Ph}}$. We postulated that by appending *tert*-butyl groups to the para position of the phenol ring, the increased steric demand at the ligand periphery would prevent any possible ligand-ligand interactions in the presence of Fe(II). When treated with NaHMDS in THF, $\text{H}_2\text{L}^{\text{tBu,Ph}}$ was converted to $\text{Na}_2\text{L}^{\text{tBu,Ph}}$. The deprotonated ligand displays a characteristic absorption at 437 nm (Figure 2.3A). Upon addition of $\text{Fe}(\text{OSO}_2\text{CF}_3)_2$ to a solution of $\text{Na}_2\text{L}^{\text{tBu,Ph}}$, the band at 437 nm decreased, concomitant with an absorption increase at 393 nm. Similar to that of $\text{Na}_2\text{L}^{\text{H,Ph}}$, the absorbance profile is unchanged after addition of 1.0 equiv of Fe(II) (Figure 2.2C). A 1:1 metal-to-ligand stoichiometry would also be consistent with the formulation $[\text{Fe}_2(\text{L}^{\text{tBu,Ph}})_2]$.

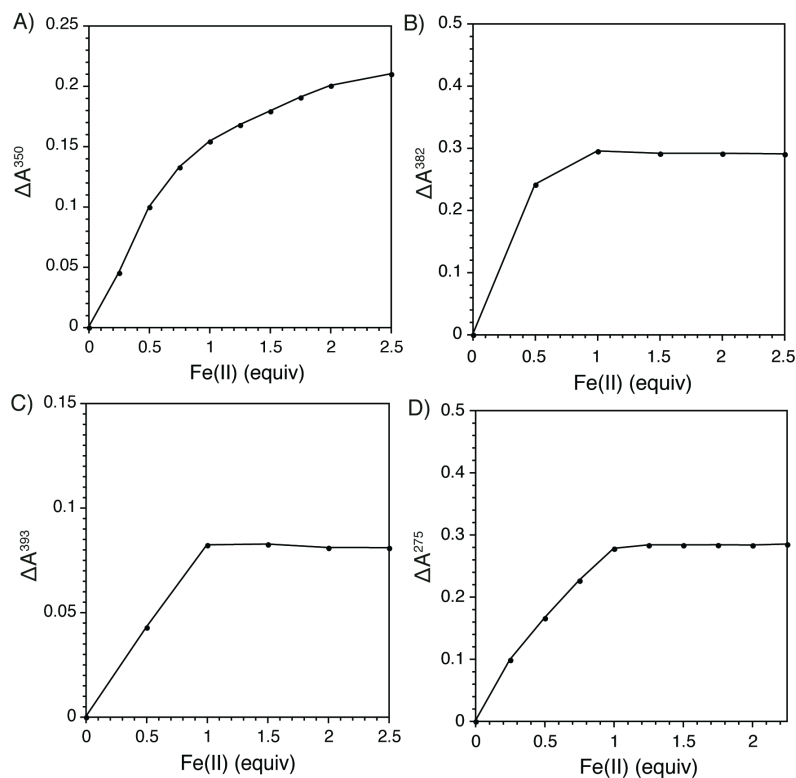


Figure 2.2. Plots of the absorbance change at a single wavelength (nm) from reaction of Fe(II) with a THF solution containing A) $\text{Na}_2\text{L}^{\text{H,H}}$, B) $\text{Na}_2\text{L}^{\text{H,Ph}}$, C) $\text{Na}_2\text{L}^{\text{tBu,Ph}}$, and D) $\text{Na}_2\text{BIPS}^{\text{Me,Ph}}$. The wavelengths were chosen to show the maximum change between successive Fe(II) titrations.

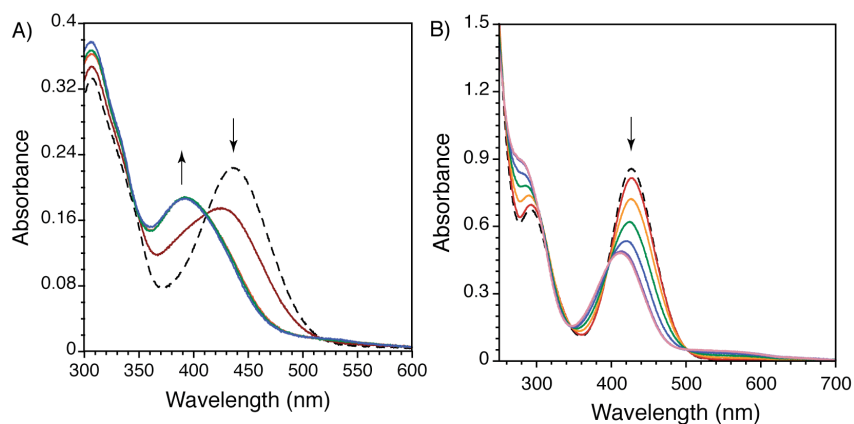


Figure 2.3. Absorption spectra from the addition of Fe(II) to a THF solution containing A) $\text{Na}_2\text{L}^{\text{tBu,Ph}}$ and B) $\text{Na}_2\text{BIPS}^{\text{Me,Ph}}$. Panel A: black dotted line = $\text{Na}_2\text{L}^{\text{tBu,Ph}}$, solid lines = spectra after addition of up to 2.0 equiv of Fe(II). Panel B: black dotted line = $\text{Na}_2\text{BIPS}^{\text{Me,Ph}}$, solid lines = spectra after addition of up to 2.0 equiv of Fe(II).

The similar results obtained for $[L^{H,Ph}]^{2-}$ and $[L^{tBu,Ph}]^{2-}$ led us to hypothesize that, although $[L^{tBu,Ph}]^{2-}$ is more sterically encumbering, free rotation about the ethynyl arms allows the $[L^{R,R'}]^{2-}$ ligands to interdigitate. To explore whether we could maintain the “V-shaped” architecture of the $[L^{R,R'}]^{2-}$ ligand design but restrict rotation of the metal-binding arms, $H_2BIPS^{Me,Ph}$ (Chart 2.2) was conceived. The bis(iminephenyl)sulfone unit is a promising alternative linker to 1,2-diethynylbenzene because it provides an ideal N–N distance for a dinucleating framework.⁴⁰ Deprotonation of $H_2BIPS^{Me,Ph}$ with NaHMDS in THF gave $Na_2BIPS^{Me,Ph}$, which has a strong absorbance at 428 nm (Figure 2.3B). When various equiv of Fe(II) were added to $Na_2BIPS^{Me,Ph}$ the band at 428 nm decreased. By evaluating the absorbance change at 275 nm, it is clear that a saturation point is reached upon addition of 1.0 equiv of Fe(II) (Figure 2.2D). Once again, this experiment indicates that a 1:1 metal-to-ligand complex is formed preferentially in solution.

Isolation and Characterization of Iron Complexes. Because the parent $[L^{H,H}]^{2-}$ ligand appeared to accommodate a 2:1 metal-to-ligand ratio, we attempted to prepare a discrete diiron complex in the presence of Fe(II), $H_2L^{H,H}$, and carboxylates (Chart 2.1, left). When $H_2L^{H,H}$ (1.0 equiv) and triphenylacetic acid (2.0 equiv) were combined with $[Fe(Mes)_4]^{2-}$ (where Mes = 2,4,6-trimethylphenyl, 1.0 equiv) in THF, a dark red solid precipitated from the reaction mixture (Scheme 2.4A). This material was insoluble in both polar and non-polar organic solvents. When the reaction was repeated using either benzoate or acetate, instead of triphenylacetate, similar results were obtained. Because phenolate groups are well known to bridge multiple metal ions,⁴⁵⁻⁴⁷ it is possible that reaction of the $[L^{H,H}]^{2-}$ ligand with Fe(II) led to the formation of undesired polymetallic species.

7.20 Å separates the two iron centers. The 1:1 Fe(II) to $[L^{R,R'}]^{2-}$ stoichiometry observed from the titration studies is reflected in the $[\text{Fe}_2(\text{L}^{\text{Me,Ph}})_2(\text{THF})_3]$ formulation. Thus, it appears that in both the solid and solution states, **1** maintains the same molecular structure. A survey of the literature revealed that only a limited number of Fe(II) complexes with terminal phenolate ligands have been characterized.^{48,49} Most iron-containing phenolate compounds are found in the Fe(III) state and/or have multiple metals bridged by the phenolate moiety.⁵⁰⁻⁵²

Table 2.1. X-ray Crystallographic Data and Refinement for $[\text{Fe}_2(\text{L}^{\text{Me,Ph}})_2(\text{THF})_3]$ (**1**).

1 ·(THF) _{3.5} (pentane) _{0.5}	
Empirical formula	Fe ₂ C _{120.5} H ₁₁₈ N ₄ O _{10.5}
Formula weight	1901.89
Temperature	110 K
Wavelength	0.71073 Å
Crystal system, space group	Triclinic, $P\bar{1}$
Unit cell dimensions	a = 15.624(3) Å α = 90.39(3)° b = 17.712(4) Å β = 98.51(3)° c = 18.838(4) Å γ = 106.33(3)°
Volume	4941.4(17) Å ³
Z, Calculated density	2, 1.278 g/mm ³
Theta range for data collection	2.07 – 26.37°
Limiting indices	-19 ≤ h ≤ 19, -21 ≤ k ≤ 22, -23 ≤ l ≤ 22
Reflections collection/ unique	75842/ 20123 [R _{int} = 0.1207]
Completeness to theta	99.5 %
Data/ restraints/ parameters	20213/ 1390/ 1268
Goodness of fit on F ²	1.017
Final R Indices	R ₁ = 0.0854, wR ₂ = 0.1860

* R₁ = $\Sigma ||F_o| - |F_c|| / \Sigma |F_o|$; wR₂ = $[\Sigma [w(F_o^2 - F_c^2)^2] / \Sigma [w(F_o^2)^2]]^{1/2}$; GOF = $[\Sigma [w(F_o^2 - F_c^2)^2] / (n-p)]^{1/2}$, where n is the number of reflections and p is the total number of parameters refined.

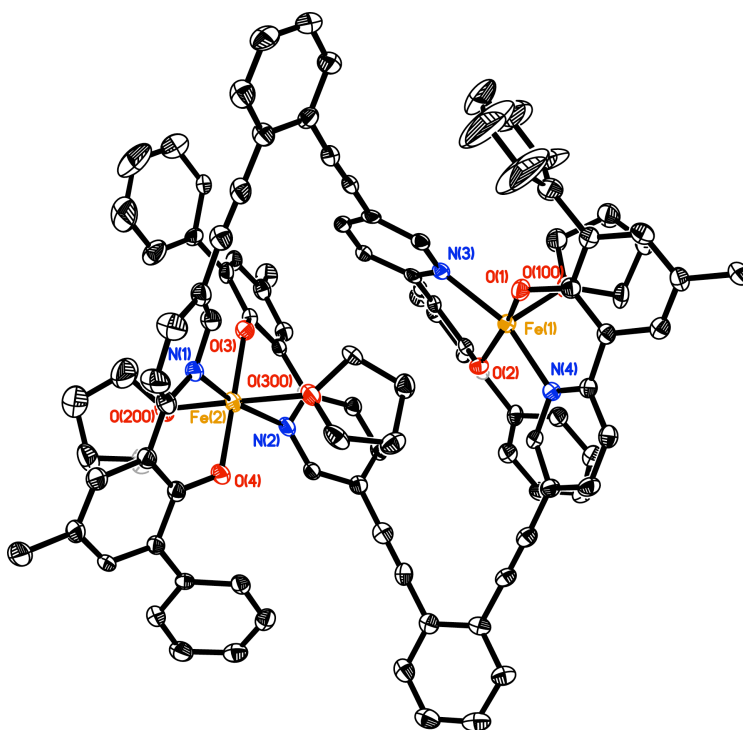


Figure 2.4. Ortep thermal ellipsoid (50%) diagram of the X-ray crystal structure of $[\text{Fe}_2(\text{L}^{\text{Me,Ph}})_2(\text{THF})_3]$ (**1**) with a partial numbering scheme. Hydrogen atoms and solvent molecules are omitted for clarity. The atoms are color coded according to the following: gray, carbon; red, oxygen; blue, nitrogen; orange, iron. Selected bond lengths (\AA) and angles (deg): Fe(1)–O(1), 1.945(3); Fe(1)–O(2), 1.936(3); Fe(1)–N(3), 2.183(4); Fe(1)–N(4), 2.193(4), Fe(1)–O(100), 2.123(3); Fe(2)–O(3), 1.967(3); Fe(2)–O(4), 1.977(3), Fe(2)–N(1), 2.180(4); Fe(2)–N(2), 2.191(4); Fe(2)–O(200), 2.203(4), Fe(2)–O(300), 2.321(3); O(1)–Fe(1)–N(4), 84.37(14); O(2)–Fe(1)–N(3), 85.98(14); O(3)–Fe(2)–N(2), 85.68(14), O(4)–Fe(2)–N(1), 85.25(14).

The absorption spectrum of **1** shows several intense features, at 235 ($\epsilon = 137,000 \text{ M}^{-1} \text{ cm}^{-1}$), 306 ($\epsilon = 94,100 \text{ M}^{-1} \text{ cm}^{-1}$), 332 (sh, $\epsilon = 63,300 \text{ M}^{-1} \text{ cm}^{-1}$) and 395 ($\epsilon = 5,130 \text{ M}^{-1} \text{ cm}^{-1}$) nm (Figure 2.5A). This spectrum matches those obtained from the $\text{Fe(II)}/\text{Na}_2\text{L}^{\text{R,R'}}$ titration studies (vide supra). Due to the limited examples of Fe(II)-phenolate compounds that have been reported in the literature, it is unclear whether any of the absorption bands correspond to a phenolate-to-Fe(II) charge transfer.

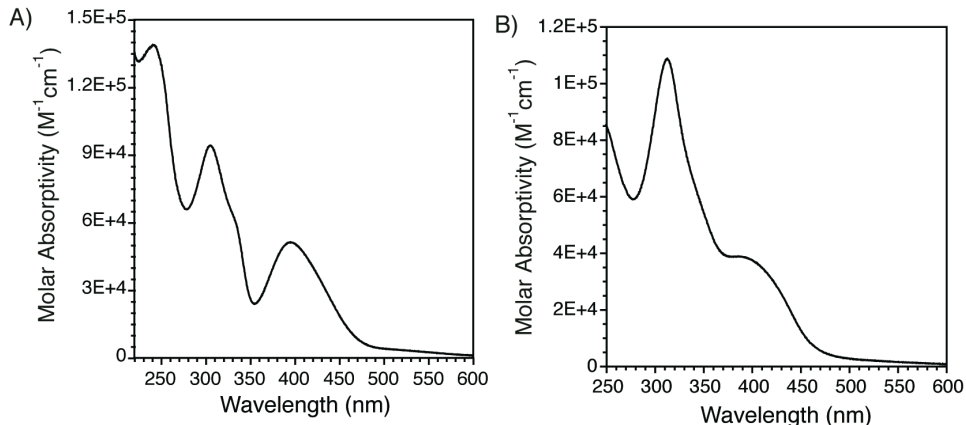


Figure 2.5. Electronic spectra of A) complex **1** and B) complex **2** in tetrahydrofuran at RT.

The ^1H NMR spectrum of **1** in $\text{THF-}d_8$ reveals the complex to be paramagnetic in solution (Figure 2.6A). The downfield signals at 44.45, 42.20, 38.08, and 36.30 ppm are most likely due to protons located either on the phenoxy or the pyridyl rings of $[\text{L}^{\text{Me,Ph}}]^{2-}$ because they are located closest to the paramagnetic iron centers. The peak at 34.14 ppm is attributed to the methyl protons of $[\text{L}^{\text{Me,Ph}}]^{2-}$ because it has the largest integrated area and is absent in the spectrum of $[\text{Fe}_2(\text{L}^{\text{H,Ph}})_2]$, which does not contain methyl groups (data not shown).

The zero-field ^{57}Fe Mössbauer spectrum of a polycrystalline sample of **1** was measured at 90 K (Figure 2.7A). The data were fit to a single quadrupole doublet, with $\delta = 1.13$ mm/s and $\Delta E_Q = 1.88$ mm/s. These parameters are typical for high-spin iron(II) centers in pseudo-octahedral environments.^{9,53} Although there are two distinct iron atoms in the solid-state structure of complex **1**, the similarities in their coordination environments make the sites indistinguishable in the absence of an applied magnetic field. This effect most likely accounts for the somewhat broadened linewidth of the quadrupole doublet ($\Gamma_{\text{R,L}} = 0.46$ mm/s).

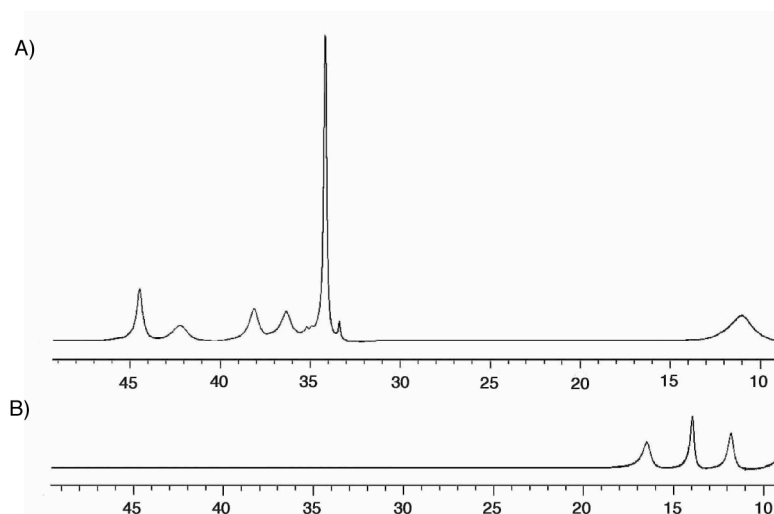


Figure 2.6. The 500 MHz ^1H NMR spectra of complex **1** (A) and **2** (B) recorded in $\text{THF-}d_8$. Only the paramagnetically shifted resonances (10–50 ppm) are shown.

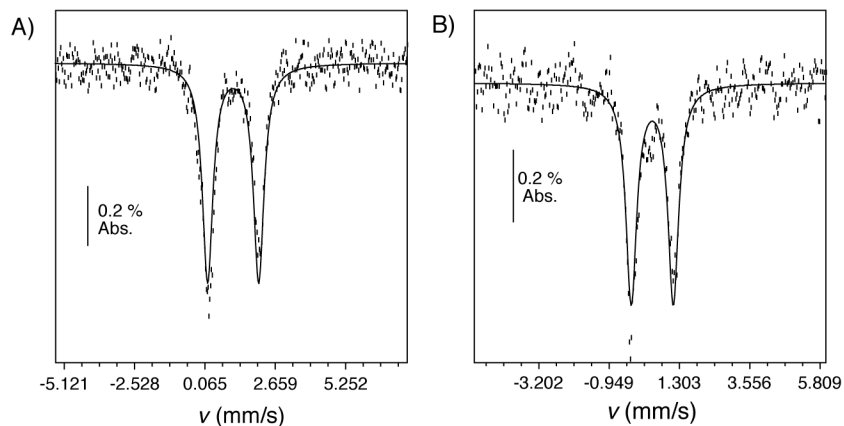


Figure 2.7. Zero-field ^{57}Fe Mössbauer spectra of polycrystalline **1** (A) and **2** (B) recorded at 90 K. Both spectra exhibit a single quadrupole doublet, with parameters $\delta = 1.13$ mm/s, $\Delta E_Q = 1.88$ mm/s, and $\Gamma_{R,L} = 0.46$ mm/s for **1** and $\delta = 0.43$ mm/s, $\Delta E_Q = 1.35$ mm/s, and $\Gamma_{R,L} = 0.42$ mm/s for **2**. Least-square fits (solid lines), assuming Lorentzian lineshapes, are overlaid on the experimental points (black hash marks).

The electrochemical properties of **1** were studied by cyclic voltammetry (CV). When the CV was performed in THF, two sequential quasi-reversible redox processes were observed, at $E_{1/2} = -31$ and -17 mV vs. ferrocene/ferrocenium (Fc/Fc^+) (Figure 2.8A). A differential pulse voltammetry (DPV) measurement of **1** in THF revealed two oxidation peaks with maximum height at -31 and -17 mV (Figure 2.8C). These events are attributed to oxidation of **1** from $\text{Fe(II)Fe(II)} \rightarrow \text{Fe(II)Fe(III)} \rightarrow \text{Fe(III)Fe(III)}$. When the CV of **1** was measured in DMF, rather than THF, the complex exhibited one quasi-reversible redox couple at $E_{1/2} = -64$ mV vs. Fc/Fc^+ (Figure 2.8B). The DPV of **1** in DMF also confirmed that only a single redox event occurs at -64 mV (Figure 2.8D). Presumably, this process corresponds to a two-electron oxidation of **1** from $\text{Fe(II)Fe(II)} \rightarrow \text{Fe(III)Fe(III)}$. Attempts to quantify the number of electrons involved in these electrochemical processes using ferrocene as a standard gave ambiguous results and were not examined further. Nevertheless, these data suggest that electronic delocalization between the two iron centers in complex **1** is solvent dependent. From the electrochemical data, a comproportionation constant (K_{com})⁵⁴ of **1** was calculated to be ~ 100 in THF and $\sim 10^5$ in DMF. According to the Robin-Day classification,⁵⁵ **1** behaves as a slightly charge-delocalized Class II species in THF, but becomes a completely charge-localized Class I complex in DMF. Because the UV-vis spectra of **1** in THF and DMF are identical, it is unlikely that the electrochemical differences are due to different speciation in solution. It is more likely that coordination of solvent molecules to the iron centers mediate the degree of electronic communication between the two iron atoms.

Because the CV of **1** shows quasi-reversible behavior, synthesis of the doubly oxidized $[\text{Fe}_2(\text{L}^{\text{Me,Ph}})_2(\text{THF})_x]^{2+}$ complex was attempted. Based on the $E_{1/2}$ values of **1** in THF (-31 and -17 mV vs. Fc/Fc^+), $[\text{FeCp}_2]\text{BF}_4$ (Cp = cyclopentadienyl) should serve as a suitable oxidant.

When aliquots of $[\text{FeCp}_2]\text{BF}_4$ in CH_2Cl_2 were added to a THF solution containing **1**, clean conversion to a new species occurred, as revealed by the UV-vis spectra (Figure 2.9). This process is accompanied by absorbance decreases at 242 and 395 nm as well as increases at 314 and 626 nm. Efforts to crystallize the iron product for X-ray crystallographic analysis were not successful.

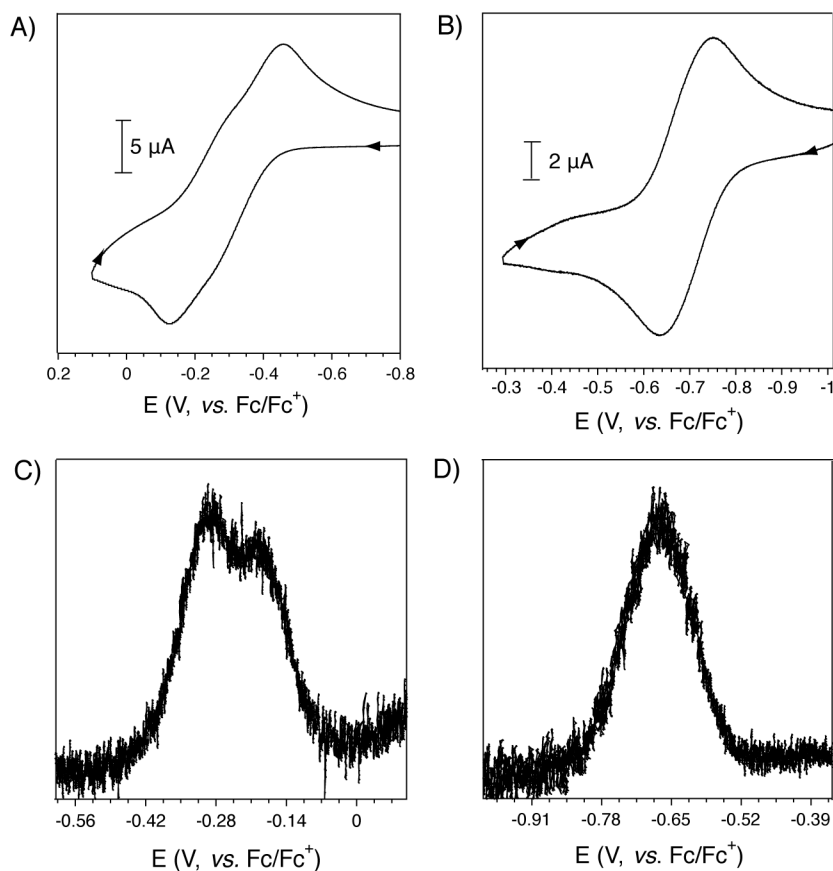


Figure 2.8. Cyclic voltammograms of a 0.2 mM solution of complex **1** containing 0.1 M tetra-*n*-butylammonium hexafluorophosphate in A) THF and B) DMF at a scan rate of 50 mV/s. Differential pulse voltammograms of **1** in C) THF and D) DMF are also shown. The measurements were carried out with a Pt electrode and referenced to the Fc/Fc⁺ redox couple.

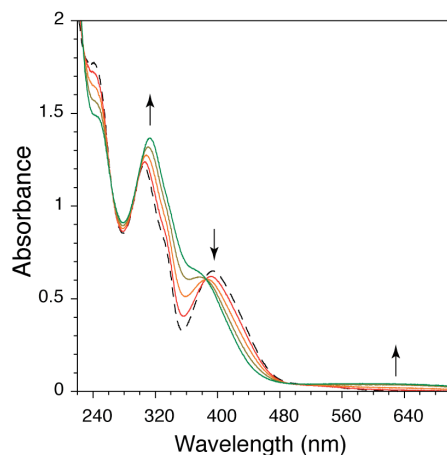


Figure 2.9. Absorption spectra from the addition of $[\text{FeCp}_2](\text{BF}_4)$ to a THF solution containing complex **1**. Black dotted line = **1**, solid lines = spectra after addition of up to 2.0 equiv of ferrocenium.

Reaction of Complex 1 with Dioxygen. The $> 7 \text{ \AA}$ separation between the iron(II) sites in complex **1** raises the question, how will it react with dioxygen? If the metal centers are rigidly confined to a fixed position, exposure of **1** to O_2 might lead to formation of two dioxygen adducts within the same molecule. Alternatively, if the $[\text{L}^{\text{Me,Ph}}]^{2-}$ framework was rotationally flexible, it is conceivable that O_2 might bridge the two iron centers. To determine the final oxygenation product, complex **1** was dissolved in a THF solution and stirred for 5 min in the presence of O_2 (Scheme 2.4B). The reaction product was dried *in vacuo* and crystallized from pentane and toluene to afford a red solid in good yield. Single crystals for X-ray diffraction studies were grown by slow diffusion of pentane into a solution of the compound in THF. Because the red crystals were very small (approx. $0.20 \times 0.08 \times 0.05 \text{ mm}^3$) a high-resolution X-ray crystal structure could not be obtained. However, the low-resolution data show that the compound contains a μ -oxodiiron(III) unit having the composition $[\text{Fe}_2(\mu\text{-O})(\text{L}^{\text{Me,Ph}})_2]$ (**2**, Figure 2.10). The presence of an oxo bridge was also confirmed by several spectroscopic methods (*vide*

infra). The structure showed that rotation of the $[L^{\text{Me,Ph}}]^{2-}$ ethynyl arms led to contraction of the iron-iron distance. Complex **2** was also prepared from a pre-assembled μ -oxodiiron(III) source. Upon deprotonation of $\text{H}_2\text{L}^{\text{Me,Ph}}$ with NaHMDS in THF and addition of $(\text{NEt}_4)_2[\text{Fe}_2\text{OCl}_6]^{29}$ a dark red solution formed (Scheme 2.4B). Evaporation of the solvent and extraction of the residue into toluene gave the desired product in moderate yield.

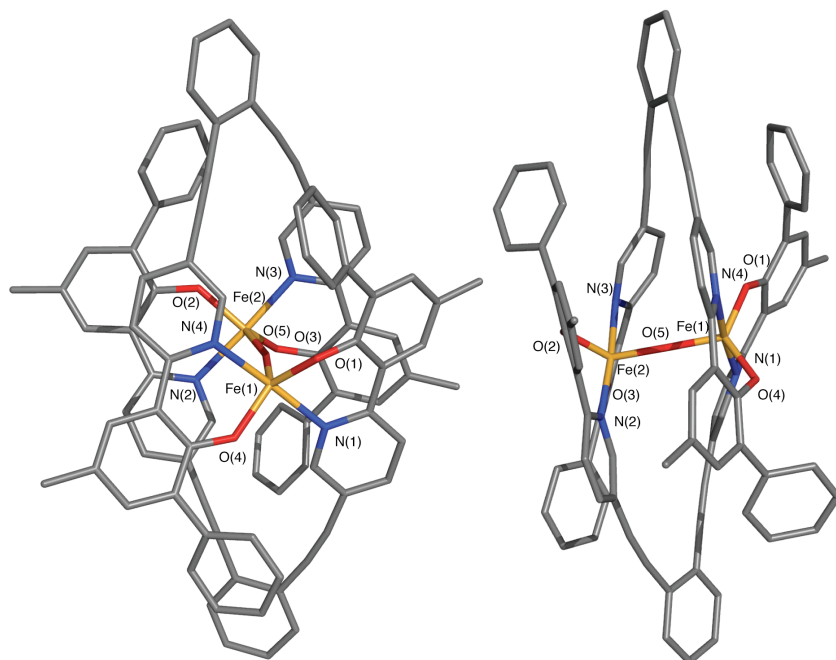


Figure 2.10. A stick figure representation of the low-resolution X-ray crystal structure of $[\text{Fe}_2(\mu\text{-O})(\text{L}^{\text{Me,Ph}})_2]$ (**2**) in two different views. Due to the poor quality of the X-ray data, only the atoms connectivity of the structure could be obtained. The atoms are color coded according to the following: gray, carbon; red, oxygen; blue, nitrogen; orange, iron.

The presence of a μ -oxodiiron(III) center in **2** was further confirmed by both vibrational and ^{57}Fe Mössbauer spectroscopy. When **2** was prepared by reaction of **1** with $^{18}\text{O}_2$, instead of $^{16}\text{O}_2$, its infrared spectrum revealed a single peak shifted from 833 cm^{-1} to 798 cm^{-1} . A survey of known μ -oxodiiron(III) complexes revealed that the asymmetric Fe–O–Fe stretch occurs

between $\sim 700\text{-}850\text{ cm}^{-1}$ and shifts to lower energy by $\sim 30\text{-}45\text{ cm}^{-1}$ when $^{18}\text{O}_2$ is substituted for $^{16}\text{O}_2$.^{56,57} Because **2** exhibits an isotopically shifted peak within this range, the data strongly support the assignment of a μ -oxodiiron(III) core. To probe further the oxidation state and coordination environment of **2**, its ^{57}Fe Mössbauer spectrum was recorded. A Lorentzian least-squares fit of the Mössbauer data gave a single quadrupole doublet with $\delta = 0.43\text{ mm/s}$ and $\Delta E_Q = 1.35\text{ mm/s}$ (Figure 2.7B). These parameters are characteristic of high-spin iron centers coordinated by mixed O,N donors. In addition to overall charge considerations, the IR and Mössbauer data suggest that **2** should be formulated as a $[\text{Fe}_2(\mu\text{-O})(\text{L}^{\text{Me,Ph}})_2]$ complex.

The electronic absorption spectrum of complex **2** was recorded in THF. An intense band at 312 nm ($\epsilon = 108,000\text{ M}^{-1}\text{ cm}^{-1}$) and a shoulder at $\sim 390\text{ nm}$ ($\epsilon = 37,500\text{ M}^{-1}\text{ cm}^{-1}$) dominate the spectrum (Figure 2.5B). Because the band at $\sim 310\text{ nm}$ also occurs in the spectrum of $\text{Na}_2\text{L}^{\text{Me,Ph}}$, it is assigned to a $p(\pi) \rightarrow p(\pi^*)$ ligand transition. Since the spectrum of **2** shows an increased absorption between $350\text{-}390\text{ nm}$, compared to that of **1**, it is possible that this overlapping feature represents one of the phenolate-to-Fe(III) charge-transfer bands.^{50,58}

A bathochromic shift of the phenolate-to-iron LMCT band is reflected in smaller NMR contact shifts of the phenolate protons due to less mixing between the metal d and ligand orbitals.⁵⁸ The ^1H NMR spectrum of **2** (Figure 2.6B) contains only three signals outside the diamagnetic region, at 16.42 , 13.90 , and 11.75 ppm . Compared to the ^1H NMR spectrum of **1**, these peaks are less paramagnetically shifted. This result indicates that there is less unpaired spin density on the $[\text{L}^{\text{Me,Ph}}]^{2-}$ ligand in complex **2** than in **1**. Consequently, the phenolate-to-iron charge transfer bands should occur at a higher energy for **2** than for **1**.

The electrochemical behavior of **2** was investigated by cyclic voltammetry (Figure 2.11). When recorded in THF, an irreversible reduction wave was observed at -780 mV (vs. Fc/Fc⁺) and an irreversible oxidation wave appeared at +720 mV (vs. Fc/Fc⁺). The absence of any reversible electrochemical processes was unexpected because phenolate complexes are typically redox active due to involvement of phenolate radicals.^{59,60} A related μ -oxodiiron(III) complex containing salen ligands exhibits two reversible redox waves due to generation of ligand-centered monoradical and diradical species.⁶¹ Perhaps due to the unique π -conjugation of the [L^{Me,Ph}]²⁻ ligand, the resulting iron complex does not exhibit any ligand-centered redox behavior, at least within the electrochemical window investigated.

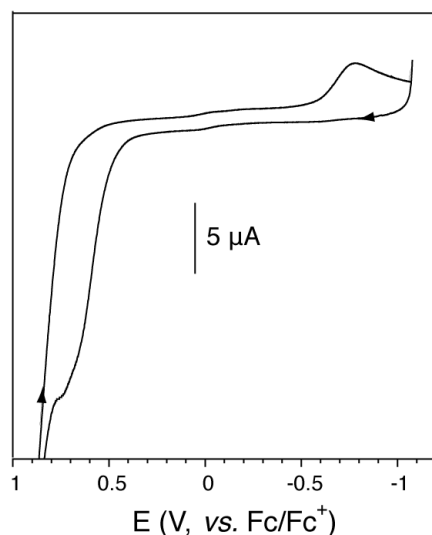


Figure 2.11. Cyclic voltammogram of a 0.2 mM solution of complex **2** containing 0.1 M tetra-*n*-butylammonium hexafluorophosphate in THF at a scan rate of 50 mV/s. The measurement was carried out with a Pt working electrode and referenced to the Fc/Fc⁺ redox couple.

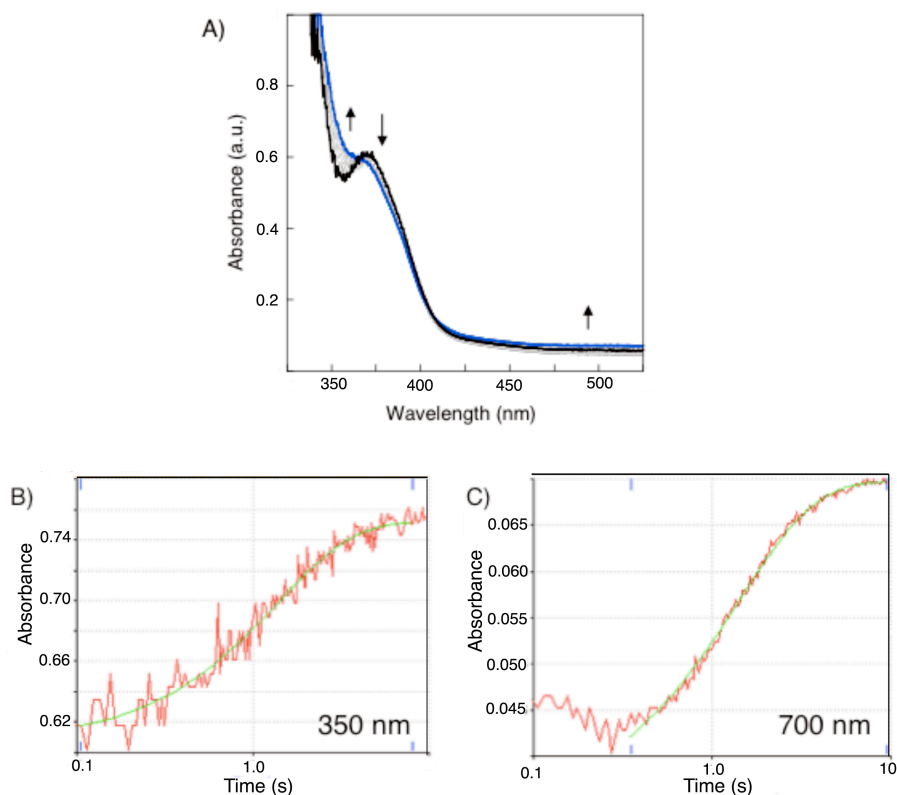


Figure 2.12. Single-mixing stopped-flow spectral data from the reaction of **1** with O₂ in THF. The absorbance spectra from 300-600 nm (A, top) show rapid conversion of **1** to **2**, with no observable intermediate species. The kinetic traces at 350 nm (B) and 700 nm (C) were fit to single exponential functions, giving pseudo-first order rate constants of $\sim 0.7 \text{ s}^{-1}$.

The rapid conversion of **1** to **2** in the presence of O₂ was studied by stopped-flow UV-vis spectrophotometry (Scheme 2.4). A single mixing experiment was carried out at $-50 \text{ }^\circ\text{C}$, in which a $26 \text{ } \mu\text{M}$ solution of **1** in THF was combined with a solution saturated with O₂ ($\sim 10 \text{ mM}$). Spectral scanning between 300-750 nm revealed that the oxygenation reaction was complete in less than 10 s (Figure 2.12A). The reaction kinetics fit well to a single exponential function (Figure 2.12B and 2.12C), giving a pseudo-first order rate constant of $\sim 0.7 \text{ s}^{-1}$. Even on the stopped-flow timescale, no intermediates were observed for conversion of **1** to **2**. Our inability to detect and characterize any transient species prevents us from speculating about the mechanism

by which **1** converts to **2**. Recent work with the ToMO enzyme system has identified an optically-silent diiron(III) oxygenated intermediate that is catalytically competent to hydroxylate arenes.⁶² When the oxygenation of **1** was performed in the presence of triphenylphosphine, gas chromatographic mass spectral analysis of the reaction product indicated that triphenylphosphine oxide was formed. The nature of the active oxidizing species and the range of substrates that could be oxidized have not yet been evaluated. It is important to note that during the course of these studies no $[\text{L}^{\text{Me,Ph}}]^{2-}$ ligand decomposition was observed.

2.4. Conclusion

In our continuing search for novel frameworks to model the active sites of O₂-activating diiron proteins, we prepared a new family of dinucleating ligands and provided a streamlined method for easy derivatization. By taking advantage of the chromophoric properties of $[\text{L}^{\text{R,R'}}]^{2-}$ and $[\text{BIPS}^{\text{Me,Ph}}]^{2-}$, the coordination chemistry of these ligands with Fe(II) was examined by UV-vis spectrophotometry. Incorporation of sterically demanding groups in the ligand scaffold prevented undesired polymer formation. A diiron(II) $[\text{Fe}_2(\text{L}^{\text{Me,Ph}})_2(\text{THF})_3]$ (**1**) complex was synthesized having a large separation (7.2 Å) between the two metal centers. Rotation about the ethynyl arms led to a substantial contraction of the diiron distance, the structural flexibility being manifest in the oxygenation product (**2**) obtained from reaction of **1** with O₂. [¹⁸O]-Isotopic infrared labeling studies and ⁵⁷Fe Mössbauer spectroscopy measurements clearly reveal that solutions of **2** retain the μ -oxodiiron(III) core found in the solid state by X-ray crystallography. Formation of $[\text{Fe}_2(\mu\text{-O})(\text{L}^{\text{Me,Ph}})_2]$ most likely involves binding of O₂ and concerted reorientation of the $[\text{L}^{\text{Me,Ph}}]^{2-}$ ligands. Preliminary studies indicate that triphenylphosphine is converted to triphenylphosphine oxide in the presence of **1** and dioxygen, but a comprehensive study of this

chemistry was not undertaken. The $[L^{\text{Me,Ph}}]^{2-}$ ligand is chemically stable under these conditions and does not participate in ligand-centered redox reactions, despite the presence of the phenolate group. Although the desired diiron complex containing a single dinucleating $[L^{\text{Me,Ph}}]^{2-}$ ligand was not achieved, the structure provides guidance for future modification of the $[L^{\text{R,R'}}]^{2-}$ framework to preclude formation of $[\text{Fe}_2(\text{syn } N\text{-donor})_2]$ units.

2.5. References

- (1) Merkx, M.; Kopp, D. A.; Sazinsky, M. H.; Blazyk, J. L.; Müller, J.; Lippard, S. J. *Angew. Chem., Int. Ed. Engl.* **2001**, *40*, 2782-2807.
- (2) Leahy, J. G.; Batchelor, P. J.; Morcomb, S. M. *FEMS Microbiol. Rev.* **2003**, *27*, 449-479.
- (3) Sazinsky, M. H.; Lippard, S. J. *Acc. Chem. Res.* **2006**, *39*, 558-566.
- (4) Cafaro, V.; Izzo, V.; Scognamiglio, R.; Notomista, E.; Capasso, P.; Casbarra, A.; Pucci, P.; Di Donato, A. *Appl. Environ. Microbiol.* **2004**, *70*, 2211-2219.
- (5) Cafaro, V.; Scognamiglio, R.; Viggiani, A.; Izzo, V.; Passaro, I.; Notomista, E.; Dal Piaz, F.; Amoresano, A.; Casbarra, A.; Pucci, P.; Di Donato, A. *Eur. J. Biochem.* **2002**, *269*, 5689-5699.
- (6) Que, L., Jr. *J. Chem. Soc., Dalton Trans.* **1997**, 3933-3940.
- (7) Fontecave, M.; Ménage, S.; Duboc-Toia, C. *Coord. Chem. Rev.* **1998**, *178-180*, 1555-1572.
- (8) Costas, M.; Chen, K.; Que, L., Jr. *Coord. Chem. Rev.* **2000**, *200-202*, 517-544.
- (9) Tshuva, E. Y.; Lippard, S. J. *Chem. Rev.* **2004**, *104*, 987-1012.
- (10) Que, L., Jr.; Tolman, W. B. *Nature* **2008**, *455*, 333-340.
- (11) Siewert, I.; Limberg, C. *Chem.–Eur. J.* **2009**, *15*, 10316-10328.

- (12) Friedle, S.; Reisner, E.; Lippard, S. J. *Chem. Soc. Rev.* **2010**, *39*, 2768-2779.
- (13) Rosenzweig, A. C.; Frederick, C. A.; Lippard, S. J.; Nordlund, P. *Nature* **1993**, *366*, 537-543.
- (14) Rosenzweig, A. C.; Lippard, S. J. *Acc. Chem. Res.* **1994**, *27*, 229-236.
- (15) Sazinsky, M. H.; Dunten, P. W.; McCormick, M. S.; DiDonato, A.; Lippard, S. J. *Biochemistry* **2006**, *45*, 15392-15404.
- (16) Kuzelka, J.; Farrell, J. R.; Lippard, S. J. *Inorg. Chem.* **2003**, *42*, 8652-8662.
- (17) Kodanko, J. J.; Morys, A. J.; Lippard, S. J. *Org. Lett.* **2005**, *7*, 4585-8.
- (18) Kodanko, J. J.; Xu, D.; Song, D.; Lippard, S. J. *J. Am. Chem. Soc.* **2005**, *127*, 16004-5.
- (19) Vetting, M. W.; D'Argenio, D. A.; Ornston, L. N.; Ohlendorf, D. H. *Biochemistry* **2000**, *39*, 7943-7955.
- (20) Brown, C. K.; Vetting, M. W.; Earhart, C. A.; Ohlendorf, D. H. *Annu. Rev. Microbiol.* **2004**, *58*, 555-585.
- (21) Guddat, L. W.; McAlpine, A. S.; Hume, D.; Hamilton, S.; de Jersey, J.; Martin, J. L. *Structure* **1999**, *7*, 757-767.
- (22) Klose, A.; Solari, E.; Floriani, C.; Chiesi-Villa, A.; Rizzoli, C.; Re, N. *J. Am. Chem. Soc.* **1994**, *116*, 9123-9135.
- (23) Sheldrick, G. M. *Acta Crystallogr., Sect. A* **2008**, *A64*, 112-122.
- (24) Sheldrick, G. M., *SADABS: Area-Detector Absorption Correction*; University of Göttingen: Göttingen, Germany, 2001.
- (25) Sheldrick, G. M., *SHELXTL97: Program for Refinement of Crystal Structures*; University of Göttingen: Göttingen, Germany, 1997.
- (26) Battino, R., Ed.; *Oxygen and Ozone*; Pergamon Press: Oxford, U.K., 1981; Vol. 7.

- (27) Edson, J. B.; Wang, Z.; Kramer, E. J.; Coates, G. W. *J. Am. Chem. Soc.* **2008**, *130*, 4968-4977.
- (28) Cram, D. J.; Dicker, I. B.; Lauer, M.; Knobler, C. B.; Trueblood, K. N. *J. Am. Chem. Soc.* **1984**, *106*, 7150-7167.
- (29) Dunbar, K. R.; Longridge, J. J.; Rawson, J. M.; Sun, J.-S.; Hagen, K. S.; Do, B. *Inorg. Synth.* **2002**, *33*, 103-107.
- (30) Cotton, S. A. *Coord. Chem. Rev.* **1972**, *8*, 185-223.
- (31) Lippard, S. J. *Angew. Chem., Int. Ed. Engl.* **1988**, *27*, 344-361.
- (32) Armstrong, W. H.; Roth, M. E.; Lippard, S. J. *J. Am. Chem. Soc.* **1987**, *109*, 6318-6326.
- (33) Shweky, I.; Pence, L. E.; Papaefthymiou, G. C.; Sessoli, R.; Yun, J. W.; Bino, A.; Lippard, S. J. *J. Am. Chem. Soc.* **1997**, *119*, 1037-1042.
- (34) Mandal, S. K., Jr.; Young, V. G.; Que, L., Jr. *Inorg. Chem.* **2000**, *39*, 1831-1833.
- (35) Hagen, K. S.; Naik, S. G.; Huynh, B. H.; Masello, A.; Christou, G. *J. Am. Chem. Soc.* **2009**, *131*, 7516-7517.
- (36) Hagadorn, J. R.; Que, L., Jr.; Tolman, W. B. *J. Am. Chem. Soc.* **1998**, *120*, 13531-13532.
- (37) Lee, D.; Lippard, S. J. *Inorg. Chim. Acta* **2002**, *341*, 1-11.
- (38) Wallar, B. J.; Lipscomb, J. D. *Chem. Rev.* **1996**, *96*, 2625-2658.
- (39) Shu, L.; Nesheim, J. C.; Kauffmann, K.; Münck, E.; Lipscomb, J. D.; Que, L., Jr. *Science* **1997**, *275*, 515-518.
- (40) Guidote, A. M., Jr.; Ando, K.-i.; Terada, K.; Kurusu, Y.; Nagao, H.; Masuyama, Y. *Inorg. Chim. Acta* **2001**, *324*, 203-211.
- (41) Boydston, A. J.; Haley, M. M.; Williams, R. V.; Armantrout, J. R. *J. Org. Chem.* **2002**, *67*, 8812-8819.

- (42) Wang, B.; Wasielewski, M. R. *J. Am. Chem. Soc.* **1997**, *119*, 12-21.
- (43) Kim, I.-B.; Dunkhorst, A.; Gilbert, J.; Bunz, U. H. F. *Macromolecules* **2005**, *38*, 4560-4562.
- (44) Fan, L.-J.; Jones, W. E., Jr. *J. Am. Chem. Soc.* **2006**, *128*, 6784-6785.
- (45) Murch, B. P.; Boyle, P. D.; Que, L., Jr. *J. Am. Chem. Soc.* **1985**, *107*, 6728-6729.
- (46) Glaser, T.; Lügger, T.; Hoffmann, R.-D. *Eur. J. Inorg. Chem.* **2004**, 2356-2362.
- (47) Boudalis, A. K.; Aston, R. E.; Smith, S. J.; Mirams, R. E.; Riley, M. J.; Schenk, G.; Blackman, A. G.; Hanton, L. R.; Gahan, L. R. *J. Chem. Soc., Dalton Trans.* **2007**, 5132-5139.
- (48) Wallasch, M.; Wolmershäuser, G.; Sitzmann, H. *Angew. Chem., Int. Ed. Engl.* **2005**, *44*, 2597-2599.
- (49) Bao, X.; Wang, F.-W.; Wei, Y.-J. *Acta Crystallogr., Sect. E* **2006**, *E62*, m1298-m1300.
- (50) Koch, S. A.; Millar, M. *J. Am. Chem. Soc.* **1982**, *104*, 5255-5257.
- (51) Snyder, B. S.; Patterson, G. S.; Abrahamson, A. J.; Holm, R. H. *J. Am. Chem. Soc.* **1989**, *111*, 5214-5223.
- (52) Stassinopoulos, A.; Schulte, G.; Papaefthymiou, G. C.; Caradonna, J. P. *J. Am. Chem. Soc.* **1991**, *113*, 8686-8697.
- (53) Yoon, S.; Lippard, S. J. *J. Am. Chem. Soc.* **2005**, *127*, 8386-8397.
- (54) Zanello, P.; *Inorganic Electrochemistry*; The Royal Society of Chemistry: Cambridge, 2003.
- (55) Robin, M. B.; Day, P. *Adv. Inorg. Chem. Radiochem.* **1967**, *10*, 247-422.
- (56) Sanders-Loehr, J.; Wheeler, W. D.; Shiemke, A. K.; Averill, B. A.; Loehr, T. M. *J. Am. Chem. Soc.* **1989**, *111*, 8084-8093.

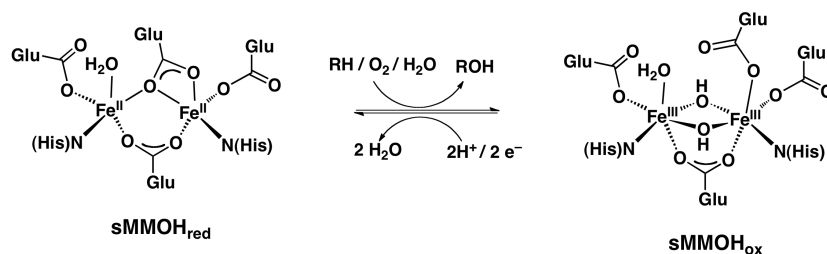
- (57) Kurtz, D. M., Jr. *Chem. Rev.* **1990**, *90*, 585-606.
- (58) Pyrz, J. W.; Roe, A. L.; Stern, L. J.; Que, L., Jr. *J. Am. Chem. Soc.* **1985**, *107*, 614-620.
- (59) Adam, B.; Bill, E.; Bothe, E.; Goerdts, B.; Haselhorst, G.; Hildenbrand, K.; Sokolowski, A.; Steenken, S.; Weyhermüller, T.; Wieghardt, K. *Chem.-Eur. J.* **1997**, *3*, 308-319.
- (60) Roy, N.; Sproules, S.; Weyhermüller, T.; Wieghardt, K. *Inorg. Chem.* **2009**, *48*, 3783-3791.
- (61) Strautmann, J. B. H.; Freiherr von Richthofen, C.-G.; George, S. D.; Bothe, E.; Bill, E.; Glaser, T. *Chem. Commun.* **2009**, 2637-2639.
- (62) Murray, L. J.; Naik, S. G.; Ortillo, D. O.; García-Serres, R.; Lee, J. K.; Huynh, B. H.; Lippard, S. J. *J. Am. Chem. Soc.* **2007**, *129*, 14500-14510.

Chapter 3

Redox Behavior and Dioxygen Reactivity of a Macrocyclic
Carboxylate-Bridged Diiron(II) Mimic of
Bacterial Monooxygenase Active Sites

3.1. Introduction

Investigations using synthetic mimics have contributed to our understanding of dioxygen activation at carboxylate-bridged diiron units.¹⁻⁵ Several notable achievements in diiron modeling include the X-ray structural characterization of (μ -1,2-peroxo)diiron(III) species,⁶⁻⁸ generation of high-valent diiron(IV) intermediates,^{9,10} and identification of possible protonation sites in oxygenated diiron complexes.¹¹ Some synthetic diiron compounds are capable of oxidizing aromatics, alkenes, and saturated hydrocarbons when exposed to dioxygen, hydrogen peroxide, alkyl peroxides, or *O*-atom transfer reagents.^{2,4,12-14} Generally, however, these reactions are unremarkable because the organic substrates have weak C–H bonds or the transformation is not performed using molecular oxygen. One significant difference between the diiron proteins and the model compounds is that most oxygenated synthetic complexes are low-spin due to their nitrogen-rich coordination environment. In contrast, biological diiron centers are high-spin and are carboxylate-rich. Density functional theoretical (DFT) calculations suggest that high-spin oxygenated diiron species are necessary to react with more chemically inert molecules.^{9,15-17}



Scheme 3.1. The diiron(II) complex of soluble methane monooxygenase hydroxylase (sMMOH_{red}) reacts with dioxygen and saturated hydrocarbons (RH) to give alcohols (ROH) and the resting diiron(III) state of the protein (sMMOH_{ox}). sMMOH_{ox} can be reduced back to sMMOH_{red} by acquiring two electrons from a reductase protein (sMMOR). The active site structures of sMMOH_{red} and sMMOH_{ox} are depicted.

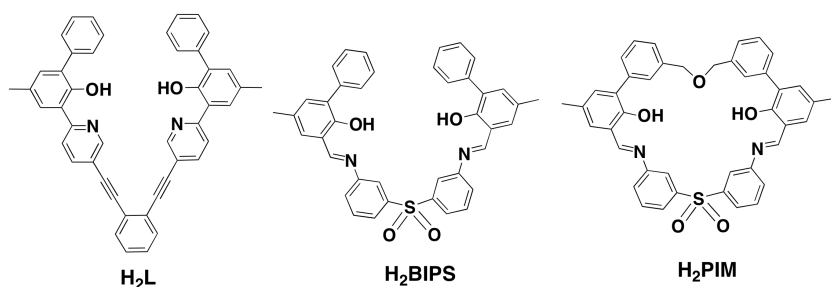


Chart 3.1. Syn *N*-donor ligands containing mixed *N,O* metal binding units. Compounds H₂L and H₂BIPS spontaneously assemble into bis(ligand) diiron complexes in the presence of base and iron(II) salts. The macrocyclic variant H₂PIM was designed to have a flexible ether linkage to prevent ligand interdigitation upon metal complexation.

As discussed in the preceding chapters, no synthetic models accurately reproduce the carboxylate-bridged diiron active site structure of the BMMs.⁵ As shown in Scheme 3.1, the reduced form of soluble methane monooxygenase hydroxylase (sMMOH_{red}) contains a diiron unit coordinated by four carboxylate residues, two bridging and two terminal, as well as two histidine groups syn with respect to the Fe–Fe vector.¹⁸⁻²⁰ Although a few model compounds have the same carboxylate and *N*-heterocyclic donors stoichiometry as the diiron core of sMMOH_{red}, the nitrogen groups are not adjacent to each other.²¹⁻²³ A recent approach in our laboratory to achieve syn *N*-stereochemistry has been to synthesize compounds that covalently link two *N*-donors into a single ligand platform. In this manner, complexation of the *N*-donors and external carboxylates to two iron atoms could afford dinuclear complexes with the same ligand arrangement as sMMOH_{red} and similar protein active sites. Our early attempts using this strategy were encouraging,^{24,25} but the diiron(II) compounds were too kinetically labile to maintain their dinuclear structure after reaction with O₂. To circumvent this problem, we designed ligands containing either phenoxyipyridyl (H₂L) or phenoxyimine (H₂BIPS) chelating groups that are anionic when deprotonated and form stable six-membered chelate rings when

bound to iron (Chart 3.1).²⁶ Unfortunately, as discussed in Chapter 2, these constructs spontaneously assembled into bis(syn *N*-donor)diiron complexes when treated with iron(II) salts.

In the present study, we prepared and investigated the iron chemistry of a new phenoxyimine ligand (H₂PIM), which structurally resembles our previous ligand designs but is more preorganized due to its macrocyclic nature (Chart 3.1). We used H₂PIM and sterically-hindered carboxylates to synthesize the first accurate structural models of the diiron(II) active sites of bacterial multi-component monooxygenases. We also report some novel chemistry of these synthetic units, including their reactions with dioxygen and other chemical oxidants.

3.2. Experimental

Materials and Methods. Reagents obtained from Strem, Aldrich Chemical Co., and Alfa Aesar were used as received. The compounds 2,6-bis(*p*-tolyl)benzoic acid²⁷ (Ar^{Tol}CO₂H, also referred to as terphenylcarboxylic acid for simplicity) and [Fe₂(Mes)₄]²⁸ (Mes = 2,4,6-trimethylphenyl) were prepared as reported. All ⁵⁷Fe-enriched compounds were prepared exactly as described for the unenriched analogues, except that [⁵⁷Fe₂(Mes)₄] was used as the starting material. All air-sensitive manipulations were performed using standard Schlenk techniques or under a nitrogen atmosphere inside an MBraun drybox. Solvents were saturated with argon and purified by passage through two columns of activated alumina. Dioxygen gas used in these experiments was obtained from a high-purity gas cylinder (Airgas) and passed through a 10-inch column of activated alumina before use.

General Physical Methods. NMR spectra were recorded on 500 MHz Varian Mercury spectrometers and chemical shifts for ¹H and ¹³C spectra were referenced to residual solvent. ¹H NMR spectral data of paramagnetic compounds were obtained by widening the sweep window

(+100 to -30 ppm) and collecting for longer acquisition times (~1024 scans). IR spectra were recorded on a ThermoNicolet Avatar 360 spectrophotometer with the OMNIC software. Absorption spectra were recorded on a Cary 50 spectrophotometer using 6Q Spectrosil quartz cuvettes (Starna) with 1 cm path lengths. X-band EPR spectra were recorded at 5 K on a Bruker EMX spectrometer. Electrochemical measurements were performed with a VersaSTAT3 Princeton Applied Research potentiostat running the V3-Studio electrochemical analysis software. A three-electrode setup was employed comprising a platinum working electrode, a platinum wire auxiliary electrode, and a 0.1 M Ag/AgNO₃ solution in acetonitrile as the reference electrode. Tetra-*n*-butylammonium hexafluorophosphate (0.1 M) was used as the supporting electrolyte. Electrochemical potentials are referenced externally to the ferrocene/ferrocenium couple at 0.00 V.

X-ray Data Collection and Refinement. Single crystals were mounted in Paratone oil using 30 μm aperture MiTeGen MicroMounts (Ithaca, NY) and frozen under a 100 K KRYO-FLEX nitrogen cold stream. Data were collected on a Bruker SMART APEX CCD X-ray diffractometer with Mo K α radiation ($\lambda = 0.71073 \text{ \AA}$) controlled by the APEX 2 (v. 2010.1-2) software package. Data reduction was performed using SAINT and empirical absorption corrections were applied using SADABS.²⁹ The structures were solved by Patterson methods with refinement by full-matrix least squares based on F^2 using the SHELXTL-97 software package³⁰ and checked for higher symmetry by the PLATON software.³¹ All non-hydrogen atoms were located and refined anisotropically. Hydrogen atoms were fixed to idealized positions unless otherwise noted and given thermal parameters equal to either 1.5 (methyl hydrogen atoms) or 1.2 (non-methyl hydrogen atoms) times the thermal parameters of the atoms to which they are attached.

X-ray diffraction quality crystals were selected out of the crystallization vials and immediately immersed in degassed Partone oil to prevent solvent loss and reaction with air. Complex **1** contains both benzene and pentane molecules in the asymmetric unit. Three of the benzene molecules were refined with full occupancy, whereas one of the benzene rings was substitutionally disordered with pentane. The benzene-to-pentane ratio refined to 55:45. The structure of **2** shows significant thermal motion within the tolyl groups of the terphenylcarboxylate ligands in the solid state, as indicated by the larger anisotropic displacement parameters of their carbon atoms compared to those of the rest of the molecule. Several solvent molecules were located in the crystal structure of **2**. In each asymmetric unit there are 1.39 pentane and 0.45 dichloromethane molecules. A pentane that is located on an inversion center shares partial occupancy with a pentane that does not lie on a special position. Another pentane molecule shares partial occupancy with dichloromethane, with a pentane/dichloromethane ratio of 39:45. The silver atom in **3** occupies two positions and is coordinated to O(6) of a bridging hydroxide, O(5) of the PIM²⁻ ligand, and an arene ring of the terphenylcarboxylate ligand. Because the H atoms of the bridging hydroxo groups in **3** could not be located from the difference electron density map, the hydrogen atoms attached to O(6) and O(7) were not included in the structure refinement. Four dichloromethane molecules per diiron complex occur in the structure of **3**, three of which are ordered and one is disordered. Complex **4** was unambiguously assigned as a (μ -hydroxo)diiron species because electron density corresponding to the hydrogen atom of O(6) was located from the difference electron density map. The asymmetric unit of **4** also contains two ordered and one disordered benzene molecules. The center of the tetranuclear complex **5** lies on an inversion center; thus, there is only half of the molecule in the asymmetric unit. In addition, there are four benzene molecules per asymmetric

cell. The structure of **6/7** clearly shows two different diiron cores, one containing a single bridging oxygen atom and another containing two bridging oxygen atoms. The occupancy of the one vs. two oxygen bridges was refined to be 76% to 24%, respectively. Each **6/7** unit also contains two ordered and one disordered acetonitrile solvent molecules. Complete X-ray refinement data for complexes **1-3** and **4-7** are shown in Tables 3.1 and 3.4, respectively.

⁵⁷Fe Mössbauer Spectroscopy. Mössbauer spectra were recorded on an MSI spectrometer (WEB Research Company) with a ⁵⁷Co source in a Rh matrix maintained at room temperature. Solid samples were prepared by suspension of the complex (~5-40 mg, depending on whether the complex is enriched in ⁵⁷Fe) in Apiezon M grease and placed in a nylon sample holder. Solution samples were prepared by freezing 400 µL of the complex (~20 mM) in a nylon sample cup and sealing with a screw cap. Samples containing natural abundance iron were measured over the course of ~5 d, whereas samples that are enriched in ⁵⁷Fe were collected over ~12 h. Data were acquired at 80 K, and isomer shift (δ) values are reported with respect to metallic iron that was used for velocity calibration at room temperature. Spectra were fit to Lorentzian lines using the WMOSS plot and fit program.

Synthesis

3,3'-(Oxybis(methylene))bis(bromobenzene) (A). 3-Bromobenzylalcohol (3.72 g, 20 mmol) was dissolved in 50 mL of dry THF and cooled to 0 °C with an ice bath. Solid sodium hydride (0.96 g, 24 mmol, 60% dispersion in mineral oil) was added portionwise to the reaction flask and the mixture was stirred for 1 h. Liquid 3-bromobenzylbromide (5.0 g, 20 mmol) was then added and the solution was stirred at reflux for 12 h. Water was then slowly introduced to quench the reaction and the organic phase was extracted into diethyl ether, dried over Na₂SO₄, filtered, and evaporated to yield a light yellow oil (7.12 g, 99%). This material was determined to be > 98%

pure by NMR spectroscopy and gas chromatography. ^1H NMR (CDCl_3 , 500 MHz): δ 7.56 (s, 2H), 7.46 (d, $J = 9.0$ Hz, 2H), 7.31 (d, $J = 7.5$ Hz, 2H), 7.25 (t, $J = 8.0$ Hz, 2H), 4.53 (s, 4H) ppm. ^{13}C NMR (CDCl_3 , 125 MHz): δ 140.38, 130.82, 130.62, 130.16, 126.18, 122.64, 71.82 ppm. GC-MS = 356 $[\text{M}]^+$ (Calcd = 355.9 $[\text{M}]^+$).

2,2'-((Oxybis(methylene))bis(5-methyl-(1,1'-biphenyl)-3',2-diyl))bis(oxy)bis(tetrahydro-2H-pyran) (B). 2-(2-Bromo-4-methylphenoxy)-tetrahydro-2H-pyran³² (16.5 g, 61.1 mmol) was dissolved in 250 mL of dry THF and cooled to -78 °C. The solution was treated with *n*-butyllithium (38 mL, 1.6 M in hexanes) and stirred for 2 h, giving a white slurry. A 50 mL solution of zinc chloride (6.66 g, 61.1 mmol) in THF was transferred by cannula to the reaction flask. After 1 h, the solution became nearly homogeneous. The reaction flask was charged with compound **A** (10.0 g, 28.1 mmol) and $\text{Pd}(\text{PPh}_3)_4$ (3.25 g, 2.81 mmol) and refluxed for 2 d. Once the reaction was complete, the solution was evaporated to dryness and the crude material was purified by silica gel column chromatography (5:95 ethyl acetate/hexanes) to afford a colorless oil (5.7 g, 35%). ^1H NMR (CDCl_3 , 500 MHz): δ 7.67 (s, 2H), 7.58 (d, $J = 8.0$ Hz, 2H), 7.45 (t, $J = 7.5$ Hz, 2H), 7.40 (d, $J = 7.5$ Hz, 2H), 7.24 (s, 2H), 7.20 (d, $J = 8.5$ Hz, 2H), 7.15 (d, $J = 8.5$ Hz, 2H), 5.42 (t, $J = 2.5$ Hz, 2H), 4.71 (s, 4H), 3.84 (m, 2H), 3.59 (m, 2H), 2.39 (s, 6H), 1.89 (m, 2H), 1.76 (m, 4H), 1.67 (m, 2H), 1.54 (m, 4H) ppm. ^{13}C NMR (CDCl_3 , 125 MHz): δ 151.80, 138.95, 137.85, 131.46, 131.30, 131.28, 129.22, 129.09, 129.00, 127.93, 126.28, 116.12, 96.89, 72.44, 61.76, 30.35, 25.34, 20.70, 18.54 ppm.

Bis(3-(2-hydroxy-5-methylphenyl)benzyl)ether (C). Compound **B** (0.90 g, 1.56 mmol) and oxalic acid (0.35 g, 3.89 mmol) were dissolved in 10 mL of THF/MeOH (1:1). The mixture was stirred at ~ 50 °C for 2 h and then evaporated to dryness. Dichloromethane (10 mL) was added and the mixture was washed with water (3 x 10 mL). The organic layer was dried over Na_2SO_4 ,

filtered, and the solvent was removed *in vacuo* to give an off-white solid. The solid was washed with hot hexanes to remove a colored impurity and the final product was isolated by filtration (0.46 g, 73%). ¹H NMR (CDCl₃, 500 MHz): δ 7.54 (s, 2H), 7.48 (d, *J* = 7.5 Hz, 2H), 7.43 (m, 4H), 7.09 (m, 4H), 6.87 (d, *J* = 8.0 Hz, 2H), 5.43 (s, 2H), 4.67 (s, 4H), 2.35 (s, 6H) ppm. ¹³C NMR (CDCl₃, 125 MHz): δ 151.00, 139.68, 138.43, 131.54, 130.70, 130.33, 129.93, 129.38, 129.21, 128.50, 127.86, 116.56, 73.02, 21.26 ppm. ESI-MS(-) = 409.1 [M-H]⁻ (Calcd = 409.2 [M-H]⁻). Mp = 128-130 °C.

Bis(3-(2-hydroxy-5-methylphenyl-3-carbaldehyde)benzyl)ether (D). All reagents and solvents should be rigorously dried before use in this reaction. Compound **C** (2.44 g, 5.95 mmol), anhydrous magnesium chloride (2.26 g, 23.8 mmol), paraformaldehyde (2.68 g, 89.2 mmol), and triethylamine (5 mL, 35.7 mmol) were combined in 200 mL of dry acetonitrile and refluxed for 3 d. The reaction completeness was determined by the disappearance of starting material as monitored by silica gel thin layer chromatography. The mixture was evaporated to dryness and the residue was dissolved in dichloromethane. The organic phase was washed with aqueous HCl, dried over Na₂SO₄, filtered, and evaporated to dryness, giving a pale yellow oil. After purification by silica gel column chromatography (10:90 ethyl acetate/hexanes), the desired product was obtained as a light yellow oil (1.7 g, 61%). ¹H NMR (CDCl₃, 500 MHz): δ 11.37 (s, 2H, CHO), 9.91 (s, 2H, OH), 7.62 (s, 2H), 7.56 (d, *J* = 7.5 Hz, 2H), 7.48-7.41 (m, 6H), 7.35 (d, *J* = 1.5 Hz, 2H), 4.69 (s, 4H), 2.39 (s, 6H) ppm. ¹³C NMR (CDCl₃, 125 MHz): δ 197.06, 157.84, 139.13, 138.55, 136.01, 133.25, 130.25, 129.39, 128.89, 128.88, 128.60, 127.31, 120.03, 72.38, 20.55 ppm. ESI-MS(-) = 465.3 [M-H]⁻ (Calcd = 465.2 [M-H]⁻).

H₂PIM. Compound **D** (1.70 g, 3.65 mmol) was dissolved in 10 mL of dichloromethane and combined with 3,3'-diaminodiphenylsulfone (0.90 g, 3.65 mmol) in 700 mL of dry acetonitrile.

About 1 mL of trifluoroacetic acid was added and the mixture was refluxed for 6 h. Over the course of ~1 h, a large amount of bright yellow-orange material formed. The solid was isolated by filtration and washed with diethyl ether to afford analytically pure product (1.80 g, 72%). ^1H NMR (CDCl_3 , 500 MHz): δ 13.16 (s, 2H), 8.63 (s, 2H), 7.89 (d, $J = 9.5$ Hz, 2H), 7.80 (m, 2H), 7.73 (s, 2H), 7.67 (t, $J = 8.0$ Hz, 2H), 7.44 (m, 4H), 7.39 (m, 4H), 7.28 (m, 2H), 7.21 (s, 2H), 4.69 (s, 4H), 2.36 (s, 6H) ppm. ^{13}C NMR (CDCl_3 , 125 MHz): δ 164.78, 156.69, 149.82, 143.08, 138.09, 137.72, 136.08, 132.20, 130.72, 130.32, 129.57, 128.69, 128.51, 128.30, 127.06, 125.30, 123.73, 123.59, 118.85, 73.03, 20.61 ppm. IR (KBr): ν 2852, 1620, 1579, 1472, 1454, 1427, 1326, 1302, 1211, 1148, 1092, 886, 783, 700, 689, 620, 524 cm^{-1} . DART-MS(-) = 677.2121 (Calc = 677.2116 $[\text{M}-\text{H}]^-$). Mp = 313-315 $^\circ\text{C}$.

$[\text{}^{57}\text{Fe}_2(\text{Mes})_4]$. A small-scale synthesis of 57-iron enriched $[\text{Fe}_4(\text{Mes})_4]$ was undertaken using a procedure adapted from the literature.^{28,33,34} 57-Iron metal (200 mg, 3.51 mmol, 95% enriched) was suspended in 4.0 mL of concentrated aqueous hydrochloric acid. The mixture was heated to 90 $^\circ\text{C}$ for ~4 h without using a stir bar, leading to dissolution of the iron metal and eventual formation of a clear brown solution. The reaction is not complete if the solution is yellow; further air oxidation must occur to convert iron(II) chloride to iron(III) chloride. Once the reaction is complete, aqueous HCl was removed *in vacuo* (without heating) to give a pale yellow solid. The solid was transferred to a 10 mL Schlenk flask under a nitrogen atmosphere and treated with 3 mL of freshly distilled thionyl chloride to dehydrate the iron(III) chloride. The mixture was heated at 80 $^\circ\text{C}$ for 30 min until the solid turned black. Excess thionyl chloride was removed by pumping on the black solid under vacuum for 3 h. About 10 mL of dry chlorobenzene was added to the reaction flask and the slurry was refluxed for 30 min to give a brown suspension, which indicates conversion of anhydrous iron(III) chloride to iron(II)

chloride. The septum-sealed reaction flask was brought inside an anaerobic glovebox for subsequent manipulations. The tan-colored solid was isolated by filtration and washed with toluene. This material was re-suspended in 3 mL of dry THF and stirred for 30 min until the brown solution became a beige color. An off-white solid was isolated by filtration as the desired $^{57}\text{FeCl}_2(\text{THF})_{1.5}$ precursor (571 mg, 53%).³⁴

Inside an anaerobic drybox, a mesitylene Grignard reagent was prepared by combining 2-bromomesitylene (1.02 g, 5.12 mmol) and magnesium metal (123 mg, 5.12 mmol) in 2 mL of dry THF. After ~ 5 h, most of the magnesium had dissolved and the solution became a pale light brown color. The Grignard reagent was placed inside a -30 °C freezer and allowed to cool. In a separate vial, solid $^{57}\text{FeCl}_2(\text{THF})_{1.5}$ (571 mg, 2.14 mmol) was suspended in 3 mL of tetrahydrofuran /1,4-dioxane (1:1) that has been cooled to -30 °C. The cold Grignard reagent was added over a 5 min period to the iron solution. The reaction mixture was stirred and allowed to warm slowly to RT. As the reaction progressed, the light brown slurry became a red color. After 2 h, a solid precipitate was removed by filtration and the filtrate was evaporated to dryness. The dried residue was extracted into diethyl ether, filtered, and placed inside a -30 °C freezer to crystallize over the course of ~14 h. A large amount of red crystalline material was isolated by filtration and dried to give [$^{57}\text{Fe}_2(\text{Mes})_4$] as a red powder (430 mg, 60%). The spectroscopic characteristics of this compound are identical to those reported for [$\text{Fe}_2(\text{Mes})_4$].²⁸ This product was stored at -30 °C inside the glovebox to prevent oxidation and thermal degradation.

[$\text{Fe}_2(\text{PIM})(\text{Ph}_3\text{CCO}_2)_2$] (1). In an anaerobic drybox, solid H_2PIM (100 mg, 147 μmol) and triphenylacetic acid (85 mg, 295 μmol) were dissolved in 2.0 mL of tetrahydrofuran. A 1.0 mL solution of tetrahydrofuran containing [$\text{Fe}_2(\text{Mes})_4$] (86 mg, 147 μmol) was added to the reaction vessel and the mixture was stirred for 1 h. The dark red solution was evaporated to dryness and

the residue was redissolved in benzene. The solution was filtered through a glass wool plug and layered with pentane. After ~12 h, a large amount of red crystals had formed that were suitable for X-ray diffraction analysis. The solid material was isolated by filtration and washed with pentane to give the desired diiron complex (171 mg, 86%). ^1H NMR (C_6D_6 , 500 MHz): δ 78.37, 74.97, 48.27, 22.78, 8.20-1.19, -5.32, -6.20, -10.37, -13.49, -21.13 ppm. IR (KBr): ν 3056, 3031, 2918, 2850, 1578, 1545, 1490, 1444, 1418, 1378, 1322, 1304, 1284, 1200, 1175, 1152, 1097, 1085, 1036, 985, 790, 745, 699, 673, 547 cm^{-1} . UV-vis (CH_2Cl_2): λ_{max} = 290 (36,300 $\text{M}^{-1}\text{cm}^{-1}$), and 410 (16,000 $\text{M}^{-1}\text{cm}^{-1}$) nm. Anal. Calcd. for $\text{Fe}_2\text{C}_{82}\text{H}_{62}\text{N}_2\text{O}_9\text{S}\cdot(\text{C}_4\text{H}_8\text{O})$ (**1**·THF): C, 71.97; H, 4.92; N, 1.95; Found: C, 71.80; H, 4.94; N, 2.22. Mp (decomp) = 302 °C. Mössbauer (polycrystalline, apiezon M grease): δ_1 = 1.18(2) mm/s, ΔE_{Q1} = 2.33(2) mm/s, $\Gamma_{(1, \text{L/R})}$ = 0.38(2) mm/s, Site 1 Area = 53%; δ_2 = 0.97(2) mm/s, ΔE_{Q2} = 2.25(2) mm/s, $\Gamma_{(2, \text{L/R})}$ = 0.35(2) mm/s, Site 2 Area = 47%.

[Fe₂(PIM)(Ar^{Tol}CO₂)₂] (2). The synthesis of **[Fe₂(PIM)(Ar^{Tol}CO₂)₂]** was performed as described for **[Fe₂(PIM)(Ph₃CCO₂)₂] (1)**, except that Ar^{Tol}CO₂H was used instead of Ph₃CCO₂H. The product crystallized upon slow diffusion of pentane into a solution of the complex in dichloromethane and was isolated as a red powder when dried (152 mg, 74%). X-ray diffraction quality crystals were readily obtained by slow diffusion of pentane into a dichloromethane solution of the complex. ^1H NMR (CD_2Cl_2 , 500 MHz): δ 76.92, 73.82, 49.00, 24.68, 7.86, 7.31, 6.22, 2.41, 1.37, 0.96, -0.41, -1.81, -5.72, -9.04, -19.60 ppm. IR (KBr): ν 3052, 3024, 2912, 2851, 1614, 1577, 1533, 1445, 1413, 1381, 1302, 1286, 1202, 1149, 1073, 819, 791, 712, 695, 542 cm^{-1} . UV-vis (CH_2Cl_2): λ_{max} = 290 (36,700 $\text{M}^{-1}\text{cm}^{-1}$), and 418 (14,000 $\text{M}^{-1}\text{cm}^{-1}$) nm. Anal. Calcd. for $\text{Fe}_2\text{C}_{84}\text{H}_{66}\text{N}_2\text{O}_9\text{S}\cdot(\text{C}_4\text{H}_8\text{O})$ (**2**·THF): C, 72.23; H, 5.10; N, 1.91; Found: C, 71.72; H, 4.92; N, 2.17. Mp (decomp) = 240 °C. Mössbauer (polycrystalline, apiezon M grease): δ_1 =

1.10(2) mm/s, $\Delta E_{Q1} = 2.04(2)$ mm/s, $\Gamma_{(1,L/R)} = 0.38(2)$ mm/s, Site 1 Area = 63%; $\delta_2 = 0.95(2)$ mm/s, $\Delta E_{Q2} = 2.02(2)$ mm/s, $\Gamma_{(2,L/R)} = 0.32(2)$ mm/s, Site 2 Area = 37%.

[Fe₂(μ -OH)₂(ClO₄)₂(PIM)(Ar^{Tol}CO₂)Ag] (3). In an anaerobic drybox, [Fe₂(PIM)(Ar^{Tol}CO₂)₂] (2) (50 mg, 35 μ mol) and silver perchlorate (18 mg, 90 μ mol) were combined in 2 mL of dichloromethane and stirred for 1 h. The reaction mixture was filtered through a glass wool plug to remove a black precipitate. The solution was concentrated to half its volume and layered with 0.5 mL of pentane. After ~14 h, a dark solid formed on the bottom of the reaction vial. This product was isolated by filtration, yielding a dark crystalline solid (31 mg, 61%). Crystals suitable for X-ray diffraction studies were obtained by slow diffusion of pentane into a solution of the complex in dichloromethane. IR (KBr): ν 3432, 2919, 2851, 1579, 1546, 1521, 1472, 1446, 1382, 1337, 1306, 1285, 1200, 1181, 1152, 1122, 1020, 796, 603, 548, 530 cm⁻¹. UV-vis (CH₂Cl₂): $\lambda_{\max} = 290$ (32,300 M⁻¹cm⁻¹), 375 (11,100 M⁻¹ cm⁻¹), 479 (sh, 3,300 M⁻¹cm⁻¹), 600 (2,300 M⁻¹cm⁻¹). Anal. Calcd. for Fe₂C₆₃H₅₁AgCl₂N₂O₁₇S·(CH₂Cl₂) (3·CH₂Cl₂): C, 50.72; H, 3.52; N, 1.85; Cl, 9.36; Found: C, 51.04; H, 3.64; N, 1.77; Cl, 9.23. Mp (decomp) = ~270 °C. Mössbauer (THF): $\delta = 0.49(2)$ mm/s, $\Delta E_Q = 1.38(2)$ mm/s, $\Gamma_{(L/R)} = 0.56(2)$ mm/s.

[Fe₂(μ -OH)(PIM)(Ph₃CCO₂)₃] (4). In an anaerobic drybox, solid [Fe₂(PIM)(Ph₃CCO₂)₂] (1) (30 mg, 22 μ mol), triphenylacetic acid (13 mg, 44 μ mol), and triethylamine (6.0 μ L) were combined in 2.0 mL of benzene. The reaction vial was sealed with a septum, brought outside of the glovebox, and bubbled with dioxygen for 5 min. When exposed to O₂, the clear red solution quickly turned dark brown. Upon vapor diffusion of pentane into the benzene solution, several large X-ray diffraction quality crystals were obtained. The product was isolated by filtration (8 mg, 22%). ¹H NMR (CDCl₃, 500 MHz): δ 51.28, 44.24, 33.02, 29.70, 23.90, 6.60, -4.52, -7.85 ppm. IR (KBr): ν 3438, 3056, 3032, 2919, 1582, 1544, 1491, 1477, 1446, 1405, 1373, 1331,

1205, 1150, 1035, 827, 789, 744, 699, 677, 642, 604, 547, 523 cm^{-1} . UV-vis (CH_2Cl_2): $\lambda_{\text{max}} = 284$ ($108,000 \text{ M}^{-1} \text{ cm}^{-1}$), 372 ($38,000 \text{ M}^{-1} \text{ cm}^{-1}$), and 570 ($10,300 \text{ M}^{-1} \text{ cm}^{-1}$) nm. Anal. Calcd. for $\text{Fe}_2\text{C}_{102}\text{H}_{78}\text{N}_2\text{O}_{12}\text{S} \cdot (\text{C}_6\text{H}_6)(\text{NC}_6\text{H}_{15})_2$ (**4**· $\text{C}_6\text{H}_6 \cdot (\text{NEt}_3)_2$): C, 73.99; H, 5.90; N, 2.88; Found: C, 74.40; H, 5.66; N, 3.22. Mp = 214-217 °C. Mössbauer (polycrystalline, apiezon M grease): $\delta = 0.52(2) \text{ mm/s}$, $\Delta E_{\text{Q}} = 0.95(2) \text{ mm/s}$, $\Gamma_{(\text{L/R})} = 0.38(2) \text{ mm/s}$.

[Fe₄(μ -OH)₆(PIM)₂(Ph₃CCO₂)₂] (5). In an anaerobic drybox, solid **[Fe₂(PIM)(Ph₃CCO₂)₂] (1)** (40 mg, 29 μmol) was combined with 2.0 mL of benzene in a septum-sealed reaction vessel. Dioxygen was bubbled through the mixture for 5 min. The solution was concentrated to approximately half its volume and then left alone to crystallize over ~1 d by slow evaporation. This method resulted in selective crystallization of the desired tetranuclear **[Fe₄(μ -OH)₆(PIM)₂(Ph₃CCO₂)₂] (5)** (hexagonal prisms) instead of the dinuclear **[Fe₂(μ -OH)(PIM)(Ph₃CCO₂)₃] (4)** (rectangular blocks). Crystals obtained from this method were suitable for X-ray diffraction studies. The desired product was isolated by filtration (10 mg, 32%). ¹H NMR (CDCl_3 , 500 MHz): δ 49.97, 43.69, 31.24, 15.60, 8.71, 5.94, 5.31, 4.14, -7.12 ppm. IR (NaCl): ν 3554, 3445, 3064, 2961, 2921, 2850, 1580, 1542, 1381, 1340, 1324, 1260, 1238, 1204, 1151, 1101, 1080, 1017, 984, 800, 789, 747, 738, 705, 692, 671, 633, 528, 416 cm^{-1} . UV-vis (CH_2Cl_2): $\lambda_{\text{max}} = 280$ ($84,200 \text{ M}^{-1} \text{ cm}^{-1}$), 370 ($25,000 \text{ M}^{-1} \text{ cm}^{-1}$), and 540 ($8,060 \text{ M}^{-1} \text{ cm}^{-1}$) nm. Anal. Calcd. for $\text{Fe}_4\text{C}_{124}\text{H}_{100}\text{N}_4\text{O}_{20}\text{S}_2$ (**5**): C, 66.09; H, 4.47; N, 2.49; Found: C, 66.09; H, 4.50; N, 2.14. Mp (decomp) = >300 °C. Mössbauer (polycrystalline, apiezon grease): $\delta = 0.51(2) \text{ mm/s}$, $\Delta E_{\text{Q}} = 1.06(2) \text{ mm/s}$, $\Gamma_{(\text{L/R})} = 0.40(2) \text{ mm/s}$.

[Fe₂(μ -O)(PIM)(Ar^{Tol}CO₂)₂] (6)/ **[Fe₂(μ -OH)₂(PIM)(Ar^{Tol}CO₂)₂] (7)**. In an anaerobic drybox, **[Fe₂(PIM)(Ar^{Tol}CO₂)₂] (2)** (200 mg, 144 μmol) was dissolved in 2 mL of tetrahydrofuran in a 20 mL vial. The vial was sealed with a rubber septum and brought outside of the drybox. Dioxygen

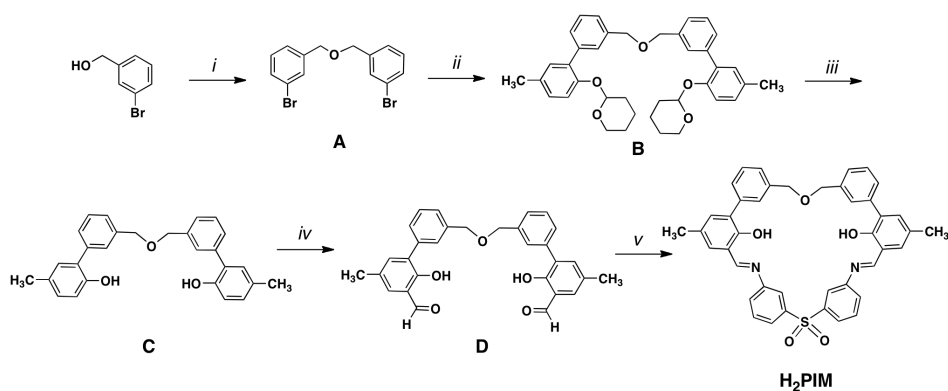
was bubbled through the reaction vial for 5 min, at which time the red solution became a dark brown. The tetrahydrofuran solvent was removed *in vacuo* and the resulting brown solid (117 mg, 58%) was isolated and stored inside the drybox to prevent further reaction with ambient moisture. Single crystals suitable for X-ray diffraction analysis were obtained by slow diffusion of diethyl ether into a solution of the complex in acetonitrile. ^1H NMR (CDCl_3 , 500 MHz): δ 26.30, 24.44, 21.84, 13.52, 15.92, 14.77, 11.56, 10.08, 9.58, 8.22, 5.44, 4.86, 4.26, 2.16, 1.80, 1.25, 0.88, -7.11 ppm. IR (KBr): ν 3448, 3021, 2918, 2856, 1613, 1582, 1545, 1515, 1473, 1448, 1383, 1336, 1304, 1286, 1205, 1152, 818, 791, 766, 700, 546, 531 cm^{-1} . UV-vis (CH_2Cl_2): λ_{max} = 380 (sh), 473, 600 nm. Anal. Calcd. for $\text{Fe}_2\text{C}_8\text{H}_6\text{N}_2\text{O}_{11}\text{S}\cdot(\text{CH}_3\text{CN})$ (**6** $\cdot\text{CH}_3\text{CN}$): C, 70.45; H, 4.88; N, 2.87. Anal. Calcd. for $\text{Fe}_2\text{C}_8\text{H}_6\text{N}_2\text{O}_{10}\text{S}\cdot(\text{CH}_3\text{CN})$ (**7** $\cdot\text{CH}_3\text{CN}$): C, 71.32; H, 4.80; N, 2.90. Found: C, 69.89; H, 4.76; N, 2.59. *As discussed in the text, compounds 6 and 7 exist as a mixture in the solid-state.* Mp (decomp) = >300 °C. Mössbauer (polycrystalline, apiezon M grease): $\delta_1 = 0.47(2)$ mm/s, $\Delta E_{Q1} = 1.52(2)$ mm/s, $\Gamma_{(1,L/R)} = 0.36(2)$ mm/s, Site 1 Area = 21%; $\delta_2 = 0.50(2)$ mm/s, $\Delta E_{Q2} = 0.97(2)$ mm/s, $\Gamma_{(2,L/R)} = 0.48(2)$ mm/s, Site 2 Area = 79%;

[Fe₄(μ -OH)₆(PIM)₂(Ar^{Tol}CO₂)₂] (8). Solid $[\text{Fe}_2(\text{PIM})(\text{Ar}^{\text{Tol}}\text{CO}_2)_2]$ (**2**) (200 mg, 144 μmol) was dissolved in 2.0 mL of benzene and stirred under dioxygen for 5 min, giving a dark brown solution. About 10 μL of water was then added to the reaction mixture and the solution was stirred for an additional 10 min, then filtered through a glass wool plug before the filtrate was evaporated to dryness. The remaining solid was isolated as a pale brown material (~120 mg, 73%). ^1H NMR ($\text{DMF-}d_7$, 500 MHz): δ 72.80, 45.00, 26.24, 14.48, 13.26, 10.40, 7.30-0.12, -3.16, -4.65, -11.36 ppm. IR (KBr): ν 3432, 3019, 2919, 2857, 1614, 1584, 1543, 1516, 1473, 1450, 1385, 1324, 1304, 1286, 1206, 1151, 791, 703, 586, 528 cm^{-1} . UV-vis (CH_2Cl_2): λ_{max} = 360 (81,700 $\text{M}^{-1}\text{cm}^{-1}$), 550 (17,100 $\text{M}^{-1}\text{cm}^{-1}$) nm. Anal. Calcd. for $\text{Fe}_4\text{C}_{126}\text{H}_{104}\text{N}_4\text{O}_{20}\text{S}_2\cdot(\text{C}_6\text{H}_6)_2$

($8 \cdot (\text{C}_6\text{H}_6)_2$): C, 67.99; H, 4.80; N, 2.30; Found: C, 67.92; H, 4.80; N, 2.43. Mp (decomp) = >300 °C. Mössbauer (THF): $\delta = 0.49(2)$ mm/s, $\Delta E_Q = 0.97(2)$ mm/s, $\Gamma_{(L/R)} = 0.44(2)$ mm/s.

3.3. Results

Ligand Design and Synthesis. A feature of our previous syn *N*-donor ligands, such as H₂L and H₂BIPS (Chart 3.1), is that their metal-binding units can rotate in such a manner as to permit spontaneous self-assembly of undesired bis(syn *N*-donor)diiron(II) complexes following treatment with a base and iron(II) salts.^{26,35} Molecular modeling studies suggested to us that by joining the phenyl rings of H₂L or H₂BIPS with an appropriate linker to form a macrocycle, it would not be possible to generate [Fe₂(syn *N*-donor)₂] species. To test this hypothesis, we designed and synthesized H₂PIM (Chart 3.1), using as the linker a three-atom ether moiety.



Scheme 3.2. *i.* a) NaH, dry THF, b) 3-bromobenzyl bromide; *ii.* a) *Aryl zinc reagent*: 2-(2-bromo-4-methylphenoxy)-tetrahydro-2H-pyran, *n*-butyllithium, ZnCl₂, THF, b) Pd(PPh₃)₄; *iii.* oxalic acid, THF/MeOH (1:1), 50 °C; *iv.* anhydrous MgCl₂, paraformaldehyde, NEt₃, CH₃CN, reflux; *v.* 3,3'-diaminodiphenylsulfone, trifluoroacetic acid, dry CH₃CN.

The H₂PIM ligand was prepared as indicated in Scheme 3.2. The dibenzyl ether linker **A** was obtained by reaction of 3-bromobenzyl alcohol with sodium hydride, followed by refluxing with 3-bromobenzyl bromide. To prepare compound **B**, a palladium catalyzed, Negishi cross-

coupling procedure was employed. After silica gel column chromatography, **B** was isolated as a colorless oil. Next, the tetrahydropyran protecting group of **B** was removed by treatment with oxalic acid in tetrahydrofuran/methanol to afford **C** as a white solid. Orthoformylation of **C** was achieved by treatment with anhydrous magnesium chloride, paraformaldehyde, and triethylamine to give **D** as a yellow oil. To prepare H₂PIM, **D** was condensed with 3,3'-diaminodiphenylsulfone, generating the desired product as a bright yellow-orange solid in good yield. The synthetic route for H₂PIM is amenable to scale-up, and the final ligand has been obtained in multi-gram quantities.

Assembly of Diiron(II) Complexes. The phenolate-to-iron charge transfer band is a useful spectroscopic probe for quantitating metal–ligand binding.²⁶ A previous study demonstrated that the non-macrocyclic syn *N*-donors L²⁻ and BIPS²⁻, the doubly deprotonated forms of H₂L and H₂BIPS (Chart 3.1), respectively, react with iron in a 1:1 ratio to form [Fe₂(syn *N*-donor)₂] species. To test whether PIM²⁻, the doubly deprotonated form of H₂PIM, exhibits different metal binding behavior, iron(II) titration experiments were conducted. When H₂PIM was treated with 2 equiv of sodium hexamethyldisilazide (NaHMDS) in tetrahydrofuran, optical bands at 240, 280, and 420 nm appeared, corresponding to formation of PIM²⁻. Addition of iron(II) triflate to the PIM²⁻ solution decreased the intensity of the 240 and 420 nm bands, with concomitant absorption increases at 280 and 375 nm (Figure 3.1A). A plot of the absorbance changes at 375 nm revealed an Fe-to-PIM²⁻ ratio of 2:1 (Figure 3.1B), consistent with binding of two iron atoms by each macrocycle to give [Fe₂(PIM)(SO₃CF₃)₂]. To examine further the nature of this diiron species, titration experiments were conducted using external carboxylates. Addition of sodium triphenylacetate to a solution containing [Fe₂(PIM)(SO₃CF₃)₂] generated new absorption features at 410 and 600 nm (Figure 3.1C). A plot of the absorbance changes at 410

nm indicated that carboxylates readily displace the triflate anions (Figure 3.1D). These results suggested that H₂PIM is a dinucleating ligand that supports a carboxylate-bridged diiron(II) structure.

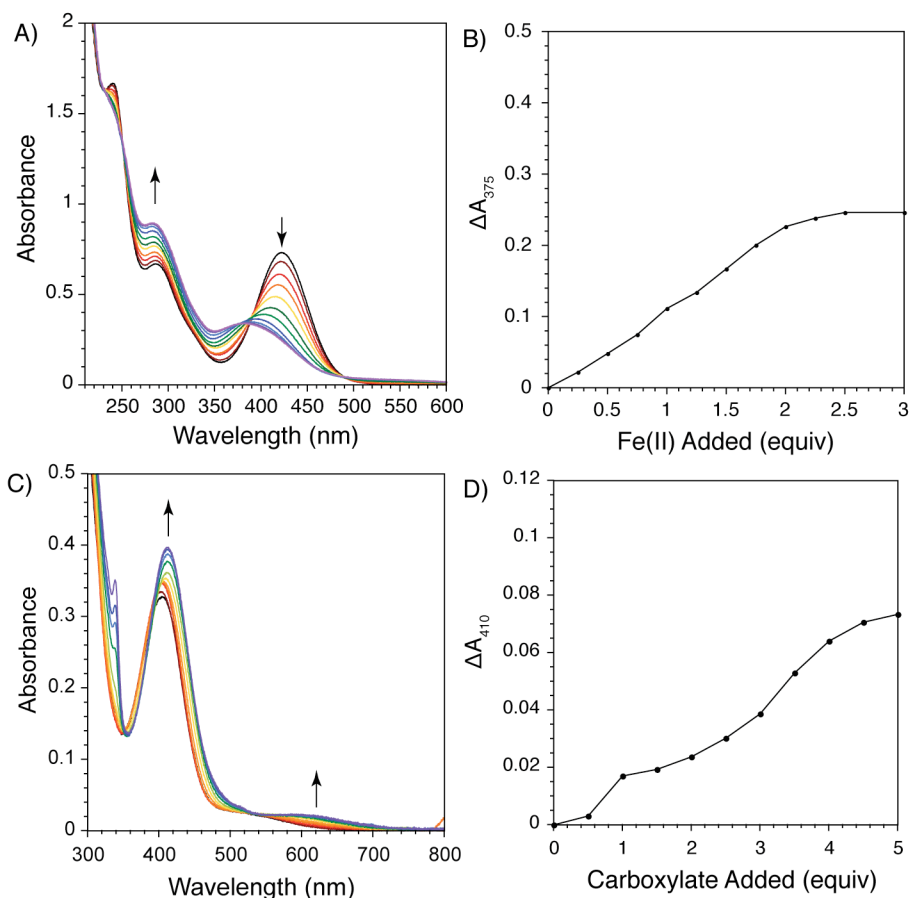


Figure 3.1. Optical changes upon addition of $\text{Fe}(\text{SO}_3\text{CF}_3)_2(\text{CH}_3\text{CN})_2$ to a $24 \mu\text{M}$ solution of PIM^{2-} in THF (A). Absorbance change at 375 nm clearly shows a 1:2 macrocycle to iron binding stoichiometry (B). Addition of sodium triphenylacetate to a THF solution containing $\text{PIM}^{2-}/2 \text{Fe}(\text{SO}_3\text{CF}_3)_2(\text{CH}_3\text{CN})_2$ led to absorption increases at ~ 410 and 600 nm (C). The single wavelength plot at 410 nm (D). Panel A: black line = Na_2PIM , colored lines = spectra after addition of up to 2.50 equiv of Fe(II). Panel C: black line = $[\text{Fe}_2(\text{PIM})(\text{SO}_3\text{CF}_3)_2]$, colored lines = spectra after addition of up to 5.0 equiv of $\text{NaO}_2\text{CCPh}_3$.

Preparative scale reactions were performed to metalate H₂PIM by treatment with $[\text{Fe}_2(\text{Mes})_4]$ and a sterically-hindered carboxylic acid, triphenylacetic acid or terphenylcarboxylic acid. A diiron(II) complex containing triphenylacetate was crystallized by slow diffusion of

pentane into a solution of the compound in benzene. X-ray diffraction studies revealed a dinuclear complex having the molecular formula $[\text{Fe}_2(\text{PIM})(\text{Ph}_3\text{CCO}_2)_2]$ (**1**, Figure 3.2, Table 3.1). The structure indicates that the PIM^{2-} ligand coordinates to two iron atoms that are bridged by two triphenylacetates, one of which is bound in an η^1, η^1 -1,3 coordination mode and the other in an η^1, η^2 -1,3 arrangement. The Fe–O(carboxylate) distances range from 2.00 to 2.25 Å. The four- and five-coordinate iron atoms are separated by 3.61 Å, with average Fe–O(phenolate) and Fe–N(imine) distances of 1.88 and 2.04 Å, respectively.

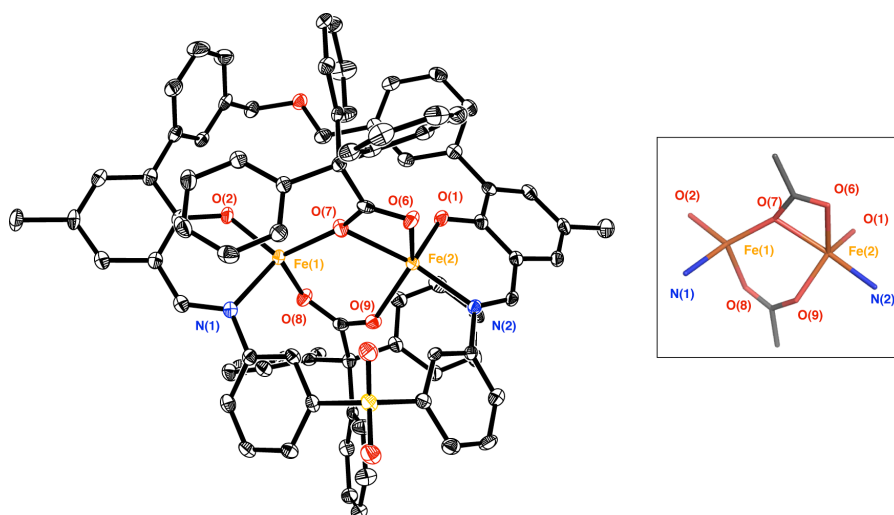


Figure 3.2. Ortep thermal ellipsoid (50%) diagram of the X-ray crystal structure of $[\text{Fe}_2(\text{PIM})(\text{Ph}_3\text{CCO}_2)_2]$ (**1**, left). An isolated view of the diiron core is shown as a stick figure representation on the right. Solvent molecules and hydrogen atoms are omitted for clarity. Color scheme: iron, orange; carbon, gray; nitrogen, blue; oxygen, red; sulfur, yellow. Selected bond distances (Å) and angles (Deg): Fe(1)–Fe(2) = 3.610; Fe(1)–N(1) = 2.048; Fe(1)–O(2) = 1.877; Fe(1)–O(7) = 1.999; Fe(1)–O(8) = 2.016; Fe(2)–N(2) = 2.039; Fe(2)–O(1) = 1.892; Fe(2)–O(7) = 2.254; Fe(2)–O(6) = 2.153; Fe(2)–O(9) = 2.024; O(2)–Fe(1)–N(1) = 92.5; O(1)–Fe(2)–N(2) = 92.4; O(7)–Fe(1)–O(8) = 103.7; O(7)–Fe(2)–O(9) = 89.1.

When the terphenylcarboxylate anion $\text{Ar}^{\text{Tol}}\text{CO}_2^-$ was employed in an analogous synthetic procedure, crystallization by slow diffusion of pentane into a saturated dichloromethane solution of the compound yielded $[\text{Fe}_2(\text{PIM})(\text{Ar}^{\text{Tol}}\text{CO}_2)_2]$ (**2**, Figure 3.3, Table 3.1). The X-ray structure of this compound revealed a dinuclear core that closely resembles the one in **1**. The iron atoms in

2 are bridged by two terphenylcarboxylate ligands, with Fe–O(carboxylate) distances of 2.00 to 2.34 Å. This diiron unit is supported by the syn *N*-donor macrocycle, resulting in Fe–O(phenolate) and Fe–N(imine) distances of 1.89 and 2.04 Å, respectively. The Fe–Fe distance in **2** is 3.61 Å, the same as in **1**. Compounds **1** and **2** have structures with features remarkably close to those at the active sites of sMMOH_{red},¹⁸ mimicking the syn arrangement of nitrogen donor atoms as well as the asymmetric bridging mode of carboxylates at the diiron(II) center.

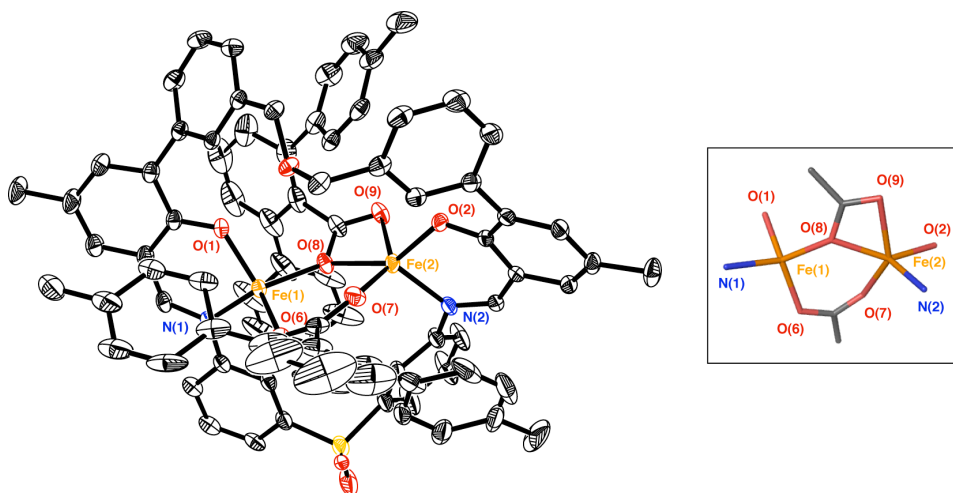


Figure 3.3. Ortep thermal ellipsoid (50%) diagram of the X-ray crystal structure of $[\text{Fe}_2(\text{PIM})(\text{Ar}^{\text{Tol}}\text{CO}_2)_2]$ (**2**, left). An isolated view of the diiron core is shown as a stick figure representation on the right. Solvent molecules and hydrogen atoms are omitted for clarity. Color scheme: iron, orange; carbon, gray; nitrogen, blue; oxygen, red; sulfur, yellow. Selected bond distances (Å) and angles (Deg): Fe(1)–Fe(2) = 3.610; Fe(1)–O(1) = 1.888; Fe(1)–N(1) = 2.037; Fe(1)–O(6) = 1.998; Fe(1)–O(8) = 2.028; Fe(2)–O(2) = 1.894; Fe(2)–N(2) = 2.045; Fe(2)–O(7) = 2.048; Fe(2)–O(8) = 2.092; Fe(2)–O(9) = 2.342; O(1)–Fe(1)–N(1) = 93.1; O(2)–Fe(2)–N(2) = 91.8; O(6)–Fe(1)–O(8) = 102.1; O(7)–Fe(2)–O(8) = 89.5.

Compounds **1** and **2** were further characterized by several spectroscopic methods (Table 3.2). As shown in Figure 3.4, they have strong absorption bands in the UV-visible region, with λ_{max} values of approximately 290 and 410 nm. The higher energy band is attributed to a π – π^* ligand transition, whereas the lower energy band is most likely due to ligand-to-metal charge transfer.^{36,37}

Table 3.1. X-ray Data Collection and Refinement Parameters for **1-3**.

	1	2	3
Empirical formula	[Fe ₂ N ₂ O ₉ SC ₈₂ H ₆₂] (C ₆ H ₆) _{3.55} (C ₅ H ₁₂) _{0.45}	[Fe ₂ N ₂ O ₉ SC ₈₄ H ₆₆] (C ₅ H ₁₂) _{1.39} (CH ₂ Cl ₂) _{0.45}	[Fe ₂ N ₂ O ₁₇ SC ₆₃ H ₄₉ Cl ₂ Ag] (CH ₂ Cl ₂) ₄
Formula weight	1672.84	1525.91	1768.28
Temperature (K)	100	100	100
Wavelength (Å)	0.71073	0.71073	0.71073
Crystal system	Triclinic	Triclinic	Monoclinic
Space group	P $\bar{1}$	P $\bar{1}$	Cc
Unit cell dimensions	a = 13.3280(9) Å b = 17.0039(12) Å c = 20.3398(14) Å α = 87.4680(10)° β = 74.1330(10)° γ = 73.7290(10)°	a = 15.1504(18) Å b = 17.190(2) Å c = 17.956(2) Å α = 117.070(2)° β = 92.599(2)° γ = 108.544(2)°	a = 16.6129(8) Å b = 20.5472(9) Å c = 21.6770(13) Å β = 107.3760(10)°
Volume (Å ³)	4253.7(5)	3846.5(8)	7061.7(6)
Z	2	2	4
Calculated density (g/mm ³)	1.306	1.317	1.663
Absorption coefficient (mm ⁻¹)	0.428	0.494	1.158
F(000)	1752	1598	3576
Crystal size (mm ³)	0.33 x 0.10 x 0.05	0.33 x 0.26 x 0.14	0.12 x 0.08 x 0.07
Θ range for data collection	1.60 to 24.87°	1.31 to 26.49°	1.62 to 25.03°
Index ranges	-15 ≤ h ≤ 15 -20 ≤ k ≤ 20 -24 ≤ l ≤ 23	-19 ≤ h ≤ 18 -21 ≤ k ≤ 21 -22 ≤ l ≤ 22	-19 ≤ h ≤ 19 -24 ≤ k ≤ 24 -25 ≤ l ≤ 25
Reflections collected	67231	68754	57426
Independent reflections	14670 [R(int) = 0.0743]	15831 [R(int) = 0.0365]	12483 [R(int) = 0.0325]
Completeness to Θ (%)	99.5	99.3	100.0
Absorption correction	Empirical	Empirical	Empirical
Max. and min. transmission	0.9789 and 0.8822	0.9340 and 0.8538	0.9233 and 0.8735
Data / restraints / parameters	14670/54/1119	15831/207/1023	12483/45/933
Goodness-of-fit on F ²	1.016	1.076	1.067
Final R indices [I > 2 σ (I)]	R1 = 0.0470 wR2 = 0.0906	R1 = 0.0982 wR2 = 0.2493	R1 = 0.0381 wR2 = 0.1020
R indices (all data)	R1 = 0.0820 wR2 = 0.1029	R1 = 0.1152 wR2 = 0.2622	R1 = 0.0406 wR2 = 0.1044
Largest diff. peak and hole (eÅ ⁻³)	0.641 and -0.638	1.726 and -1.776	0.907 and -0.909

* R1 = $\Sigma ||F_o| - |F_c|| / \Sigma |F_o|$; wR2 = $[\Sigma [w(F_o^2 - F_c^2)^2] / \Sigma [w(F_o^2)^2]]^{1/2}$; GOF = $[\Sigma [w(F_o^2 - F_c^2)^2] / (n-p)]^{1/2}$, where n is the number of reflections and p is the total number of parameters refined.

Table 3.2. Spectroscopic Data for **1-8**.

	Optical ^a		Mössbauer ^b						X-ray	
	λ , nm [ϵ , M ⁻¹ cm ⁻¹]	$\delta(\text{Fe1})$ [mm/s]	$\Delta E_{\text{Q}}(\text{Fe1})$ [mm/s]	$\Gamma(\text{Fe1})$ [mm/s]	Area(Fe1) [%]	$\delta(\text{Fe2})$ [mm/s]	$\Delta E_{\text{Q}}(\text{Fe2})$ [mm/s]	$\Gamma(\text{Fe2})$ [mm/s]	Area(Fe2) [%]	Fe–Fe (Å)
1	290 (36,300) 410 (16,000)	1.18	2.33	0.38	53	0.97	2.25	0.35	47	3.61
2	290 (36,700) 418 (14,000)	1.10 1.23*	2.04 2.58*	0.38 0.57*	63 59*	0.95 1.15*	2.02 1.75*	0.32 0.49*	37 41*	3.61
3	290 (32,300) 375(11,100) 479 (3,300, sh) 600 (2,300)	0.49*	1.38*	0.56*	100*	—	—	—	—	3.01
4	284 (108,000) 372 (38,000) 570 (10,300)	0.52	0.95	0.38	100	—	—	—	—	3.49
5	370 (25,000) 540 (8,060)	0.51	1.06	0.40	100	—	—	—	—	3.06 3.78 ^c
6/7	380 (sh) 473 600	0.47 0.46 ^d 0.51*	1.52 1.59 ^d 1.24*	0.36 0.58 ^d 0.62*	21 85 ^d 61*	0.50 0.48 ^d 0.49*	0.97 1.03 ^d 0.78*	0.48 0.34 ^d 0.44*	79 15 ^d 36*	3.44
8	360 (81,700) 550 (17,100)	0.49*	0.97*	0.44*	100*	—	—	—	—	—

^aAbsorption spectra were recorded in dichloromethane. ^bMössbauer spectra were acquired at 80 K; polycrystalline samples were prepared by mixing with Apiezon M grease and solution samples, which are marked with an asterisk (*), were prepared in tetrahydrofuran. ^cThis value corresponds to the Fe–Fe distance between two diiron units. ^dThe polycrystalline sample of **6/7** was dried under vacuum at 150 °C for 24 h.

The zero-field Mössbauer spectrum of polycrystalline **1** at 80 K displays two quadrupole doublets, with parameters $\delta_1 = 1.18(2)$ mm/s, $\Delta E_{\text{Q}1} = 2.33(2)$ mm/s, $\delta_2 = 0.97(2)$ mm/s, and $\Delta E_{\text{Q}2} = 2.25(2)$ mm/s (Figure 3.5). Each iron site accounts for ~50% of the total iron content in the sample, consistent with the X-ray structure of **1**, which shows two geometrically different iron atoms. The Mössbauer spectrum of polycrystalline **2** recorded at 80 K contains two quadrupole doublets, which were fit with parameters $\delta_1 = 1.10(2)$ mm/s, $\Delta E_{\text{Q}1} = 2.04(2)$ mm/s, $\delta_2 = 0.95(2)$ mm/s, and $\Delta E_{\text{Q}2} = 2.02(2)$ mm/s (Table 3.2). The isomer shift values of **1** and **2** (>1.0 mm/s) are typical of high-spin iron(II) complexes and the quadrupole splitting parameters are as expected for iron coordinated by *O,N*-donors.^{5,38} A comparison of the Mössbauer parameters of **1** and **2** to

those reported for sMMOH_{red} indicates that, qualitatively, the synthetic compounds are electronically similar to the protein active sites. Although the X-ray structure of sMMOH_{red} revealed a diiron core with two different iron environments, the Mössbauer data could be fit to a single quadrupole doublet ($\delta_1 = 1.3$ mm/s, $\Delta E_{Q1} = 3.0$ mm/s).³⁹ The primary difference between **1** and **2** compared to sMMOH_{red} is the identity of several donor groups, phenolates in place of carboxylates and imines in place of imidazoles.

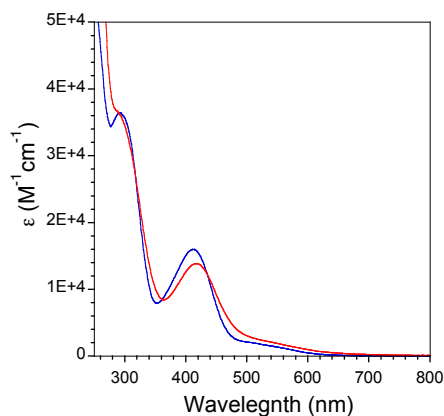


Figure 3.4. Absorption spectra of **1** (blue) and **2** (red) in dichloromethane. Both compounds exhibit optical bands at ~ 290 and 410 nm.

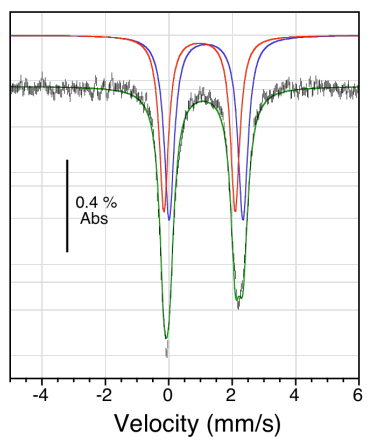


Figure 3.5. Zero-field ^{57}Fe Mössbauer spectrum of a polycrystalline sample of $[\text{Fe}_2(\text{PIM})(\text{Ph}_3\text{CCO}_2)]$ (**1**) at 80 K. The raw data (black hash lines) were fit to two distinct iron sites (green trace). The single site fits are shown as blue and red traces using the following parameters: $\delta_1 = 1.18(2)$ mm/s, $\Delta E_{Q1} = 2.33(2)$ mm/s, $\Gamma_{L/R(1)} = 0.38(2)$ mm/s; $\delta_2 = 0.97(2)$ mm/s, $\Delta E_{Q2} = 2.25(2)$ mm/s, $\Gamma_{L/R(1)} = 0.35(2)$ mm/s.

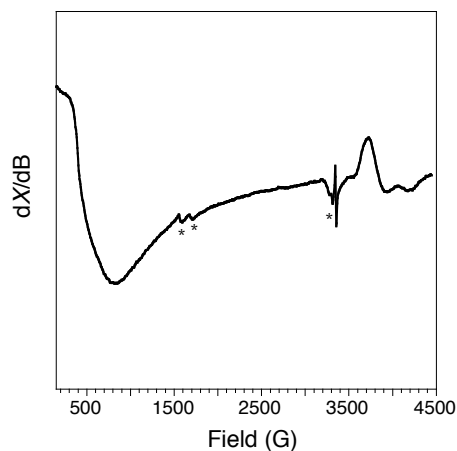


Figure 3.6. EPR spectrum of a frozen solution of $[\text{Fe}_2(\text{PIM})(\text{Ph}_3\text{CCO}_2)]$ (**1**) in 2-methyltetrahydrofuran measured at 5 K. The peaks marked with an asterisk are due to contaminants from the instrument cavity. The broad feature centered at $g = \sim 15$ is attributed to **1**, whereas the peaks at $g = \sim 1.7$ are of unknown origin. Instrument parameters: 9.281 GHz microwave frequency; 2.002 mW microwave power; 1.00×10^4 receiver gain; 100.0 kHz modulation frequency; 2.00 G modulation amplitude; 2.560 ms time constant.

To evaluate further its electronic structure, an EPR spectrum of **1** in 2-methyltetrahydrofuran was recorded at 5 K (Figure 3.6). The spectrum exhibits a broad signal with $g = \sim 15$, similar to that recorded for $\text{sMMOH}_{\text{red}}$, in which two $S = 2$ iron(II) centers are ferromagnetically coupled.⁴⁰ The EPR spectrum of **2** was not measured, but because its UV-visible and Mössbauer spectra are similar to those of **1**, complex **2** most likely has the same electronic structure.

The paramagnetism of **1** and **2** was verified by NMR spectroscopy. ^1H NMR spectra of **1** (Figure 3.7A) and **2** (Figure 3.7B) in dichloromethane- d_2 display resonances ranging from approximately 80 to -20 ppm. Although these paramagnetically shifted resonances cannot be assigned without more detailed studies,^{41,42} the peaks at 78.37, 74.97, 48.27, 22.78, -5.32, -10.37, -21.13 ppm for **1** and at 76.92, 73.82, 49.00, 24.68, -5.72, -9.04, -19.60 ppm for **2** are attributed to the PIM^{2-} ligand because their chemical shifts and relative intensities are nearly identical.

Because dichloromethane is a non-coordinating solvent, the solution structures of **1** and **2** in CD_2Cl_2 are probably similar to those in the solid state. When the ^1H NMR spectrum of **2** was recorded in acetonitrile- d_3 (Figure 3.7C), there were significant shifts in the proton peaks compared to the spectrum acquired in dichloromethane- d_2 . Most notably, new resonances at 69.33, 55.70, 48.28, 45.03, 42.85, 39.54, 38.55, and 35.55 ppm were observed. Because acetonitrile is coordinating, it is possible that solvent molecules bind to the iron centers and/or displace the carboxylate ligands. These results suggest that the solution structures of **1** and **2** depend on the coordinating abilities of the solvent.

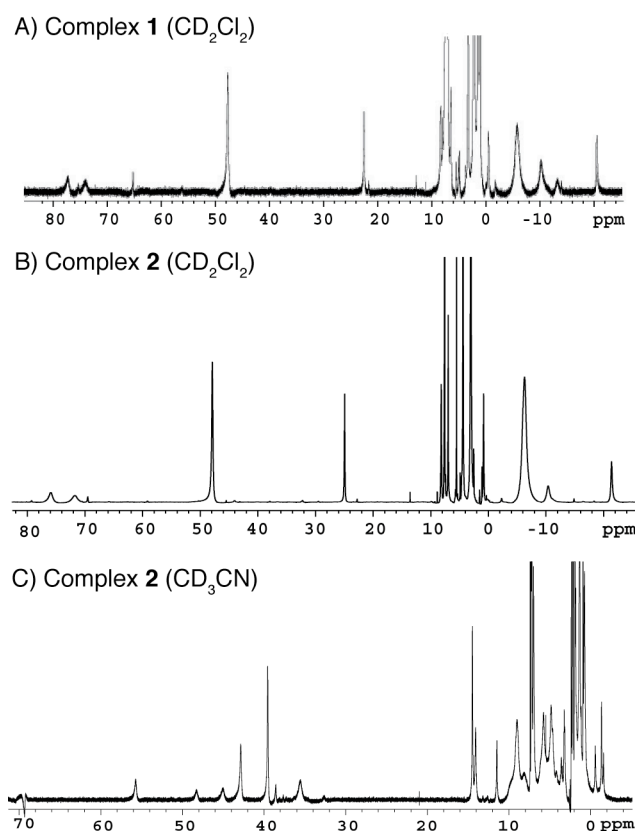


Figure 3.7. ^1H NMR spectra (500 MHz) of ~ 5 mM A) $[\text{Fe}_2(\text{PIM})(\text{Ph}_3\text{CCO}_2)_2]$ (**1**) in dichloromethane- d_2 and $[\text{Fe}_2(\text{PIM})(\text{Ar}^{\text{Tol}}\text{CO}_2)_2]$ (**2**) in B) dichloromethane- d_2 and C) acetonitrile- d_3 at room temperature.

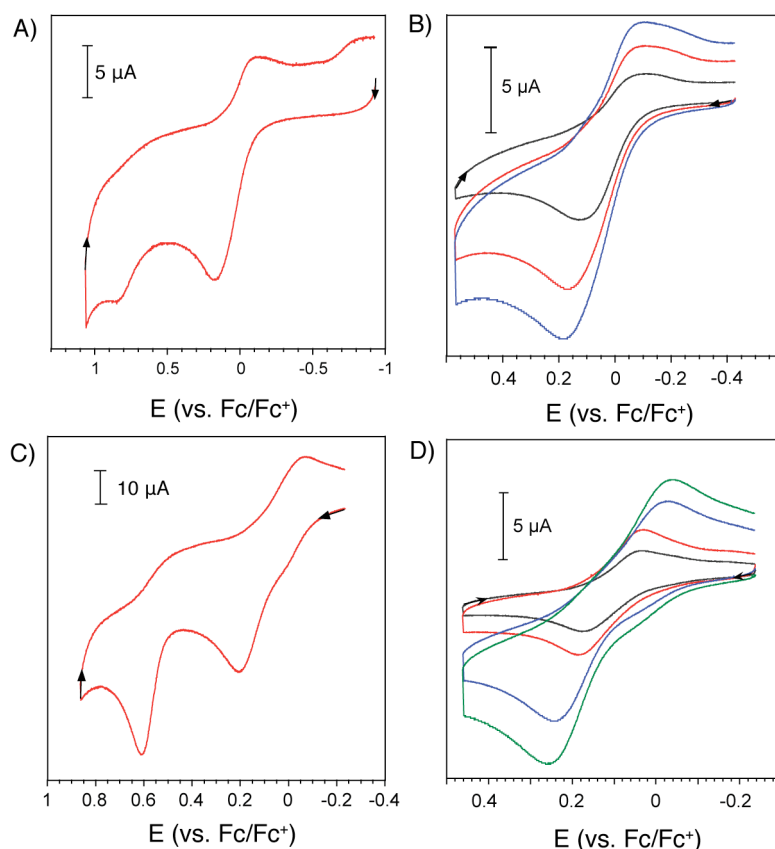


Figure 3.8. Cyclic voltammograms of 1.0 mM solutions of **1** (A and B) and **2** (C and D) in dichloromethane. The plots on the left show the full sweep width at a scan rate of 500 mV/s, and the plots on the right display the isolated sweep windows at various scan rates. Tetra-*n*-butylammonium hexafluorophosphate (0.2 M) was used as the supporting electrolyte. All data were obtained using a platinum working electrode and electrochemical potentials are referenced externally to the ferrocene/ferrocenium couple. Quasi-reversible redox couples at +16 mV and +108 mV were measured for **1** and **2**, respectively, at a scan rate of 100 mV/s. Panel B: black line = 100 mV/s, red line = 300 mV/s, blue line = 500 mV/s. Panel D: black line = 50 mV/s, red line = 100 mV/s, blue line = 300 mV/s, green line = 500 mV/s.

Redox Chemistry. A characteristic property of carboxylate-bridged diiron proteins is their tendency to undergo single electron transfer reactions.⁴⁰ For example, treatment of sMMOH_{ox}, which contains a diiron(III) unit, with sodium dithionite or gamma radiation from a Co-60 source led to formation of a mixed-valent diiron(II,III) species (H_{mv}). Because **1** and **2** are accurate small-molecule models of sMMOH in its reduced state, their electrochemical behavior is of interest. A cyclic voltammogram (CV) of **1** measured in dichloromethane using a platinum

working electrode and (*n*-Bu₄N)PF₆ as supporting electrolyte revealed two electrochemical events (Figures 3.8A and 3.8B). At a scan rate of 100 mV/s, a quasi-reversible redox couple at +16 mV, with a relatively large peak-to-peak separation of +210 mV, and an irreversible oxidation at +840 mV were observed. The CV of **2** was recorded under the same conditions (Figures 3.8C and 3.8D) and displayed a similar voltammogram, showing a quasi-reversible oxidation at +108 mV ($\Delta E_p = +198$ mV) and an irreversible oxidation at +600 mV. The quasi-reversible waves are tentatively assigned to metal-centered oxidations, probably conversion of diiron(II,II) to diiron(II,III). Ligand-centered redox chemistry, observed in some phenolate iron complexes,⁴³⁻⁴⁵ cannot be ruled out at this time. Unlike that of **1** and **2**, the CV of Na₂PIM does not exhibit any reversible redox events.

The redox chemistry of complex **2** was explored further by using chemical oxidants. Because the Ag⁺/Ag⁰ redox couple has an E_{1/2} value of +650 mV (vs. ferrocene/ferrocenium) in dichloromethane,⁴⁶ silver(I) reagents were anticipated to be able to oxidize **2** (E_{1/2} = +108 mV). Treatment of **2** with ~1 equiv of AgClO₄ in dichloromethane gradually converted the initial dark red solution to pale yellow brown. After stirring for about 1 h, a black precipitate formed, presumed to be silver metal. This insoluble material was removed by filtration and the absorption spectrum of the filtrate revealed that a new product had formed having optical bands at 290, 375, 479 (sh), and 600 nm (Figure 3.9A). The filtrate was concentrated and pentane was introduced by diffusion to afford X-ray diffraction quality crystals. Structural analysis of these crystals revealed the product to be [Fe₂(μ -OH)₂(ClO₄)₂(PIM)(Ar^{Tol}CO₂)₂Ag] (**3**), containing a di(μ -hydroxo)diiron(III) unit and a silver(I) ion. Because the synthesis of **3** was performed under anhydrous anaerobic conditions, the most likely source of the OH⁻ groups is trace water in the reaction mixture.

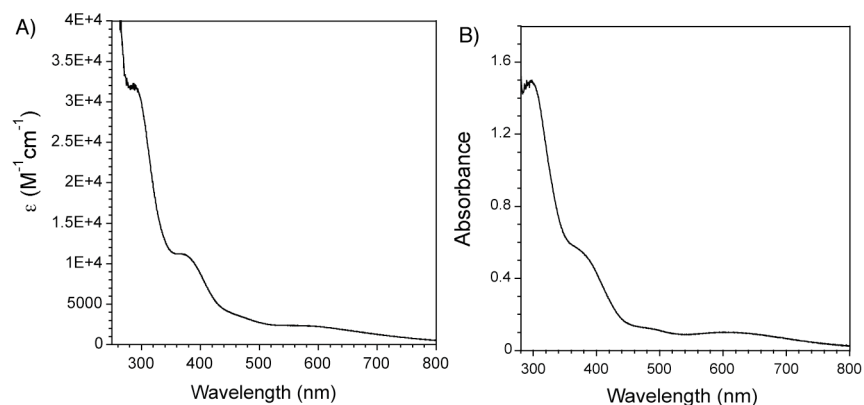


Figure 3.9. Absorption spectra of A) $[\text{Fe}_2(\mu\text{-OH})_2(\text{ClO}_4)_2(\text{PIM})(\mu\text{-Ar}^{\text{Tol}}\text{CO}_2)\text{Ag}]$ (**3**) and the tetranuclear product from the reaction of **2**/ AgSbF_6 . The data were recorded in dichloromethane at RT. Panel A: $\lambda_{\text{max}} = 290, 375, 475$ (sh), and 600 nm. Panel B: $\lambda_{\text{max}} = 300, 374,$ and 605 nm.

The octahedral iron atoms ($\text{Fe}\text{-Fe} = 3.01 \text{ \AA}$) in **3** are bridged by two hydroxide ions ($\text{Fe}\text{-O}_{\text{ave}} = 2.02 \text{ \AA}$) and one terphenylcarboxylate ligand ($\text{Fe}\text{-O}_{\text{ave}} = 2.04 \text{ \AA}$) (Figure 3.10). The hydrogen atoms of the hydroxides were not located, but the protonation state could be confidently assigned based on the $\text{Fe}\text{-O}$ bond distances. Whereas bridging hydroxides afford $\text{Fe}\text{-O}$ distance of 1.9-2.1 \AA , bridging oxides have $\text{Fe}\text{-O}$ bond lengths in the 1.7-1.8 \AA range.^{47,48} The phenolate ($\text{Fe}\text{-O}_{\text{ave}} = 1.86 \text{ \AA}$) and imine ($\text{Fe}\text{-N}_{\text{ave}} = 2.12 \text{ \AA}$) donors of PIM^{2-} and a perchlorate anion ($\text{Fe}\text{-O}_{\text{ave}} = 2.13 \text{ \AA}$) make up the rest of the iron coordination sphere. A Ag(I) ion is encapsulated within the macrocyclic framework, showing strong interactions with a hydroxide ligand ($\text{Ag}\text{-O}(6) = 2.25 \text{ \AA}$), the ether oxygen of PIM^{2-} ($\text{Ag}\text{-O}(5) = 2.36 \text{ \AA}$), and a $\text{C}=\text{C}$ π bond of the terphenylcarboxylate moiety ($\text{Ag}\text{-C}(60) = 2.49 \text{ \AA}$, $\text{Ag}\text{-C}(61) = 2.74 \text{ \AA}$). The $\text{Ag}\text{-C}$ distances are within the 2.36 to 2.77 \AA limit reported for other silver(I)-aryl species.⁴⁹⁻⁵¹ A bond valence sum (BVS),^{52,53} an empirical quantity used to determine the oxidation state of metal ions in coordination compounds based on crystallographically determined metal-ligand distances, returned values of 3.12 and 3.07 for $\text{Fe}(1)$ and $\text{Fe}(2)$, respectively (Table 3.3), indicating that the iron centers in **3** are both in the +3 oxidation state.

Table 3.3. Bond Valence Sum Analyses for **3**, **6**, and **7**.

Complex	Bond	Bond Length (Å)	Bond Valence ^a	Bond Valence Sum (BVS) ^b	
3	Fe(1)–O(1)	1.848	0.786	3.116	
	Fe(1)–O(6)	2.049	0.457		
	Fe(1)–O(7)	1.997	0.526		
	Fe(1)–O(8)	2.029	0.482		
	Fe(1)–O(13)	2.122	0.375		
	Fe(1)–N(1)	2.119	0.490		
	Fe(2)–O(2)	1.865	0.751	3.068	
	Fe(2)–O(6)	2.045	0.462		
	Fe(2)–O(7)	1.976	0.556		
	Fe(2)–O(9)	2.048	0.458		
	Fe(2)–O(15)	2.137	0.360		
	Fe(2)–N(2)	2.126	0.481		
	6	Fe(1)–O(1)	1.880	0.721	3.053
		Fe(1)–O(6)	1.744	1.041	
Fe(1)–O(7)		2.084	0.415		
Fe(1)–O(8)		2.133	0.364		
Fe(1)–N(1)		2.103	0.512		
Fe(2)–O(2)		1.898	0.751	3.034	
Fe(2)–O(6)		1.753	1.011		
Fe(2)–O(9)		2.113	0.384		
Fe(2)–O(10)		2.092	0.406		
Fe(2)–N(2)		2.125	0.482		
7	Fe(1)–O(1)	1.880	0.721	2.808	
	Fe(1)–O(100)	2.110	0.387		
	Fe(1)–O(101)	2.090	0.409		
	Fe(1)–O(7)	2.084	0.415		
	Fe(1)–O(8)	2.133	0.364		
	Fe(1)–N(1)	2.103	0.512		
	Fe(2)–O(2)	1.898	0.751	2.824	
	Fe(2)–O(100)	2.092	0.406		
	Fe(2)–O(101)	2.103	0.395		
	Fe(2)–O(9)	2.113	0.384		
	Fe(2)–O(10)	2.092	0.406		
	Fe(2)–N(2)	2.125	0.482		

^a The bond valence (s_{ij}), between cation i and anion j , was calculated using the equation: $s_{ij} = \exp [(r_o - r)/B]$, where r_o and B are empirically determined parameters and r is the observed bond distance. The following values were used in these calculations: $r_o(\text{Fe}^{+3}\text{–O}) = 1.759$, $r_o(\text{Fe}^{+3}\text{–N}) = 1.855$, $B = 0.37$. ^b The bond valence sum (BVS) = $\sum s_{ij}$.^{52,53}

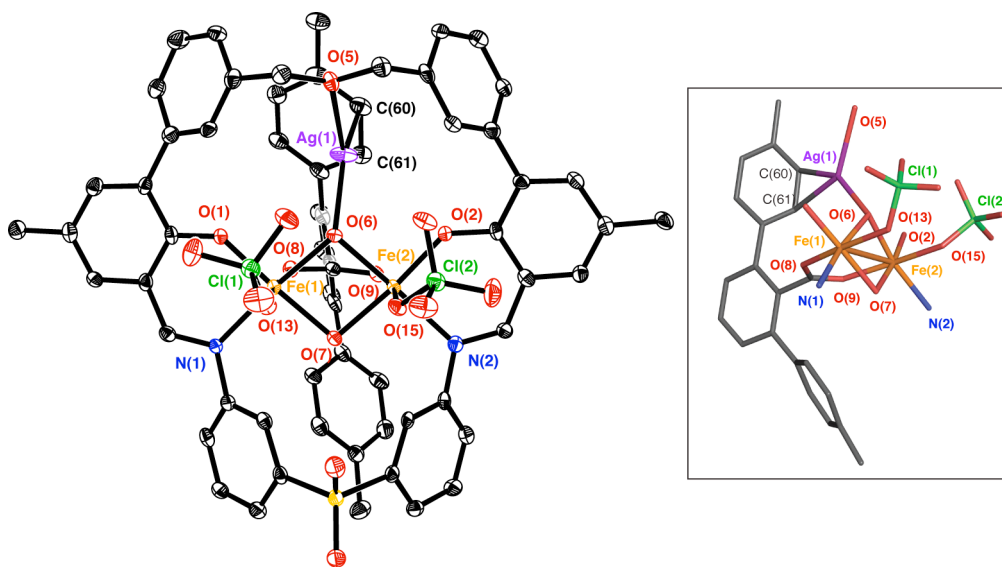


Figure 3.10. Ortep thermal ellipsoid (50%) diagram of the X-ray crystal structure of $[\text{Fe}_2(\mu\text{-OH})_2(\text{ClO}_4)_2(\text{PIM})(\text{Ar}^{\text{Tol}}\text{CO}_2)\text{Ag}]$ (**3**, left). An isolated view of the heterometallic core is shown as a stick figure representation on the right. Solvent molecules and hydrogen atoms are omitted for clarity. Color scheme: iron, orange; carbon, gray; nitrogen, blue; oxygen, red; sulfur, yellow; green, chlorine; purple, silver. Selected bond distances (Å) and angles (Deg): $\text{Fe}(1)\text{--}\text{Fe}(2) = 3.012$; $\text{Fe}(1)\text{--}\text{O}(1) = 1.848$; $\text{Fe}(1)\text{--}\text{N}(1) = 2.119$; $\text{Fe}(1)\text{--}\text{O}(6) = 2.049$; $\text{Fe}(1)\text{--}\text{O}(7) = 1.997$; $\text{Fe}(1)\text{--}\text{O}(8) = 2.029$; $\text{Fe}(1)\text{--}\text{O}(13) = 2.122$; $\text{Fe}(2)\text{--}\text{O}(2) = 1.865$; $\text{Fe}(2)\text{--}\text{N}(2) = 2.126$; $\text{Fe}(2)\text{--}\text{O}(6) = 2.045$; $\text{Fe}(2)\text{--}\text{O}(7) = 1.976$; $\text{Fe}(2)\text{--}\text{O}(9) = 2.048$; $\text{Fe}(2)\text{--}\text{O}(15) = 2.137$; $\text{Ag}(1)\text{--}\text{O}(6) = 2.261$; $\text{Ag}(1)\text{--}\text{O}(5) = 2.420$; $\text{Ag}(1)\text{--}\text{C}(60) = 2.344$; $\text{Ag}(1)\text{--}\text{C}(61) = 2.588$; $\text{O}(1)\text{--}\text{Fe}(1)\text{--}\text{N}(1) = 88.5$; $\text{O}(2)\text{--}\text{Fe}(2)\text{--}\text{N}(2) = 88.8$; $\text{Fe}(1)\text{--}\text{O}(6)\text{--}\text{Fe}(2) = 94.7$; $\text{Fe}(1)\text{--}\text{O}(7)\text{--}\text{Fe}(2) = 98.6$; $\text{O}(5)\text{--}\text{Ag}(1)\text{--}\text{O}(6) = 109.1$; $\text{O}(5)\text{--}\text{Ag}(1)\text{--}\text{C}(60) = 100.4$; $\text{O}(6)\text{--}\text{Ag}(1)\text{--}\text{C}(61) = 117.7$.

To provide further evidence for this assignment, the Mössbauer spectrum of a frozen solution of **3** in tetrahydrofuran was recorded at 80 K (Table 3.2). The data could be satisfactorily fit to a single quadrupole doublet, with $\delta = 0.49(2)$ mm/s and $\Delta E_Q = 1.38(2)$ mm/s, parameters typical of iron(III) complexes having mixed oxygen and nitrogen donor groups. The single quadrupole doublet in the Mössbauer spectrum is consistent with the X-ray crystal structure of **3**, which has two chemically equivalent iron centers.

Because chemical oxidation of **2** using AgClO_4 led to metal binding by the perchlorate anion, the oxidation was repeated using the silver salt of a less coordinating anion, AgSbF_6 .

Reaction of **2** with 1 equiv of AgSbF₆ in dichloromethane yielded a heterogeneous dark brown solution formed over the course of ~1 h. After removal of a black solid, the UV-vis spectrum of the filtrate revealed bands at 300, 374, and 605 nm (Figure 3.9B), suggesting formation of a new species. Single crystals of the product were grown by slow diffusion of diethyl ether into an acetonitrile solution containing the material. X-ray diffraction studies revealed a tetranuclear complex, [Fe₄(μ-X)₄(μ-Y)₂(PIM)₂(Ar^{Tol}CO₂)₂], where the identity of atoms X and Y is probably F⁻. We have not been able to fully solve this structure owing to unresolved disorder in the crystal. Based on its optical spectrum, however, we can rule out [Fe₄(μ-OH)₆(PIM)₂(Ar^{Tol}CO₂)₂] (**8**) as a possible product (*vide infra*).

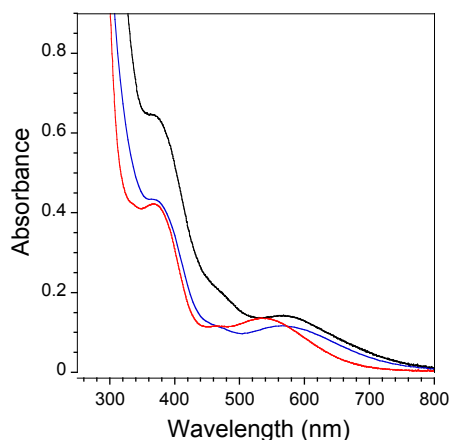


Figure 3.11. Absorption spectra of **1** + O₂ (black, λ_{max} = ~370, 570 nm), **4** (blue, λ_{max} = ~370, 570 nm), and **5** (red, λ_{max} = ~370, 540 nm) in dichloromethane.

Reactivity with O₂. To determine whether **1** and **2** exhibit the same functional activity as the BMM proteins,⁵⁴ their reactivity with dioxygen was investigated. Exposure of a dichloromethane solution of **1** to dioxygen at RT led to an instantaneous color change and the appearance of new optical bands at 370 and 570 nm (Figure 3.11, black trace). Facile reactivity of **1** with O₂ was confirmed by NMR spectroscopy. Injecting O₂ into a septum-sealed NMR tube containing **1** in dichloromethane-*d*₂ afforded the ¹H NMR spectrum shown in Figure 3.12A. The

numerous proton resonances in the spectrum, ranging from approximately 80 to -15 ppm, suggest the presence of multiple species in the reaction mixture.

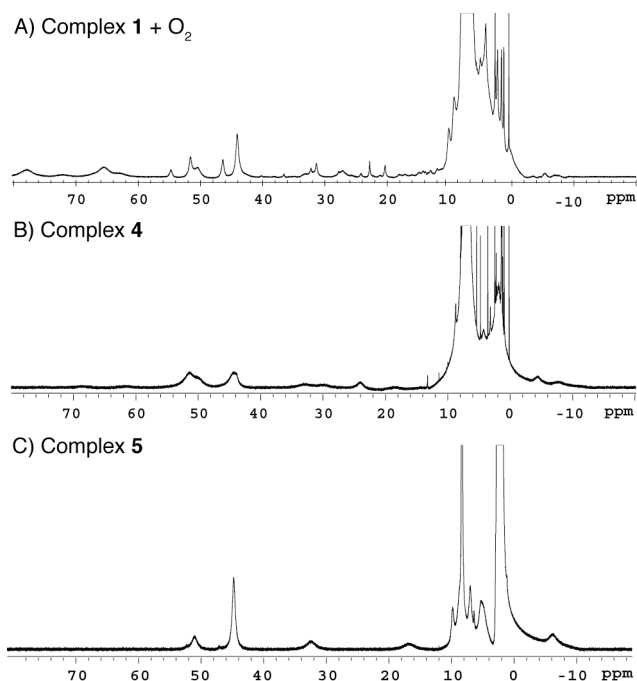


Figure 3.12. ^1H NMR spectra (500 MHz) of A) $[\text{Fe}_2(\text{PIM})(\text{Ph}_3\text{CCO}_2)_2]$ (**1**) + O_2 ; B) $[\text{Fe}_2(\mu\text{-OH})(\text{PIM})(\text{Ph}_3\text{CCO}_2)_3]$ (**4**); and C) $[\text{Fe}_4(\mu\text{-OH})_6(\text{PIM})(\text{Ph}_3\text{CCO}_2)_2]$ (**5**). Comparison of spectrum A to that of B and C reveals that reaction of **1** with O_2 leads to formation of **4** and **5**, in addition to at least one other product. All spectra were recorded at room temperature with diiron complex concentrations of ~ 5 mM. All spectra were acquired in CDCl_3 . Relative peak heights are *not* normalized between spectra. Panel A: δ (selected peaks) = 77.39, 65.13, 54.24, 51.17, 50.39, 45.94, 43.64, 31.77, 30.88, 26.75, 22.33, 19.89 ppm. Panel B: δ (selected peaks) = 51.28, 44.24, 33.02, 29.70, 23.90 ppm. Panel C: δ (selected peaks) = 49.97, 43.69, 31.20, 15.80 ppm.

To characterize the reaction product(s), single crystals of the material were grown by slow diffusion of pentane into a benzene solution containing the dark red-brown solid. After several days, a mixture of dark brown rectangular blocks and dark brown hexagonal prisms were obtained in addition to an amorphous solid. X-ray diffraction analysis of the rectangular-shaped crystals showed that the compound has a (μ -hydroxo)diiron(III) core and the molecular formula $[\text{Fe}_2(\mu\text{-OH})(\text{PIM})(\text{Ph}_3\text{CCO}_2)_3]$ (**4**, Figure 3.13, Table 3.4). The distorted-octahedral iron centers

are separated by 3.49 Å, with Fe(1)–O(6) and Fe(2)–O(6) bond lengths of 1.95 and 1.97 Å, respectively. The hydrogen atom on O(6), the bridging hydroxide ion, was located from a difference Fourier map. The diiron core is supported by the PIM²⁻ ligand, with average Fe–O(phenoxyl) and Fe–N(imine) distances of 1.31 and 2.12 Å, respectively, and three triphenylacetate groups. Two of the carboxylates coordinate to the iron atoms in a terminal bidentate mode, giving average Fe–O distances of 2.11 Å, and the remaining carboxylate bridges the diiron core, with an average Fe–O distance of 2.02 Å.

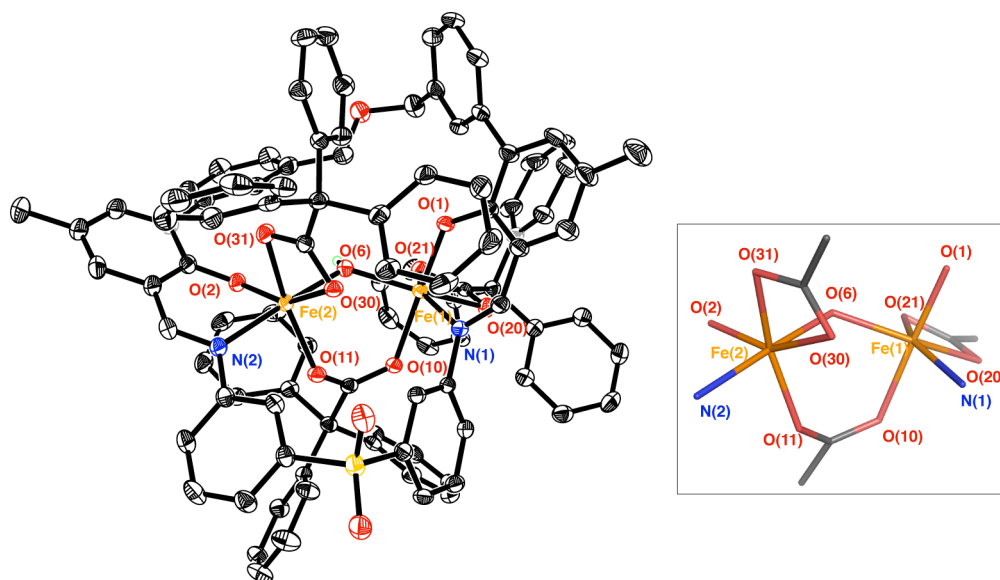


Figure 3.13. Ortep thermal ellipsoid (50%) diagram of the X-ray crystal structure of $[\text{Fe}_2(\mu\text{-OH})(\text{PIM})(\text{Ph}_3\text{CCO}_2)_3]$ (**4**, left). An isolated view of the diiron core is shown as a stick figure representation on the right. Solvent molecules and hydrogen atoms are omitted for clarity. Color scheme: iron, orange; carbon, gray; nitrogen, blue; oxygen, red; sulfur, yellow. Selected bond distances (Å) and angles (Deg): Fe(1)–Fe(2) = 3.487; Fe(1)–O(1) = 1.890; Fe(1)–N(1) = 2.115; Fe(1)–O(6) = 1.952; Fe(1)–O(10) = 2.063; Fe(1)–O(20) = 2.075; Fe(1)–O(21) = 2.132; Fe(2)–O(2) = 1.872; Fe(2)–N(2) = 2.136; Fe(2)–O(6) = 1.969; Fe(2)–O(11) = 1.979; Fe(2)–O(30) = 2.141; Fe(2)–O(31) = 2.093; O(1)–Fe(1)–N(1) = 87.4; O(2)–Fe(2)–N(2) = 87.5; Fe(1)–O(6)–Fe(2) = 125.6; O(6)–Fe(1)–O(10) = 88.3; O(6)–Fe(2)–O(11) = 88.9.

X-ray diffraction studies of the hexagonal prisms, isolated from the $1/\text{O}_2$ reaction mixture, revealed a tetranuclear $[\text{Fe}_4(\mu\text{-OH})_6(\text{PIM})_2(\text{Ph}_3\text{CCO}_2)_2]$ complex (**5**), in which two di(μ -hydroxo)(μ -triphenylacetato)diiron(III) units are linked by two bridging hydroxide ions (Figure

3.14, Table 3.4). The tetrairon(III) unit is located on a crystallographic inversion center. The diiron subunit bound by the PIM²⁻ ligand has an Fe–Fe distance of 3.06 Å and is bridged by two hydroxide ligands (Fe–O_{ave} = 2.02 Å). The separation of iron atoms between two Fe₂ macrocyclic monomers is 3.78 Å, and the linkages involve only one hydroxo bridge (Fe–O_{ave} = 1.98 Å). The average Fe–O(phenoxyl) and Fe–N(imine) bond lengths were observed at approx. 1.91 and 2.20 Å, respectively. Finally, two bridging carboxylate groups (Fe–O_{ave} = 2.06 Å) cap the tetranuclear cluster at opposite ends.

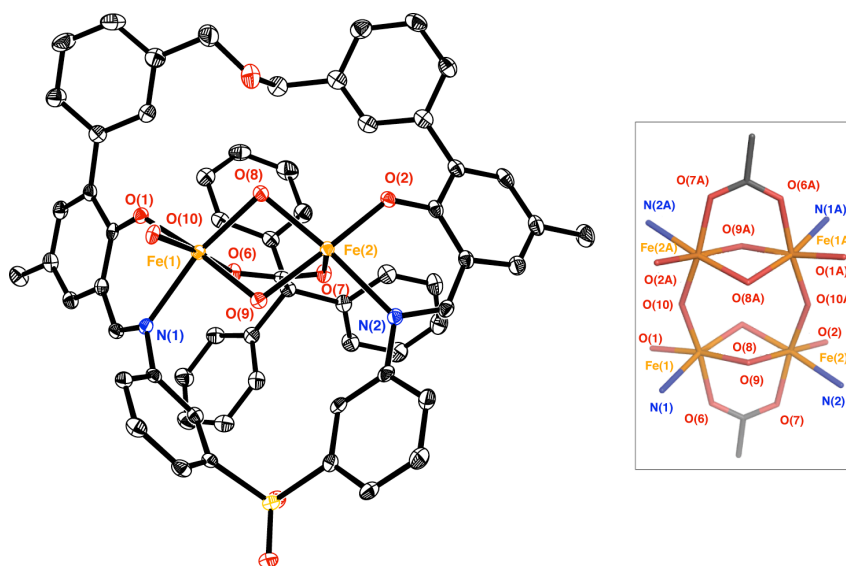


Figure 3.14. Ortep thermal ellipsoid (50%) diagram of the asymmetric unit of the X-ray crystal structure of $[\text{Fe}_4(\mu\text{-OH})_6(\text{PIM})(\text{Ph}_3\text{CCO}_2)_2]$ (**5**, left). The center of the complex is located on a crystallographic inversion center. An isolated view of the tetrairon core is depicted as a stick figure representation on the right. Solvent molecules and hydrogen atoms are omitted for clarity. Color scheme: iron, orange; carbon, gray; nitrogen, blue; oxygen, red; sulfur, yellow. Selected bond distances (Å) and angles (Deg): Fe(1)–Fe(2) = 3.056; Fe(1)–Fe(2A) = 3.780; Fe(1)–O(1) = 1.911; Fe(1)–N(1) = 2.172; Fe(1)–O(6) = 2.042; Fe(1)–O(8) = 2.030; Fe(1)–O(9) = 1.997; Fe(1)–O(10) = 1.978; Fe(2)–O(2) = 1.910; Fe(2)–N(2) = 2.229; Fe(2)–O(7) = 2.072; Fe(2)–O(8) = 2.028; Fe(2)–O(9) = 2.011; N(1)–Fe(1)–O(1) = 83.4; N(2)–Fe(2)–O(2) = 85.4; Fe(1)–O(8)–Fe(2) = 97.7; Fe(1)–O(9)–Fe(2) = 99.4; Fe(1)–O(10)–Fe(2A) = 146.6.

Table 3.4. X-ray Data Collection and Refinement Parameters for 4-7.

	4	5	6/7
Empirical formula	[Fe ₂ N ₂ O ₁₂ SC ₁₀₂ H ₇₈] (C ₆ H ₆) ₃	[Fe ₄ N ₄ O ₂₀ S ₂ C ₁₂₄ H ₁₀₀] (C ₆ H ₆) ₈	[Fe ₂ N ₂ O _{10.24} SC ₈₄ H ₆₃] (CH ₃ CN) ₃
Formula weight	1901.75	2878.46	1531.15
Temperature (K)	100	100	100
Wavelength (Å)	0.71073	0.71073	0.71073
Crystal system	Monoclinic	Triclinic	Orthorhombic
Space group	P2 ₁ /n	P $\bar{1}$	Pbca
Unit cell dimensions	a = 15.2273(15) Å b = 16.6307(16) Å c = 37.426(4) Å β = 92.975(2)°	a = 14.2464(8) Å b = 15.8784(9) Å c = 19.3834(11) Å α = 66.3850(10)° β = 69.7520(10)° γ = 64.3010(10)°	a = 12.2687(10) Å b = 25.927(2) Å c = 48.485(4) Å
Volume (Å ³)	9464.9(16)	3540.4(3)	15423(2)
Z	4	1	8
Calculated density (g/mm ³)	1.335	1.350	1.319
Absorption coefficient (mm ⁻¹)	0.396	0.503	0.468
F(000)	3976	1504	6375
Crystal size (mm ³)	0.40 x 0.35 x 0.21	0.14 x 0.08 x 0.07	0.19 x 0.16 x 0.10
Θ range for data collection	1.47 to 26.43°	1.17 to 25.03°	1.57 to 24.71°
Index ranges	-19 ≤ h ≤ 19 -20 ≤ k ≤ 20 -46 ≤ l ≤ 46	-16 ≤ h ≤ 16 -18 ≤ k ≤ 18 -22 ≤ l ≤ 23	-14 ≤ h ≤ 14 -30 ≤ k ≤ 30 -57 ≤ l ≤ 57
Reflections collected	133480	50303	227221
Independent reflections	19402 [R(int) = 0.0677]	12460 [R(int) = 0.0677]	13160 [R(int) = 0.1197]
Completeness to Θ (%)	99.7	99.8	100.0
Absorption correction	Empirical	Empirical	Empirical
Max. and min. transmission	0.9214 and 0.8575	0.9656 and 0.9329	0.9547 and 0.9163
Data / restraints / parameters	19402/0/1240	12460/49/922	13160/82/998
Goodness-of-fit on F ²	1.040	1.084	1.154
Final R indices [I>2σ(I)]	R1 = 0.0472 wR2 = 0.1245	R1 = 0.0468 wR2 = 0.1033	R1 = 0.0969 wR2 = 0.2015
R indices (all data)	R1 = 0.0609 wR2 = 0.1334	R1 = 0.0718 wR2 = 0.1131	R1 = 0.1218 wR2 = 0.2135
Largest diff. peak and hole (eÅ ⁻³)	1.287 and -0.559	1.034 and -0.646	1.516 and -1.390

* R1 = $\sum ||F_o| - |F_c|| / \sum |F_o|$; wR2 = $[\sum [w(F_o^2 - F_c^2)^2] / \sum [w(F_o^2)^2]]^{1/2}$; GOF = $[\sum [w(F_o^2 - F_c^2)^2] / (n-p)]^{1/2}$, where n is the number of reflections and p is the total number of parameters refined.

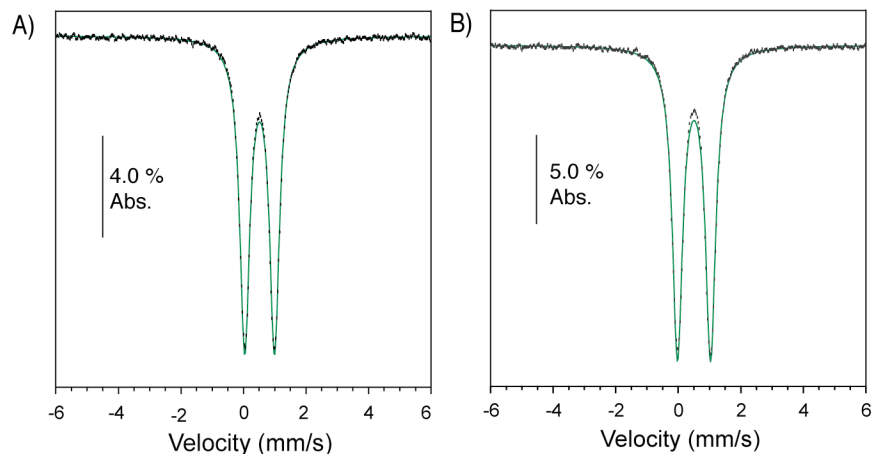


Figure 3.15. Zero-field Mössbauer spectrum (80 K) of polycrystalline samples of $[\text{}^{57}\text{Fe}_2(\text{OH})(\text{PIM})(\text{Ph}_3\text{CCO}_2)_3]$ (**4**, left) and $[\text{}^{57}\text{Fe}_4(\text{OH})_6(\text{PIM})_2(\text{Ph}_3\text{CCO}_2)_2]$ (**5**, right). Spectrum A gave Mössbauer parameters $\delta = 0.52(2)$ mm/s, $\Delta E_Q = 0.95(2)$ mm/s, and $\Gamma = 0.38(2)$ mm/s, whereas spectrum B returned Mössbauer parameters $\delta = 0.51(2)$ mm/s, $\Delta E_Q = 1.06(2)$ mm/s, and $\Gamma = 0.40(2)$ mm/s. Raw data are shown in black and the spectral fits are shown in green.

Analytically pure samples of **4** and **5** were prepared for spectroscopic characterization. The dinuclear compound **4** was synthesized by combining triphenylacetic acid, triethylamine, and **1** in benzene, followed by exposure to dioxygen. Vapor diffusion of pentane into the benzene reaction solution over the course of ~ 24 h afforded dark brown crystals. X-ray diffraction analysis of these crystals confirmed the desired (μ -hydroxo)diiron(III) species **4**. The UV-visible spectrum of **4** exhibits absorption bands at 370 and 570 nm (Figure 3.11, blue trace). The higher energy band is most likely a ligand π - π^* transition, whereas the visible band is most likely a hydroxo-to-iron(III) charge transfer.⁴⁸ The ^1H NMR spectrum of **4** was recorded in chloroform- d_1 (Figure 3.12B). As expected for a paramagnetic compound, the spectrum shows several broad resonances, ranging from approximately 70 to -10 ppm. Assignment of the metal oxidation states in **4** as iron(III) is supported by zero-field Mössbauer spectroscopic measurements. Polycrystalline ^{57}Fe -enriched **4** displays a single quadrupole doublet in the Mössbauer spectrum, with parameters $\delta = 0.52(2)$ mm/s and $\Delta E_Q = 0.95(2)$ mm/s (Figure 3.15A,

Table 3.2). Although the two iron atoms in **4** are not chemically equivalent, similarities in their coordination geometry and donor groups make them indistinguishable by zero-field Mössbauer spectroscopy.

The tetrairon(III) complex **5** was also fully characterized. The compound was isolated as brown crystals by slow evaporation of a benzene solution containing **1** and dioxygen under ambient conditions. To ensure that the bulk product did not contain **4**, several representative crystals were analyzed by X-ray crystallography. In all cases, tetranuclear **5** was obtained. The absorption spectrum has peaks with λ_{max} at 370 and 540 nm (Figure 3.11, red trace). The visible band, which is blue-shifted by approximately 30 nm from the 570 nm absorption feature in **4**, is most likely a ligand-to-metal transition involving the diiron-hydroxo unit.⁴⁸ The ¹H NMR spectrum of **5** in chloroform-*d*₁ exhibits paramagnetically broadened peaks at ~50, 44, 32, 26, and -8 ppm (Figure 3.12C). The simpler ¹H NMR spectrum of **5**, compared to that of **4**, is consistent with its higher molecular symmetry (pseudo C_{2h} for **5** versus C₁ for **4**). The zero-field Mössbauer spectrum of ⁵⁷Fe-enriched **5** was fit with parameters that are distinct from those of **4**, giving $\delta = 0.51(2)$ mm/s and $\Delta E_Q = 1.06(2)$ mm/s (Figure 3.15B, Table 3.2). Because the four iron sites in **5** are chemically equivalent, a single quadrupole doublet is observed in the Mössbauer spectrum, consistent with its X-ray structure.

Comparison of the ¹H NMR spectrum of **1**/O₂ (Figure 3.12A) with those of **4** (Figure 3.12B) and **5** (Figure 3.12C) reveals that not all of the peaks are accounted for, particularly a broad resonance at ~76 ppm and other sharper features between 10 to 40 ppm. To evaluate the number of iron-containing species generated upon reaction of **1** with dioxygen, the crude **1**/O₂ solid was examined by Mössbauer spectroscopy (Figure 3.16). The Mössbauer data display three overlapping quadrupole doublets, with the following characteristics: $\delta_1 = 0.50(2)$ mm/s, $\Delta E_{Q1} =$

0.78(2) mm/s, Area 1 = 24%; $\delta_2 = 0.51(2)$ mm/s, $\Delta E_{Q2} = 1.12(2)$ mm/s, Area 2 = 37%; $\delta_3 = 0.52(2)$ mm/s, $\Delta E_{Q3} = 1.59(2)$ mm/s, Area 3 = 39%. The three sites have nearly identical isomer shift values, but differ in their quadrupole splitting parameters. Based on their similarities to the Mössbauer parameters of the crystallographically characterized species, sites 1 and 2 are ascribed to compounds **4** and **5**, respectively. The nature of the third site, which comprises about 39% of total iron in the **1**/O₂ sample, has not yet been identified.

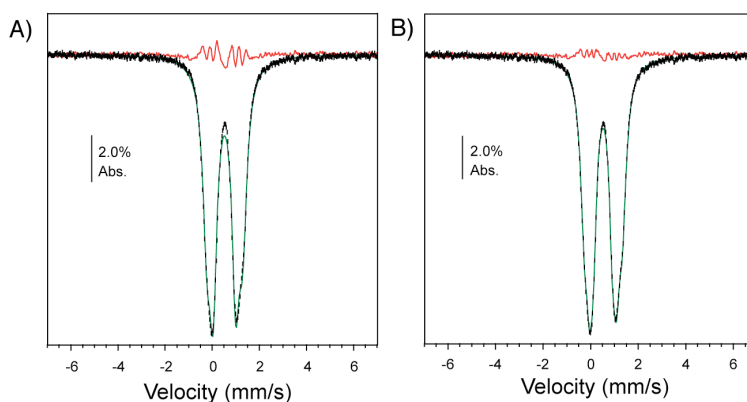


Figure 3.16. Zero-field Mössbauer spectrum (80K) of a frozen benzene-*d*₆ solution of [⁵⁷Fe₂(PIM)(Ph₃CCO₂)₂] (⁵⁷Fe-**1**)/O₂ (black lines). The ¹H NMR spectrum of this sample is shown in Figure 3.12A. Spectral simulations are represented in green and fit residuals in red. Both plots show the same data, but are overlaid with different spectral fits for comparing their overall goodness of fit. Spectrum A was fit to a two-site model, with $\delta_1 = 0.50(2)$ mm/s, $\Delta E_{Q1} = 0.95(2)$ mm/s, $\Gamma_1 = 0.39(2)$ mm/s, Area 1 = 54%, $\delta_2 = 0.52(2)$ mm/s, $\Delta E_{Q2} = 1.52(2)$ mm/s, $\Gamma_2 = 0.44(2)$ mm/s, and Area 2 = 46%. Spectrum B was fit to a three-site model, with $\delta_1 = 0.50(2)$ mm/s, $\Delta E_{Q1} = 0.78(2)$ mm/s, $\Gamma_1 = 0.30(2)$ mm/s, Area 1 = 24%, $\delta_2 = 0.51(2)$ mm/s, $\Delta E_{Q2} = 1.12(2)$ mm/s, $\Gamma_2 = 0.34(2)$ mm/s, Area 2 = 37%, $\delta_3 = 0.52(2)$ mm/s, $\Delta E_{Q3} = 1.59(2)$ mm/s, $\Gamma_3 = 0.41(2)$ mm/s, and Area 3 = 39%. Comparing the fit residuals between A and B clearly demonstrate that the three-site model in B is a better representation of the data.

The dioxygen reactivity of the diiron(II) compound **2**, which contains sterically demanding terphenylcarboxylates rather than triphenylacetates, was also examined. Exposing a dichloromethane solution of **2** to O₂ led to an immediate color change from bright red to dark brown. The absorption spectrum of dioxygen-treated **2** has features at approximately 380, 473, and 600 nm (Figure 3.17, blue trace). The ¹H NMR spectrum revealed new resonances between

26 and -8 ppm (Figure 3.18). Unlike the ^1H NMR spectrum of **1**/ O_2 (Figure 3.12A), which shows multiple chemical species in solution, the data suggest that reaction of **2** with O_2 forms fewer products.

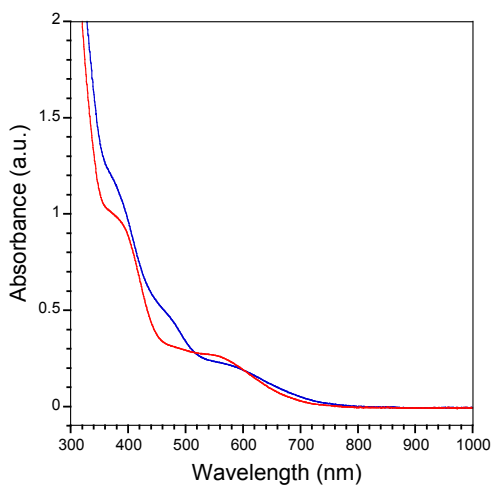


Figure 3.17. Absorption spectra of complex **2** + O_2 (blue, $\lambda_{\text{max}} = 380, 473, 600$ nm) and complex **2** + $\text{O}_2/\text{H}_2\text{O}$ (red, $\lambda_{\text{max}} = 380, 473, 600$ nm) in dichloromethane. The blue spectrum arises from a mixture of $[\text{Fe}_2(\mu\text{-O})(\text{PIM})(\text{Ar}^{\text{Tol}}\text{CO}_2)_2]$ (**6**) and $[\text{Fe}_2(\mu\text{-OH})_2(\text{PIM})(\text{Ar}^{\text{Tol}}\text{CO}_2)_2]$ (**7**) species. The red spectrum is assigned to a tetranuclear $[\text{Fe}_4(\mu\text{-OH})_6(\text{PIM})_2(\text{Ar}^{\text{Tol}}\text{CO}_2)_2]$ (**8**) complex.

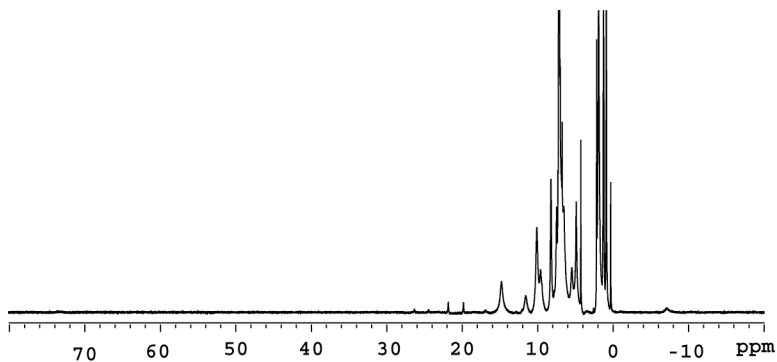


Figure 3.18. ^1H NMR spectrum (CD_2Cl_2 , 500 MHz) of $[\text{Fe}_2(\text{PIM})(\text{Ar}^{\text{Tol}}\text{CO}_2)_2]$ (**2**) after exposure to dioxygen. The spectrum was recorded at room temperature at a diiron complex concentration of ~ 5.0 mM.

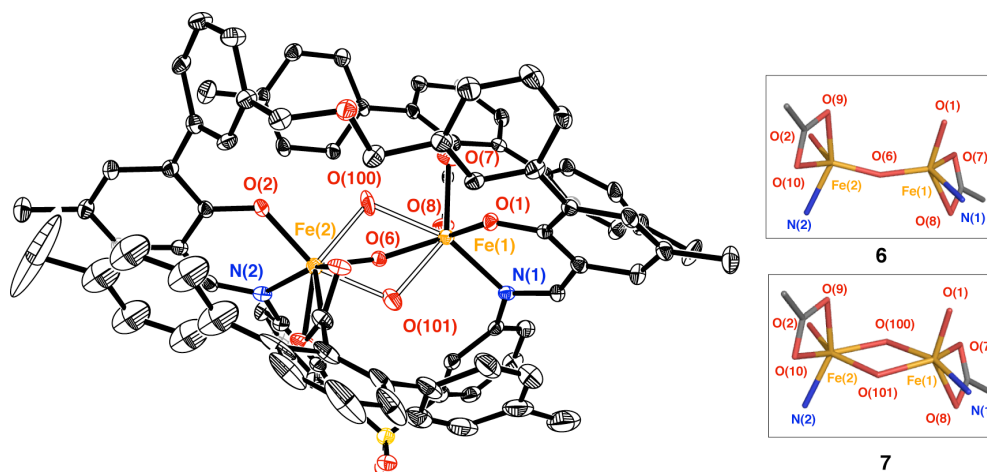


Figure 3.19. Ortep thermal ellipsoid (35%) diagram of the X-ray crystal structure of $[\text{Fe}_2(\mu\text{-O})(\text{PIM})(\text{Ar}^{\text{Tol}}\text{CO}_2)_2]$ (**6**) and $[\text{Fe}_2(\mu\text{-OH})_2(\text{PIM})(\text{Ar}^{\text{Tol}}\text{CO}_2)_2]$ (**7**) on the left. The two complexes occur in a single crystal and differ only in their $(\mu\text{-oxo})$ diiron(III) and di $(\mu\text{-hydroxo})$ diiron(III) cores, respectively. Stick figure representations of the diiron core of **6** and **7** are shown on the right. The ratio of **6**:**7** was determined to be 76:24. Solvent molecules and hydrogen atoms are omitted for clarity. Color scheme: iron, orange; carbon, gray; nitrogen, blue; oxygen, red; sulfur, yellow. Selected bond distances (Å) and angles (Deg): Fe(1)–Fe(2) = 3.436; Fe(1)–O(1) = 1.880; Fe(1)–N(1) = 2.103; Fe(1)–O(6) = 1.744; Fe(1)–O(7) = 2.084; Fe(1)–O(8) = 2.133; Fe(1)–O(100) = 2.110; Fe(1)–O(101) = 2.090; Fe(2)–O(2) = 1.898; Fe(2)–N(2) = 2.125; Fe(2)–O(6) = 1.753; Fe(2)–O(9) = 2.113; Fe(2)–O(10) = 2.092; Fe(2)–O(100) = 2.103; Fe(2)–O(101) = 2.090; O(1)–Fe(1)–N(1) = 87.2; O(2)–Fe(2)–N(2) = 88.00; Fe(1)–O(6)–Fe(2) = 158.6; Fe(1)–O(100)–Fe(2) = 109.1; Fe(1)–O(101)–Fe(2) = 110.8.

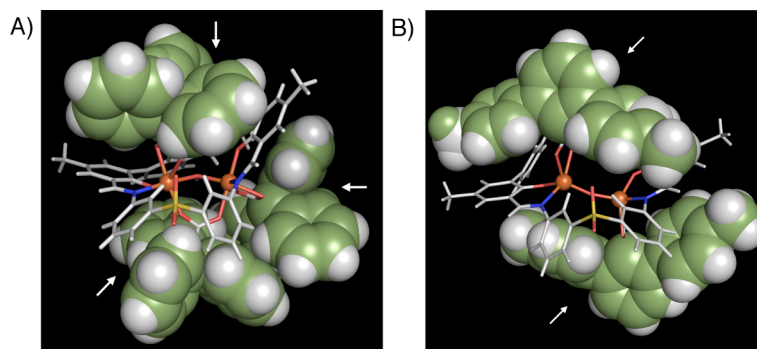


Figure 3.20. Hybrid stick and space-filling diagrams of $[\text{Fe}_2(\mu\text{-OH})(\text{PIM})(\text{Ph}_3\text{CCO}_2)_3]$ (**4**, A) and $[\text{Fe}_2(\mu\text{-O})(\text{PIM})(\text{Ar}^{\text{Tol}}\text{CO}_2)_2]$ (**6**, B). The aromatic rings of the carboxylate ligands are represented as spheres (carbon = green, hydrogen = white) to emphasize their shape and volume. The location of the carboxylate unit, either $\text{Ph}_3\text{CCO}_2^-$ or $\text{Ar}^{\text{Tol}}\text{CO}_2^-$, is indicated by a white arrow. The PIM^{2-} framework is displayed in stick form (carbon/hydrogen, gray; nitrogen, blue; oxygen, red; sulfur, yellow) with the iron atoms shown as orange spheres.

To determine the composition of the **2**/O₂ product, preparative-scale reactions were performed to obtain sufficient material for characterization. Single crystals of oxygenated **2** were grown by slow diffusion of diethyl ether into a solution of the complex in acetonitrile. An X-ray structural investigation revealed that each single crystal contains a mixture of two species, a (μ -oxo)diiron(III) [Fe₂(μ -O)(PIM)(Ar^{Tol}CO₂)₂] (**6**) compound and a di(μ -hydroxo)diiron(III) [Fe₂(OH)₂(PIM)(Ar^{Tol}CO₂)₂] (**7**) compound (Figure 3.19, Table 3.4). This result was verified by analyzing several crystals independently prepared by the same method. The structures of **6** and **7** are identical except for the nature of their bridging oxygen atoms, which was modeled with positional disorder and partial occupancies assigned to atoms O(6) [in **6**] and O(100)/O(101) [in **7**]. Data refinement converged with **6** having an occupancy of 76% and **7** of 24%. The iron atoms in both structures are separated by 3.44 Å. Complex **6** is designated as a (μ -oxo)diiron(III) species because of its short Fe(1)–O(6) and Fe(2)–O(6) distances of 1.74 and 1.75 Å, respectively.⁴⁸ In contrast, **7** is a di(μ -hydroxo)diiron(III) complex with the longer Fe–O(100) and Fe–O(101) bond length of 2.10 Å (averaged), more typical of a dinuclear structure with bridging hydroxide ligands. The iron atoms of **6** and **7** are coordinated by the PIM²⁻ ligand, with average Fe–O(phenoxy) distances of 1.89 Å and average Fe–N(imine) distances of 2.11 Å. Furthermore, each iron site contains a terminal terphenylcarboxylate (Fe–O_{ave} = 2.11 Å). The iron atoms in **6** and **7** have bond valence sums of 3.0 and 2.8, respectively (Table 3.3), indicating that the iron centers are in the +3 oxidation state. Although three triphenylacetate ligands are accommodated by the PIM²⁻ platform in **4** (Figure 3.20A), only two terphenylcarboxylates could occupy the same space in **6** (Figure 3.20B). These observations underscore the importance of considering both shape and size when selecting an appropriate carboxylate for synthetic

modeling studies; a fan-shaped terphenylcarboxylate is preferable over the cone-shaped triphenylacetate for producing dinuclear oxygenated products using the PIM²⁻ ligand framework.

The presence of both (μ -oxo)diiron(III) and di(μ -hydroxo)diiron(III) species in the reaction product of **2** with dioxygen was further supported by zero-field Mössbauer measurements. Polycrystalline **2**/O₂ gave a Mössbauer spectrum that was best fit to two quadrupole doublets, $\delta_1 = 0.47(2)$ mm/s, $\Delta E_{Q1} = 1.52(2)$ mm/s, $\delta_2 = 0.50(2)$ mm/s, and $\Delta E_{Q2} = 0.97(2)$ mm/s. Sites 1 and 2 were refined with areas of 21% and 79%, respectively. Because (μ -oxo)diiron(III) species typically have larger ΔE_Q values (>1.0 mm/s) than (μ -hydroxo)diiron(III) complexes (<1.0 mm/s), site 1 is attributed to complex **6** and site 2 to complex **7**. When the **2**/O₂ solid reaction product was further dried under vacuum at 150 °C for 24 h, Mössbauer measurements yielded a **6**:**7** ratio of 85:15 (Table 3.2), which is similar to the **6**:**7** ratio of 76:24 determined by X-ray crystallography (Figure 3.19), suggesting that **6** can be obtained from **7** by extrusion of H₂O. To examine the **6**:**7** ratio in solution, an ⁵⁷Fe-enriched sample of the **2**/O₂ solid dissolved in tetrahydrofuran was studied by Mössbauer spectroscopy at 80 K, yielding the following parameters: $\delta_1 = 0.51(2)$ mm/s, $\Delta E_{Q1} = 1.24(2)$ mm/s, $\delta_2 = 0.49(2)$ mm/s, and $\Delta E_{Q2} = 0.78(2)$ mm/s, with sites 1 and 2 having occupancies of 61% and 36%, respectively (Figure 3.21B). Because site 1 has a larger ΔE_Q value than site 2, the ratio for **6**:**7** in tetrahydrofuran is 61:36. The varying percentages of **6** and **7**, as determined from X-ray crystallographic and Mössbauer spectroscopic measurements, are probably due to the different amounts of H₂O present in each **2**/O₂ sample. Regardless, these Mössbauer results unequivocally show that both **6** and **7** are produced in the reaction of **2** with dioxygen. So far we have been unable to isolate complexes **6** and **7** in pure form.

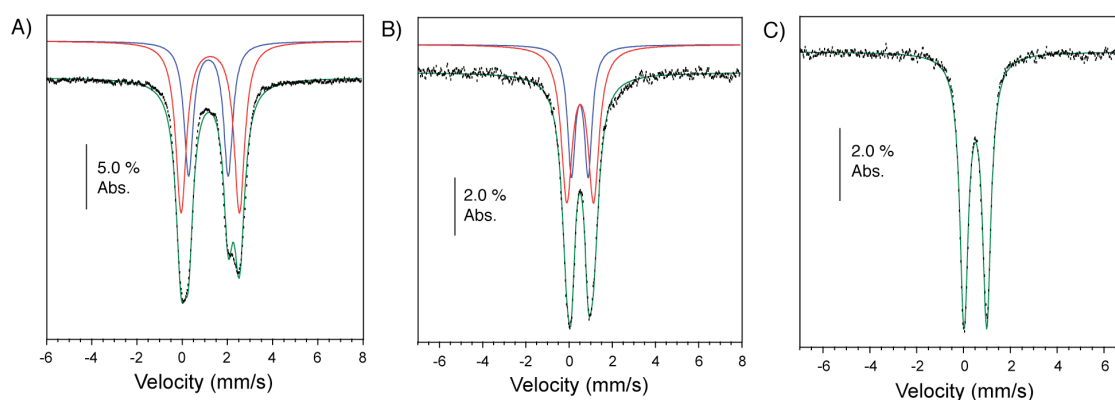


Figure 3.21. Zero field Mössbauer spectra (80 K) of a 22 mM $[\text{}^{57}\text{Fe}_2(\text{PIM})(\text{Ar}^{\text{Tol}}\text{CO}_2)_2]$ (**2**) solution in tetrahydrofuran (A) that was frozen after exposure to dioxygen (B) or dioxygen/water (C). Spectrum A was best fit to a two-site model, which is consistent with the two different iron environments in **2**. The spectrum in B is assigned to two diiron species **6** and **7**, whereas the spectrum in C is assigned to a tetranuclear complex **8** containing equivalent iron sites. See Table 3.2 for solution Mössbauer parameters for species **2**, **6/7**, and **8**. Raw data are represented in black; spectral fits are shown in green, with unique iron sites displayed as either red or blue lines.

Because **7** differs from **6** by a single water molecule, we explored whether addition of H_2O could convert the (μ -oxo)diiron(III) species **6** to the di(μ -hydroxo)diiron(III) complex **7**. When a **6/7** mixture was treated with 10 μL of H_2O , ~ 15 equiv relative to the diiron complexes, in dichloromethane, the brown solution instantly turned pale red. New optical bands at 360 and 550 nm were observed (Figure 3.17, red trace), which are reminiscent of those displayed by the tetrairon complex $[\text{Fe}_4(\mu\text{-OH})_6(\text{PIM})_2(\text{Ph}_3\text{CCO}_2)_2]$ (**5**, Figure 3.11, red trace). To obtain further spectroscopic characterization, a sample containing ^{57}Fe -enriched **6/7** and 15 equiv of H_2O in tetrahydrofuran was studied by Mössbauer spectroscopy at 80 K (Figure 3.21C). The spectrum was fit to a single quadrupole doublet, with $\delta = 0.49(2)$ mm/s and $\Delta E_Q = 0.97(2)$ mm/s. These parameters are nearly identical to those obtained for **5** (Table 3.2). Although we are unable to crystallize this material, the spectroscopic data suggest that the compound has the molecular formula $[\text{Fe}_4(\mu\text{-OH})_6(\text{PIM})_2(\text{Ar}^{\text{Tol}}\text{CO}_2)_2]$ (**8**).

3.4. Discussion

Macrocyclic Ligands for Constructing Biomimetic Carboxylate-Bridged Diiron Models. To obtain more accurate structural mimics of carboxylate-bridged diiron protein active sites,⁵ we designed and synthesized dinucleating ligands that enforce the syn stereochemistry of nitrogen donor atoms. Early work with 1,2-bis(3-ethynyl-8-carboxylatequinoline)-4,5-diethylbenzene ethyl ester ($\text{Et}_2\text{BCQEB}^{\text{Et}}$) led to isolation of a tri(μ -carboxylato)(syn *N*-donor)diiron(II) species that resembles the BMM protein active sites,²⁴ but this compound produced an intractable mixture when exposed to dioxygen. Other syn *N*-donor variants primarily afforded bis(ligand)diiron complexes formed through interdigitation of two dinucleating ligands when complexed with iron(II).^{26,35} To prevent such interactions the H_2PIM ligand (Chart 3.1), was designed. By linking two phenoxyimine chelates covalently, H_2PIM still enforces syn arrangement of the nitrogen donors but has a more pre-organized conformation. This compound was synthesized by the procedure outlined in Scheme 3.2 and could be prepared in multi-gram quantities. The H_2PIM ligand is also amenable to electronic and geometric modifications by introduction of various substituents on the aromatic rings.

The H_2PIM macrocycle facilitated the preparation of new diiron(II) synthetic analogues of $\text{sMMOH}_{\text{red}}$ and related enzyme active sites.^{55,56} In the presence of sterically demanding carboxylic acids, treatment of H_2PIM with $[\text{Fe}_2(\text{Mes})_4]$ led to spontaneous self-assembly of di(μ -carboxylato)(PIM)diiron(II) species (Figure 3.22A). Compounds **1** and **2** reproduce several key features of the $\text{sMMOH}_{\text{red}}$ active site, including: the bridging μ - $\eta^1\eta^2$ and μ - $\eta^1\eta^1$ modes of carboxylates, syn stereochemistry of nitrogen donors, neutral charge of the complex, $S = 2$ spin state of the irons, and the stoichiometry of the ligands. The main differences are the substitution of carboxylate and imidazole groups with related donors. We used phenolate and imine moieties

because they provide both synthetic and functional advantages. Phenol is a versatile building block. A variety of substituents could be readily appended on the ring, allowing access to different molecular architectures. Although the phenolate anion (pK_a of phenol = $\sim 12-19$ in DMSO) is more basic than a carboxylate (pK_a of carboxylic acid = $\sim 9-13$ in DMSO),^{57,58} more electron-rich oxygen donors may stabilize iron in higher oxidation states, such as the diiron(IV) unit of intermediate Q.⁵⁹ Alternatively, the basicity of the phenolate groups could be lowered to match better the donor strength of glutamate and aspartate side chains by introducing electron-withdrawing substituents on the PIM^{2-} ligand. An additional advantage of the phenolate ligand is that its iron complexes display visible absorption bands that provide a spectroscopic handle for studying otherwise optically silent species. Finally, imine groups are valuable in the H_2PIM framework because they form through Schiff base condensation reactions that are efficient in producing large macrocyclic structures with syn nitrogen donors.^{60,61}

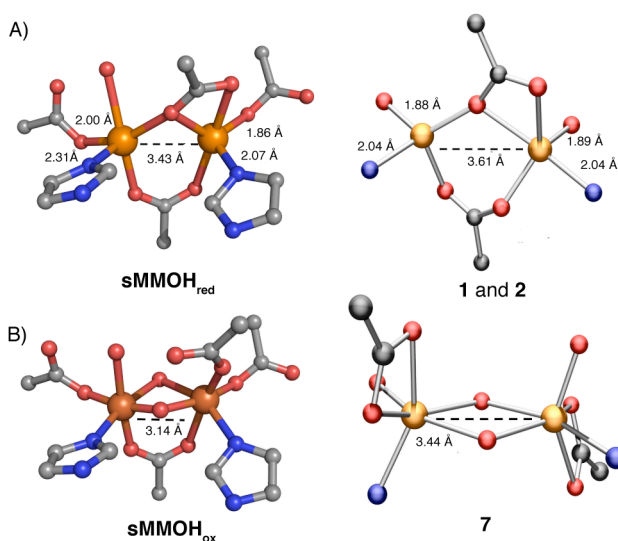
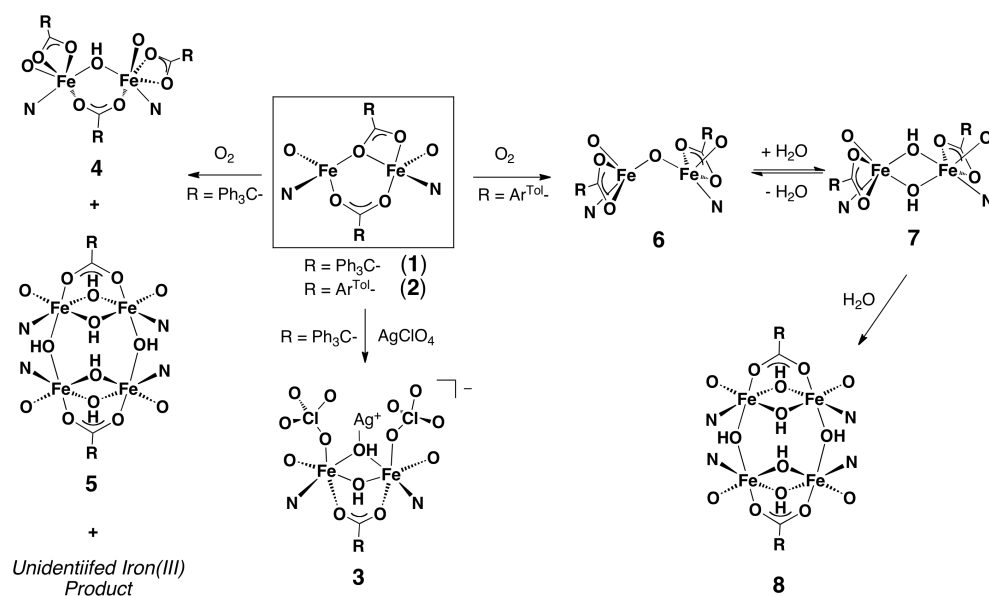


Figure 3.22. Depiction of the X-ray crystal structures of the diiron sites of sMMOH_{red} (top, left) and sMMOH_{ox} (bottom, left). For structural comparison, synthetic complexes that mimic each protein state are shown on its right. Some relevant bond lengths are provided; the distances shown for **1** and **2** are averaged over the two complexes. Color scheme: iron, orange; nitrogen, blue; oxygen, red; carbon, gray.

Reactivity of Diiron(II) Mimics and Their Biological Implications. Cyclic voltammograms of compounds **1** and **2** show quasi-reversible redox couples at +16 and +108 mV (vs. ferrocene/ferrocenium), respectively (Figure 3.8). These electrochemical events are assigned to diiron(II,II) to diiron(II,III) metal-centered oxidation processes. To investigate further the redox behavior of compound **2**, chemical oxidation with silver perchlorate was attempted. This reaction afforded an organometallic di(μ -hydroxo)(μ -carboxylato)diiron(III)silver(I) (**3**) species (Scheme 3.3). The bridging hydroxo ions are most likely derived from adventitious water in the reaction mixture. When oxidation of **2** was performed using silver hexafluoroantimonate, which contains the less-coordinating SbF_6^- anion compared to ClO_4^- , a tetrairon(III) cluster was isolated. Although the cyclic voltammograms of **1** and **2** suggest that reversible oxidation of these carboxylate-bridge diiron units might be possible, we were unable to isolate the one-electron oxidized forms using chemical methods. One difficulty is that the diiron PIM^{2-} compounds have a propensity to be bridged by small nucleophiles, such as the OH^- ligands in **3**, which were *not deliberately* introduced into the reaction mixture. We cannot determine at this time whether our inability to isolate the oxidized product of **1** or **2** is due to their inherent instability or to our experimental conditions. The structure of **3**, however, demonstrates two important features of our model system. Firstly, its di(μ -hydroxo)(μ -carboxylato)diiron(III) core indicates that our macrocyclic framework could support the unusual asymmetric resting state structure of the sMMOH_{ox} active site.¹⁸ Secondly, the oxophilic character of the diiron(II) complexes may facilitate rapid reaction with dioxygen.

A summary of the dioxygen reactivity of **1** and **2** is shown in Scheme 3.3. Exposure of **1** to O_2 generates (μ -hydroxo)diiron(III) (**4**) and hexa(μ -hydroxo)tetrairon(III) (**5**) complexes together with a third iron(III) product. Because an additional triphenylacetate ligand is required

to form **4** from **1** and O_2 , some of the remaining diiron(III) units might dimerize to generate **5**. Comparison of the spectroscopic data for analytically pure samples of **4** and **5** with those of the $1/O_2$ reaction product indicates that these compounds do not account for all of the species formed. A Mössbauer spectrum (Figure 3.16) shows that at least one additional iron(III) compound is present in the oxygenated product of **1**, the identity of which is currently unknown.



Scheme 3.3. Summary of reaction products characterized in this study. Full representation of the PIM^{2-} ligand is omitted for clarity; only its phenolate oxygen and imine nitrogen atoms are depicted. See Chart 3.1 for the structure of H_2PIM , the doubly protonated form of PIM^{2-} .

When **2** was treated with dioxygen, a mixture of dinuclear species was generated. X-ray crystallographic studies show that the products are close chemical relatives, (μ -oxo)diiron(III) (**6**) and di(μ -hydroxo)diiron(III) (**7**) complexes (Figure 3.19). Unlike **4**, which contains three carboxylate ligands per diiron unit, **6** and **7** retain a carboxylate-to-iron ratio of two (Figure 3.20). These results demonstrate that the shape and size of the carboxylate ligands in the diiron(II) complexes are critical for controlling the nature of the oxygenation products. From X-ray crystallographic and solid/solution Mössbauer spectroscopic investigations, we discovered

that the ratio of **6**:**7** could vary due to uncontrolled amounts of water present during oxygenation of **2**. The occurrence of both (μ -oxo)diiron(III) and di(μ -hydroxo)diiron(III) species in a single crystal suggests that the energetic barrier for their interconversion is low. Complex **6** probably forms directly from reaction of **2** with dioxygen and convert to **7** by subsequent reaction with water. Such interconversion between (μ -oxo)dimetallic and di(μ -hydroxo)dimetallic units has previously been observed. Mössbauer spectroscopic studies revealed that drying of a $[\text{Fe}^{\text{III}}_2(\mu\text{-OH})_2]$ complex resulted in extrusion of water to give a $[\text{Fe}^{\text{III}}_2(\mu\text{-O})]$ species.⁶² More recently, crystal-to-crystal conversion of a (μ -oxo)divanadium polyoxometalate cluster to a di(μ -hydroxo)divandium analogue was discovered following exposure of the starting complex to water vapor.⁶³ These synthetic studies suggest that similar processes occur at the cores of carboxylate-bridged diiron proteins.

The structure of **7** closely mimics that of the oxidized core of sMMOH_{ox},¹⁸ which also contains a di(μ -hydroxo)diiron(III) unit (Figure 3.22B). We attribute the longer Fe–Fe distance in **7** compared to sMMOH_{ox}, however, to the lack of a bridging carboxylate. Notably, switching of a bridging $\text{Ar}^{\text{Tot}}\text{CO}_2^-$ in **2** to a terminal position in **7** reproduces the redox dependent *carboxylate-shift* observed in the BMM proteins.⁶⁴

Upon exposure to excess H₂O, **7** dimerizes to form the tetranuclear species **8** (Scheme 3.3). The tendency for iron complexes to aggregate in this manner is well-documented in the porphyrin as well as the synthetic diiron literature.^{65,66} Unlike the BMMs, which encapsulate diiron cofactors within a protein matrix to avoid unwanted side reactions, small-molecule mimics do not have such exquisite steric protection. By installing more bulky groups around the PIM²⁻ ligand periphery, however, it should be possible to prevent formation of polynuclear species. Furthermore, having a bulkier ligand platform may allow assembly of diiron(II) models with less

sterically encumbering carboxylate units and facilitate dioxygen binding or improve hydrocarbon substrate access to the diiron core.

3.5. Conclusion

Using ligand design, we constructed more accurate models of the carboxylate-bridged diiron active sites of bacterial multi-component monooxygenases. To do so we developed the new macrocyclic ligand H₂PIM, which could be readily prepared in multi-gram quantities and in good yields. In the presence of external carboxylates and [Fe₂(Mes)₄], H₂PIM self-assembles to form diiron(II) complexes that reproduce the syn orientation of nitrogen donors as well as the bridging modes of carboxylate ligands in the proteins. Electrochemical studies of the diiron(II) units suggest that isostructural diiron(II,III) species may be isolable, or at least trappable, for characterization. These diiron(II) compounds react rapidly with dioxygen to give a variety of iron-containing species, including (μ -hydroxo)diiron(III), (μ -oxo)diiron(III), di(μ -hydroxo)diiron(III), and hexa(μ -hydroxo)tetrairon(III) complexes. The composition of the oxygenation products is determined in part by the nature of the carboxylate ligand and the presence of water. Because we can now access both the reduced and oxidized forms of the BMMs in a single synthetic platform, detailed studies of the O₂ reaction pathway using these models should be able to address some remaining questions concerning the chemistry of carboxylate-bridged diiron proteins.

3.6. References

- (1) Du Bois, J.; Mizoguchi, T. J.; Lippard, S. J. *Coord. Chem. Rev.* **2000**, 200-202, 443-485.

- (2) Fontecave, M.; Ménage, S.; Duboc-Toia, C. *Coord. Chem. Rev.* **1998**, *178-180*, 1555-1572.
- (3) Que, L., Jr. *Dalton Trans.* **1997**, 3933-3940.
- (4) Que, L., Jr.; Tolman, W. B. *Nature* **2008**, *455*, 333-340.
- (5) Tshuva, E. Y.; Lippard, S. J. *Chem. Rev.* **2004**, *104*, 987-1012.
- (6) Dong, Y.; Yan, S.; Young, V. G., Jr.; Que, L., Jr. *Angew. Chem. Int. Ed.* **1996**, *35*, 618-620.
- (7) Kim, K.; Lippard, S. J. *J. Am. Chem. Soc.* **1996**, *118*, 4914-4915.
- (8) Ookubo, T.; Sugimoto, H.; Nagayama, T.; Masuda, H.; Sato, T.; Tanaka, K.; Maeda, Y.; Ōkawa, H.; Hayashi, Y.; Uehara, A.; Suzuki, M. *J. Am. Chem. Soc.* **1996**, *118*, 701-702.
- (9) Wang, D.; Farquhar, E. R.; Stubna, A.; Münck, E.; Que, L., Jr. *Nature Chem.* **2009**, *1*, 145-150.
- (10) Xue, G.; Wang, D.; De Hont, R.; Fiendler, A. T.; Shan, X.; Münck, E.; Que, L., Jr. *Proc. Natl. Acad. Sci. U.S.A.* **2007**, *104*, 20713-20718.
- (11) Do, L. H.; Hayashi, T.; Moënné-Loccoz, P.; Lippard, S. J. *J. Am. Chem. Soc.* **2010**, *132*, 1273-1275.
- (12) Foster, T. L.; Caradonna, J. P. *J. Am. Chem. Soc.* **2003**, *125*, 3678-3679.
- (13) Mukerjee, S.; Stassinopoulos, A.; Caradonna, J. P. *J. Am. Chem. Soc.* **1997**, *119*, 8097-8098.
- (14) Xue, G.; De Hont, R.; Münck, E.; Que, L., Jr. *Nature Chem.* **2010**, *2*, 400-405.
- (15) Baik, M.-H.; Gherman, B. F.; Friesner, R. A.; Lippard, S. J. *J. Am. Chem. Soc.* **2002**, *124*, 14608-14615.

- (16) Gherman, B. F.; Dunietz, B. D.; Whittington, D. A.; Lippard, S. J.; Friesner, R. A. *J. Am. Chem. Soc.* **2001**, *123*, 3836-3837.
- (17) Gherman, B. F.; Lippard, S. J.; Friesner, R. A. *J. Am. Chem. Soc.* **2005**, *127*, 1025-1037.
- (18) Rosenzweig, A. C.; Nordlund, P.; Takahara, P. M.; Frederick, C. A.; Lippard, S. J. *Chem. Biol.* **1995**, *2*, 409-418.
- (19) Rosenzweig, A. C.; Frederick, C. A.; Lippard, S. J.; Nordlund, P. *Nature* **1993**, *366*, 537-543.
- (20) Rosenzweig, A. C.; Lippard, S. J. *Acc. Chem. Res.* **1994**, *27*, 229-236.
- (21) Lee, D.; Lippard, S. J. *Inorg. Chem.* **2002**, *41*, 2704-2719.
- (22) Hagadorn, J. R.; Que, L., Jr.; Tolman, W. B. *J. Am. Chem. Soc.* **1998**, *120*, 13531-13532.
- (23) LeCloux, D. D.; Barrios, A. M.; Mizoguchi, T. J.; Lippard, S. J. *J. Am. Chem. Soc.* **1998**, *120*, 9001-9014.
- (24) Kuzelka, J.; Farrell, J. R.; Lippard, S. J. *Inorg. Chem.* **2003**, *42*, 8652-8662.
- (25) Kodanko, J. J.; Xu, D.; Song, D.; Lippard, S. J. *J. Am. Chem. Soc.* **2005**, *127*, 16004-16005.
- (26) Do, L. H.; Lippard, S. J. *Inorg. Chem.* **2009**, *48*, 10708-10719.
- (27) Chen, C.-T.; Siegel, J. S. *J. Am. Chem. Soc.* **1994**, *116*, 5959-5960.
- (28) Klose, A.; Solari, E.; Floriani, C.; Chiesi-Villa, A.; Rizzoli, C.; Re, N. *J. Am. Chem. Soc.* **1994**, *116*, 9123-9135.
- (29) Sheldrick, G. M., *SADABS: Area Detector Absorption Correction*; University of Göttingen: Göttingen, Germany, 2001.
- (30) Sheldrick, G. M. *Acta Cryst., Sect. A* **2008**, *A64*, 112-122.

- (31) Spek, A. L., *PLATON*, A Mutipurpose Crystallographic Tool; Utrecht University, Utrecht, The Netherlands, 2000.
- (32) Edson, J. B.; Wang, Z.; Kramer, E. J.; Coates, G. W. *J. Am. Chem. Soc.* **2008**, *130*, 4968-4977.
- (33) Pray, A. r. *Inorg. Synth.* **1990**, *28*, 321-323.
- (34) Morrow, J. R.; Astruc, D. *Bull. Soc. Chem. Fr.* **1992**, *129*, 319-328.
- (35) Kodanko, J. J.; Lippard, S. J. *Inorg. Chim. Acta* **2008**, *361*, 894-900.
- (36) Koch, S. A.; Millar, M. *J. Am. Chem. Soc.* **1982**, *104*, 5255-5257.
- (37) Pyrz, J. W.; Roe, A. L.; Stern, L. J.; Que, L., Jr. *J. Am. Chem. Soc.* **1985**, *107*, 614-620.
- (38) Yoon, S.; Lippard, S. J. *J. Am. Chem. Soc.* **2005**, *127*, 8386-8397.
- (39) Liu, K. E.; Valentine, A. M.; Wang, D.; Huynh, B. H.; Edmondson, D. E.; Salifoglou, A.; Lippard, S. J. *J. Am. Chem. Soc.* **1995**, *117*, 10174-10185.
- (40) DeWitt, J. G.; Bentsen, J. G.; Rosenzweig, A. C.; Hedman, B.; Green, J.; Pilkington, S.; Papaefthymiou, G. C.; Dalton, H.; Hodgson, K. O.; Lippard, S. J. *J. Am. Chem. Soc.* **1991**, *113*, 9219-9235.
- (41) Bertini, I.; Luchinat, C., In *Physical Methods*; Drago, R. S., Ed.: Surfside Scientific Publishers: Gainsville, 1992, p.500-558.
- (42) Iggo, J. A., *NMR Spectroscopy in Inorganic Chemistry*; Oxford University Press, Inc: New York, 1999
- (43) Adam, B.; Bill, E.; Bothe, E.; Goerdts, B.; Haselhorst, G.; Hildenbrand, K.; Sokolowski, A.; Steenken, S.; Weyhermüller, T.; Wieghardt, K. *Chem.-Eur. J.* **1997**, *3*, 308-319.
- (44) Roy, N.; Sproules, S.; Weyhermüller, T.; Wieghardt, K. *Inorg. Chem.* **2009**, *48*, 3783-3791.

- (45) Strautmann, J. B. H.; Freiherr von Richthofen, C.-G.; DeBeer George, S.; Bothe, E.; Bill, E.; Glaser, T. *Chem. Commun.* **2009**, 2637-2639.
- (46) Connelly, N. G.; Geiger, W. E. *Chem. Rev.* **1996**, *96*, 877-910.
- (47) Sanders-Loehr, J.; Wheeler, W. D.; Shiemke, A. K.; Averill, B. A.; Loehr, T. M. *J. Am. Chem. Soc.* **1989**, *111*, 8084-8093.
- (48) Kurtz, D. M., Jr. *Chem. Rev.* **1990**, *90*, 585-606.
- (49) Kang, H. C.; Hanson, A. W.; Eaton, B.; Boekelheide, V. *J. Am. Chem. Soc.* **1985**, *107*, 1979-1985.
- (50) Xu, W.; Puddephatt, R. J.; Muir, K. W.; Torabi, A. A. *Organometallics* **1994**, *13*, 3054-3062.
- (51) Ning, G. L.; Wu, L. P.; Sugimoto, K.; Munakata, M.; Kuroda-Sowa, T.; Maekawa, M. *Dalton Trans.* **1999**, 2529-2536.
- (52) Brown, I. D.; Altermatt, D. *Acta Cryst.* **1985**, *B41*, 240-244.
- (53) Thorp, H. H. *Inorg. Chem.* **1992**, *31*, 1585-1588.
- (54) Merckx, M.; Kopp, D. A.; Sazinsky, M. H.; Blazyk, J. L.; Müller, J.; Lippard, S. J. *Angew. Chem. Int. Ed.* **2001**, *40*, 2782-2807.
- (55) Feig, A. L.; Lippard, S. J. *Chem. Rev.* **1994**, *94*, 759-805.
- (56) Wallar, B. J.; Lipscomb, J. D. *Chem. Rev.* **1996**, *96*, 2625-2658.
- (57) Bordwell, F. G.; Algrim, D. *J. Org. Chem.* **1976**, *41*, 2507-2508.
- (58) Bordwell, F. G.; McCallum, R. J.; Olmstead, W. N. *J. Org. Chem.* **1984**, *49*, 1424-1427.
- (59) Shu, L.; Nesheim, J. C.; Kauffmann, K.; Münck, E.; Lipscomb, J. D.; Que, L., Jr. *Science* **1997**, *275*, 515-518.

- (60) Sessler, J. L.; Tomat, E.; Mody, T. D.; Lynch, V. M.; Veauthier, J. M.; Miraidov, U.; Markert, J. T. *Inorg. Chem.* **2005**, *44*, 2125-2127.
- (61) Tomat, E.; Cuesta, L.; Lynch, V. M.; Sessler, J. L. *Inorg. Chem.* **2007**, *46*, 6224-6226.
- (62) Boudalis, A. K.; Clemente-Juan, J. M.; Dahan, F.; Psycharis, V.; Raptopoulou, C. P.; Donnadieu, B.; Sanakis, Y.; Tuchagues, J.-P. *Inorg. Chem.* **2008**, *47*, 11314-11323.
- (63) Uehara, K.; Mizuno, N. *J. Am. Chem. Soc.* **2011**, *133*, 1622-1625.
- (64) Rardin, R. L.; Tolman, W. B.; Lippard, S. J. *New J. Chem.* **1991**, *15*, 417-430.
- (65) Collman, J. P.; Gagne, R. R.; Reed, C. A.; Halbert, T. R.; Lang, G.; Robinson, W. T. *J. Am. Chem. Soc.* **1975**, *97*, 1427-1439.
- (66) Lippard, S. J. *Angew. Chem. Int. Ed.* **1988**, *27*, 344-361.

Chapter 4

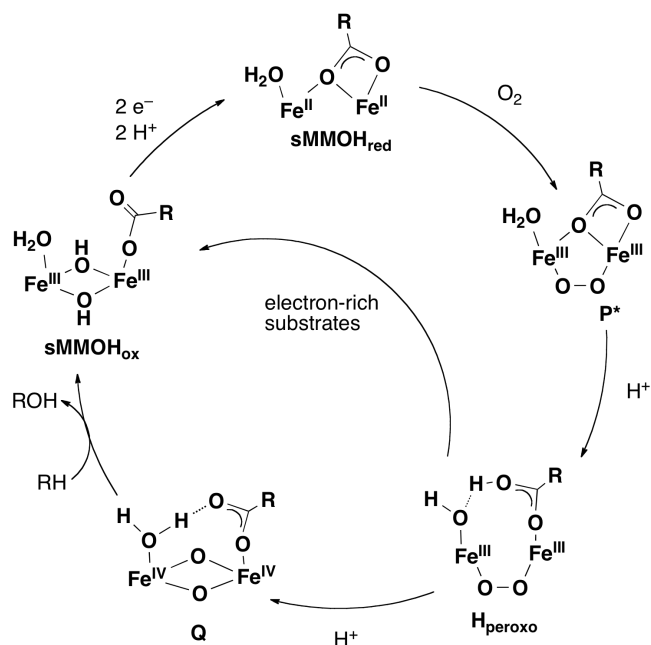
Carboxylate as the Protonation Site in (Peroxo)diiron(III) Model Complexes of Soluble Methane Monooxygenase and Related Diiron Proteins

Portions of this chapter have appeared in print:

Loi H. Do, Takahiro Hayashi, Pierre Moënne-Loccoz, Stephen J. Lippard. “Carboxylate as the Protonation Site in (Peroxo)diiron(III) Model Complexes of Soluble Methane Monooxygenase and Related Diiron Proteins.” *J. Am. Chem. Soc.*, **2010**, 132(4), 1273–1275.

4.1. Introduction

An important subclass of the diiron protein family is the bacterial multi-component monooxygenases (BMMs),¹ which comprises soluble methane monooxygenase (sMMO),² toluene/*o*-xylene monooxygenase (ToMO),³⁻⁵ phenol hydroxylase (PH),⁶ and alkene monooxygenase (AMO),⁷ among others.^{8,9} All of these enzymes require multiple proteins for efficient chemical catalysis, including a hydroxylase component that contains two identical carboxylate-bridge diiron cofactors, a reductase component that delivers electrons from nicotinamide adenine dinucleotide (NADH) through a [2Fe–2S] cluster to the hydroxylase, and a regulatory component that is postulated to control electron transfer and substrate oxidation. Exposing O₂ to the diiron(II) form of the hydroxylase leads to formation of (peroxo)diiron(III) intermediates that are capable of hydroxylating and epoxidizing hydrocarbons. In the unique case of soluble methane monooxygenase hydroxylase (sMMOH), one of two natural biological systems known to convert methane to methanol,¹⁰ the (peroxo)diiron(III) (H_{peroxo}) species forms a higher-valent diiron(IV) complex (intermediate Q)¹¹ before decaying to the resting state of the enzyme (sMMOH_{ox}) (Scheme 4.1). Despite many years of research by our group and others on the structural and mechanistic details of the BMM proteins,¹²⁻¹⁴ important aspects of their biochemistry are still unknown. Some remaining questions are: What are the structures of the oxygenated intermediates? Does oxygen–atom transfer by (peroxo)diiron(III) species to substrates occur through heterolytic or homolytic O–O bond scission? What features allow sMMOH to generate a diiron(IV) species that is distinct from that of other BMMs?¹⁵⁻¹⁸



Scheme 4.1. The proposed catalytic cycle of soluble methane monooxygenase hydroxylase (sMMOH). Conversion of P* to H_{peroxo} and H_{peroxo} to Q occur more rapidly under low pH conditions. Intermediates H_{peroxo} and Q are both capable of oxidizing organic substrates but exhibit different reactivity profiles.¹⁹

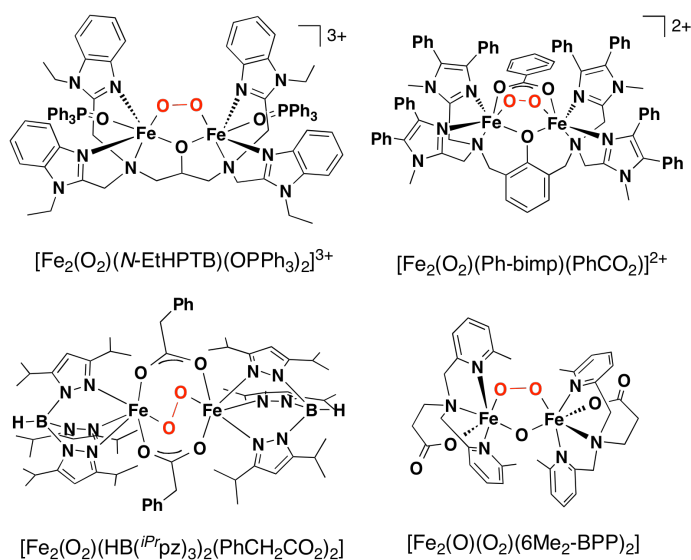
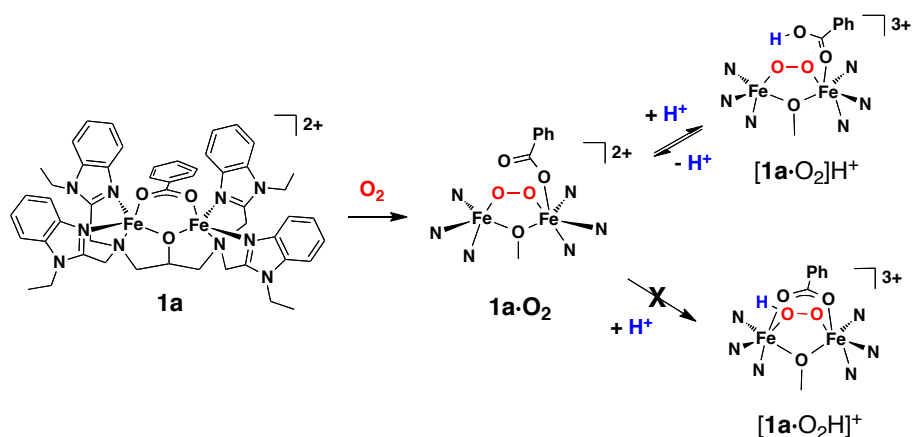


Chart 4.1. The four (peroxo)diiron(III) model complexes that have been structurally characterized by X-ray diffraction analysis. They are $[\text{Fe}_2(\mu\text{-O}_2)(N\text{-EtHPTB})(\text{OPPh}_3)_2]^{3+}$ (top left),²⁰ $[\text{Fe}_2(\mu\text{-O}_2)(\text{Ph-bimp})(\text{PhCO}_2)_2]^{2+}$ (top right),²¹ $[\text{Fe}_2(\mu\text{-O}_2)(\text{HB}(iPr)\text{pz})_3)_2(\text{PhCH}_2\text{CO}_2)_2]$ (bottom left),²² and $[\text{Fe}_2(\mu\text{-O})(\mu\text{-O}_2)(6\text{Me}_2\text{-BPP})_2]$ (bottom right).²³

Re-investigation of the dioxygen activation pathway in sMMOH from *Methylococcus capsulatus* (Bath, *Mc*) revealed that the rates corresponding to P* decay/H_{peroxo} formation as well as H_{peroxo} decay/Q formation are significantly slower at high pH (Scheme 4.1).²⁴ The pH dependence for these events was taken as evidence that protons are required for further activation of the (peroxo)diiron(III) units, in P* and H_{peroxo}. Similar results have also been reported for studies of sMMOH obtained from *Methylosinus trichosporium* OB3b.^{13,25} Given the complexity of the protein environment, indentifying the sites involved in proton translocation and their effect on the O₂ reduction pathway has been difficult to examine directly in the biological system. To shed light on the possible role of protons in the dioxygen activation chemistry at carboxylate-bridged diiron enzyme active sites, several structurally characterized (peroxo)diiron(III) complexes were examined as possible synthetic mimics of P* and H_{peroxo} (Chart 4.1).²⁰⁻²³ Although the structure of the (μ -peroxo)(μ -carboxylato)diiron(III) complex [Fe₂(μ -O₂)(*N*-EtHPTB)(μ -PhCO₂)]²⁺ (**1a**·O₂) is not known, its spectroscopic features suggest an Fe₂O₂ core similar to that of the crystallographically determined [Fe₂(μ -O₂)(*N*-EtHPTB)(OPPh₃)₂]³⁺ analogue (Chart 4.1, top left).^{20,26} The dinucleating *N*-EtHPTB ligand provides kinetic stabilization of the Fe₂O₂ core and the benzoate group serves as a good mimic of the Asp and Glu carboxylate side chains in the protein diiron centers. We postulated that addition of an H⁺ donor to **1a**·O₂ would result in either protonation of the bridging carboxylate ([**1a**·O₂]H⁺) or the reduced dioxygen moiety ([**1a**·O₂H]⁺) (Scheme 4.2). Through application of several spectroscopic methods, we show that the reaction of H⁺ with **1a**·O₂ results in protonation at the carboxylate unit rather than the peroxo ligand and that the process is reversible. This work provides experimental support for recent theoretical studies suggesting that (hydroperoxo)-

diiron(III) species of non-heme diiron enzymes are too reactive to be isolable protein intermediates.²⁷



Scheme 4.2. Reaction of **1a** with dioxygen leads to formation of a $(\mu-1,2\text{-peroxo})$ diiron(III) complex, $1a \cdot O_2$, that is stable at temperatures below $-30^\circ C$. Addition of H^+ to $1a \cdot O_2$ was postulated to protonate either the carboxylate group, giving $[1a \cdot O_2]H^+$, or the peroxo moiety, giving $[1a \cdot O_2H]^+$. The spectroscopic data suggest that the carboxylate is the preferred protonation site. Treatment of $[1a \cdot O_2]H^+$ with triethylamine results in conversion back to $1a \cdot O_2$.

4.2. Experimental

Materials and Methods: Commercial reagents were used as received without further purification. All air-sensitive manipulations were performed using standard Schlenk techniques or under a nitrogen atmosphere inside an MBraun drybox. Solvents were saturated with argon and purified by passage through two columns of activated alumina. The H-*N*-EtHPTB ligand,²⁸ $[Fe_2(N\text{-EtHPTB})(PhCO_2)](BF_4)_2$ complex,²⁶ and $[H(OEt_2)_2][(3,5\text{-}(CF_3)_2C_6H_3)_4B]$ ($H[BAr^F_4]$)^{29,30} compound were synthesized according to literature procedures. The 40% iron-57 enriched $Fe(OSO_2CF_3)_2 \cdot 2CH_3CN$ salt was prepared from $^{57}Fe/^{56}Fe$ metal (2:3) and trifluoromethanesulfonic acid.³¹ Benzoic acid 99% enriched with ^{13}C at the carboxylate carbon atom was purchased from Cambridge Isotopes Laboratories, Inc.

General Physical Methods: NMR spectra were recorded on 500 MHz Varian Mercury spectrometers. Chemical shifts for 1H NMR spectra were referenced to residual solvent peaks

and ^{19}F NMR spectra were referenced externally to trifluoromethylbenzene ($\delta = -63.72$ ppm). Electrospray ionization mass spectra were obtained using an Agilent Technologies 1100 Series LC-MSD Trap. Absorption spectra were acquired on a Cary 50 spectrophotometer using a custom-made quartz cuvette (path length = 1.74 cm) containing a jacketed dewar. An acetonitrile/dry ice bath was used to maintain the samples at -30 °C. Zero field ^{57}Fe Mössbauer spectra were recorded at 90 K on an MSI spectrometer (WEB Research Company) with a ^{57}Co source in a Rh matrix. The isomer shift (δ) values are reported with respect to metallic iron that was used for velocity calibration and the spectra were fit to Lorentzian lines using the WMOSS program. Resonance Raman spectra were measured by Dr. Takahiro Hayashi and Prof. Pierre Moënne-Loccoz at Oregon Health and Science University and were acquired with a custom-built McPherson 2061/207 spectrometer equipped with a Princeton Instrument liquid N_2 cooled CCD detector. All samples were obtained with 647 nm laser excitation at 110 K. Solid state and solution FTIR spectra of air-stable compounds were acquired with a ThermoNicolet Avatar 360 spectrophotometer using the OMNIC software. Solid samples were prepared as KBr pellets and solutions were injected into a Specac OMNI liquid IR cell (CaF_2 windows, 0.10 mm spacer). Air-sensitive solution IR measurements were collected with a Mettler Toledo ReactIR ic 10 unit equipped with a SiComp K4 conduit probe (ATR). Data were recorded using the ic IR software (v. 4.0) and baseline corrected using the OMNIC program.

Synthesis

$[\text{Fe}_2(\text{N-EtHPTB})(\text{PhCO}_2)](\text{BPh}_4)_2$ [**1a**·(BPh_4) $_2$]. Inside a nitrogen drybox, H-*N*-EtHPTB (300 mg, 0.417 mmol), benzoic acid (51 mg, 0.417 mmol), sodium tetraphenylborate (571 mg, 1.67 mmol) and triethylamine (0.13 mL, 0.917 mmol) were combined with 5 mL of CH_3CN and stirred at RT. Upon addition of $\text{FeCl}_2\cdot 4\text{H}_2\text{O}$ (166 mg, 0.833 mmol), the mixture became a light

yellow color. The heterogeneous solution was stirred for 2 h at RT and then filtered to remove the insoluble material. After removal of CH₃CN *in vacuo*, the resulting solid was extracted into CH₂Cl₂. The remaining solid was removed by filtration and the DCM solution was evaporated to dryness and layered with diethyl ether to afford a light yellow powder upon standing at -30 °C (532 mg, 80 %). ¹H NMR (CD₃CN, 500 MHz): 153.71, 107.44, 78.72, 55.11, 34.12, 22.78, 20.89, 19.21, 14.37, 12.61, 11.46, 8.78, 7.06, 5.57, 4.66, 4.09, 3.10, 0.21, -9.32 ppm. IR (KBr): ν 3055, 2978, 1593, 1578, 1550 (asym. COO⁻ stretch), 1490, 1480, 1453, 1425, 1401 (sym. COO⁻ stretch), 1330, 1294, 1267, 1236, 747, 695 cm⁻¹. UV-vis: λ_{max} (CH₃CN) = 335 nm (1210 cm⁻¹M⁻¹). Mp = 175-179 °C. ESI-MS(+) = 1273.6 [**1a**+BPh₄]⁺. Anal. Calc. for **1a**·(BPh₄)₂, Fe₂C₉₈H₉₄B₂N₁₀O₃: C, 73.88; H, 5.95; N, 8.79. Found: C, 73.74; H, 6.00; N, 8.82.

[Fe₂(*N*-EtHPTB)(Ph¹³CO₂)](BPh₄)₂ [**1b**·(BPh₄)₂]. The same procedure was used as described for the synthesis of [**1a**·(BPh₄)₂], except that carbon-13 enriched PhCO₂H was employed instead of natural abundance benzoic acid. IR (KBr): ν 3055, 2978, 1578, 1518 (asym. COO⁻ stretch), 1490, 1485, 1453, 1425, 1375 (sym. COO⁻ stretch), 1330, 1294, 1267, 1236, 747, 695 cm⁻¹. ESI-MS = 1274.9 [**1b** + BPh₄]⁺.

[⁵⁷Fe₂(*N*-EtHPTB)(PhCO₂)](OSO₂CF₃)₂ [⁵⁷Fe-**1a**·(OSO₂CF₃)₂]. Inside a nitrogen drybox, *N*-EtHPTB (100 mg, 0.139 mmol), benzoic acid (17 mg, 0.139 mmol), ⁵⁷Fe(OSO₂CF₃)₂·2CH₃CN (121 mg, 0.278 mmol), and triethylamine (0.13 mL, 0.917 mmol) were combined with 3 mL of CH₃CN and stirred at RT for 1 h. The resulting solid was isolated by filtration and washed with diethyl ether to afford a light yellow material (110 mg, 63%). ¹H NMR (CD₃CN, 500 MHz): 153.29, 106.58, 78.73, 55.56, 34.58, 22.69, 20.92, 20.60, 13.90, 12.60, 11.42, 8.71, 7.47, 7.36, 4.61, 4.10, 1.56, 0.11, -8.87 ppm. IR (KBr): ν 2981, 2944, 1597, 1554, 1492, 1454, 1400, 1339, 1260, 1224, 1156, 1030, 980, 952, 928, 894, 748, 718, 638, 573, 518 cm⁻¹. UV-vis: λ_{max}

(CH₃CN) = 335 nm (1490 cm⁻¹M⁻¹). Mp = 300 °C (decomp.). ESI-MS(+) = 1103.7 [1a+OSO₂CF₃⁻]⁺. Anal. Calc. for 1a·(OSO₂CF₃)₂, Fe₂C₅₂H₅₄F₆N₁₀O₉S₂: C, 49.85; H, 4.34; N, 11.18. Found: C, 49.22; H, 4.40; N, 11.28.

[Fe₂(N-EtHPTB)(C₆F₅CO₂)](OSO₂CF₃)₂ [2·(OSO₂CF₃)₂]. Inside a nitrogen drybox, H-N-EtHPTB (500 mg, 0.694 mmol), pentafluorobenzoic acid (147 mg, 0.694 mmol), Fe(OSO₂CF₃)₂·2CH₃CN (606 mg, 1.39 mmol), and triethylamine (0.22 mL, 1.53 mmol) were combined with 5 mL of CH₃CN and stirred at RT for 1 h. The resulting solid was isolated by filtration and washed with diethyl ether to afford a light yellow material (690 mg, 74%). ¹H NMR (CD₃CN, 500 MHz): 151.54, 106.10, 80.99, 56.80, 39.30, 20.76, 18.52, 13.41, 12.42, 11.14, 8.70, 7.75, 7.15, 4.22, 3.86, 2.61, 1.65, 0.16, -6.56 ppm. ¹⁹F NMR (CD₃CN, 470 MHz): -77.8 (s, 6F), -113.87 (s, 2F), -135.71 (s, 2F), -148.12 (s, 1F) ppm. IR (KBr): ν 2984, 2942, 1650, 1607, 1530, 1490, 1455, 1380, 1341, 1276, 1262, 1224, 1162, 1030, 1003, 986, 893, 748, 638, 574, 517 cm⁻¹. UV-vis: λ_{max} (CH₂Cl₂) = 315 nm (sh, 1170 cm⁻¹M⁻¹). Mp = 302 °C (decomp.). ESI-MS(+) = 1193.2 [2+OSO₂CF₃⁻]⁺. Anal. Calc. for 2·(OSO₂CF₃)₂, Fe₂C₅₂H₄₉F₁₁N₁₀O₉S₂: C, 46.51; H, 3.68; N, 10.43. Found: C, 46.49; H, 3.70; N, 10.34.

[⁵⁷Fe₂(N-EtHPTB)(C₆F₅CO₂)](OSO₂CF₃)₂ [⁵⁷Fe-2·(OSO₂CF₃)₂]. The same procedure was used as described for the synthesis of [2·(OSO₂CF₃)₂], except that 40% iron-57 enriched Fe(OSO₂CF₃)₂·2CH₃CN was employed instead of the natural abundance iron(II) salt.

[Fe₂(N-EtHPTB)(C₆F₅CO₂)](BPh₄)₂ [2·(BPh₄)₂]. The same procedure was used as for the synthesis of [1a·(BPh₄)₂], except that pentafluorobenzoic acid was used instead of benzoic acid. The final product was isolated as a light yellow solid (340 mg, 50%). ¹H NMR (CD₃CN, 500 MHz): 151.85, 106.43, 80.57, 56.31, 39.57, 20.70, 10.17, 12.27, 11.00, 8.58, 7.60, 7.28, 7.13, 6.99, 6.84, 4.27, 3.77, 2.56, 1.69, -0.20, -6.78 ppm. ¹⁹F NMR (CD₃CN, 282 MHz): -117.26 (s,

2F), -140.21 (s, 2F), -148.70 (s, 1F) ppm. IR (KBr): ν 3054, 2983, 1651, 1608, 1580, 1522, 1491, 1481, 1453, 1427, 1397, 1330, 1294, 1269, 1132, 1110, 997, 891, 746, 706, 612 cm^{-1} . UV-vis: λ_{max} (CH_2Cl_2) = 315 nm (sh, 2070 $\text{cm}^{-1}\text{M}^{-1}$). Mp = 185-189 °C. ESI-MS(+) = 1363.6 [$\mathbf{2} + \text{BPh}_4^-$] $^+$. Anal. Calc. for $\mathbf{2} \cdot (\text{BPh}_4)_2$, $\text{Fe}_2\text{C}_98\text{H}_{89}\text{F}_5\text{B}_2\text{N}_{10}\text{O}_3$: C, 69.93; H, 5.33; N, 8.32. Found: C, 69.88; H, 5.18; N, 8.19.

Spectroscopic Studies

UV-Vis Spectroscopy: Addition of $\text{H}[\text{BAr}^{\text{F}}_4]$ to a CH_3CN solution containing either $\mathbf{1a} \cdot \text{O}_2(\text{BF}_4)_2$ or $\mathbf{2} \cdot \text{O}_2(\text{OSO}_2\text{CF}_3)_2$ at -30 °C. Inside a nitrogen glovebox, a 6.0 mL aliquot of a 112 μM CH_3CN solution of $\mathbf{1a} \cdot (\text{BF}_4)_2$ or $\mathbf{2} \cdot (\text{OSO}_2\text{CF}_3)_2$ was added to a low temperature UV-vis cell, which was sealed with a septum. The cell was brought outside of the glovebox and cooled to -30 °C with an acetonitrile/dry ice bath. To generate the (peroxo)diiron(III) species, the septum seal was removed and the sample solution was exposed to air and stirred for 15 min. A UV-vis spectrum was recorded. Successive aliquots of a 1.78 mM solution of $\text{H}[\text{BAr}^{\text{F}}_4]$ in CH_3CN were added to the (peroxo)diiron(III) solution via syringe and the spectral changes were measured. For the protonated complex of $\mathbf{1a} \cdot \text{O}_2(\text{BF}_4)_2$, addition of 2.0 equiv of triethylamine (relative to $\mathbf{1a} \cdot (\text{BF}_4)_2$) led to restoration of the $\mathbf{1a} \cdot \text{O}_2(\text{BF}_4)_2$ spectrum. Spectra were corrected for dilution where appropriate.

^{57}Fe Mössbauer Spectroscopy: Addition of $\text{H}[\text{BAr}^{\text{F}}_4]$ to a CH_3CN solution containing either $^{57}\text{Fe} \cdot \mathbf{1a} \cdot \text{O}_2(\text{OSO}_2\text{CF}_3)_2$ or $^{57}\text{Fe} \cdot \mathbf{2} \cdot \text{O}_2(\text{OSO}_2\text{CF}_3)_2$. A 8.0 mM CH_3CN solution of either $^{57}\text{Fe} \cdot \mathbf{1a} \cdot (\text{OSO}_2\text{CF}_3)_2$ or $^{57}\text{Fe} \cdot \mathbf{2} \cdot (\text{OSO}_2\text{CF}_3)_2$ was prepared anaerobically and cooled to -30 °C. The diiron(II) compound was exposed to air for 15 min and the resulting mixture was divided into two portions. One portion was frozen in liquid nitrogen in a Nylon Mössbauer sample cup and the other was treated with 1.0 equiv of $\text{H}[\text{BAr}^{\text{F}}_4]$, relative to $^{57}\text{Fe} \cdot \mathbf{1a} \cdot \text{O}_2$ or $^{57}\text{Fe} \cdot \mathbf{2} \cdot \text{O}_2$, and then

frozen in a second sample cup. The Mössbauer spectra of the samples were recorded over a period of ~12 h. In all cases, the data were best fit to a single quadrupole doublet.

Resonance Raman Spectroscopy: *Addition of $H[BAr^F_4]$ to a CH_3CN solution containing either $1a \cdot O_2(BF_4)_2$ or $2 \cdot O_2(OSO_2CF_3)_2$.* A 5.9 mM CH_3CN solution of either $1a \cdot (BF_4)_2$ or $2 \cdot (OSO_2CF_3)_2$ was prepared anaerobically and cooled to -30 °C. The diiron(II) compound was exposed to air for 15 min to generate the (peroxo)diiron(III) complex. A 200 μ L aliquot of the $1a \cdot O_2$ or $2 \cdot O_2$ solution was quickly transferred to an NMR tube and frozen in liquid nitrogen. To prepare the protonated $1a \cdot O_2$ and $2 \cdot O_2$ samples, 500 μ L of the starting (peroxo)diiron(III) solution was combined with the appropriate volume of a 59.3 mM solution of $H[BAr^F_4]$ and diluted with cold CH_3CN to give a final diiron concentration of ~5.0 mM. Approx. 200 μ L of the resulting solutions were added into separate NMR tubes and frozen.

Solution IR Spectroscopy: *Measurement of diiron(II) complexes in CH_2Cl_2 .* Inside a nitrogen glovebox, a 3.0 mL solution of $1a \cdot (BPh_4)_2$, $1b \cdot (BPh_4)_2$, or $2 \cdot (BPh_4)_2$ (15.0 mM) was transferred to a ReactIR Schlenk vessel and sealed with a Teflon screwcap. The flask was brought outside of the glovebox, opened under a stream of nitrogen, and attached to the ReactIR probe. Measurements were made at RT. Solvent peaks were subtracted from all spectral data.

Addition of $H[BAr^F_4]$ to a CH_2Cl_2 or CD_3CN solution containing either $1a \cdot O_2(BPh_4)_2$ or $1b \cdot O_2(BPh_4)_2$. Inside a nitrogen drybox, a ~55 mM solution of $1a \cdot (BPh_4)_2$ or $1b \cdot (BPh_4)_2$ was sealed in a scintillation vial. The solution was brought outside of the drybox, cooled to -30 °C, and stirred in air for 5 min to generate the (peroxo)diiron(III) species. An aliquot of the dark blue-green mixture was treated with an appropriate amount of $H[BAr^F_4]$ and stirred for an additional 5 min. Approximately 100 μ L of each solution was injected into a liquid IR cell that has been pre-cooled over dry ice. IR spectra of the cold samples were recorded over a period of

~30 sec. Identical measurements using the ReactIR system, which maintains a constant low temperature throughout the experiment, gave the same results, demonstrating that the (peroxo)diiron(III) species are stable during data acquisition in the liquid IR cell. Spectral data were subtracted from a nitrogen background and baseline corrected, but not solvent subtracted.

¹H and ¹⁹F NMR Spectroscopy: *Addition of H[BAr^F₄] to a solution containing either **1a**·O₂(BF₄)₂ or **2**·O₂(OSO₂CF₃)₂.* A 8.0 mM solution of **1a**·(BF₄)₂ or **2**·(OSO₂CF₃)₂ was prepared anaerobically and cooled to -30 °C. The sample was exposed to air to form the (peroxo)diiron(III) species and divided into two equal portions. One portion was transferred to an NMR tube as the **1a**·O₂ or **2**·O₂ sample. To the other solution, 1.0 equiv of H[BAr^F₄] was added and then transferred to a second NMR tube. Both the NMR samples and probe were maintained at -30 °C to ensure the stability of the (peroxo)diiron(III) species throughout the experiment.

4.3. Results and Discussion

To aid spectral interpretation of results obtained during studies of the parent [Fe₂(N-EtHPTB)(PhCO₂)]²⁺ complex (**1a**), two related diiron(II) precursors were synthesized. One is [Fe₂(N-EtHPTB)(Ph¹³CO₂)]²⁺ (**1b**), which contains a ¹³C-enriched carboxylate ligand, and the other is [Fe₂(N-EtHPTB)(C₆F₅CO₂)]²⁺ (**2**), in which the benzoate ring is fully fluorinated.

Exposure of **1a** to O₂ in CH₃CN at -30 °C generated a deep blue-green solution (**1a**·O₂) with λ_{max} at 590 nm.²⁶ Addition of an acetonitrile solution of [H(OEt₂)₂][(3,5-(CF₃)₂C₆H₃)₄B] (H[BAr^F₄]) to **1a**·O₂ shifted the peroxo-to-iron(III) charge transfer band to ~600 nm (Figure 4.1A). This absorption was assigned to the formation of a new [**1a**·O₂]H⁺ species that maximized with addition of ~1.5 equiv of H[BAr^F₄]. The spectrum of **1a**·O₂ was restored upon addition of 2.0 equiv of NEt₃ (Figure 4.1B), indicating that protonation does not lead to irreversible

decomposition of the $\mathbf{1a}\cdot\text{O}_2$ unit. Reaction of $\mathbf{2}$ with O_2 afforded $[\text{Fe}_2(\mu\text{-O}_2)(N\text{-EtHPTB})(\text{C}_6\text{F}_5\text{CO}_2)]^{2+}$ ($\mathbf{2}\cdot\text{O}_2$), which exhibits a broad absorption feature centered at ~ 600 nm. When $\text{H}[\text{BAr}^{\text{F}}_4]$ was titrated into a solution of $\mathbf{2}\cdot\text{O}_2$, a small bathochromic shift to ~ 610 nm occurred (Figure 4.2). Unlike $\mathbf{1a}\cdot\text{O}_2$, $\mathbf{2}\cdot\text{O}_2$ required ~ 3.0 equiv of $\text{H}[\text{BAr}^{\text{F}}_4]$ to fully generate the protonated species $[\mathbf{2}\cdot\text{O}_2]\text{H}^+$. Given that pentafluorobenzoate, for which the acid has a $\text{p}K_a$ of 1.2, is more electron deficient than benzoate (acid $\text{p}K_a = 4.6$), the greater amount of H^+ necessary to produce $[\mathbf{2}\cdot\text{O}_2]\text{H}^+$ from $\mathbf{2}\cdot\text{O}_2$ compared to $[\mathbf{1a}\cdot\text{O}_2]\text{H}^+$ from $\mathbf{1a}\cdot\text{O}_2$ suggested that either the carboxylate ligand influences the basicity of the protonation site or that it itself is the proton acceptor.

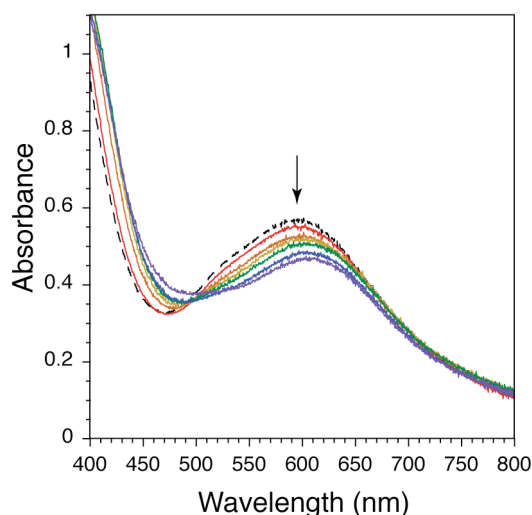


Figure 4.1. UV-vis absorption spectra of A) $\mathbf{1a}\cdot\text{O}_2$ ($112 \mu\text{M}$ in CH_3CN , -30°C) before (dotted trace) and after (blue trace) addition of 2.0 equiv of $\text{H}[\text{BAr}^{\text{F}}_4]$ and B) restoration of the initial spectrum (orange trace) upon treatment with 2.0 equiv of triethylamine.

To determine whether a (hydroperoxo)diiron(III) species may form upon addition of H^+ to $\mathbf{1a}\cdot\text{O}_2$ or $\mathbf{2}\cdot\text{O}_2$, ^{57}Fe Mössbauer and resonance Raman (RR) spectra were recorded to examine possible changes in the Fe_2O_2 core. In the absence of H^+ , the Mössbauer spectrum of a frozen

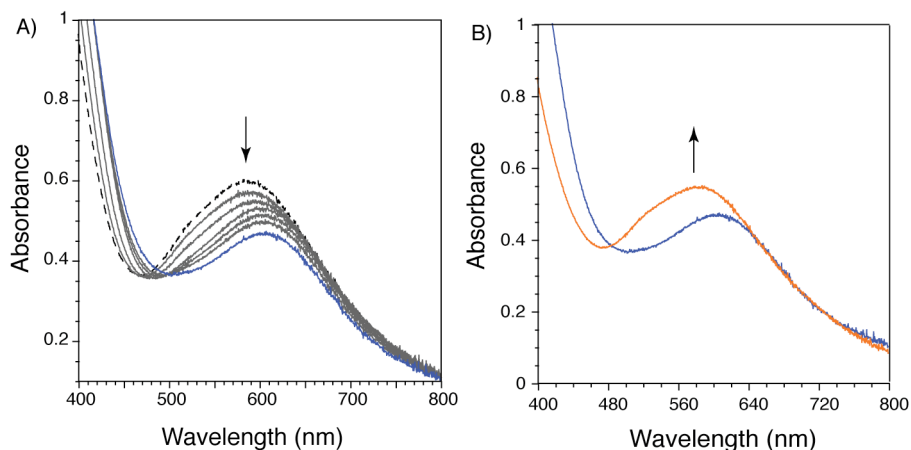
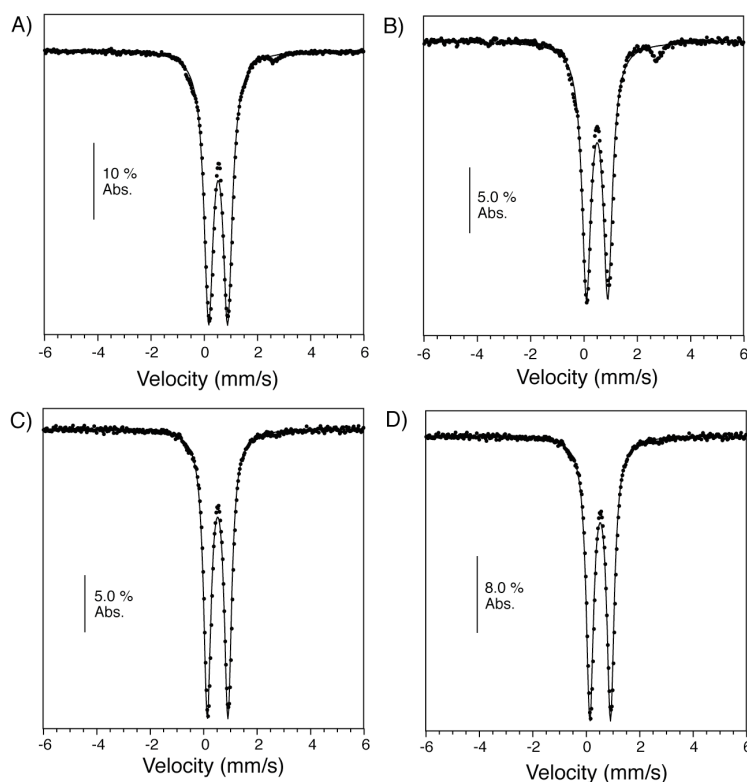


Figure 4.2. UV-vis absorption spectra of $[\text{Fe}_2(\mu\text{-O}_2)(N\text{-EtHPTB})(\text{C}_6\text{F}_5\text{CO}_2)](\text{OSO}_2\text{CF}_3)_2$ (112 μM in CH_3CN , -30°C) after addition of up to 4.8 equiv of $\text{H}[\text{BAr}^{\text{F}}_4]$, relative to the diiron complex. The (peroxo)diiron(III) species displays a λ_{max} at ~ 600 nm, whereas the protonated complex shows a shifted absorption band centered at ~ 610 nm. Black dotted line = compound $\mathbf{2}\cdot\text{O}_2$, solid lines = spectra after addition of up to 4.8 equiv of $\text{H}[\text{BAr}^{\text{F}}_4]$.

solution of $\mathbf{1a}\cdot\text{O}_2$ in CH_3CN was fit to a single iron site, with $\delta = 0.53(2)$ mm/s and $\Delta E_{\text{Q}} = 0.71(2)$ mm/s (Figure 4.3A, Table 4.1). Addition of $\text{H}[\text{BAr}^{\text{F}}_4]$ to $\mathbf{1a}\cdot\text{O}_2$ gave $[\mathbf{1a}\cdot\text{O}_2]\text{H}^+$ having the same isomer shift ($\delta = 0.53(2)$ mm/s) and a slightly larger quadrupole splitting parameter ($\Delta E_{\text{Q}} = 0.80(2)$ mm/s) (Figure 4.3B, Table 4.1). For comparison, the Mössbauer spectra of $\mathbf{2}\cdot\text{O}_2$ and $[\mathbf{2}\cdot\text{O}_2]\text{H}^+$ were also recorded. The (peroxo)diiron(III) complex of $\mathbf{2}$ has parameters $\delta = 0.53(2)$ mm/s and $\Delta E_{\text{Q}} = 0.77(2)$ mm/s (Figure 4.3C, Table 4.1), whereas the protonated $[\mathbf{2}\cdot\text{O}_2]\text{H}^+$ form exhibits parameters of $\delta = 0.54(2)$ mm/s and $\Delta E_{\text{Q}} = 0.84(2)$ mm/s (Figure 4.3D). The similar isomer shifts obtained for $\mathbf{1a}\cdot\text{O}_2$, $[\mathbf{1a}\cdot\text{O}_2]\text{H}^+$, $\mathbf{2}\cdot\text{O}_2$, and $[\mathbf{2}\cdot\text{O}_2]\text{H}^+$ are indicative of iron(III) centers and the small increase in ΔE_{Q} values for the protonated forms implies that only minor changes occur in the coordination environment.

Table 4.1. UV-Vis, Mössbauer, RR, and FTIR Data for $\mathbf{1a}\cdot\text{O}_2$, $[\mathbf{1a}\cdot\text{O}_2]\text{H}^+$, $\mathbf{2}\cdot\text{O}_2$, and $[\mathbf{2}\cdot\text{O}_2]\text{H}^+$.

	λ_{max} , nm (ϵ , $\text{M}^{-1}\text{cm}^{-1}$)	δ , mm/s	ΔE_{Q} , mm/s	$\nu(\text{Fe}-\text{O})$, cm^{-1} ($\Delta^{18}\text{O}$)	$\nu(\text{O}-\text{O})$, cm^{-1} ($\Delta^{18}\text{O}$)	$\nu_{\text{as}}(\text{COO}^-)$ cm^{-1} ($\Delta^{13}\text{C}$)	$\nu_{\text{s}}(\text{COO}^-)$ cm^{-1} ($\Delta^{13}\text{C}$)	$\Delta\nu_{\text{as-s}}$ cm^{-1}
$\mathbf{1a}\cdot\text{O}_2$	590 (3100)	0.53(2)	0.71(2)	466/474 (-18)	897 (-50)	1607/1572 (>-22)	1358 (-29)	>200
$[\mathbf{1a}\cdot\text{O}_2]\text{H}^+$	600 (2360)	0.53(2)	0.80(2)	467/478 (-20)	896 (-53)	1553 (-32)	-	-
$\mathbf{2}\cdot\text{O}_2$	600 (3300)	0.53(2)	0.77(2)	466/475 (-18)	897 (-50)	-	-	-
$[\mathbf{2}\cdot\text{O}_2]\text{H}^+$	610 (2700)	0.54(2)	0.84(2)	478 (-19)	897 (-50)	-	-	-

**Figure 4.3.** Zero-field ^{57}Fe Mössbauer spectra of frozen CH_3CN solutions containing ~ 8 mM A) $[\text{}^{57}\text{Fe}_2(\mu\text{-O}_2)(N\text{-EtHPTB})(\text{PhCO}_2)](\text{OSO}_2\text{CF}_3)_2$ ($\delta = 0.53(2)$ mm/s, $\Delta E_{\text{Q}} = 0.71(2)$ mm/s, $\Gamma = 0.42(2)$ mm/s); B) $[\text{}^{57}\text{Fe}_2(\mu\text{-O}_2)(N\text{-EtHPTB})(\text{PhCO}_2)](\text{OSO}_2\text{CF}_3)_2/\text{H}[\text{BAR}^{\text{F}}_4]$ (1:1) ($\delta = 0.53(2)$ mm/s, $\Delta E_{\text{Q}} = 0.80(2)$ mm/s, $\Gamma = 0.43(2)$ mm/s); C), $[\text{}^{57}\text{Fe}_2(\mu\text{-O}_2)(N\text{-EtHPTB})(\text{C}_6\text{F}_5\text{CO}_2)](\text{OSO}_2\text{CF}_3)_2$ ($\delta = 0.53(2)$ mm/s, $\Delta E_{\text{Q}} = 0.77(2)$ mm/s, $\Gamma = 0.34(2)$ mm/s); and D) $[\text{}^{57}\text{Fe}_2(\mu\text{-O}_2)(N\text{-EtHPTB})(\text{C}_6\text{F}_5\text{CO}_2)](\text{OSO}_2\text{CF}_3)_2/\text{H}[\text{BAR}^{\text{F}}_4]$ (1:1) ($\delta = 0.54(2)$ mm/s, $\Delta E_{\text{Q}} = 0.84(2)$ mm/s, $\Gamma = 0.36(2)$ mm/s). The spectra were acquired at 90 K and the raw data (\bullet) were fit to Lorentzian

least square lineshapes (black trace). The minor peaks in spectra A and B were not included in the data fitting and are attributed to unreacted diiron(II) starting material.

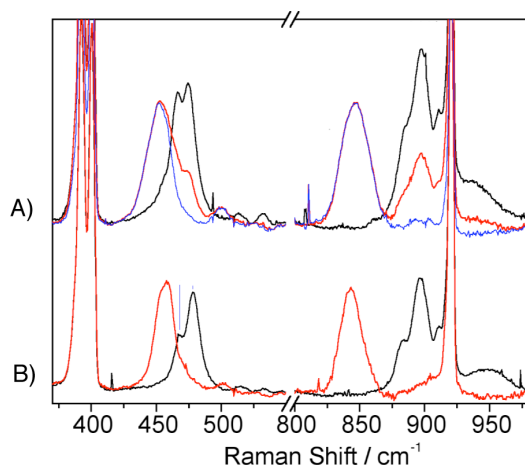


Figure 4.4. Resonance Raman spectra of frozen CH_3CN solutions of $[\text{Fe}_2(\mu\text{-O}_2)(N\text{-EtHPTB})(\text{PhCO}_2)](\text{BF}_4)_2$ ($^{16}\text{O}_2$: black; $^{18}\text{O}_2$: red; and $^{18}\text{O}_2$ -sample minus $^{16}\text{O}_2$ -contaminant: blue) with (A, top) and without (B, bottom) addition of 1.0 equiv of $\text{H}[\text{BAr}^{\text{F}}_4]$, relative to the diiron complex. Each spectrum was normalized based on the solvent bands at 392, 400, and 920 cm^{-1} . Top spectra: $\nu = 897$ (847), 532/513 (500), 474/466 (452) cm^{-1} . Bottom spectra: $\nu = 896$ (843), 533/514 (501), 478/467 (458) cm^{-1} .

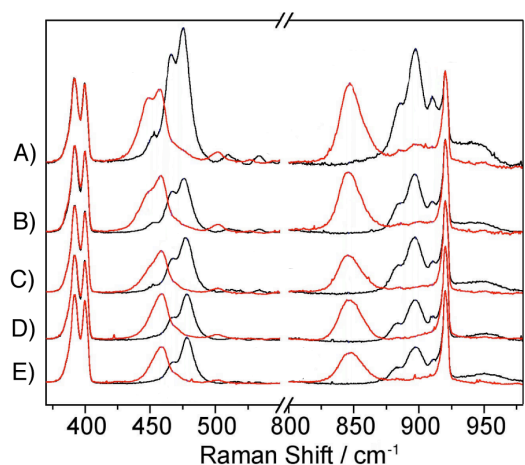


Figure 4.5. Resonance Raman spectra of $2 \cdot ^{16}\text{O}_2$ (black) and $2 \cdot ^{18}\text{O}_2$ (red) after addition of 0 (A), 0.5 (B), 1.0 (C), 1.5 (D), and 2.0 (E) equiv of $\text{H}[\text{BAr}^{\text{F}}_4]$. Each spectrum was normalized based on the solvent CH_3CN bands at 392, 400, and 920 cm^{-1} . Before addition of protons: $\nu = 910/897/886$ (847), 532/513 (500), 475/466 (457/449) cm^{-1} . After addition of protons: $\nu = 910/897/886$ (847), 532/513 (500), 478/467 (459) cm^{-1} .

To investigate more directly the nature of the peroxo moiety, Fe–O and O–O vibrations were measured by resonance Raman (RR) spectroscopy for species generated with both $^{16}\text{O}_2$ and $^{18}\text{O}_2$. As previously reported,²⁶ $\mathbf{1a}\cdot\text{O}_2$ exhibits Fe–O and O–O stretching vibrations with Fermi splitting (hereafter “/”) centered at 470 and 897 cm^{-1} , respectively (Figure 4.4). Also observed are weaker bands at 513/532 cm^{-1} that shifted to 500 cm^{-1} with $^{18}\text{O}_2$, which we assigned to the asymmetric Fe–O stretch of the Fe_2O_2 core. Addition of H^+ to $\mathbf{1a}\cdot\text{O}_2$ only marginally affects its RR spectrum, with small upshift in Fe–O and downshift in O–O vibrations (Figure 4.4, Table 4.1). These shifts in RR frequencies upon H^+ addition may reflect subtle changes in Fe–O–O–Fe angles,³² but are too small to support the conclusion that a (μ -1,2-peroxo)diiron(III) unit has been converted to a (hydroperoxo)diiron(III) species. The RR spectrum of $\mathbf{2}\cdot\text{O}_2$ is practically identical to that of $\mathbf{1a}\cdot\text{O}_2$, with symmetric and asymmetric Fe–O modes at 466/475 and 513/532 cm^{-1} , respectively, and Fermi-coupled O–O stretches centered at 897 cm^{-1} (Figure 4.5). Addition of up to 2.0 equiv of $\text{H}[\text{BAr}^{\text{F}}_4]$ to generate $[\mathbf{2}\cdot\text{O}_2]\text{H}^+$ primarily affects the symmetric Fe–O stretch, which upshifts only a few wavenumbers compared to the spectrum of $\mathbf{2}\cdot\text{O}_2$ (Table 4.1). From the RR data and Mössbauer parameters for $\mathbf{1a}\cdot\text{O}_2$, $[\mathbf{1a}\cdot\text{O}_2]\text{H}^+$, $\mathbf{2}\cdot\text{O}_2$, and $[\mathbf{2}\cdot\text{O}_2]\text{H}^+$, we conclude that protonation does not lead to formation of a (hydroperoxo)diiron(III) species.

Since the benzimidazole, amine, and propoxyl groups of *N*-EtHPTB are less accessible due to the multidentate nature of the ligand, we assign the carboxylate unit as the site of protonation. To test this hypothesis, we examined the carboxylate stretches of $\mathbf{1a}$ and $\mathbf{1b}$, and their peroxo complexes by FTIR spectroscopy. The assignment of frequencies in terms of coordination geometry is complicated by mixing of the COO^- symmetric stretch with the O–C–O bend and C–C stretch.³³ Nevertheless, if the asymmetric and symmetric COO^- stretches could be

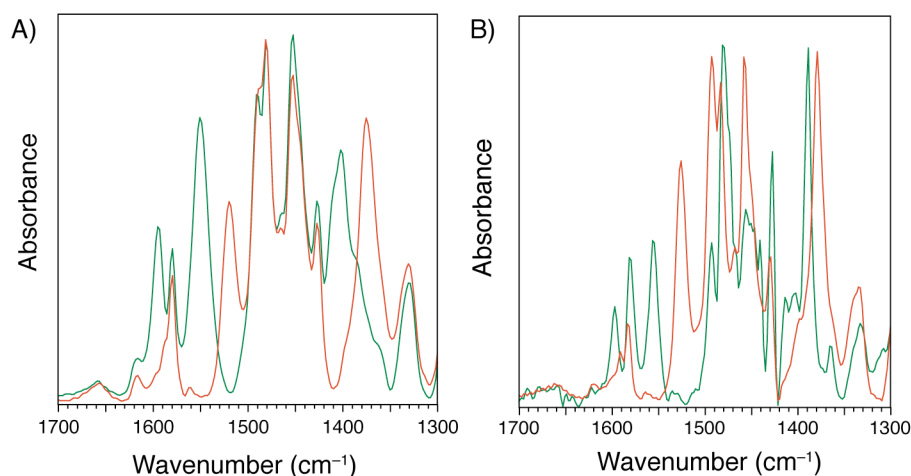


Figure 4.6. Infrared spectra of $[\text{Fe}_2(\text{N-EtHPTB})(\text{PhCO}_2)](\text{BPh}_4)_2$ (**1a**, green) and $[\text{Fe}_2(\text{N-EtHPTB})(\text{Ph}^{13}\text{CO}_2)](\text{BPh}_4)_2$ (**1b**, orange) in the solid state (KBr pellet, panel A) and in solution (CH_2Cl_2 , panel B). Panel A: $\nu_{1a} = 1330, 1401, 1425, 1453, 1480, 1490, 1550, 1573, 1593 \text{ cm}^{-1}$. $\nu_{1b} = 1330, 1375, 1425, 1453, 1480, 1490, 1518, 1573 \text{ cm}^{-1}$. Panel B: $\nu_{1a} = 1332, 1389, 1426, 1457, 1479, 1493, 1555, 1580, 1597 \text{ cm}^{-1}$. $\nu_{1b} = 1332, 1377, 1426, 1457, 1479, 1493, 1526, 1580 \text{ cm}^{-1}$. The peaks at 1550 (1555) and 1518 (1526) cm^{-1} are assigned to asymmetric COO^- stretches (where values in parentheses are for the solution data), and peaks at 1401 (1389) and 1375 (1377) cm^{-1} are attributed to symmetric COO^- vibration modes.

identified, the binding geometry of the carboxylate ligand could be derived from the difference in the two, $\Delta\nu_{\text{as-s}}$.³⁴⁻³⁶ Specifically, $\Delta\nu_{\text{as-s}}$ should be close to that of the free ionic form for carboxylates bridging two metal ions (150 cm^{-1} for PhCOO^-), larger in unidentate coordination geometry, and smaller in bidentate mononuclear complexes. As expected, **1a** and **1b** exhibited $\Delta\nu_{\text{as-s}}$ values of 149 and 166 cm^{-1} , respectively, consistent with μ -1,3 bridging carboxylate groups (Figure 4.6). In CH_2Cl_2 , **1a** $\cdot\text{O}_2$ displayed ν_{as} and ν_{s} stretches at 1572/1607 and 1358 cm^{-1} , respectively, whereas **1b** $\cdot\text{O}_2$ showed peaks at 1550 and 1329 cm^{-1} (Figure 4.7A). These frequencies give $\Delta\nu_{\text{as-s}} > 200 \text{ cm}^{-1}$ and suggest a switch from bridging to unidentate coordination for the carboxylate groups in **1a** $\cdot\text{O}_2$ and **1b** $\cdot\text{O}_2$. Shifting of a phosphinate ligand from a bridging to a terminal position has been reported for the (peroxo)diiron(III) unit supported by *N*-EtHPTB.³⁷ A bridging benzoate, however, has been observed in the X-ray structure of a

(peroxo)diiron(III) complex containing a related ligand system.²¹ Generation of $[\mathbf{1a}\cdot\text{O}_2]\text{H}^+$ and $[\mathbf{1b}\cdot\text{O}_2]\text{H}^+$ was associated with downshift of the ν_{as} modes by at least 20 cm^{-1} , whereas ν_{s} modes were not observed, possibly shifting below 1300 cm^{-1} (Figure 4.7B and 4.8D). The FTIR spectra in CH_2Cl_2 are similar to those in CD_3CN and do not show evidence for free benzoic acid in the H^+ treated samples. With the use of the less basic carboxylate $\text{C}_6\text{F}_5\text{CO}_2^-$, present in **2**, protonation leads to free pentafluorobenzoic acid, but only in the coordinating solvent acetonitrile and not in dichloromethane (Figure 4.8). The peaks at 1529 , 1654 , and 1739 cm^{-1} are diagnostic of uncoordinated pentafluorobenzoic acid.

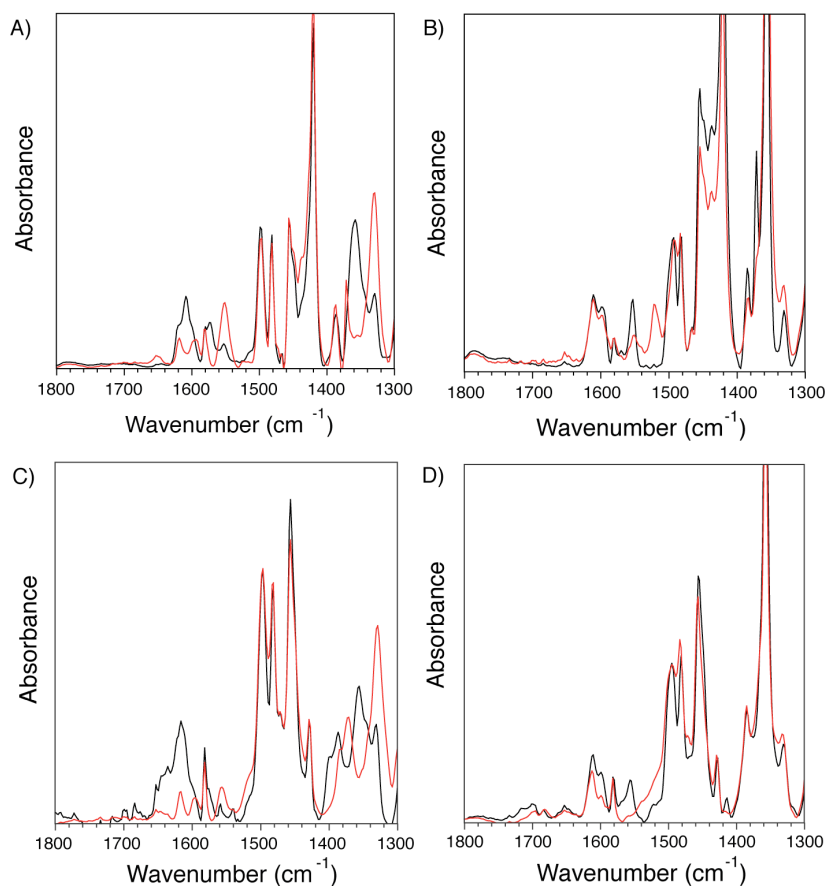


Figure 4.7. Solution FTIR spectra of $\mathbf{1a}\cdot\text{O}_2$ (black) and $\mathbf{1b}\cdot\text{O}_2$ (red) before (A and C) and after (B and D) the addition of 1.5 equiv of $\text{H}[\text{BARF}_4]$. Spectra A and B were acquired in CH_2Cl_2 whereas spectra C and D were measured in CD_3CN . The samples were recorded at approx. -30

°C with a diiron concentration of ~55 mM. The intense peaks at 1354/1356 and 1420 cm^{-1} are due to the $[\text{BAR}^{\text{F}}_4]^-$ anion and solvent, respectively. Panel A: $\nu_{1\text{a}} = 1358, 1389, 1456, 1481, 1497, 1572, 1607 \text{ cm}^{-1}$. $\nu_{1\text{b}} = 1329, 1369, 1389, 1456, 1481, 1497, 1550 \text{ cm}^{-1}$. Panel B: $\nu_{1\text{a}} = 1372, 1456, 1483, 1494, 1553, 1596, 1609 \text{ cm}^{-1}$. $\nu_{1\text{b}} = 1456, 1483, 1494, 1521, 1596, 1609 \text{ cm}^{-1}$. Panel C: $\nu_{1\text{a}} = 1356, 1388, 1456, 1481, 1495, 1579, 1616 \text{ cm}^{-1}$. $\nu_{1\text{b}} = 1326, 1372, 1456, 1481, 1495, 1557, 1579 \text{ cm}^{-1}$. Panel D: $\nu_{1\text{a}} = 1386, 1455, 1481, 1496, 1554, 1597, 1611 \text{ cm}^{-1}$. $\nu_{1\text{b}} = 1386, 1455, 1481, 1496, 1518, 1597, 1611 \text{ cm}^{-1}$.

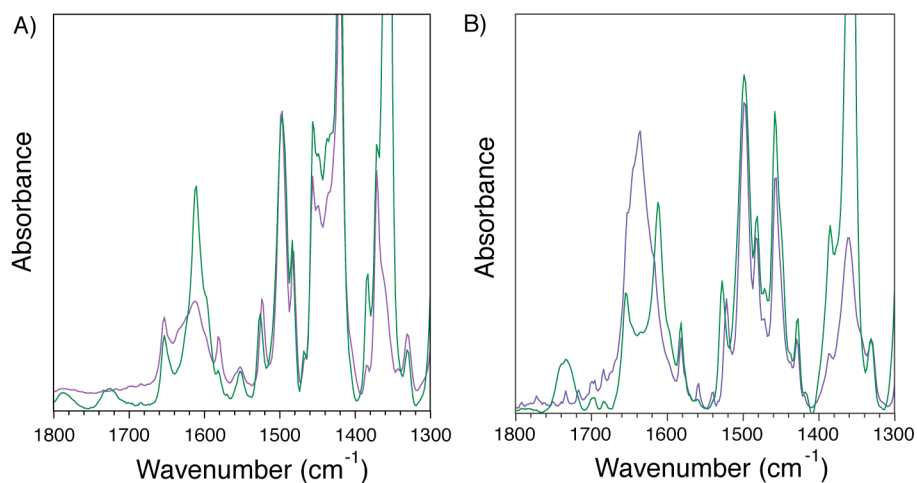


Figure 4.8. Solution FTIR spectra of $2 \cdot \text{O}_2$ before (purple) and after (green) the addition of 3.0 equiv of $\text{H}[\text{BAR}^{\text{F}}_4]$. Spectra in A were acquired in CH_2Cl_2 and spectra in B were obtained in CD_3CN at -30°C with a diiron concentration of ~55 mM. For A, the intense peaks at 1356 and 1420 cm^{-1} due to the $[\text{BAR}^{\text{F}}_4]^-$ anion and CH_2Cl_2 , respectively. For B, the resonances at 1529, 1654, and 1739 cm^{-1} ($\nu_{\text{C}=\text{O}}$) are attributed to formation of free pentafluorobenzoic acid. The absence of the 1739 cm^{-1} absorbance in A is taken as evidence that pentafluorobenzoic acid is not liberated in CH_2Cl_2 . Panel A: $\nu_{\text{purple}} = 1370, 1454, 1497, 1525, 1610, 1652 \text{ cm}^{-1}$. $\nu_{\text{green}} = 1370, 1382, 1454, 1497, 1525, 1610, 1652 \text{ cm}^{-1}$. Panel B: $\nu_{\text{purple}} = 1360, 1456, 1497, 1529, 1635 \text{ cm}^{-1}$. $\nu_{\text{green}} = 1385, 1456, 1497, 1529, 1610, 1654, 1739 \text{ cm}^{-1}$.

A comparison of the ^1H NMR spectra of the benzoate and pentafluorobenzoate diiron complexes allowed the phenyl ring protons of the former to be identified in $1\text{a} \cdot \text{O}_2$ as paramagnetically broadened peaks at 7.01, 8.74, and 11.40 ppm (Figure 4.9A). Upon addition of $\text{H}[\text{BAR}^{\text{F}}_4]$, these resonances shifted to 7.50, 7.99, and 9.82 ppm (Figure 4.9C), in support of the protonation of the benzoate ligand. This conclusion was confirmed by analysis of the ^{19}F NMR spectra of $2 \cdot \text{O}_2$ and $[2 \cdot \text{O}_2]\text{H}^+$. The parent complex **2** displayed resonances at -113.87, -135.71, and -148.12 ppm (Figure 4.10A). Upon oxygenation in dichloromethane, the peaks for $2 \cdot \text{O}_2$

appeared more upfield at -134.34, -154.44, and -159.02 ppm (Figure 4.10D) and shifted to -111.30, -142.096, and -154.79 ppm when 3 equiv of $\text{H}[\text{BAr}^{\text{F}}_4]$ was introduced (Fig. 4.10E). The paramagnetically broadened resonances in Figure 4.10D and 4.10F, demonstrate that the $\text{C}_6\text{F}_5\text{CO}_2\text{H}$ ligand is bound to iron in dichloromethane. Once again, only in the coordinating solvent acetonitrile are resonances for free pentafluorobenzoic acid at -139.47, -150.29, and -161.96 ppm observed (Figure 4.10C).

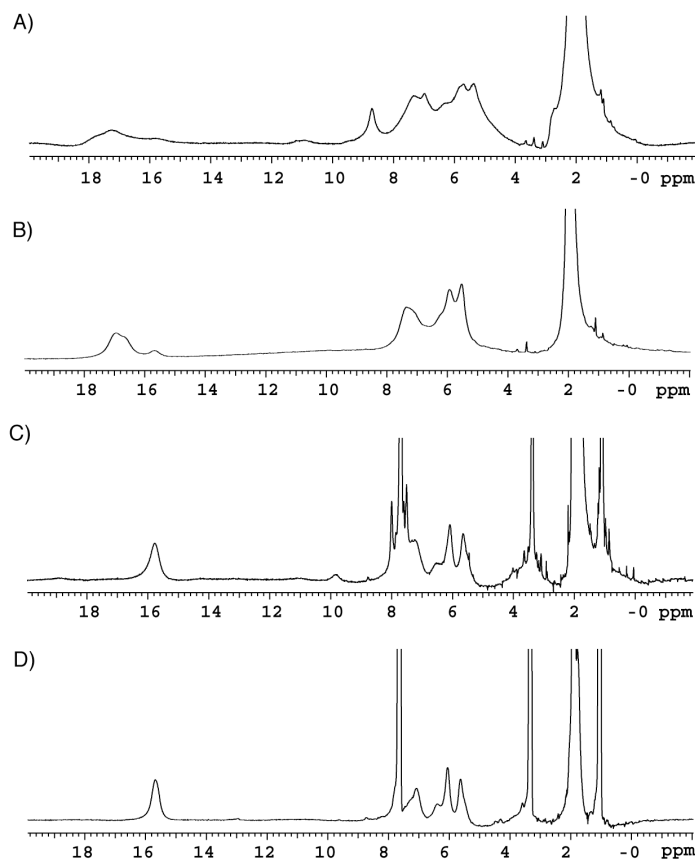


Figure 4.9. ^1H NMR spectra (CD_3CN , 500 MHz, $-30\text{ }^\circ\text{C}$) of A) $[\text{Fe}_2(\mu\text{-O}_2)(N\text{-EtHPTB})(\text{PhCO}_2)](\text{BF}_4)_2$, B) $[\text{Fe}_2(\mu\text{-O}_2)(N\text{-EtHPTB})(\text{C}_6\text{F}_5\text{CO}_2)](\text{OSO}_2\text{CF}_3)_2$, C) $[\text{Fe}_2(\mu\text{-O}_2)(N\text{-EtHPTB})(\text{PhCO}_2)](\text{BF}_4)_2/\text{H}[\text{BAr}^{\text{F}}_4]$ (1:1), and D) $[\text{Fe}_2(\mu\text{-O}_2)(N\text{-EtHPTB})(\text{C}_6\text{F}_5\text{CO}_2)](\text{OSO}_2\text{CF}_3)_2/\text{H}[\text{BAr}^{\text{F}}_4]$ (1:1). Spectral comparison between the benzoate and pentafluorobenzoate diiron analogs (A vs B and C vs. D) reveals proton peaks arising from the aromatic benzoate ring. The peaks at 11.40, 8.74, and 7.01 ppm are assigned to the benzoate protons in $[\text{Fe}_2(\mu\text{-O}_2)(N\text{-EtHPTB})(\text{PhCO}_2)](\text{BF}_4)_2$. When $\text{H}[\text{BAr}^{\text{F}}_4]$ was added to the (peroxo)diiron(III) solutions, the benzoate protons shifted to 9.82, 7.99, and 7.50 ppm. The aromatic protons of the $[\text{BAr}^{\text{F}}_4]^-$

anion appear at 7.7 ppm. Spectrum A: $\delta = 5.41, 5.81, 7.01, 7.39, 8.74, 11.40, 18.08$ ppm. Spectrum B: $\delta = 5.52, 5.92, 7.36, 15.68, 16.94$ ppm. Spectrum C: $\delta = 5.65, 6.08, 7.23, 7.50, 7.99, 9.82, 15.78$ ppm. Spectrum D: $5.66, 6.09, 7.11, 15.67$ ppm.

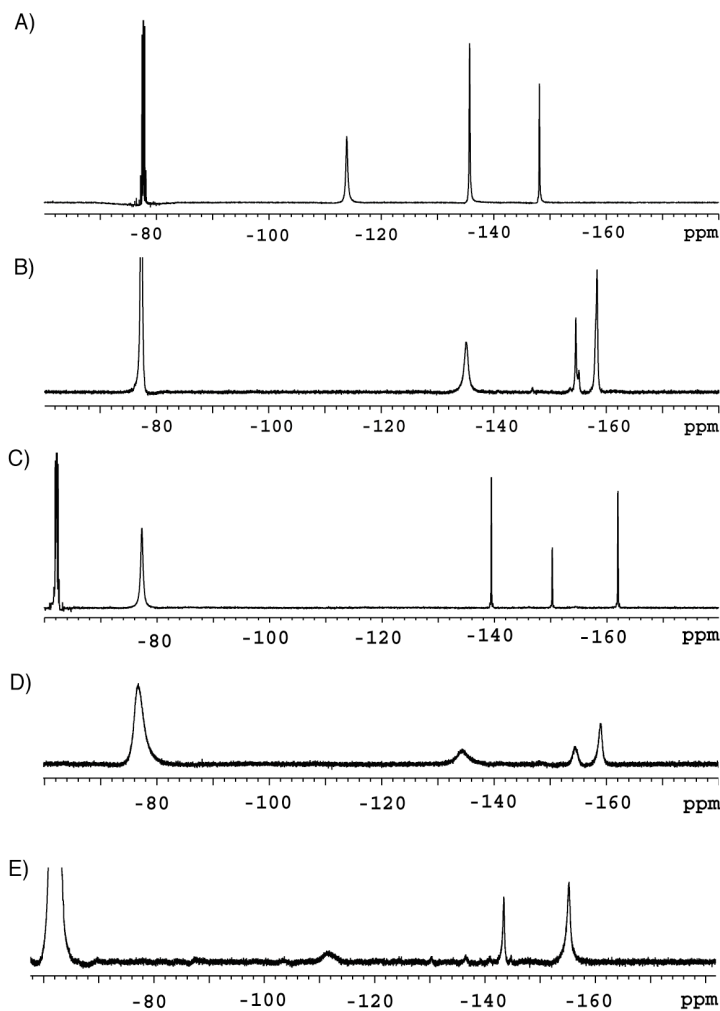


Figure 4.10. ^{19}F NMR spectra (470 MHz, $-30\text{ }^\circ\text{C}$) of A) compound **2** in CD_3CN , B) $[\mathbf{2}\cdot\text{O}_2](\text{OSO}_2\text{CF}_3)_2$ in CD_3CN , C) $[\mathbf{2}\cdot\text{O}_2](\text{OSO}_2\text{CF}_3)_2/\text{H}[\text{BAr}^{\text{F}}_4]$ (1:3) in CD_3CN , D) $[\mathbf{2}\cdot\text{O}_2](\text{OSO}_2\text{CF}_3)_2$ in CH_2Cl_2 , and E) $[\mathbf{2}\cdot\text{O}_2](\text{OSO}_2\text{CF}_3)_2/\text{H}[\text{BAr}^{\text{F}}_4]$ (1:3) in CH_2Cl_2 . The signals at approx. -77 and -62 ppm are ascribed to the fluorine atoms of the triflate and $[\text{BAr}^{\text{F}}_4]^-$ anions, respectively. The narrow peaks in spectrum C are indicative of free pentafluorobenzoic acid. It is uncertain why spectrum E does not display a peak at -77 ppm for the triflate anion. Spectrum A: $\delta = -113.87, -135.71, -148.12$ ppm. Spectrum B: $\delta = -135.16, -154.62, -158.39$ ppm. Spectrum C: $\delta = -139.47, -150.29, -161.96$ ppm. Spectrum D: $\delta = -134.34, -154.44, -159.02$ ppm. Spectrum E: $\delta = -111.30, -142.96, -154.79$ ppm.

4.4. Conclusion

In conclusion, the spectroscopic evidence (Table 4.1) clearly indicate that the carboxylate is preferred over the peroxo ligand as the site of protonation in these (peroxo)diiron(III) model complexes, a possible structure for which is depicted in Scheme 4.2. Our results suggest that, during the O₂ activation steps in the catalytic cycle of sMMO and related enzymes, protons might generate and/or transform the (peroxo)diiron(III) core by inducing a carboxylate shift,^{16,18} possibly increasing the electrophilicity of the diiron unit and facilitating substrate access to the active site. Preliminary studies demonstrate, however, that [1a·O₂]H⁺ does not display significantly enhanced reactivity toward external substrates compared to that of 1a·O₂ but this oxidation chemistry must be examined in more detail before any conclusions could be drawn.

4.5. References

- (1) Leahy, J. G.; Batchelor, P. J.; Morcomb, S. M. *FEMS Microbiol. Rev.* **2003**, *27*, 449-479.
- (2) Merkx, M.; Kopp, D. A.; Sazinsky, M. H.; Blazyk, J. L.; Müller, J.; Lippard, S. J. *Angew. Chem., Int. Ed. Engl.* **2001**, *40*, 2782-2807.
- (3) Cafaro, V.; Izzo, V.; Scognamiglio, R.; Notomista, E.; Capasso, P.; Casbarra, A.; Pucci, P.; Di Donato, A. *Appl. Environ. Microbiol.* **2004**, *70*, 2211-2219.
- (4) Cafaro, V.; Scognamiglio, R.; Viggiani, A.; Izzo, V.; Passaro, I.; Notomista, E.; Dal Piaz, F.; Amoresano, A.; Casbarra, A.; Pucci, P.; Di Donato, A. *Eur. J. Biochem.* **2002**, *269*, 5689-5699.
- (5) Arengi, F. L. G.; Berlanda, D.; Galli, E.; Sello, G.; Barbieri, P. *Appl. Environ. Microbiol.* **2001**, *67*, 3304-3308.

- (6) Cadieux, E.; Vrajmasu, V.; Achim, C.; Powlowski, J.; Münck, E. *Biochemistry* **2002**, *41*, 10680-10691.
- (7) Gallagher, S. C.; Cammack, R.; Dalton, H. *Eur. J. Biochem.* **1997**, *247*, 635-641.
- (8) Kotani, T.; Yamamoto, T.; Yurimoto, H.; Sakai, Y.; Kato, N. *J. Bacteriol.* **2003**, *185*, 7120-7128.
- (9) Hamamura, N.; Storfa, R. T.; Semprini, L.; Arp, D. *J. Appl. Environ. Microbiol.* **1999**, *65*, 4586-4593.
- (10) Lieberman, R. L.; Rosenzweig, A. C. *Crit. Rev. Biochem. Mol. Biol.* **2004**, *39*, 147-164.
- (11) Shu, L.; Nesheim, J. C.; Kauffmann, K.; Münck, E.; Lipscomb, J. D.; Que, L., Jr. *Science* **1997**, *275*, 515-518.
- (12) Liu, K. E.; Valentine, A. M.; Wang, D.; Huynh, B. H.; Edmondson, D. E.; Salifoglou, A.; Lippard, S. J. *J. Am. Chem. Soc.* **1995**, *117*, 10174-10185.
- (13) Brazeau, B. J.; Lipscomb, J. D. *Biochemistry* **2000**, *39*, 13503-13515.
- (14) Rosenzweig, A. C.; Nordlund, P.; Takahara, P. M.; Frederick, C. A.; Lippard, S. J. *Chem. Biol.* **1995**, *2*, 409-418.
- (15) Baik, M.-H.; Newcomb, M.; Friesner, R. A.; Lippard, S. J. *Chem. Rev.* **2003**, *103*, 2385-2419.
- (16) Dunitz, B. D.; Beachy, M. D.; Cao, Y.; Whittington, D. A.; Lippard, S. J.; Friesner, R. A. *J. Am. Chem. Soc.* **2000**, *122*, 2828-2839.
- (17) Friesner, R. A.; Baik, M.-H.; Gherman, B. F.; Guallar, V.; Wirstam, M.; Murphy, R. B.; Lippard, S. J. *Coord. Chem. Rev.* **2003**, *238-239*, 267-290.
- (18) Rinaldo, D.; Philipp, D. M.; Lippard, S. J.; Friesner, R. A. *J. Am. Chem. Soc.* **2007**, *129*, 3135-3147.

- (19) Tinberg, C. E.; Lippard, S. J. *Biochemistry* **2010**, *49*, 7902-7912.
- (20) Dong, Y.; Yan, S.; Young, V. G., Jr.; Que, L., Jr. *Angew. Chem., Int. Ed. Engl.* **1996**, *35*, 618-620.
- (21) Ookubo, T.; Sugimoto, H.; Nagayama, T.; Masuda, H.; Sato, T.; Tanaka, K.; Maeda, Y.; Ōkawa, H.; Hayashi, Y.; Uehara, A.; Suzuki, M. *J. Am. Chem. Soc.* **1996**, *118*, 701-702.
- (22) Kim, K.; Lippard, S. J. *J. Am. Chem. Soc.* **1996**, *118*, 4914-4915.
- (23) Zhang, X.; Furutachi, H.; Fujinami, S.; Nagatomo, S.; Maeda, Y.; Watanabe, Y.; Kitagawa, T.; Suzuki, M. *J. Am. Chem. Soc.* **2004**, *127*, 826-827.
- (24) Tinberg, C. E.; Lippard, S. J. *Biochemistry* **2009**, *48*, 12145-12158.
- (25) Lee, S.-K.; Lipscomb, J. D. *Biochemistry* **1999**, *38*, 4423-4432.
- (26) Dong, Y.; Ménage, S.; Brennan, B. A.; Elgren, T. E.; Jang, H. G.; Pearce, L. L.; Que, L., Jr. *J. Am. Chem. Soc.* **1993**, *115*, 1851-1859.
- (27) Jensen, K. P.; Bell, C. B., III; Clay, M. D.; Solomon, E. I. *J. Am. Chem. Soc.* **2009**, *131*, 12155-12171.
- (28) McKee, V.; Zvagulis, M.; Dagdigian, J. V.; Patch, M. G.; Reed, C. A. *J. Am. Chem. Soc.* **1984**, *106*, 4765-4772.
- (29) Brookhart, M.; Grant, B.; Volpe, A. F., Jr. *Organometallics* **1992**, *11*, 3920-3922.
- (30) Yakelis, N. A.; Bergman, R. G. *Organometallics* **2005**, *24*, 3579-3581.
- (31) Hagen, K. S. *Inorg. Chem.* **2000**, *39*, 5867-5869.
- (32) Brunold, T. C.; Tamura, N.; Kitajima, N.; Moro-oka, Y.; Solomon, E. I. *J. Am. Chem. Soc.* **1998**, *120*, 5674-5690.
- (33) Nara, M.; Torii, H.; Tasumi, M. *J. Phys. Chem.* **1996**, *100*, 19812-19817.
- (34) Deacon, G. B.; Phillips, R. J. *Coord. Chem. Rev.* **1980**, *33*, 227-250.

- (35) Nakamoto, K.; *Part B: Applications in Coordination, Organometallic, and Bioinorganic Chemistry*; 5th ed.; John Wiley & Sons, Inc.: New York, 1997.
- (36) Costas, M.; Cady, C. W.; Kryatov, S. V.; Ray, M.; Ryan, M. J.; Rybak-Akimova, E. V.; Que, L., Jr. *Inorg. Chem.* **2003**, *42*, 7519-7530.
- (37) Frisch, J. R.; Vu, V. V.; Martinho, M.; Münck, E.; Que, L., Jr. *Inorg. Chem.* **2009**, *48*, 8325-8336.

Chapter 5

Characterization of Synthetic (μ -1,2-Peroxo)diiron(III)

Complexes by Nuclear Resonance Vibrational Spectroscopy

5.1. Introduction

To understand the molecular mechanism of O₂ activation by carboxylate-bridged diiron enzymes,^{1,2} it is necessary to determine the kinetic behavior of the oxygenation process as well as the structure of protein intermediates that occur along the reaction pathway. Exposure of dioxygen to the Fe^{II}₂ cores of diiron proteins often generates transient (peroxo)diiron(III) intermediates.³⁻⁹ Chart 5.1 depicts the possible coordination modes of a bridging O₂ ligand at a dinuclear center.^{1,10} Studies of the peroxide units in the R2 subunit of ribonucleotide reductase (RNR),^{11,12} soluble methane monooxygenase hydroxylase (sMMOH),^{13,14} toluene 4-monooxygenase hydroxylase (T4MoH),¹⁵ and Δ^9 desaturase¹⁶ have suggested that the reduced O₂ molecule is bound to the diiron core in a μ -1,2 fashion. Recent theoretical investigations of the T201S mutant of toluene/*o*-xylene monooxygenase hydroxylase (ToMOH)^{17,18} reveal that both μ -1,2- and μ -1,1-(peroxo)diiron species form upon reaction with dioxygen; the terminally bridged dioxygen adduct is believed to be protonated and further stabilized by hydrogen-bonding interaction with a nearby threonine residue.¹⁹ Attempts to characterize the ToMOH intermediates by either resonance Raman spectroscopy or X-ray crystallography have not yet been successful. Although quantum mechanical/ molecular mechanical (QM/MM) studies have provided some insight into the nature of these Fe₂(O₂) units,²⁰⁻²⁴ new tools are required to study the protein intermediates directly.

A powerful technique to examine the primary coordination sphere of iron-containing materials is nuclear resonance vibrational spectroscopy (NRVS).²⁵⁻²⁸ In this method, the vibrational spectra of Mössbauer-active nuclei are obtained by tuning the incident photon energy to excite vibrational states that are coincident with nuclear excitations. NRVS is more selective

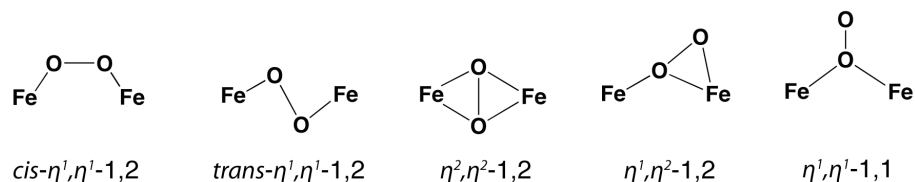


Chart 5.1. Possible geometries of the (μ -peroxo)diiron unit.

and comprehensive than Raman or infrared spectroscopy because it reveals all vibrations involving motion of the probe nucleus. NRVS measurements require synchrotron radiation and are limited to nuclei that have favorable properties, such as an excitation energy that is within the range of available monochromators, a sufficiently long nuclear excitation lifetime, a sensitive nuclear response, and a scattering energy that does not exceed the detection limit of an avalanche photodiode detector (APD). NRVS is an invaluable addition to the bioinorganic toolbox.²⁹⁻³¹ For example, it has been used to assign the vibrational modes of diatomic molecules coordinated to synthetic porphyrins^{27,32,33} and to detect nitrosylated iron-sulfur clusters in proteins.^{34,35} NRVS and density functional theoretical (DFT) studies of mononuclear Fe(III)-OOH³⁶ and Fe(IV)=O^{37,38} compounds have provided insight into their unique chemical properties.

To evaluate whether NRVS could be applied to interrogate the binding mode of O₂ at the diiron centers of oxygenated protein intermediates, synchrotron-based vibrational measurements of synthetic (peroxo)diiron(III) compounds were undertaken. Among the various Fe₂(O₂) geometries that are shown in Chart 5.1, only the *cis*- $\eta^1, \eta^1-1,2$ - and *trans*- $\eta^1, \eta^1-1,2$ -dioxygen adducts of Fe₂ units have been crystallographically characterized.³⁹⁻⁴² The $\eta^2, \eta^2-1,2$ -,⁴³ $\eta^1, \eta^2-1,2$ -⁴⁴ and $\eta^1, \eta^1-1,1$ -dioxygen⁴⁵⁻⁴⁷ bridging motifs have been reported for other dinuclear transition metal complexes. In the present NRVS study, the compounds [Fe₂(μ -O₂)(*N*-EtHPTB)(PhCO₂)]²⁺ (**1**·O₂, where *N*-EtHPTB = anion of *N,N,N',N'*-tetrakis(2-benzimidazolylmethyl)-2-hydroxy-1,3-

diaminopropane)^{39,48} and $[\text{Fe}_2(\mu\text{-O}_2)(\text{HB}(\text{iPrpz})_3)_2(\text{PhCH}_2\text{CO}_2)_2]$ ($4 \cdot \text{O}_2$, where $\text{HB}(\text{iPrpz})_3 = \text{tris}(3,5\text{-diisopropylpyrazoyl})\text{hydroborate}$)^{40,49} were selected as representative examples of *cis*- η^1, η^1 -1,2- and *trans*- η^1, η^1 -1,2-dioxygen bound diiron species, respectively (Figure 5.2). This chapter describes the first successful characterization of (peroxo)diiron(III) complexes by NRVS and their normal coordinate analysis.

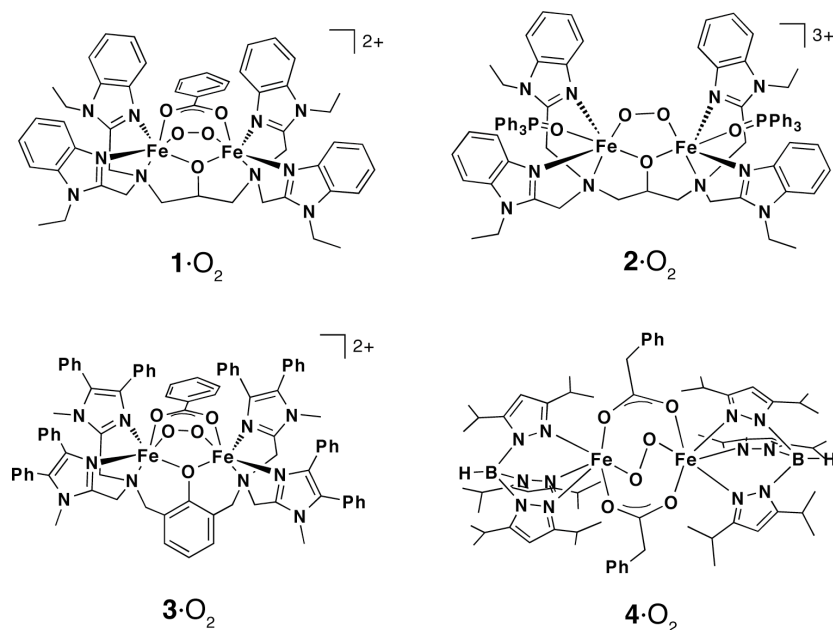


Chart 5.2. A depiction of the proposed structure of $[\text{Fe}_2(\mu\text{-O}_2)(\text{N-EtHPTB})(\text{PhCO}_2)]^{2+}$ ($1 \cdot \text{O}_2$, top left). The X-ray structures of $[\text{Fe}_2(\mu\text{-O}_2)(\text{N-EtHPTB})(\text{OPPh}_3)_2]^{3+}$ ($2 \cdot \text{O}_2$, top right),³⁹ $[\text{Fe}_2(\mu\text{-O}_2)(\text{Ph-bimp})(\text{PhCO}_2)_2]^{2+}$ ($3 \cdot \text{O}_2$, bottom left),⁴¹ and $[\text{Fe}_2(\mu\text{-O}_2)(\text{HB}(\text{iPrpz})_3)_2(\text{PhCH}_2\text{CO}_2)_2]$ ($4 \cdot \text{O}_2$, bottom right)⁴⁰ have been determined. The Cartesian coordinates of the $\text{Fe}_2\text{N}_6\text{O}(\mu\text{-O}_2)(\mu\text{-PhCO}_2)$ core of $3 \cdot \text{O}_2$ was used for normal mode calculations of $1 \cdot \text{O}_2$.

5.2. Experimental

Materials and Methods: Commercial reagents were used as received without further purification. Air-sensitive manipulations were performed using standard Schlenk techniques or under a nitrogen atmosphere inside an MBraun drybox. Solvents were saturated with argon and purified by passage through two columns of activated alumina. The $[\text{}^{57}\text{Fe}_2(\text{N-}$

EtHPTB)(PhCO₂)](BPh₄)₂ complex,⁵⁰ and K[HB(ⁱPrpz)₃] ligand⁵¹ were synthesized according to literature procedures. The 57-iron(II) bromide salt was prepared from ⁵⁷Fe metal (98%) and concentrated hydrobromic acid.⁵² 18-Dioxygen (99%) was obtained from ICON isotopes and used as received.

General Physical Methods: NMR spectra were recorded on 500 MHz Varian Mercury spectrometers. Chemical shifts for ¹H NMR spectra were referenced to residual solvent peaks. Absorption spectra were acquired on a Cary 50 spectrophotometer using a custom-made quartz cuvette (path length = 1.74 cm) containing a jacketed dewar. An acetonitrile/dry ice bath was used to maintain the samples at -30 °C. Solid-state FTIR spectra were acquired with a ThermoNicolet Avatar 360 spectrophotometer using the OMNIC software.

Synthesis

[⁵⁷Fe(HB(ⁱPrpz)₃)Br] (**4-Br**). The following procedure was slightly modified from that reported for unenriched **4-Br**.⁴⁰ Solid ⁵⁷FeBr₂ (400 mg, 794 μmol) and K[HB(ⁱPrpz)₃] (172 mg, 794 μmol) were dissolved in 3 mL of THF and stirred for 3 h. The solution was evaporated to dryness and the product was extracted into CH₂Cl₂ (3 mL). The solution was filtered through a glass wool plug and the filtrate was concentrated to half its volume. The CH₂Cl₂ solution was transferred to a small tube and the tube was placed inside a sealed vial containing a solution of toluene. After standing overnight, most of the CH₂Cl₂ solution had diffused out of the tube, leaving a pink crystalline solid. The solid was isolated by filtration and washed with diethyl ether (158 mg, 33%). The IR spectrum of the product matched that previously reported.⁴⁰ ¹H NMR (CD₃CN, 500 MHz, paramagnetically broadened): δ 60.86, 16.19, 3.79, -2.76, -6.25 ppm.

[⁵⁷Fe(HB(ⁱPrpz)₃)(PhCH₂CO₂)] (**4**). The following procedure was modified from that reported for unenriched **4**.⁴⁰ Solid [⁵⁷Fe(HB(ⁱPrpz)₃)Br] (158 mg, 263 μmol) was dissolved in 1 mL of

CH₂Cl₂/THF (1:1) and added to a 1 mL solution of thallium triflate (93 mg, 263 μmol) in THF. Upon combining the two solutions, the mixture instantaneously became cloudy and a white precipitate began to form. After stirring for 2 h, the insoluble TlBr was removed by filtration. Sodium phenylacetate (42 mg, 263 μmol) was added to the colorless filtrate and the mixture was stirred for 4 h. The slightly murky solution was filtered through a glass wool plug and the solvent was removed *in vacuo*. The product was extracted into pentane, filtered, and the filtrate was evaporated to afford a sparkly white solid (155 mg, 90%). The IR spectrum of the product matches that previously reported.⁴⁰ ¹H NMR (CD₃CN, 500 MHz, paramagnetically broadened): δ 76.60, 60.76, 16.33, 6.38, 6.05, 3.72-1.28, -22.56 ppm.

Preparation of [⁵⁷Fe₂(O₂)(N-EtHPTB)(PhCO₂)](BPh₄)₂ for NRVS. A 50 mM THF solution (0.5 mL) of [⁵⁷Fe₂(N-EtHPTB)(PhCO₂)](BPh₄)₂ was prepared inside the glovebox and added to a septum-sealed vessel. The flask was brought outside of the glovebox and cooled to -78 °C using a dry ice/acetone cooling bath. For the **1**·¹⁶O₂ sample, the diiron(II) solution was injected with 10 mL of ¹⁶O₂ using a syringe. For the **1**·¹⁸O₂ sample, ¹⁸O₂ gas was directly transferred to the diiron(II) solution using a high-vacuum manifold. After stirring for ~10 min, 150 μL of the deep blue solution was transferred via syringe, pre-cooled to ensure that the oxygenated solution does not warm up above -30 °C, to an NRVS cell and immediately frozen in liquid nitrogen.

Preparation of [⁵⁷Fe₂(O₂)(HB(ⁱPrpz)₃)₂(PhCH₂CO₂)₂] for NRVS. A 21 mM pentane/diethyl ether (1:1) solution (0.5 mL) of the mononuclear [⁵⁷Fe(HB(ⁱPrpz)₃)(PhCH₂CO₂)] complex was prepared inside the glovebox and added to a septum-sealed vessel. The flask was brought outside of the glovebox and cooled to -78 °C using a dry ice/acetone cooling bath. To generate **4**·¹⁶O₂ and **4**·¹⁸O₂, about 5 mL of ¹⁶O₂ or ¹⁸O₂, respectively, was injected into the iron(II) solution. After stirring for ~10 min, 150 μL of the deep green solution was transferred via syringe (pre-cooled to

ensure that the oxygenated solution does not warm up above -30 °C) to an NRVS cell and immediately frozen in liquid nitrogen.

Nuclear Resonance Vibrational Spectroscopy (NRVS)

Data Acquisition. NRVS measurements were performed in collaboration with Dr. Hongxin Wang (UCD), Dr. Christine E. Tinberg (MIT), Dr. Yoshitaka Yoda (SPring-8, Japan), and Prof. Stephen P. Cramer (UCD). Samples were loaded into $3 \times 7 \times 1 \text{ mm}^3$ (interior dimensions) Lucite cuvettes wrapped with Mylar tape. ^{57}Fe NRVS spectra were recorded using published procedures²⁸ at the BL09XU beamline at SPring-8, Japan. Fluxes were on the order of $\sim 2 \times 10^9$ photons/sec in a 1.2 eV bandpass. During NRVS measurements, samples were maintained at low temperatures using a liquid He cryostat (head temperature $< 10 \text{ K}$). The real sample temperatures were calculated from the ratio of anti-Stokes to Stokes intensity by the expression²⁷ $S(-E) = S(E)e^{(-E/kT)}$ and determined to be at $\sim 35\text{-}50 \text{ K}$. Nuclear fluorescence and delayed Fe K fluorescence were recorded with an APD array. Each scan took about 50 min, and all scans were added and normalized to the intensity of the incident beam using the PHOENIX program.⁵³ Spectra were recorded between 0 and 600 cm^{-1} . The number of scans acquired for each sample are as follows: one for **1**, five for **1**· $^{16}\text{O}_2$, three for **1**· $^{18}\text{O}_2$, two for **4**, five for **4**· $^{16}\text{O}_2$, and three for **4**· $^{18}\text{O}_2$.

Empirical Force Field Normal Mode Analysis. Empirical normal mode calculations were performed by Eric Dowty (Shape Software) and conducted using the program VIBRATZ,^{54,55} which uses the Urey-Bradley force field. Analysis of **1** utilized only the Cartesian coordinates of the $\text{Fe}_2\text{N}_6\text{O}_2(\mu\text{-PhCO}_2)$ core to reduce the complexity of the calculations. Since the Fe–N/O modes are “uncoupled” in this virtual model, differences in the calculated peak intensities compared to those observed for **1** are not meaningful because they depend on the precise

stretching force constants and bond angles of *all* the atoms involved in the vibration. The normal mode calculations for $[\text{Fe}_2(\mu\text{-O}_2)(N\text{-EtHPTB})(\text{PhCO}_2)]^{2+}$ ($\mathbf{1}\cdot\text{O}_2$) employed the Cartesian coordinates of the $\text{Fe}_2\text{N}_6\text{O}(\mu\text{-O}_2)(\mu\text{-PhCO}_2)$ core from the X-ray structure of $[\text{Fe}_2(\mu\text{-O}_2)(\text{Ph-bimp})(\text{PhCO}_2)_2]^{2+}$ ($\mathbf{3}\cdot\text{O}_2$, Chart 5.2)⁴¹ using a C_s point group. It was necessary to use $\mathbf{3}\cdot\text{O}_2$ as an approximate model for $\mathbf{1}\cdot\text{O}_2$ because the structure of $\mathbf{1}\cdot\text{O}_2$ is not available. The calculated results are intended to provide a qualitative description of the modes that involve significant motion of the $\text{Fe}_2(\text{O}_2)$ core, rather than a complete description of the full molecule. Because the simulated frequencies do not take into account the complex bonding interactions of the *N*-EtHPTB ligand with the diiron centers, the calculated intensities are not an exact match to those observed in the NRVS of $\mathbf{1}\cdot\text{O}_2$. Nevertheless, the modes above 350 cm^{-1} can be assigned unequivocally to the $\text{Fe}_2(\text{O}_2)$ unit because they are well separated from the main Fe–N/O manifold ranging from $\sim 150\text{-}350\text{ cm}^{-1}$.

5.3. Results and Discussion

NRVS of Diiron *N*-EtHPTB Complexes. To determine the iron-ligand modes that arise from the *N*-EtHPTB and benzoate groups, the parent diiron(II) $[\text{}^{57}\text{Fe}_2(N\text{-EtHPTB})(\text{PhCO}_2)]^{2+}$ ($\mathbf{1}$)⁵⁰ complex was studied by NRVS. As shown in Figure 5.1, polycrystalline $\mathbf{1}$ exhibits intense features ranging from 150 to 350 cm^{-1} . Because of the mixed ligand environment of $\mathbf{1}$, this large envelope consists of several overlapping Fe–N and Fe–O vibrations from the benzimidazole, amine, alkoxide, and carboxylate units that are coordinated to the iron atoms. The simulated peak intensities are not an exact match to those observed in the NRVS because knowledge of the precise force constants and bonding angles of all the atoms involved in a given mode is necessary to obtain meaningful simulations of the vibrational intensities.

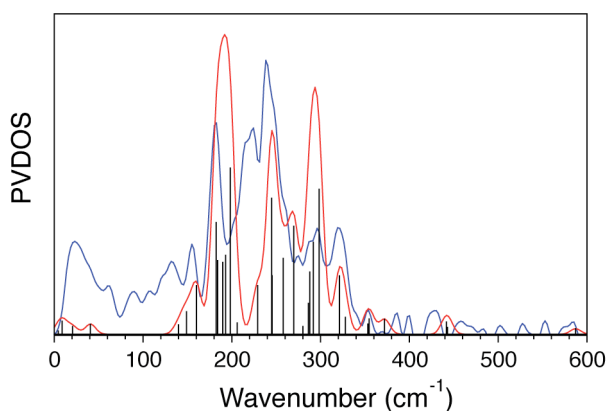


Figure 5.1. ^{57}Fe partial vibrational density of states (PVDOS) for polycrystalline $[\text{}^{57}\text{Fe}_2(\text{N-EtHPTB})(\text{PhCO}_2)]^{2+}$ (**1**) measured by NRVS at ~ 10 K. Blue spectrum: selected peaks = 182, 224, 240, 298, and 321 cm^{-1} . Red spectrum = 192, 146, 195 cm^{-1} . Color scheme: raw data in blue, empirical data fit in red, and individual eigenmode frequencies/intensities before broadening in black.

When a solution of **1** in tetrahydrofuran was exposed to dioxygen a deep blue color rapidly developed, indicating generation of the (peroxo)diiron(III) complex $[\text{}^{57}\text{Fe}_2(\mu\text{-O}_2)(\text{N-EtHPTB})(\text{PhCO}_2)]^{2+}$ (**1**· O_2).^{48,50} The NRVS of **1**· $^{16}\text{O}_2$ and **1**· $^{18}\text{O}_2$ display intense bands between 150-300 cm^{-1} (Figure 5.2A and 5.2B, respectively), assigned to iron-ligand modes based on the spectrum of **1**. In addition to these features, higher energy frequencies at 338 and 467/480 cm^{-1} are observed for **1**· $^{16}\text{O}_2$, which shift upon ^{18}O -isotopic labeling to 311 and 446/458 cm^{-1} , respectively (Figure 5.2C) (the bands separated by “/” are attributed to Fermi splitting). By comparison to the un-oxygenated spectrum of **1**, it is clear that these higher energy modes in the NRVS of **1**· O_2 are due to motions involving the (peroxo)diiron(III) unit. These data are consistent with resonance Raman spectra that were previously reported.^{48,50} Most notably, the RR spectrum of **1**· $^{16}\text{O}_2$ exhibited bands at 466/474 cm^{-1} that shifted to a single peak at 452 cm^{-1} when $^{18}\text{O}_2$ was substituted for $^{16}\text{O}_2$ (Figure 5.3A). The 300-350 cm^{-1} region of the RR spectra does not show any resonance enhanced vibrations (Figure 5.3B). The fact that NRVS revealed a

distinct $\text{Fe}_2(\text{O}_2)$ mode not previously observed, at 338 cm^{-1} for $\mathbf{1}\cdot^{16}\text{O}_2$ and 311 cm^{-1} for $\mathbf{1}\cdot^{18}\text{O}_2$, illustrates the utility of this new spectroscopic tool.

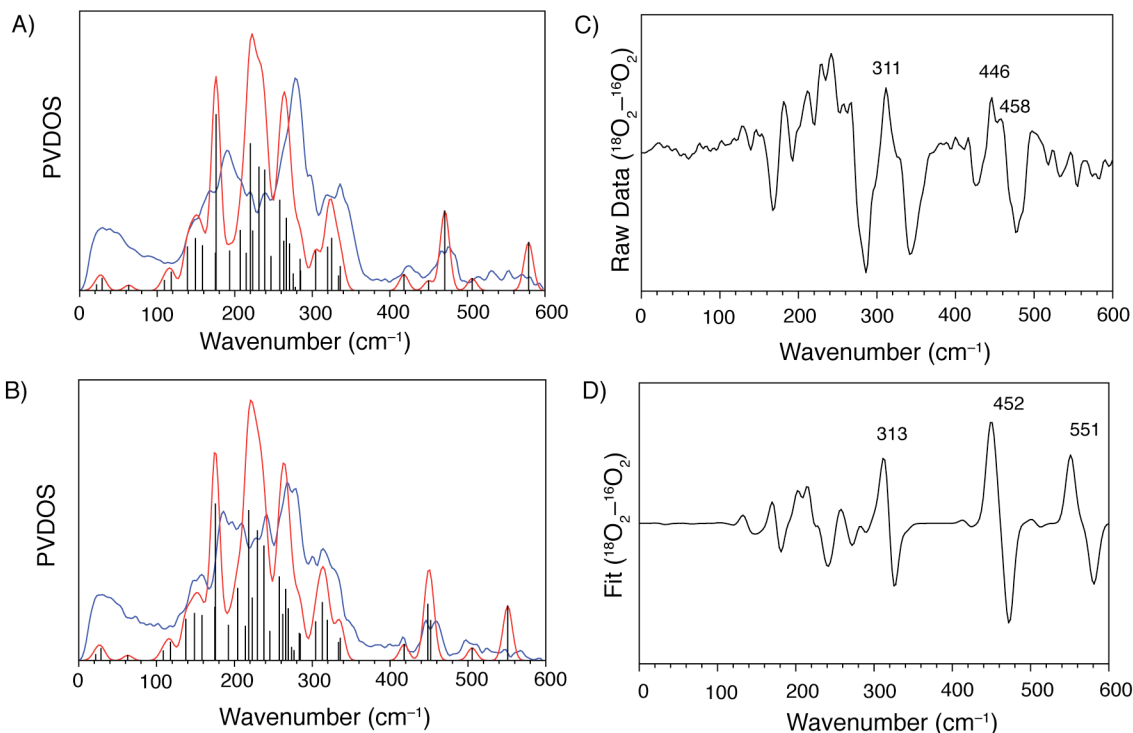


Figure 5.2. ^{57}Fe partial vibrational density of states (PVDOS) for frozen THF solutions of $[\text{}^{57}\text{Fe}_2(\mu\text{-}^{16}\text{O}_2)(N\text{-EtHPTB})(\text{PhCO}_2)]^{2+}$ ($\mathbf{1}\cdot^{16}\text{O}_2$, A) and $[\text{}^{57}\text{Fe}_2(\mu\text{-}^{18}\text{O}_2)(N\text{-EtHPTB})(\text{PhCO}_2)]^{2+}$ ($\mathbf{1}\cdot^{18}\text{O}_2$, B) measured by NRVS at $\sim 10\text{ K}$. The $\mathbf{1}\cdot^{18}\text{O}_2$ minus $\mathbf{1}\cdot^{16}\text{O}_2$ difference plots for the raw data and the empirical fits are shown in C and D, respectively. Panel A: blue spectrum (selected peaks) = 190, 280, 338, 467, 480 cm^{-1} ; red spectrum (selected peaks) = 176, 225, 264, 325, 471, 579 cm^{-1} . Panel B: blue spectrum (selected peaks) = 186, 241, 281, 311, 446, 458 cm^{-1} ; red spectrum (selected peaks) = 175, 224, 262, 313, 452, 551 cm^{-1} . Color scheme for plots A and B: raw data in blue, empirical data fit in red, and individual eigenmode frequencies/intensities before broadening in black.

NRVS of Iron $\text{HB}(\text{}^i\text{Prpz})_3^-$ Complexes. The NRVS of the mononuclear $[\text{Fe}(\text{HB}(\text{}^i\text{Prpz})_3^-)(\text{PhCH}_2\text{CO}_2)]$ (**4**) complex exhibits several Fe–N(pyrazole) and Fe–O(carboxylate) bands below 350 cm^{-1} (Figure 5.4, black). Upon addition of O_2 to **4** in pentane/diethyl ether (1:1) a dark green color appeared, indicating formation of the corresponding $\mathbf{4}\cdot\text{O}_2$ species.^{40,49} When the NRVS of

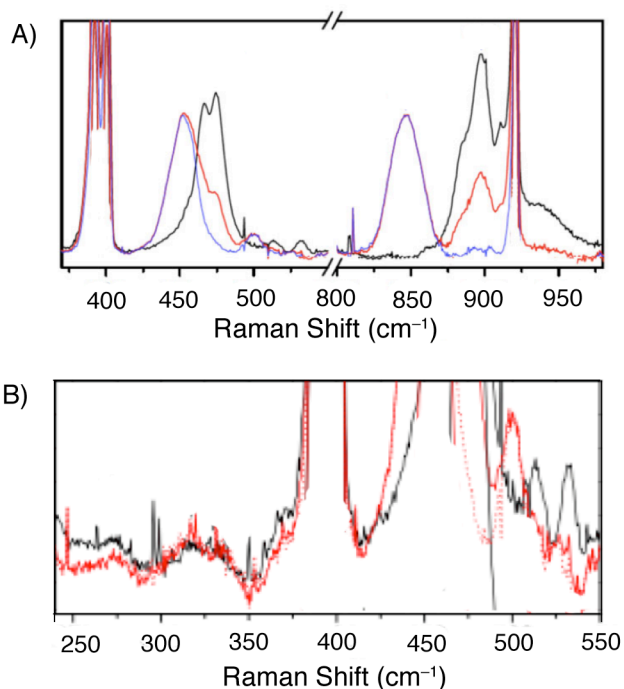


Figure 5.3. Resonance Raman spectra of $[\text{}^{57}\text{Fe}_2(\mu\text{-}^{16}\text{O}_2)(N\text{-EtHPTB})(\text{PhCO}_2)]^{2+}$ ($\mathbf{1}\text{-}^{16}\text{O}_2$, black) and $[\text{}^{57}\text{Fe}_2(\mu\text{-}^{18}\text{O}_2)(N\text{-EtHPTB})(\text{PhCO}_2)]^{2+}$ ($\mathbf{1}\text{-}^{18}\text{O}_2$, blue) previously reported.⁵⁰ In panel A ($\nu = 897$ (847), 532/513 (500), 474/466 (452) cm^{-1}), the red spectrum represents the $\mathbf{1}\text{-}^{18}\text{O}_2$ sample before a $\mathbf{1}\text{-}^{16}\text{O}_2$ impurity was subtracted. The lower energy region, in panel B, does not exhibit any clear isotopically shifted resonances.

$\mathbf{4}\text{-}^{16}\text{O}_2$ was recorded (Figure 5.4, red) the data suggested that the sample contained mostly starting material because its spectrum was nearly identical to that of $\mathbf{4}$ (Figure 5.4, black). Furthermore, RR measurements indicate that a new $\nu(\text{Fe-O})$ band should be observed at 415 cm^{-1} for $\mathbf{4}\text{-}^{16}\text{O}_2$.⁴⁰ Fortunately, the reaction of $\mathbf{4}$ with $^{18}\text{O}_2$ generated $\mathbf{4}\text{-}^{18}\text{O}_2$ and the product was detected by NRVS. As shown in Figure 5.4 (blue), $\mathbf{4}\text{-}^{18}\text{O}_2$ has several higher energy frequencies at 404, 444, and 486 cm^{-1} . Because an NRVS of $\mathbf{4}\text{-}^{16}\text{O}_2$ is not available for comparison to that of $\mathbf{4}\text{-}^{18}\text{O}_2$, it was not possible to identify peaks involving the $\text{Fe}_2(\text{O}_2)$ unit. Prior RR studies, however, attributed the frequency at 404 cm^{-1} to the $\nu(\text{Fe-O})$ mode of the iron-peroxo group in $\mathbf{4}\text{-}^{18}\text{O}_2$.^{48,50}

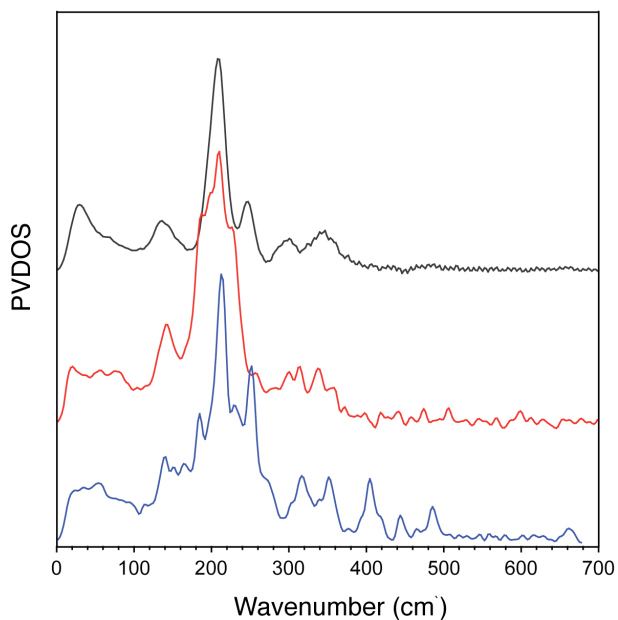


Figure 5.4. ^{57}Fe partial vibrational density of states (PVDOS) for $[\text{}^{57}\text{Fe}(\text{HB}(\text{}^i\text{Pr}_3\text{pz}_3))(\text{PhCH}_2\text{CO}_2)]$ (**4**, polycrystalline, black), $[\text{}^{57}\text{Fe}(\text{HB}(\text{}^i\text{Pr}_3\text{pz}_3))(\text{PhCH}_2\text{CO}_2)]/^{16}\text{O}_2$ (**4**/ $^{16}\text{O}_2$, pentane/diethyl ether 1:1, red), and $[\text{}^{57}\text{Fe}(\text{HB}(\text{}^i\text{Pr}_3\text{pz}_3))(\text{PhCH}_2\text{CO}_2)]/^{18}\text{O}_2$ (**4**/ $^{18}\text{O}_2$, pentane/diethyl ether 1:1, blue) measured by NRVS at ~ 10 K. The reaction of $[\text{}^{57}\text{Fe}(\text{HB}(\text{}^i\text{Pr}_3\text{pz}_3))(\text{PhCH}_2\text{CO}_2)]$ with $^{16}\text{O}_2$ does not appear to have proceeded to completion, as demonstrated by the similarity of its spectrum (red trace) to that of the starting iron(II) material (black trace). Black spectrum: $\nu = 133, 209, 248, 302, 346$ cm^{-1} ; red spectrum: $\nu = 141, 209, 298, 313, 338, 357$ cm^{-1} ; blue spectrum: $\nu = 138, 184, 214, 253, 316, 353, 404, 444, 486$ cm^{-1} .

Empirical Normal Coordinate Analysis. To obtain qualitative descriptions of the modes that show significant $^{16}\text{O}_2/^{18}\text{O}_2$ isotopic shifts in the NRVS, the data for **1**· $^{16}\text{O}_2$ and **1**· $^{18}\text{O}_2$ were subjected to normal coordinate calculations by the program VIBRATZ.^{54,55} Although a more quantitative analysis could be obtained using density functional theoretical (DFT) methods,³⁷ empirical data fitting is less computationally intensive and adequately models the features of interest. To test the validity of the VIBRATZ analysis, the NRVS of **1** was calculated using the Cartesian coordinates of the iron-bound atoms from its X-ray structure.⁴⁸ As shown by the red trace in Figure 5.1, the calculated spectrum reproduces the experimental one (blue) to a good first approximation. A rigorous assignment of this spectral region is beyond the scope of

this study. Most importantly, the calculated NRVS of **1** does not show any peaks above 350 cm^{-1} .

Because the exact structure of **1**·O₂ is not known, its primary coordination sphere was modeled using the Cartesian coordinates from the X-ray structure of [Fe₂(μ -O₂)(Phbimp)(PhCO₂)₂]²⁺ (**3**·O₂, Chart 5.2, bottom left).⁴¹ Although the structure of [Fe₂(μ -O₂)(N-EtHPTB)(OPPh₃)₂]³⁺ (**2**·O₂, Chart 5.2, top right), an analogue of **1**·O₂, has been determined by X-ray crystallography,³⁹ it has two triphenylphosphine oxide ligands rather than a benzoate group. Using the Fe₂N₆O(μ -O₂)(μ -PhCO₂) core of **3**·O₂ as a structural model, the NRVS of **1**·¹⁶O₂ and **1**·¹⁸O₂ were simulated (Figure 5.2A and 5.2B, respectively, red traces). The difference spectrum (**1**·¹⁸O₂ minus **1**·¹⁶O₂) shows that ¹⁸O₂ substitution afforded three main isotopically shifted peaks in the 0-600 cm^{-1} region (Figure 5.2D). A fourth isotope sensitive mode was also calculated at 898(-51) cm^{-1} , where the number in parentheses represents the change in wavenumbers upon ¹⁸O₂ substitution, outside of the window that was recorded for the **1**·O₂ samples.

The highest energy calculated feature, 898(-51) cm^{-1} , is primarily a symmetric O–O stretching mode (ν_1 , Figure 5.5). Because ν_1 does not involve significant motion of the iron atoms, it is not likely to be very intense in the NRVS. The experimentally determined value for the symmetric $\nu(\text{O}–\text{O})$ mode of **1**·O₂ is 897(-50) cm^{-1} (Figure 5.3A),⁵⁰ in good agreement with the calculated one. The second highest energy mode falls at 579(-28) cm^{-1} and is essentially the asymmetric O–O stretching/rotation of the peroxo ligand against the iron atoms (ν_2 , Figure 5.5).

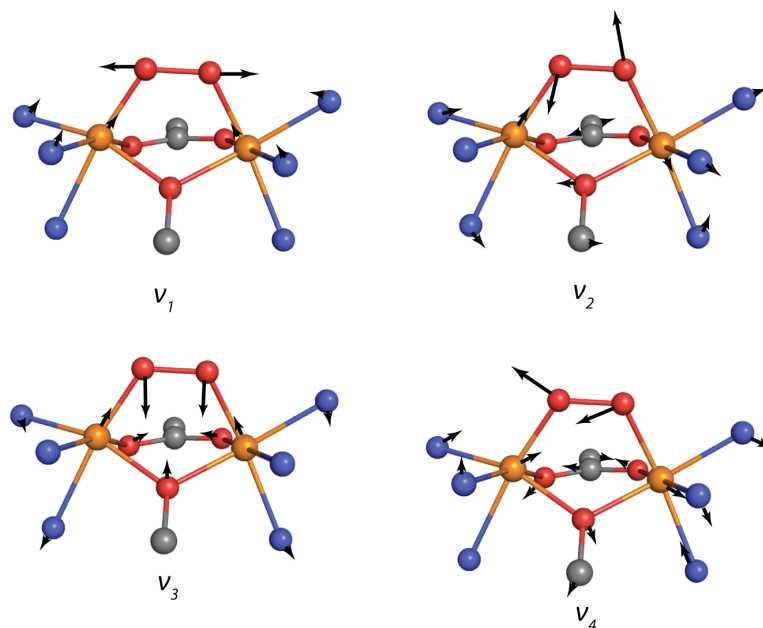


Figure 5.5. Normal mode calculations for $\mathbf{1}\cdot\text{O}_2$ using the X-ray coordinates of $[\text{Fe}_2(\mu\text{-O}_2)(\text{Ph-bimp})(\text{PhCO}_2)_2]^{2+} (\mathbf{3}\cdot\text{O}_2)$, showing the vibrations that involve the Fe_2O_2 unit. The black arrows indicate the direction and relative degree of motion of the atoms to which they are attached. Color scheme: orange, iron; red, oxygen; blue, nitrogen; and gray, carbon.

Although the net stretching of the Fe–O(peroxo) bonds is minimal, ν_2 is expected to be observable by NRVS. The spectra of $\mathbf{1}\cdot\text{O}_2$, however, do not show any features in this region. The absence of a clear signal at this frequency may be due to the lower resolution of the NRVS spectrum at higher wavenumbers. It is possible that the weak features at $532/513\text{ cm}^{-1}$ in the RR of $\mathbf{1}\cdot\text{O}_2$ (Figure 5.3A) may correspond to this ν_2 mode.⁵⁰ The calculated value at $471(-19)\text{ cm}^{-1}$ (ν_3) is attributed to the symmetric Fe–O–O–Fe stretching motion and the frequency is dependent almost entirely on the Fe–OO force constant (Figure 5.5). The theoretical frequency of ν_3 (471 cm^{-1}) matches well to those of $\mathbf{1}\cdot^{16}\text{O}_2$ observed at $467/480\text{ cm}^{-1}$ in the NRVS (Figure 5.2A) and at $466/474\text{ cm}^{-1}$ in the RR spectra (Figure 5.3A).⁵⁰ Lastly, the isotopically shifted peak that occurs at lowest energy was at $325(-12)\text{ cm}^{-1}$ (ν_4 , Figure 5.5). In this mode, the O–O group moves as a unit parallel to the Fe–Fe vector and perpendicular to the pseudo-mirror plane that

bisects the Fe₂(O₂) atoms. It is possible that the ν_4 mode is absent in the RR spectrum because it is not strongly coupled to the electronic transition induced by the 647 nm excitation wavelength employed in the experiment.

5.4. Conclusion

The vibrational profiles of two synthetic (peroxo)diiron(III) complexes have been revealed by nuclear resonance vibrational spectroscopy. Through ¹⁶O₂/¹⁸O₂ isotopic labeling, the frequencies that correspond to motions of the Fe₂(O₂) unit in [Fe₂(μ -O₂)(*N*-EtHPTB)(PhCO₂)]²⁺ have been definitively assigned. Most notably, a lower energy mode at ~338 cm⁻¹ involving parallel motion between the Fe–Fe and O–O groups has been detected by NRVS, a feature that was not previously observed by resonance Raman spectroscopy. The NRVS of [Fe₂(μ -¹⁸O₂)(HB(^{*iPr*}pZ)₃)₂(PhCH₂CO₂)₂)] displays several distinct modes above 350 cm⁻¹ but these frequencies have not been assigned. A more comprehensive study is needed to correlate the vibrational characteristics of a (peroxo)diiron unit to its O₂ coordination geometry. Nevertheless, these results demonstrate that synchrotron-based NRVS is a useful tool to investigate the structural and chemical nature of oxygenated diiron protein intermediates and may help to clarify many remaining questions regarding the mechanism of O₂ activation in non-heme diiron enzymes.

5.5. References

- (1) Feig, A. L.; Lippard, S. J. *Chem. Rev.* **1994**, *94*, 759-805.
- (2) Wallar, B. J.; Lipscomb, J. D. *Chem. Rev.* **1996**, *96*, 2625-2658.
- (3) Edmondson, D. E.; Huynh, B. H. *Inorg. Chim. Acta*, *252*, 399-404.

- (4) Liu, K. E.; Wang, D.; Huynh, B. H.; Edmondson, D. E.; Salifoglou, A.; Lippard, S. J. *J. Am. Chem. Soc.* **1994**, *116*, 7465-7466.
- (5) Broadwater, J. A.; Ai, J.; Loehr, T. M.; Sanders, L.; Fox, B. G. *Biochemistry* **1998**, *37*, 14664-14671.
- (6) Moënné-Loccoz, P.; Krebs, C.; Herlihy, K.; Edmondson, D. E.; Theil, E. C.; Huynh, B. H.; Loehr, T. M. *Biochemistry* **1999**, *38*, 5290-5295.
- (7) Murray, L. J.; Naik, S. G.; Ortillo, D. O.; García-Serres, R.; Lee, J. K.; Huynh, B. H.; Lippard, S. J. *J. Am. Chem. Soc.* **2007**, *129*, 14500-14510.
- (8) Vu, V. V.; Emerson, J. P.; Martinho, M.; Kim, Y. S.; Münck, E.; Park, M. H.; Que, L., Jr. *Proc. Natl. Acad. Sci. U.S.A.* **2009**, *106*, 14814-14819.
- (9) Korboukh, V. K.; Li, N.; Barr, E. W.; Bollinger, J. M., Jr.; Krebs, C. *J. Am. Chem. Soc.* **2009**, *131*, 13608-13609.
- (10) Cotton, F. A.; Wilkinson, G.; Murillo, C. A.; Bochmann, M., 11-10. Dioxygen, Superoxo, and Peroxo Ligands. *Advances Inorganic Chemistry*, 6th Ed.; John Wiley & Sons, Inc.: New York, 2004, pp.468-470.
- (11) Moënné-Loccoz, P.; Baldwin, J.; Ley, B. A.; Loehr, T. M.; Bollinger, J. M., Jr. *Biochemistry* **1998**, *37*, 14659-14663.
- (12) Skulan, A. J.; Brunold, T. C.; Baldwin, J.; Saleh, L.; Bollinger, J. M.; Solomon, E. I. *J. Am. Chem. Soc.* **2004**, *126*, 8842-8855.
- (13) Merckx, M.; Kopp, D. A.; Sazinsky, M. H.; Blazyk, J. L.; Müller, J.; Lippard, S. J. *Angew. Chem., Int. Ed.* **2001**, *40*, 2782-2807.
- (14) Tinberg, C. E.; Lippard, S. J. *Acc. Chem. Res.* **2011**, ASAP.
- (15) Bailey, L. J.; Fox, B. G. *Biochemistry* **2009**, *48*, 8932-8939.

- (16) Broadwater, J. A.; Achim, C.; Münck, E.; Fox, B. G. *Biochemistry* **1999**, *38*, 12197-12204.
- (17) Arengi, F. L. G.; Berlanda, D.; Galli, E.; Sello, G.; Barbieri, P. *Appl. Environ. Microbiol.* **2001**, *67*, 3304-3308.
- (18) Cafaro, V.; Scognamiglio, R.; Viggiani, A.; Izzo, V.; Passaro, I.; Notomista, E.; Dal Piaz, F.; Amoresano, A.; Casbarra, A.; Pucci, P.; Di Dinato, A. *Eur. J. Biochem.* **2002**, *269*, 5689-5699.
- (19) Bochevarov, A. D.; Li, J.; Song, W. J.; Friesner, R. A.; Lippard, S. J. *J. Am. Chem. Soc.* **2011**, ASAP.
- (20) Ambundo, E. A.; Friesner, R. A.; Lippard, S. J. *J. Am. Chem. Soc.* **2002**, *124*, 8770-8771.
- (21) Baik, M.-H.; Gherman, B. F.; Friesner, R. A.; Lippard, S. J. *J. Am. Chem. Soc.* **2002**, *124*, 14608-14615.
- (22) Dunietz, B. D.; Beachy, M. D.; Cao, Y.; Whittington, D. A.; Lippard, S. J.; Friesner, R. A. *J. Am. Chem. Soc.* **2000**, *122*, 2828-2839.
- (23) Friesner, R. A.; Baik, M.-H.; Gherman, B. F.; Guallar, V.; Wirstam, M.; Murphy, R. B.; Lippard, S. J. *Coord. Chem. Rev.* **2003**, *238-239*, 267-290.
- (24) Rinaldo, D.; Philipp, D. M.; Lippard, S. J.; Friesner, R. A. *J. Am. Chem. Soc.* **2007**, *129*, 3135-3147.
- (25) Sturhahn, W.; Toellner, T. S.; Alp, E. E.; Zhang, X.; Ando, M.; Yoda, Y.; Kikuta, S.; Seto, M.; Kimball, C. W.; Dabrowski, B. *Phys. Rev. Lett.* **1995**, *74*, 3832-3835.
- (26) Scheidt, W. R.; Durbin, S. M.; Sage, J. T. *J. Inorg. Biochem.* **2005**, *99*, 60-71.
- (27) Zeng, W.; Silvernail, N. J.; Scheidt, W. R.; Sage, J. T. *App. Phy. Meth. Inorg. Bioinorg. Chem.* **2007**, 1-21.

- (28) Sturhahn, W. *J. Phys. Condens. Matter* **2004**, *16*, S497-S530.
- (29) Xiao, Y.; Fisher, K.; Smith, M. C.; Newton, W. E.; Case, D. A.; George, S. J.; Wang, H.; Sturhahn, W.; Alp, E. E.; Zhao, J.; Yoda, Y.; Cramer, S. P. *J. Am. Chem. Soc.* **2006**, *128*, 7608-7612.
- (30) George, S. J.; Igarashi, R. Y.; Xiao, Y.; Hernandez, J. A.; Demuez, M.; Zhao, D.; Yoda, Y.; Ludden, P. W.; Rubio, L. M.; Cramer, S. P. *J. Am. Chem. Soc.* **2008**, *130*, 5673-5680.
- (31) Xiao, Y.; Tan, M.-L.; Ichiye, T.; Wang, H.; Guo, Y.; Smith, M. C.; Meyer, J.; Sturhahn, W.; Alp, E. E.; Zhao, J.; Yoda, Y.; Cramer, S. P. *Biochemistry* **2008**, *47*, 6612-6627.
- (32) Paulat, F.; Berto, T. C.; DeBeer George, S.; Goodrich, L.; Praneeth, V. K. K.; Sulok, C. D.; Lehnert, N. *Inorg. Chem.* **2008**, *47*, 11449-11451.
- (33) Lehnert, N.; Galinato, M. G. I.; Paulat, F.; Richter-Addo, G. B.; Sturhahn, W.; Xu, N.; Zhao, J. *Inorg. Chem.* **2010**, *49*, 4133-4148.
- (34) Tinberg, C. E.; Tonzetich, Z. J.; Wang, H.; Do, L. H.; Yoda, Y.; Cramer, S. P.; Lippard, S. J. *J. Am. Chem. Soc.* **2010**, 18168-18176.
- (35) Tonzetich, Z. J.; Wang, H.; Mitra, D.; Tinberg, C. E.; Do, L. H.; Jenney, F. E.; Adams, M. W. W.; Cramer, S. P.; Lippard, S. J. *J. Am. Chem. Soc.* **2010**, *132*, 6914-6916.
- (36) Liu, L. V.; Bell, C. B., III; Wong, S. D.; Wilson, S. A.; Kwak, Y.; Chow, M. S.; Zhao, J.; Hodgson, K. O.; Hedman, B.; Solomon, E. I. *Proc. Natl. Acad. Sci. U.S.A.* **2010**, *107*, 22419-22424.
- (37) Bell, C. B., III; Wong, S. D.; Xiao, Y.; Klinker, E. J.; Tenderholt, A. L.; Smith, M. C.; Rohde, J.-U.; Que, L., Jr.; Cramer, S. P.; Solomon, E. I. *Angew. Chem., Int. Ed. Engl.* **2008**, *47*, 9071-9074.

- (38) Wong, S. D.; Bell, C. B., III; Liu, L. V.; Kwak, Y.; England, J.; Alp, E. E.; Zhao, J.; Que, L., Jr.; Solomon, E. I. *Angew. Chem., Int. Ed. Engl.* **2011**, ASAP.
- (39) Dong, Y.; Yan, S.; Young, V. G., Jr.; Que, L., Jr. *Angew. Chem., Int. Ed. Engl.* **1996**, *35*, 618-620.
- (40) Kim, K.; Lippard, S. J. *J. Am. Chem. Soc.* **1996**, *118*, 4914-4915.
- (41) Ookubo, T.; Sugimoto, H.; Nagayama, T.; Masuda, H.; Sato, T.; Tanaka, K.; Maeda, Y.; Ōkawa, H.; Hayashi, Y.; Uehara, A.; Suzuki, M. *J. Am. Chem. Soc.* **1996**, *118*, 701-702.
- (42) Zhang, X.; Furutachi, H.; Fujinami, S.; Nagatomo, S.; Maeda, Y.; Watanabe, Y.; Kitagawa, T.; Suzuki, M. *J. Am. Chem. Soc.* **2004**, *127*, 826-827.
- (43) Kodera, M.; Kajita, Y.; Tachi, Y.; Katayama, K.; Kano, K.; Hirota, S.; Fujinami, S.; Suzuki, M. *Angew. Chem., Int. Ed. Engl.* **2004**, *43*, 334-337.
- (44) Gavrilova, A. L.; Qin, C. J.; Sommer, R. D.; Rheingold, A. L.; Bosnich, B. *J. Am. Chem. Soc.* **2002**, *124*, 1714-1722.
- (45) Thewalt, U.; Marsh, R. E. *J. Am. Chem. Soc.* **1967**, *89*, 6364-6365.
- (46) Itoh, K.; Hayashi, H.; Furutachi, H.; Matsumoto, T.; Nagatomo, S.; Tosha, T.; Terada, S.; Fujinami, S.; Suzuki, M.; Kitagawa, T. *J. Am. Chem. Soc.* **2005**, *127*, 5212-5223.
- (47) Mishra, S.; Hubert-Pfalzgraf, L. G.; Rolland, M.; Chermette, H. *Inorg. Chem. Commun.* **2007**, *10*, 15-19.
- (48) Dong, Y.; Ménage, S.; Brennan, B. A.; Elgren, T. E.; Jang, H. G.; Pearce, L. L.; Que, L., Jr. *J. Am. Chem. Soc.* **1993**, *115*, 1851-1859.
- (49) Kitajima, N.; Tamura, N.; Amagai, H.; Fukui, H.; Moro-oka, Y.; Mizutani, Y.; Kitagawa, T.; Mathur, R.; Heerwegh, K.; Reed, C. A.; Randall, C. R.; Que, L., Jr.; Tatsumi, K. *J. Am. Chem. Soc.* **1994**, *116*, 9071-9085.

- (50) Do, L. H.; Hayashi, T.; Moëne-Loccoz, P.; Lippard, S. J. *J. Am. Chem. Soc.* **2010**, *132*, 1273-1275.
- (51) Kitajima, N.; Fujisawa, K.; Fujimoto, C.; Morooka, Y.; Hashimoto, S.; Kitagawa, T.; Toriumi, K.; Tatsumi, K.; Nakamura, A. *J. Am. Chem. Soc.* **1992**, *114*, 1277-1291.
- (52) Winter, G. *Inorg. Synth.* **1973**, *14*, 101-104.
- (53) Sturhahn, W. *Hyperfine Interact.* **2000**, *125*, 149-172.
- (54) Dowty, E. *Phys. Chem. Miner.* **1987**, *14*, 67-79.
- (55) *Shape Software*, www.shapesoftware.com.

Appendix A

Evaluating the Identity of an Electron-Rich Bis(tris(pyridyl-2-methyl)amine)diiron(III) Complex and Its Involvement
in the Hydrolysis of Acetonitrile

AI. Introduction

Because of their importance in the chemistry of non-heme diiron enzymes,^{1,2} understanding the chemical and physical characteristics of synthetic diiron(IV) units is of significant interest.³⁻⁵ Among the various constructs employed to access such species, one convenient platform is based on a tripodal tris(pyridyl-2-methyl)amine (TPA) ligand. Stable dinuclear species can be readily prepared by linking two monomeric [Fe(TPA)] complexes through oxo-, hydroxo-, or carboxylato bridges.⁶⁻⁸ A notable achievement in diiron modeling chemistry is the crystallographic characterization of a mixed-valent di(μ -oxo)diiron(III,IV) unit, [Fe₂(μ -O)₂(5-Et₃-TPA)₂](ClO₄)₃ (where 5-Et₃-TPA = tris((5-ethylpyridyl)-2-methyl)amine) (**A**, Chart A.1).^{9,10} Complex **A** contains the quadrilateral Fe₂O₂ core believed to be present in the diiron(IV) intermediate Q of soluble methane monooxygenase hydroxylase (sMMOH).^{11,12}

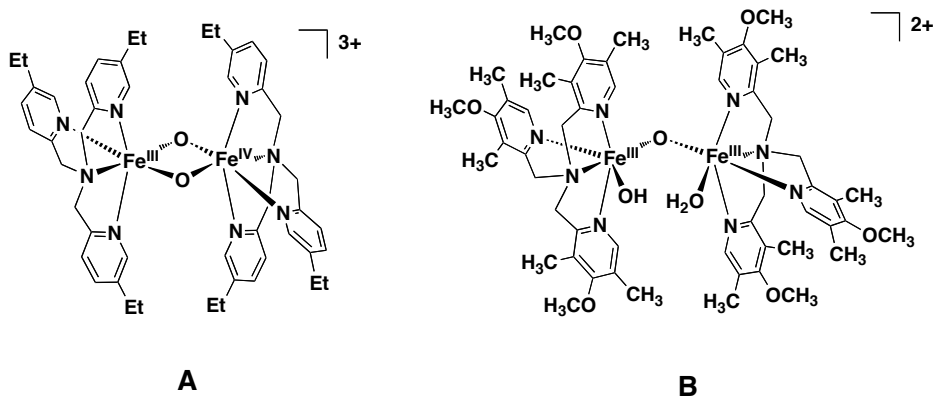
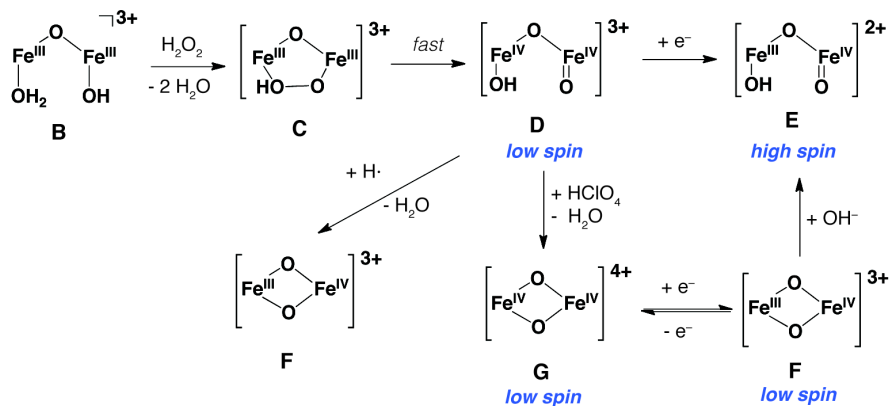


Chart A.1. The [Fe₂(μ -O)₂(5-Et-TPA)₂]³⁺ (**A**) complex was the first di(μ -oxo)diiron(III,IV) species structurally characterized by X-ray crystallography. The [Fe₂(μ -O)(OH)(H₂O)(R₃TPA)₂]³⁺ (**B**) compound was reported to be a versatile starting material for generating diiron(III,IV) and diiron(IV,IV) species.



Scheme A.1. Reactions of a putative $[\text{Fe}^{\text{III}}_2(\mu\text{-O})(\text{OH})(\text{H}_2\text{O})(\text{R}_3\text{TPA})_2]^{3+}$ species (**B**) leading to formation of high-valent diiron units. See references for more details.¹³⁻¹⁵

The electronic and steric properties of the diiron TPA complexes can be tuned by appending various substituents around the pyridine rings. Recently, studies using an electron-rich tris((3,5-dimethyl-4-methoxy)pyridyl-2-methyl)amine (R_3TPA) derivative have enabled high-valent diiron units to be prepared.¹³⁻¹⁵ It was reported that, upon treatment with hydrogen peroxide, the diiron(III) precursor $[\text{Fe}_2(\mu\text{-O})(\text{OH})(\text{H}_2\text{O})(\text{R}_3\text{TPA})_2](\text{ClO}_4)_3$ (**B**, Chart A.1) converts to a di(μ -oxo)diiron(III,IV) $[\text{Fe}_2(\mu\text{-O})_2(\text{R}_3\text{TPA})_2](\text{ClO}_4)_3$ (**F**) species.¹⁵ When **F** was subjected to controlled bulk electrolysis at an applied potential of +900 mV (vs. ferrocene/ferrocenium) in acetonitrile at -40 °C, a diiron(IV) $[\text{Fe}_2(\mu\text{-O})_2(\text{R}_3\text{TPA})_2]^{4+}$ (**G**) species was obtained quantitatively (Scheme A.1). Compound **G** could also be accessed via chemical methods.¹⁴ Reaction of **B** with hydrogen peroxide and protons rapidly leads to formation of **G**, through the transient generation of (μ -hydroperoxo)diiron(III,III) (**C**) and (μ -oxo)(hydroxo)(oxo)diiron(IV) (**D**) intermediates (Scheme A.1). Compound **G**, however, exhibits poor H-atom abstraction ability. When the valence-delocalized diiron(III,IV) **F** was treated with tetrabutylammonium hydroxide or the diiron(IV) unit **D** was reduced by ferrocene, a valence-localized species **E** was obtained.¹³ Compound **E** was determined to be a high-spin species,

unlike the low-spin units previously characterized, and displayed a million-fold rate enhancement in H-atom abstraction compared to **G**.

To obtain spectroscopic standards for the di(μ -oxo)diiron(IV) unit, efforts were made to prepare compound **G** as described in the literature. During the course of these studies, several inconsistent results were obtained that prompted more detailed investigations. This report clarifies the identity of the diiron(III) starting material and describes its ability to hydrolyze acetonitrile to acetate. Attempts were not made to evaluate the validity of Scheme A.1 in light of these new findings, but a more thorough investigation is necessary to address the concerns enumerated in this report.

A.2. Experimental

Materials and Methods. Reagents obtained from commercial suppliers were used as received. The tris((3,5-dimethyl-4-methoxypyridyl)-2-methyl)amine (R_3 TPA) ligand that is deuterated at the benzylic positions was prepared as previously described.¹⁵ All manipulations were performed in air using standard laboratory techniques. Solvents were used as received from the commercial suppliers without further purification.

General Physical Methods. NMR spectra were recorded on 500 MHz Varian Mercury spectrometers and chemical shifts for ^1H and ^{13}C spectra were referenced to residual solvent. ^1H NMR spectral data of paramagnetic compounds were obtained by widening the sweep window (+100 to -30 ppm) and collecting for longer acquisition times (~1024 scans). IR spectra were recorded on a ThermoNicolet Avatar 360 spectrophotometer with the OMNIC software. Absorption spectra were recorded on a Cary 50 spectrophotometer using 6Q Spectrosil quartz cuvettes (Starna) with 1 cm path lengths. For low temperature UV-vis measurements, a custom-

made quartz cuvette (path length = 1.74 cm) containing a jacketed dewar was employed. An acetonitrile/dry ice bath was used to maintain the samples at -30 °C. Mössbauer spectra were recorded on an MSI spectrometer (WEB Research Company) with a ^{57}Co source in a Rh matrix maintained at room temperature. Solid samples were prepared by suspension of the complex (~40 mg) in Apiezon M grease and placement in a nylon sample holder. Samples were measured over the course of ~5 d at 80 K. Isomer shift (δ) values are reported with respect to metallic iron that was used for velocity calibration at room temperature. Spectra were fit to Lorentzian lines using the WMOSS plot and fit program.

X-ray Data Collection and Refinement. Single crystals were mounted in Paratone oil using 30 μm aperture MiTeGen MicroMounts (Ithaca, NY) and frozen under a 100 K KRYO-FLEX nitrogen cold stream. Data were collected on a Bruker SMART APEX CCD X-ray diffractometer with Mo $K\alpha$ radiation ($\lambda = 0.71073 \text{ \AA}$) controlled by the APEX 2 (v. 2010.1-2) software package. Data reduction was performed using SAINT and empirical absorption corrections were applied using SADABS.¹⁶ The structures were solved by direct methods with refinement by full-matrix least squares based on F^2 using the SHELXTL-97 software package¹⁷ and checked for higher symmetry by the PLATON software.¹⁸ All non-hydrogen atoms were located and refined anisotropically. Hydrogen atoms were fixed to idealized positions unless otherwise noted and given thermal parameters equal to either 1.5 (methyl hydrogen atoms) or 1.2 (non-methyl hydrogen atoms) times the thermal parameters of the atoms to which they are attached.

Complex **1** occurs on an inversion center; thus, only half of the molecule is present in the asymmetric unit, along with 1.5 perchlorate anions and two acetonitrile molecules. Both perchlorate groups exhibit positional disorder and were modeled accordingly. One of the ClO_4^-

anions are located on a special position and was refined with 50% occupancy by suppressing generation of special position constraints. Due to charge considerations, the Fe₂O₂ core of **1** is best described as a (μ-oxo)(μ-hydroxo)diiron(III) unit, the overall complex having the empirical formula [Fe₂(μ-O)(μ-OH)(R₃TPA)₂](ClO₄)₃. Thus, the observed Fe–O distances must result from a disorder imposed by the symmetry of the unit cell averaged over the Fe–O(oxo) and Fe–O(hydroxo) bond lengths. Although the core structures of **4A** and **4B** are identical, both containing the cationic [Fe₂(μ-O)(μ-CH₃CO₂)(R₃TPA)₂]³⁺ unit, they differ in the number of solvent molecules in their crystal lattices as well as their unit cell dimensions. The asymmetric unit of **4A** contains a single [Fe₂(μ-O)(μ-CH₃CO₂)(R₃TPA)₂]³⁺ ion, together with three perchlorate anions and three acetonitrile moieties. Two of the ClO₄[−] groups were modeled with positional disorder using appropriate similarity restraints and equal anisotropic displacement parameters. In contrast to that in **4A**, the asymmetric unit of **4B** has two independent molecules of [Fe₂(μ-O)(μ-CH₃CO₂)(R₃TPA)₂](ClO₄)₃, five acetonitrile molecules and one diethyl ether. The diethyl ether unit is severely disordered, as evident by the large anisotropic displacement parameters of its component atoms. Attempts to model this disorder did not give a stable refinement; thus, no attempt was made to do so in the final structure.

Kinetic Measurements. The rate of hydrolysis of acetonitrile by **1** was determined by UV-vis spectroscopic measurements. The data were recorded by scanning at 5 min intervals for 900 min. The absorption changes at 550 nm were fit to an A→B→C reaction sequence (Eq. 1), with rate constants k_1 and k_2 , respectively. The constants ϵ_A , ϵ_B , and ϵ_C are the molar absorptivities of species A, B, and C, respectively and $[A]_0$ is the initial concentration of A.

$$\text{Abs}_\lambda(t) = [A]_0 e^{-k_1 t} (\epsilon_A - \epsilon_C) + \frac{k_1}{k_2 - k_1} [A]_0 (e^{-k_1 t} - e^{-k_2 t}) (\epsilon_B - \epsilon_C) + [A]_0 \epsilon_C \quad (1)$$

Synthesis

[Fe₂(μ-O)(μ-OH)(R₃TPA)₂](ClO₄)₃ (1). This compound was prepared exactly as described for the purported synthesis of [Fe₂(μ-O)(OH)(H₂O)(R₃TPA)₂](ClO₄)₃ (**B**),¹⁵ except that the final material was extracted into dichloromethane and filtered to removed an insoluble impurity. The organic filtrate was evaporated to dryness to afford a red powder (114 mg, 42%). Red crystals for X-ray crystallographic analysis were obtained by vapor diffusion of diethyl ether into a solution of the compound in acetonitrile. Crystals obtained from dichloromethane/diethyl ether were smaller than those grown from acetonitrile/diethyl ether. Note that hydrolysis of coordinated acetonitrile could occur to give [Fe₂(μ-O)(μ-CH₃CO₂)(R₃TPA)₂](ClO₄)₃; crystals of the acetate bound diiron complex are yellow rather than red. ¹H NMR (CD₂Cl₂, 500 MHz): δ 4.70, 4.00, 3.89, 3.60, 3.42, 2.79, 2.24, 1.63 ppm. UV-vis (CH₂Cl₂): λ_{max} = 370, 550 nm. FT-IR (KBr): ν = 2950, 2863, 1599, 1575, 1478, 1456, 1402, 1385, 1292, 1267, 1095, 1080, 997, 875, 800, 623 cm⁻¹. ⁵⁷Fe Mössbauer (80 K, apiezon grease): δ = 0.44(2) mm/s; ΔE_Q = 1.46(2) mm/s; Γ_{L/R} = 0.47(2) mm/s. Mp = 190 °C.

[Fe₂(μ-O)(μ-CH₃CO₂)(R₃TPA)₂](ClO₄)₃ (4B). Solid R₃TPA (200 mg, 426 μmol), Fe(ClO₄)₃·10 H₂O (230 mg, 426 μmol), sodium acetate (17 mg, 213 μmol), and triethylamine (59 μL, 426 μmol) were dissolved in 2.0 mL of CH₃OH and stirred at RT for 3 h. A solid precipitate was isolated by filtration and washed with MeOH to afford a pale yellow material (198 mg, 66%). Single crystals suitable for X-ray diffraction analysis were obtained from slow diffusion of diethyl ether into a solution of the compound in either acetonitrile or dichloromethane. ¹H NMR (CD₂Cl₂, 500 MHz): δ 3.91, 3.77, 3.67, 3.28, 2.92, 2.71, 2.44 ppm. UV-vis (CH₂Cl₂): λ_{max} = 332 (14,500 M⁻¹cm⁻¹), 374 (9,850 M⁻¹cm⁻¹), 454 (1,460 M⁻¹cm⁻¹), 504 (1,390 M⁻¹cm⁻¹), 700 (294 M⁻¹cm⁻¹) nm. FT-IR (KBr): ν = 2960, 1599, 1532, 1478, 1402, 1264, 1092, 994, 875, 801, 764, 623

cm⁻¹. ⁵⁷Fe Mössbauer (80 K, apiezon grease): $\delta = 0.44(2)$ mm/s; $\Delta E_Q = 1.49(2)$ mm/s; $\Gamma_{L/R} = 0.38(2)$ mm/s. Anal. Calcd. for Fe₂C₅₆H₇₅N₈O₂₁Cl₃·(CH₃OH): C, 47.33; H, 5.51; N, 7.75; Found: C, 47.06; H, 5.32; N, 7.78. Mp (decomp) = 195 °C.

A.3. Results and Discussion

Characterization of Diiron(III) Complexes. Preparation of [Fe₂(μ -O)(OH)(H₂O)-(R₃TPA)₂](ClO₄)₃ (**B**) was attempted according to the literature procedure.¹⁵ Reaction of iron(III) perchlorate decahydrate, R₃TPA, and sodium hydroxide in methanol and water afforded a red powder as described, which was reported to be pure **B**. This bulk material, however, was determined to be a heterogeneous mixture. Initially, this conclusion was derived from simple solubility tests, in which only some of the red solid could be extracted into common organic solvents, such dichloromethane or acetonitrile. The fact that this crude compound was red, rather than green like other [Fe₂(μ -O)(OH)(H₂O)(L)₂]³⁺ (where L = a polynitrogen ligand) compounds reported in the literature,^{7,19,20} was also unexpected. Because the only characterization data reported for “**B**” was an elemental analysis and its synthetic yield was not given,¹⁵ further studies of this material were undertaken.

The zero-field ⁵⁷Fe Mössbauer spectrum of the crude red powder was best fit to three quadrupole doublets (Figure A.1A), giving parameters $\delta_1 = 0.44$ mm/s, $\Delta E_{Q1} = 1.16$ mm/s, Area 1 = 36%; $\delta_2 = 0.44$ mm/s, $\Delta E_{Q2} = 1.66$ mm/s, Area 2 = 28%; and $\delta_3 = 0.44$ mm/s, $\Delta E_{Q3} = 0.71$ mm/s, Area 3 = 36% (Table A.1). If the material contained pure **B**, a maximum of two quadrupole doublets would be expected if both of its iron atoms had distinct coordination environments. A three-site model suggests that at least two different iron-containing species are present in the sample, perhaps accounting for the organic soluble and organic insoluble fractions.

When the crude powder was extracted into dichloromethane, filtered, and evaporated to dryness, a slightly lighter red solid was obtained, hereafter referred to as compound **1**. As shown in Figure A.1B, this product exhibits a single quadrupole doublet, having values of $\delta = 0.44$ mm/s and $\Delta E_Q = 1.46$ mm/s (Table A.1). The Mössbauer parameters of **1** are most similar to those of either site 1 or 2 in the crude material, suggesting that the dichloromethane extraction and filtration steps were necessary purification procedures.

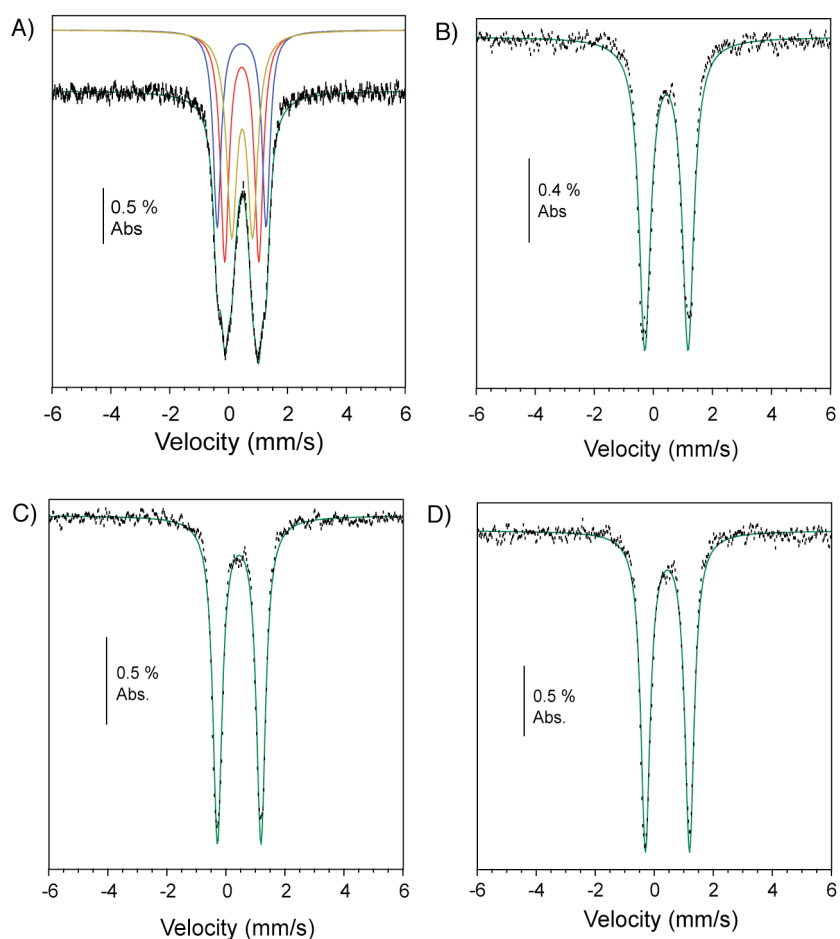


Figure A.1. Zero-field Mössbauer spectra (80 K) of A) the crude material from reaction of R_3TPA and iron(III) perchlorate, B) compound **1**, C) compound **4A**, and D) compound **4B**. Spectrum A was best fit to three quadrupole doublets, whereas those of B, C, and D were adequately fit to single site models. Raw data are in black, simulated fits are in green, and individual sites are in blue, yellow, and red. Mössbauer parameters are given in Table A.1.

Table A.1. Summary of Spectroscopic Data.

	Crude Solid			1	4A	4B
Mössbauer^a	Site 1	Site 2	Site 3	Site 1	Site 1	Site 1
δ (mm/s)	0.44	0.44	0.44	0.44	0.44	0.44
ΔE_Q (mm/s)	1.16	1.66	0.71	1.46	1.47	1.49
Γ (mm/s)	0.35	0.32	0.40	0.47	0.38	0.38
	36%	28%	36%			
UV-visible^b	* heterogeneous solution			370, 550	452, 492, 504, 700	452, 492, 504, 700
λ_{\max} (nm)						
Infrared^c	2945	2947	2927	2960		
ν (cm ⁻¹)	1600	1599	1598	1599		
	1575	1575	1576	1570		
			1540	1532		
	1478	1478	1478	1478		
	1456	1455	1450	1450		
	1401	1402	1402	1402		
	1384	1384	1384	1384		
	1293	1292	1292	1291		
	1267	1268	1267	1264		
	1077	1076	1091	1092		
	1096					
	995	995	994	995		
	874	874	875	875		
		800 (w)		800		
	768(w)	763(w)	765	764		
	660	657(w)				
	623	624	623	623		
¹H NMR^d	* heterogeneous solution			4.70, 4.00, 3.89, 3.60,	3.92, 3.68, 3.28, 2.94,	3.91, 3.67, 3.28, 2.93,
δ (ppm)				3.42, 2.79, 2.24, 1.63	2.45	2.44

^aPolycrystalline samples recorded at 80 K. ^bRecorded in dichloromethane at RT. ^cMeasured as KBr pellets; IR peaks designated with a “w” indicate weak intensity. ^dRecorded in chloroform-*d*.

For further comparison of the properties of the unpurified material versus compound **1**, IR spectroscopy was employed. The IR spectra of the crude solid and **1** are shown in Figure A.2A (black and red traces, respectively). As expected, both solids display intense bands at ~ 1100 cm⁻¹, indicative of the perchlorate anion. The spectral envelope ranging from 500 to 1700 cm⁻¹ is essentially identical for the two samples (Table A.1), with some slight variations in the weak baseline features. These data suggest that the insoluble fraction either has few IR active features or has a composition similar to that of **1**.

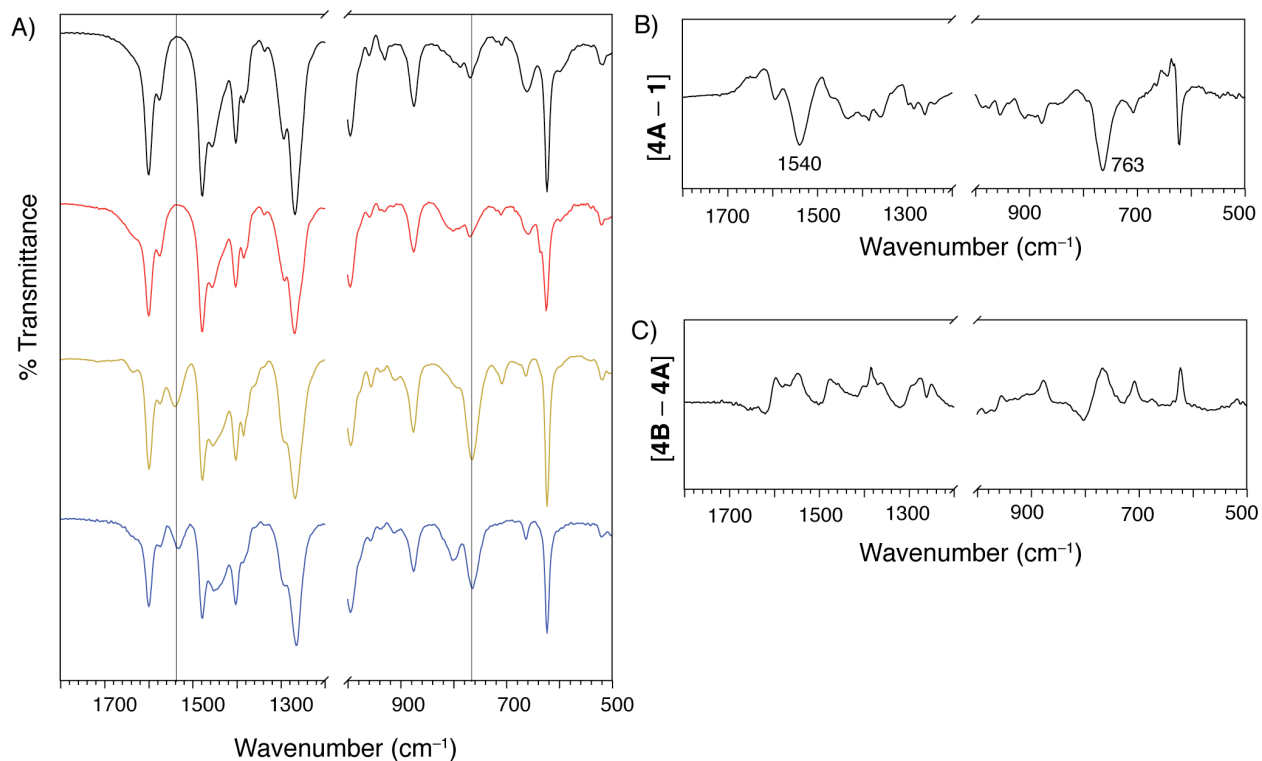


Figure A.2. Panel A shows plots of the FTIR spectra (KBr pellets) of the crude material from reaction of R₃TPA with iron(III) perchlorate (black), compound **1** (red), compound **4A** (yellow), and compound **4B** (blue). The difference spectra of **1/4A** (panel B) and **4A/4B** (panel C) are depicted to the right. The spectrum of **4A**, compared to that of **1**, displays two new peaks at 763 and 1540 cm⁻¹. No significant differences were observed in the spectrum of **4A** compared to that of **4B**. The spectral region from 1000-1200 cm⁻¹ exhibits strong absorption from the perchlorate anion and has been omitted for clarity.

Crystallization of **1** was attempted by slow diffusion of diethyl ether into a solution of the complex in acetonitrile. After several days, two different types of crystals were obtained, some red and others yellow. X-ray diffraction analysis of the red crystals revealed a diiron structure with an Fe₂O₂ core (Figure A.3, Table A.2). The iron atoms are separated by 2.79 Å and have a pseudo-octahedral coordination environment (Table A.3). Each metal center is bound by the tetradentate R₃TPA ligand, with Fe–N(amine) and Fe–N(pyridyl)_{ave} distances of 2.18 and 2.14 Å, respectively. Two oxygen atoms bridge the iron centers, with Fe–O bond lengths of 1.88 and 1.93 Å. Because each diiron unit is associated with three perchlorate anions, charge balance

considerations dictate that the oxygen atom bridges are best described as oxo and hydroxo ligands, giving the molecular formula $[\text{Fe}_2(\mu\text{-O})(\mu\text{-OH})(\text{R}_3\text{TPA})_2](\text{ClO}_4)_3$. Because the molecule is located on an inversion center, the Fe–O distances are an average of the iron-oxo and iron hydroxo bond lengths. The structural parameters of $[\text{Fe}_2(\mu\text{-O})(\mu\text{-OH})(\text{R}_3\text{TPA})_2](\text{ClO}_4)_3$ fall within the ranges exhibited by two isostructural diiron TPA complexes that differ only in their oxygen protonation states, $[\text{Fe}_2(\mu\text{-O})(\mu\text{-OH})(6\text{-Me}_3\text{TPA})_2](\text{ClO}_4)_3$ ²¹ and $[\text{Fe}_2(\mu\text{-O})_2(6\text{-Me}_3\text{TPA})_2](\text{ClO}_4)_2$ ²² (where 6-Me₃TPA = tris((6-methylpyridyl)-2-methyl)amine) (Table A.3). Based on the similar spectroscopic characteristics of the red crystals compared to those of the red powder before crystallization, **1** is assigned as a (μ -oxo)(μ -hydroxo)diiron(III) complex, $[\text{Fe}_2(\mu\text{-O})(\mu\text{-OH})(\text{R}_3\text{TPA})_2](\text{ClO}_4)_3$ (*vide infra*).

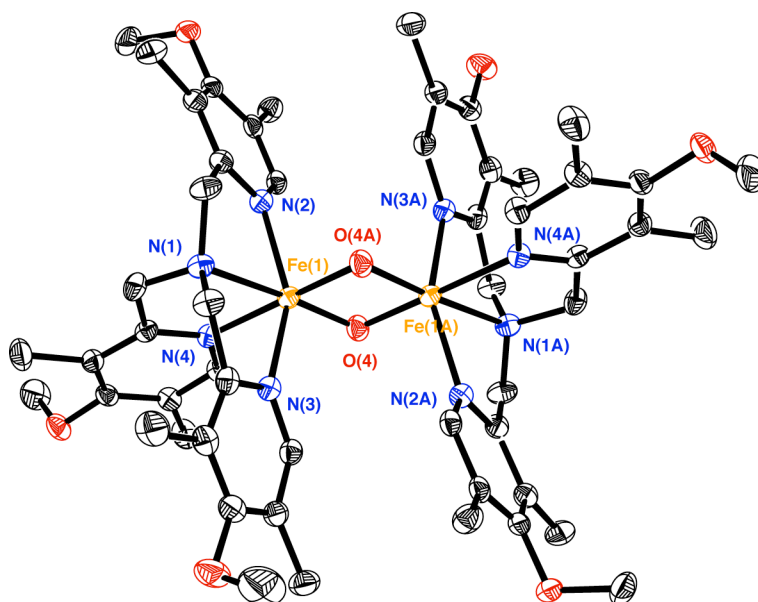


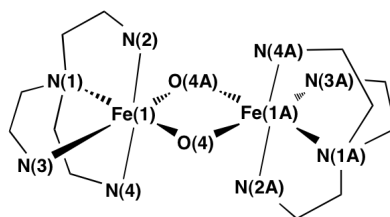
Figure A.3. The thermal ellipsoid (50%) diagram of the X-ray structure of $[\text{Fe}_2(\mu\text{-O})(\mu\text{-OH})(\text{R}_3\text{TPA})_2](\text{ClO}_4)_3 \cdot (\text{CH}_3\text{CN})_4$ (**1**). Hydrogen atoms, solvent molecules, and perchlorate anions are omitted for clarity. Color scheme: iron, orange; oxygen, red; nitrogen, blue; carbon, black. See Table A.2 and Table A.3 for refinement and structural parameters of **1**, respectively.

Table A.2. X-ray Data Collection and Refinement Parameters for **1**, **4A**, and **4B**.

	1	4A	4B
Empirical formula	[Fe ₂ N ₈ O ₈ C ₅₄ H ₇₂](ClO ₄) ₃ ·(CH ₃ CN) ₄	[Fe ₂ N ₈ O ₉ C ₅₆ H ₇₅](ClO ₄) ₃ ·(CH ₃ CN) ₃	[Fe ₂ N ₈ O ₉ C ₅₆ H ₇₅](ClO ₄) ₃ ·(CH ₃ CN) _{2.5} (C ₄ H ₁₀ O) _{0.5}
Formula weight	1535.46	1537.45	1548.94
Temperature (K)	100	100	100
Wavelength (Å)	0.71073	0.71073	0.71073
Crystal system	Monoclinic	Triclinic	Triclinic
Space group	C2/c	P $\bar{1}$	P $\bar{1}$
Unit cell dimensions	a = 28.2258(19) Å b = 11.7652(8) Å c = 22.4938(15) Å β = 106.6850(10)°	a = 13.6256(9) Å b = 14.0402(9) Å c = 20.2928(13) Å α = 81.2320(10)° β = 72.8600(10)° γ = 71.0910(10)°	a = 13.6723(12) Å b = 22.640(2) Å c = 24.640(2) Å α = 99.8960(10)° β = 98.875(2)° γ = 102.9360(10)°
Volume (Å ³)	7155.3(8)	3503.6(4)	7135.5(11)
Z	2	2	2
Calculated density (g/mm ³)	1.425	1.458	1.442
Absorption coefficient (mm ⁻¹)	0.596	0.610	0.600
F(000)	3212	1600	3236
Crystal size (mm ³)	0.32 x 0.17 x 0.13	0.20 x 0.10 x 0.07	0.20 x 0.16 x 0.12
Θ range for data collection	1.51 to 26.73°	1.54 to 26.41°	1.14 to 26.77°
Index ranges	-35 ≤ h ≤ 35 -14 ≤ k ≤ 14 -20 ≤ l ≤ 20	-16 ≤ h ≤ 17 -17 ≤ k ≤ 17 -25 ≤ l ≤ 25	-17 ≤ h ≤ 17 -28 ≤ k ≤ 28 -30 ≤ l ≤ 30
Reflections collected	63728	61129	123942
Independent reflections	7549 [R(int) = 0.0340]	14283 [R(int) = 0.0532]	30171 [R(int) = 0.0564]
Completeness to Θ (%)	99.3	99.4	99.1
Absorption correction	Empirical	Empirical	Empirical
Max. and min. transmission	0.9265 and 0.8321	0.9586 and 0.8878	0.9315 and 0.8895
Data / restraints / parameters	7549/85/473	14283/0/952	30171/4/1808
Goodness-of-fit on F ²	1.077	1.016	1.030
Final R indices [I > 2σ(I)]	R1 = 0.0652 wR2 = 0.1759	R1 = 0.0552 wR2 = 0.1259	R1 = 0.0673 wR2 = 0.1747
R indices (all data)	R1 = 0.0722 wR2 = 0.1815	R1 = 0.0810 wR2 = 0.1381	R1 = 0.0967 wR2 = 0.1937
Largest diff. peak and hole (eÅ ⁻³)	1.828 and -0.693	1.429 and -1.188	2.467 and -1.199

* R1 = $\sum ||F_o| - |F_c|| / \sum |F_o|$; wR2 = $[\sum [w(F_o^2 - F_c^2)^2] / \sum [w(F_o^2)^2]]^{1/2}$; GOF = $[\sum [w(F_o^2 - F_c^2)^2] / (n-p)]^{1/2}$, where n is the number of reflections and p is the total number of parameters refined.

Table A.3. Selected Structural Parameters of $[\text{Fe}_2(\mu\text{-O})(\mu\text{-OH})(\text{R}_3\text{TPA})_2](\text{ClO}_4)_3$ (**1**), $[\text{Fe}_2(\mu\text{-O})(\mu\text{-OH})(6\text{-Me}_3\text{TPA})_2](\text{ClO}_4)_3$,²¹ and $[\text{Fe}_2(\mu\text{-O})_2(6\text{-Me}_3\text{TPA})_2](\text{ClO}_4)_2$.²²



	1	$[\text{Fe}_2(\mu\text{-O})(\mu\text{-OH})(6\text{-Me}_3\text{TPA})_2](\text{ClO}_4)_3$ ^b	$[\text{Fe}_2(\mu\text{-O})_2(6\text{-Me}_3\text{TPA})_2](\text{ClO}_4)_2$ ^c
Bond Distances (Å)^a			
Fe(1)–Fe(1A)	2.7920(9)	2.95(1), 2.94(1)	2.716(2)
Fe(1)–O(4)	1.883(3)	1.906(8), 1.91(1)	1.844(3)
Fe(1)–O(4A)	1.934(2)	1.981(8), 1.960(9)	1.916(4)
Fe(1)–N(1)	2.183(3)	2.174(9), 2.18(1)	2.194(4)
Fe(1)–N(2)	2.147(3)	2.239(9), 2.28(1)	2.255(4)
Fe(1)–N(3)	2.151(3)	2.194(9), 2.196(9)	2.279(4)
Fe(1)–N(4)	2.134(3)	2.188(9), 2.18(1)	2.244(4)
Bond Angles (deg)^a			
Fe(1)–O(4)–Fe(1A)	94.01(11)	98.7(4), 98.7(6)	92.5(2)
O(4)–Fe(1)–O(1A)	85.99(11)	81.3(4), 81.3(6)	87.5(2)
N(1)–Fe(1)–N(2)	76.24(10)	77.2(3), 76.0(5)	75.7(1)
N(1)–Fe(1)–N(3)	76.24(10)	81.2(4), 81.5(4)	74.7(2)
N(1)–Fe(1)–N(4)	79.74(10)	75.1(3), 75.6(4)	79.0(2)
N(1)–Fe(1)–O(4)	176.66(10)	170.6(4), 168.7(4)	175.1(2)
N(1)–Fe(1)–O(4A)	96.12(10)	89.4(4), 88.0(5)	87.8(2)

^aA generalized numbering scheme, depicted in the above cartoon representation, is used. These atom labels do not necessarily correspond to those assigned in their respective X-ray structures. ^bPreviously reported; see ref. 21. Each asymmetric unit contains two independent diiron units. ^cPreviously reported; see ref. 22.

The yellow crystals obtained from crystallization of **1** in acetonitrile/diethyl ether were also evaluated by X-ray crystallography (Figure A.4, Table A.4). The compound has a dinuclear structure with an Fe–Fe distance of 3.25 Å. Each pseudo-octahedral iron atom is capped by a R₃TPA group, with Fe–N(amine)_{ave} = 2.20 Å and Fe–N(pyridyl)_{ave} = 2.15 Å, and is linked by two bridging ligands. One of the bridges is an oxo atom, indicated by short Fe–O bond lengths of ~1.80 Å. The difference electron density map reveals that the second bridging ligand contains four non-hydrogen atoms arranged in a trigonal planar geometry. Assigning this group to an

acetate moiety allowed the structure to refine to convergence, the Fe–O distances being 2.04 and 1.96 Å. The presence of an acetate moiety in this structure is surprising because no CH_3CO_2^- was used during the preparation of **1** or in the crystallization procedure. Because each diiron unit is associated with three perchlorate anions, the molecular formula of this compound is assigned as $[\text{Fe}_2(\mu\text{-O})(\mu\text{-CH}_3\text{CO}_2)(\text{R}_3\text{TPA})_3](\text{ClO}_4)_3$ (**4A**).

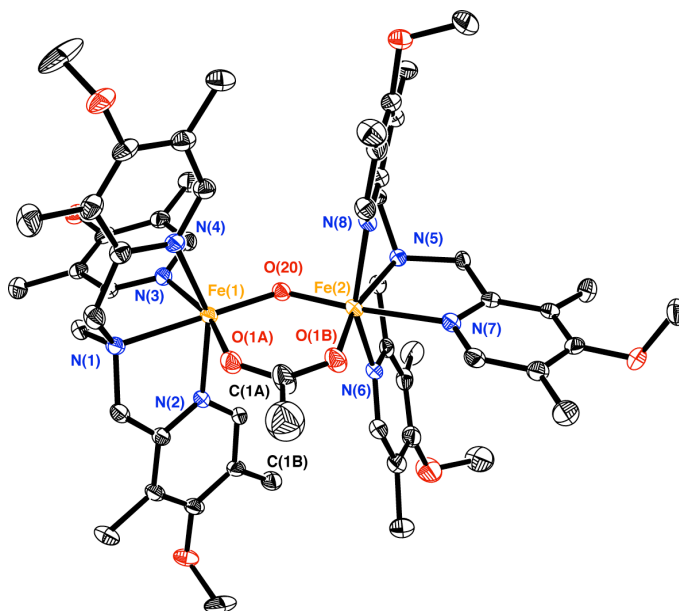
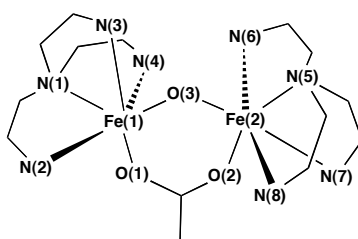


Figure A.4. The thermal ellipsoid (50%) diagram of the cation observed in the X-ray structure of $[\text{Fe}_2(\mu\text{-O})(\mu\text{-CH}_3\text{CO}_2)(\text{R}_3\text{TPA})_2](\text{ClO}_4)_3 \cdot (\text{CH}_3\text{CN})_3$ (**4A**). Hydrogen atoms are omitted for clarity. Color scheme: iron, orange; oxygen, red; nitrogen, blue; carbon, black. See Table A.2 and Table A.4 for refinement and structural parameters of **4A**, respectively.

As expected, compounds **1** and **4A** display distinct optical profiles (Figure A.5). The absorption spectrum of **1** has λ_{max} values at 370 and 550 nm, which are characteristic of $(\mu\text{-oxo})(\mu\text{-hydroxo})$ diiron(III) rather than $\text{di}(\mu\text{-oxo})$ diiron(III) species.⁸ The visible band at 550 nm has been attributed to an oxo-to-iron(III) charge transfer. In contrast, **4A** exhibits optical bands at 332, 454, 492, and 700 nm. These features are nearly identical to those reported for other $(\mu\text{-oxo})(\mu\text{-carboxylato})$ diiron(III) TPA species.⁶

Table A.4. Selected Structural Parameters of **4A** and **4B**.

	4A	4B^b
Bond Distances (Å)^a		
Fe(1)–Fe(2)	3.252(3)	3.250(3), 3.250(3)
Fe(1)–O(1)	2.044(2)	2.042(3), 2.038(3)
Fe(1)–O(3)	1.783(2)	1.794(3), 1.788(3)
Fe(1)–N(1)	2.212(3)	2.216(3), 2.221(3)
Fe(1)–N(2)	2.114(3)	2.137(3), 2.119(3)
Fe(1)–N(3)	2.128(3)	2.135(2), 2.131(3)
Fe(1)–N(4)	2.146(3)	2.138(3), 2.151(3)
Fe(2)–O(2)	1.962(2)	1.984(3), 1.966(3)
Fe(2)–O(3)	1.801(2)	1.808(3), 1.803(3)
Fe(2)–N(5)	2.182(3)	2.191(3), 2.191(3)
Fe(2)–N(6)	2.138(3)	2.121(3), 2.134(3)
Fe(2)–N(7)	2.228(3)	2.228(3), 2.233(3)
Fe(2)–N(8)	2.128(3)	2.131(3), 2.136(3)
Bond Angles (deg)^a		
Fe(1)–O(3)–Fe(2)	130.15(13)	128.98(15), 129.62(15)
O(3)–Fe(1)–O(1)	98.47(10)	99.63(12), 99.39(12)
O(3)–Fe(2)–O(2)	102.39(10)	102.14(12), 101.70(12)
N(1)–Fe(1)–N(2)	77.70(10)	75.81(12), 76.58(12)
N(1)–Fe(1)–N(3)	79.20(10)	79.01(13), 78.95(13)
N(1)–Fe(1)–N(4)	75.07(10)	76.18(12), 75.59(12)
N(5)–Fe(2)–N(6)	76.09(10)	78.52(12), 77.11(13)
N(5)–Fe(2)–N(7)	77.98(10)	76.93(12), 77.49(12)
N(5)–Fe(2)–N(8)	76.69(10)	75.89(12), 76.98(12)

^aA generalized numbering scheme, depicted in the above cartoon representation, is used. These atom labels do not necessarily correspond to those assigned in their respective X-ray structures. ^bThere are two independent diiron units of **4B** in the asymmetric cell; parameters for both cations are provided.

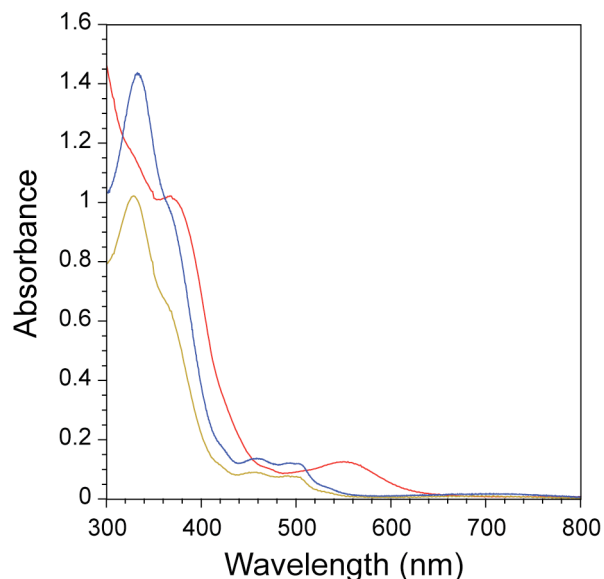


Figure A.5. UV-vis spectra of complexes **1** (red), **4A** (yellow), and **4B** (blue) recorded in dichloromethane at RT. Red spectrum: $\lambda_{\text{max}} = 370, 550$ nm; yellow spectrum: $\lambda_{\text{max}} = 332, 454, 492$ nm; blue spectrum: $\lambda_{\text{max}} = 332, 454, 492$ nm.

The IR spectra of the red and yellow crystals of **1** and **4A**, respectively, were recorded (Figure A.2A). Because of similarities in their molecular composition, **1** and **4A** share several prominent features in the spectral range between $500\text{--}1700\text{ cm}^{-1}$. In addition to the vibrational modes present in the spectrum of **1**, however, compound **4A** displays peaks at 763 and 1540 cm^{-1} (Figure A.2B). The former is ascribed to an asymmetric stretching mode of the Fe–O–Fe unit and the latter to an asymmetric C–O–O[−] vibration of the bridging acetate. Based on comprehensive analyses of synthetic oxo-bridged diiron(III) compounds,^{23,24} it has been established that the Fe–O stretching frequency of an $\{\text{Fe}_2\text{O}\}^{4+}$ unit is strongly correlated with its Fe–O–Fe angle. Because the Fe–O–Fe angle in **1** (94°) is significantly smaller than that of **4A** (130°), the $\nu_{\text{Fe-O}}$ stretching frequencies of **1** are expected to occur at higher energies than those in **4A**. ¹⁸O isotopic labeling experiments are required to definitively assign the $\nu_{\text{Fe-O}}$ modes.

Nevertheless, the IR data are fully consistent with the formulation of **1** as $[\text{Fe}_2(\mu\text{-O})(\mu\text{-OH})(\text{R}_3\text{TPA})_2](\text{ClO}_4)_3$ and **4A** as $[\text{Fe}_2(\mu\text{-O})(\mu\text{-CH}_3\text{CO}_2)(\text{R}_3\text{TPA})_2](\text{ClO}_4)_3$.

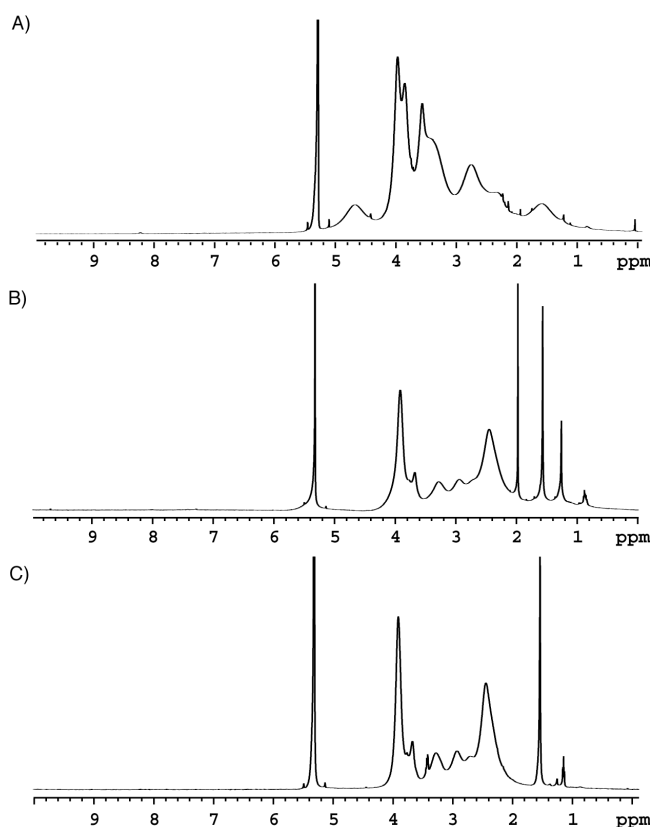


Figure A.6. ^1H NMR spectra (CD_2Cl_2 , 500 MHz) of A) complex **1**, B) complex **4A**, and C) complex **4B** recorded at RT at concentrations of approx. 5 mM. Spectrum A: $\delta = 1.63, 2.24, 2.79, 3.42, 3.60, 3.89, 4.00, 4.70$ ppm; spectrum B: $\delta = 2.45, 2.94, 3.28, 3.68, 3.92$ ppm; spectrum C: $\delta = 2.44, 2.93, 3.28, 3.67, 3.91$ ppm. Peaks attributed to solvent: δ (dichloromethane) = 5.2 ppm; δ (water) = 1.6 ppm; δ (diethyl ether) = 1.2, 2.0 ppm.

The ^1H NMR spectra of **1** and **4A** are indicative of paramagnetic species at room temperature. The spectrum of **1** shows several significantly broadened peaks at 4.70, 4.00, 3.89, 3.60, 3.42, 2.79, 2.24, and 1.63 ppm (Figure A.6A), whereas those for **4A** appear at 3.92, 3.68, 3.28, 2.94, and 2.45 ppm (Figure A.6B). Previous studies of iron TPA complexes have indicated

that the β protons of its pyridine rings are highly sensitive to the electronic properties of the iron centers; no attempts were made to examine this property in the present study.⁸

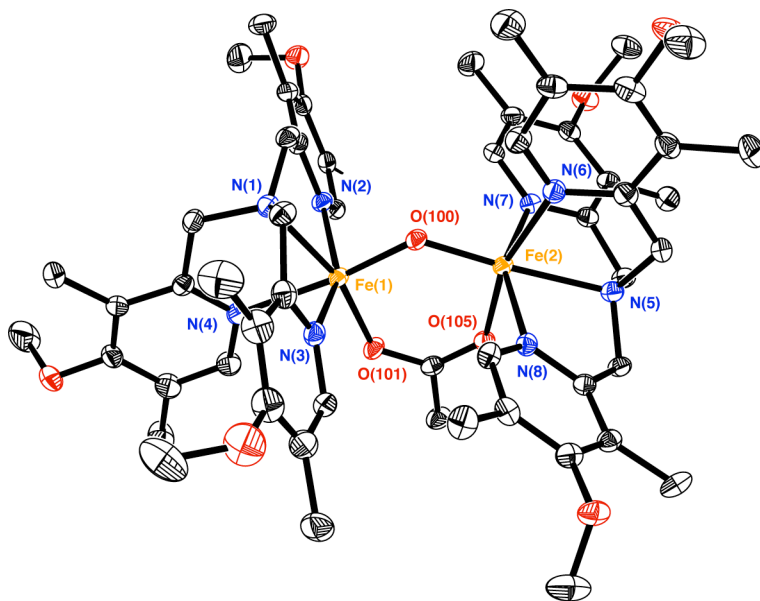


Figure A.7. The thermal ellipsoid (50%) diagram of the X-ray structure of $[\text{Fe}_2(\mu\text{-O})(\mu\text{-CH}_3\text{CO}_2)(\text{R}_3\text{TPA})_2](\text{ClO}_4)_3 \cdot (\text{CH}_3\text{CN})_{2.5}(\text{Et}_2\text{O})_{0.5}$ (**4B**). Two independent molecules of **4B** occur in the asymmetric unit; only one of them is shown in the diagram. Hydrogen atoms, solvent molecules, and perchlorate anions are omitted for clarity. Color scheme: iron, orange; oxygen, red; nitrogen, blue; carbon, black. See Table A.2 and Table A.4 for refinement and structural parameters of **4B**, respectively.

To confirm the identity of complex **4A**, particularly the assignment of acetate as its bridging ligand, efforts were made to prepare $[\text{Fe}_2(\mu\text{-O})(\mu\text{-CH}_3\text{CO}_2)(\text{R}_3\text{TPA})_2](\text{ClO}_4)_3$ independently. Reaction of solid R_3TPA , iron(III) perchlorate decahydrate, sodium acetate, and triethylamine in a 2:2:1:2 ratio in a methanol solution afforded a yellow precipitate that was readily isolated by filtration. Single crystals of the compound were obtained by slow diffusion of diethyl ether into an acetonitrile solution. X-ray diffraction analysis of these yellow blocks showed two molecules of $[\text{Fe}_2(\mu\text{-O})(\mu\text{-CH}_3\text{CO}_2)(\text{R}_3\text{TPA})_2]^{3+}$ in the asymmetric unit (Figure A.7), along with six perchlorate anions, five acetonitrile molecules, and one diethyl ether. For

comparison purposes, the $[\text{Fe}_2(\mu\text{-O})(\mu\text{-CH}_3\text{CO}_2)(\text{R}_3\text{TPA})_2](\text{ClO}_4)_3$ compound obtained from this preparation will hereafter be referred to as **4B**. Table A.4 lists the metrical parameters of the structures of **4A** and **4B**. The two structures have essentially identical bond distances and angles, with deviations that are no greater than $\sim 0.01 \text{ \AA}$ or $\sim 1 \text{ deg.}$, respectively. The small structural differences between **4A** and **4B** can be accounted for by crystal packing, for the two unit cells have different dimensions as a result of having different numbers of solvent molecules in their lattices (Table A.2).

To obtain further confirmation that **4A** and **4B** are indeed the same compound, ^{57}Fe Mössbauer spectra were recorded. The spectra of **4A** and **4B** both display a single quadrupole doublet. The data for **4A** were fit with $\delta = 0.44 \text{ mm/s}$ and $\Delta E_Q = 1.47 \text{ mm/s}$, whereas those for **4B** were fit with $\delta = 0.44 \text{ mm/s}$ and $\Delta E_Q = 1.49 \text{ mm/s}$ (Table A.1). Although the two iron atoms in $[\text{Fe}_2(\mu\text{-O})(\mu\text{-CH}_3\text{CO}_2)(\text{R}_3\text{TPA})_2](\text{ClO}_4)_3$ are not related by molecular symmetry, the similarity in their coordination environments make them indistinguishable by zero-field Mössbauer spectroscopy. These Mössbauer parameters are typical for iron in the +3 oxidation state and compare favorably with those of other $(\mu\text{-oxo})(\mu\text{-carboxylato})\text{diiron(III)}$ TPA compounds.⁶

Finally, the UV-vis (Figure A.5, blue) and ^1H NMR spectra of **4B** (A.6C) are identical to those of **4A** (Figure A.5, yellow and Figure A.6B, respectively), unequivocally showing that the four-atom bridging ligand in **4A** is acetate.

Effect of Solvent, Water, and Temperature on the Stability of 1. To examine the stability of the $(\mu\text{-oxo})(\mu\text{-hydroxo})\text{diiron(III)}$ core in solution, the absorption spectrum of **1** was recorded in different solvents at room temperature (Figure A.8). The oxo-to-iron(III) charge transfer band at 550 nm is present when **1** was dissolved in either neat dichloromethane or acetonitrile. Dissolution of **1** in an equal mixture of dichloromethane and methanol, however, led

to complete loss of this optical feature. The disappearance of the 550 nm band indicates that there is a change in the diiron core, perhaps resulting from a loss of one of the bridging ligands, conversion of the hydroxide to a methoxide bridge, or dissociation into mononuclear iron species. Because this behavior was observed when methanol was introduced into dichloromethane, other protic solvents may also affect the structural integrity of **1**.

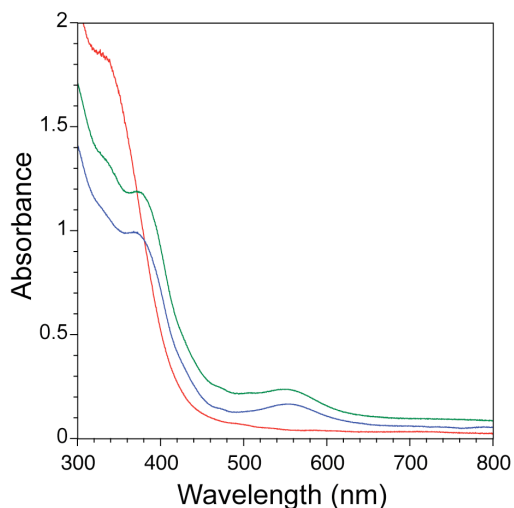


Figure A.8. UV-vis spectra of complex **1** recorded in different solvents. The 370 and 550 nm bands are observed in dichloromethane (green) and acetonitrile (blue) but not in a dichloromethane/methanol (1:1) mixture (red).

The (μ -oxo)(μ -hydroxo)diiron(III) core can convert to a (μ -oxo)(hydroxo)(aqua)-diiron(III) unit through temperature-dependent aquation.^{8,20} When a solution of **1** in acetonitrile was cooled to -30 °C under ambient conditions, the prominent band at 550 nm decreased in intensity (Figure A.9, red trace) and completely diminished upon treatment with ~8000 equiv of H₂O (green trace). Upon warming the solution to room temperature, the 550 nm band of **1** was partially restored (blue trace). When **1** is cooled to -30 °C, partial aquation may occur to afford [Fe₂(μ -O)(OH)(H₂O)(R₃TPA)₂](ClO₄)₃ (**B**), resulting in an absorption decrease at 550 nm (Scheme A.2). When water was deliberately added to the solution at -30 °C, all of **1** was

converted to **B**. This equilibrium shifted back predominantly toward **1** when the solution was warmed to room temperature.

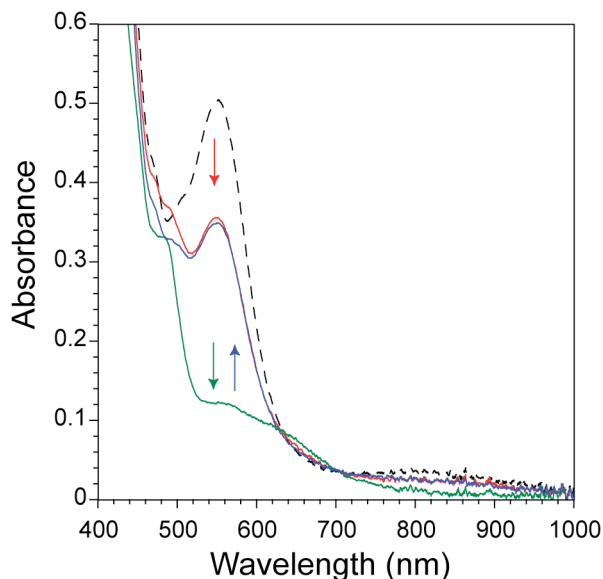
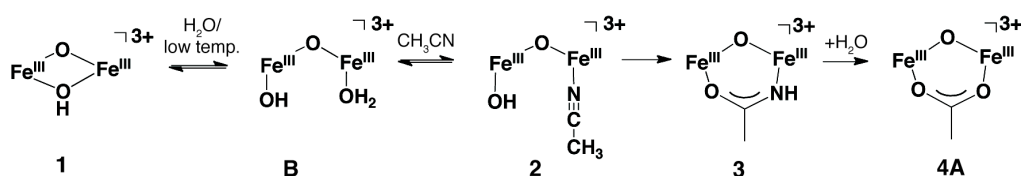


Figure A.9. Plot showing the effect of temperature and water on the UV-vis spectra of a 0.7 mM acetonitrile solution of complex **1**. At RT, **1** exhibits a prominent band at 550 nm (black dashed line). When cooled to -30°C , this absorption decreases (red) and is completely diminished upon addition of ~ 8000 equiv of water (green), relative to the diiron complex. The band at 550 nm was partially restored upon warming the solution back to RT (blue).



Scheme A.2. Proposed pathway for the complete hydrolysis of acetonitrile to acetate mediated by the $[\text{Fe}_2(\mu\text{-O})(\mu\text{-OH})(\text{R}_3\text{TPA})_2]^{3+}$ (**1**) complex.

Hydrolysis of Acetonitrile to Acetate. The yellow crystals of **4A** isolated from crystallization of **1** in acetonitrile could result either from a contaminant or through a chemical

process that converts **1** to **4A** under the conditions employed. Because no sources of acetate were used during the preparation of **1** and the results were verified by multiple independent experiments, the latter hypothesis is more likely. Dimetallic complexes can promote the hydrolysis of organonitriles in the presence of water.²⁵⁻²⁷ As depicted in Scheme A.2, we propose that trace amounts of water in the solvent reacts with **1** to give **B**. A possible mechanism would be for the coordinated water in **B** to be displaced by an acetonitrile molecule to generate **2**. In the first irreversible step, the hydroxide ligand bound to the other iron atom in **2** attacks the electrophilic nitrile group, affording a (μ -oxo)(μ -acetamido)diiron(III) species **3**. For most nitrogen-rich diiron compounds, the hydrolysis of CH₃CN does not proceed beyond the carboxamide.^{7,19} Because **4A**, rather than **3**, was isolated from the crystallization of **1**, hydrolysis of the acetamide in **3** must occur to afford the acetate.

To obtain evidence for the complete hydrolysis of CH₃CN, the absorption spectrum of compound **1** in acetonitrile was recorded over the course of ~900 min. The reaction was performed with wet solvent in air to reproduce the conditions under which **4A** was crystallized. Although the reaction is slow, spectral changes were observed between 340-380 nm as well as at 550 nm (Figure A.10A). A kinetic analysis of the data at 553 nm were fit satisfactorily to a two consecutive unimolecular reaction model, yielding rate constants of $k_1 = 2.04 \pm 0.16 \times 10^{-2} \text{ min}^{-1}$ and $k_2 = 1.98 \pm 0.06 \times 10^{-3} \text{ min}^{-1}$ (Figure A.10B). These processes are tentatively attributed to conversion of **1** to **3** and of **3** to **4A**. A (μ -oxo)(μ -acetamido)diiron(III) complex **3** has not been isolated from the reaction mixture, but is a logical precursor to **4A**.

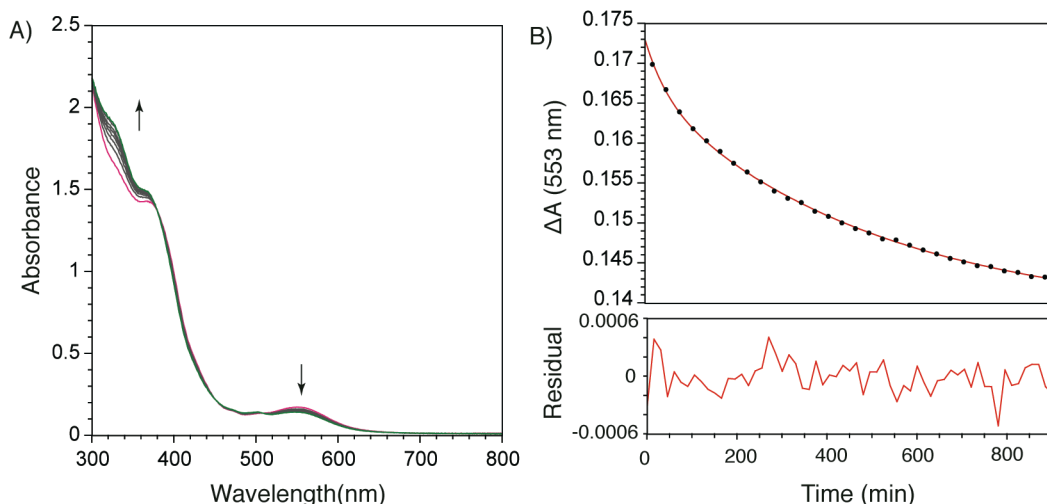


Figure A.10. Decay of **1** in acetonitrile (283 μM) (solvent-grade, not pre-dried) at RT followed by UV-vis absorption spectroscopy. The complete optical profile is shown in panel A. The absorption changes at 553 nm are shown in panel B as black dots. The data were fit to an $\text{A} \rightarrow \text{B} \rightarrow \text{C}$ kinetic model (red trace), yielding the parameters: $k_1 = 2.04 \pm 0.16 \times 10^{-2} \text{ min}^{-1}$, $k_2 = 1.98 \pm 0.06 \times 10^{-3} \text{ min}^{-1}$, $\epsilon_A = 610.9 \pm 0.5 \text{ M}^{-1}\text{cm}^{-1}$, $\epsilon_B = 578.5 \pm 1.4 \text{ M}^{-1}\text{cm}^{-1}$, $\epsilon_C = 488.8 \pm 1.0 \text{ M}^{-1}\text{cm}^{-1}$, $\chi^2 = 1.72 \times 10^{-6}$, and $R = 0.99977$. See Eq. 1 in the experimental section for the mathematical expression used.

Validity of the Reported Results. The present study indicates that a more thorough investigation is required to evaluate the reaction scheme proposed in Scheme A.1. Firstly, it is important to determine whether the reaction of hydrogen peroxide with $[\text{Fe}_2(\mu\text{-O})_2(\text{R}_3\text{TPA})_2](\text{ClO}_4)_3$ (**1**) proceeds in a manner similar to that with $[\text{Fe}_2(\mu\text{-O})(\text{OH})(\text{H}_2\text{O})(\text{R}_3\text{TPA})_2](\text{ClO}_4)_3$ (**4A**). To enable such studies, the conditions that favor either **1** or **4A** in solution have been delineated. Secondly, diiron(III) R_3TPA reactivity studies should be conducted in non-nitrile containing solvents, such as tetrahydrofuran or methanol. Although the hydrolysis of CH_3CN is slow in the presence of **1** and trace amounts of water, it is possible that additives such as hydrogen peroxide or acids would enhance the rate of this reaction. If so, there would be an additional competing reaction pathway that may complicate interpretation of the experimental data. It is noteworthy in this context that the reported Mössbauer spectra for the

high-valent diiron R₃TPA compounds showed significant amounts (30-48%) of “iron(III)” that were subtracted from the raw data. It is unclear whether these contributions come from the starting material, the decayed product, or another species generated during the reaction. Because of the complicated nature of the reactions that produce these high-valent species, the Mössbauer data required 15 parameters to be fit during ~1000 simulations.²⁸⁻³⁰ Perhaps by altering the experimental conditions under which the diiron(IV) units are generated, more homogeneous samples could be obtained to provide cleaner spectra for data analysis.

A.4. Conclusion

The putative diiron(III) starting material, [Fe₂(μ-O)(OH)(H₂O)(R₃TPA)₂](ClO₄)₃, is formed only in solution in the presence of excess amounts of water and at low temperature. The reported synthetic procedure affords the organic solvent soluble [Fe₂(μ-O)(μ-OH)(R₃TPA)₂](ClO₄)₃ compound as well as an intractable iron(III) material. The (μ-oxo)(μ-hydroxo)diiron(III) core opens up in the presence of water to enable binding of acetonitrile. The bound CH₃CN group is fully hydrolyzed to the CH₃COO⁻ anion. Further studies are necessary to clarify the hydrogen peroxide reactivity of the diiron(III) complexes characterized in this report.

A.5. References

- (1) Feig, A. L.; Lippard, S. J. *Chem. Rev.* **1994**, *94*, 759-805.
- (2) Wallar, B. J.; Lipscomb, J. D. *Chem. Rev.* **1996**, *96*, 2625-2658.
- (3) Du Bois, J.; Mizoguchi, T. J.; Lippard, S. J. *Coord. Chem. Rev.* **2000**, *200-202*, 443-485.
- (4) Que, L., Jr.; Tolman, W. B. *Nature* **2008**, *455*, 333-340.
- (5) Friedle, S.; Reisner, E.; Lippard, S. J. *Chem. Soc. Rev.* **2010**, *39*, 2768-2779.

- (6) Norman, R. E.; Yan, S.; Que, L., Jr.; Backes, G.; Ling, J.; Sanders-Loehr, J.; Zhang, J. H.; O'Connor, C. J. *J. Am. Chem. Soc.* **1990**, *112*, 1554-1562.
- (7) Hazell, A.; Jensen, K. B.; McKenzie, C. J.; Toftlund, H. *Inorg. Chem.* **1994**, *33*, 3127-3134.
- (8) Zheng, H.; Zang, Y.; Dong, Y.; Young, V. G.; Que, L., Jr. *J. Am. Chem. Soc.* **1999**, *121*, 2226-2235.
- (9) Dong, Y.; Fujii, H.; Hendrich, M. P.; Leising, R. A.; Pan, G.; Randall, C. R.; Wilkinson, E. C.; Zang, Y.; Que, L., Jr.; Fox, B. G.; Kauffmann, K.; Münck, E. *J. Am. Chem. Soc.* **1995**, *117*, 2778-2792.
- (10) Hsu, H.-F.; Dong, Y.; Shu, L.; Young, V. G.; Que, L., Jr. *J. Am. Chem. Soc.* **1999**, *121*, 5230-5237.
- (11) Shu, L.; Nesheim, J. C.; Kauffmann, K.; Münck, E.; Lipscomb, J. D.; Que, L., Jr. *Science* **1997**, *275*, 515-518.
- (12) Tinberg, C. E.; Lippard, S. J. *Accounts of Chemical Research* **2011**, ASAP.
- (13) Xue, G.; De Hont, R.; Münck, E.; Que, L., Jr. *Nat. Chem.* **2010**, *2*, 400-405.
- (14) Xue, G.; Fiedler, A. T.; Martinho, M.; Münck, E.; Que, L., Jr. *Proc. Natl. Acad. Sci. U.S.A.* **2008**, *105*, 20615-20620.
- (15) Xue, G.; Wang, D.; De Hont, R.; Fiedler, A. T.; Shan, X.; Münck, E.; Que, L., Jr. *Proc. Natl. Acad. Sci. U.S.A.* **2007**, *104*, 20713-20718.
- (16) Sheldrick, G. M., *SADABS: Area Detector Absorption Correction*; University of Göttingen: Göttingen, Germany, 2001.
- (17) Sheldrick, G. M. *Acta Cryst., Sect. A* **2008**, *A64*, 112-122.

- (18) Spek, A. L., *PLATON*, A Mutipurpose Crystallographic Tool; Utrecht University, Utrecht, The Netherlands, 2000.
- (19) Wilkinson, E. C.; Dong, Y.; Que, L., Jr. *J. Am. Chem. Soc.* **1994**, *116*, 8394-8395.
- (20) Poussereau, S.; Blondin, G.; Cesario, M.; Guilhem, J.; Chottard, G.; Gonnet, F.; Girerd, J.-J. *Inorg. Chem.* **1998**, *37*, 3127-3132.
- (21) Zang, Y.; Pan, G.; Que, L., Jr.; Fox, B. G.; Münck, E. *J. Am. Chem. Soc.* **1994**, *116*, 3653-3654.
- (22) Zang, Y.; Dong, Y.; Que, L., Jr.; Kauffmann, K.; Münck, E. *J. Am. Chem. Soc.* **1995**, *117*, 1169-1170.
- (23) Sanders-Loehr, J.; Wheeler, W. D.; Shiemke, A. K.; Averill, B. A.; Loehr, T. M. *J. Am. Chem. Soc.* **1989**, *111*, 8084-8093.
- (24) Kurtz, D. M., Jr. *Chem. Rev.* **1990**, *90*, 585-606.
- (25) Curtis, N. J.; Hagen, K. S.; Sargeson, A. M. *J. Chem. Soc., Chem. Commun.* **1984**, 1571-1573.
- (26) Kukushkin, V. Y.; Pombeiro, A. J. L. *Chem. Rev.* **2002**, *102*, 1771-1802.
- (27) Borriello, C.; Centore, R.; Roviello, G. *Inorg. Chem. Commun.* **2005**, *8*, 755-758.
- (28) Münck, E.; De Hont, R. F.; Xue, G.; Hendrich, M. P.; Que, L., Jr.; Bominaar, E. L., Mössbauer, EPR, and DFT Studies of Synthetic μ -Oxo Bridged $\text{Fe}^{\text{IV}}\text{Fe}^{\text{IV}}$ and $\text{Fe}^{\text{IV}}\text{Fe}^{\text{III}}$ Complexes Containing an $\text{Fe}^{\text{IV}}=\text{O}$ Site: An Exchange-Driven Spin Transition and a Million-Fold Reactivity Increase Upon Core Opening. In *Frontiers In Metallobiochemistry*, Proceedings of the 29th Summer Symposium in Molecular Biology, Penn State University, June 4, 2010.

- (29) Martinho, M.; Xue, G.; Fiedler, A. T.; Que, L., Jr.; Bominaar, E. L.; Münck, E. *J. Am. Chem. Soc.* **2009**, *131*, 5823-5830.
- (30) De Hont, R. F.; Xue, G.; Hendrich, M. P.; Que, L., Jr.; Bominaar, E. L.; Münck, E. *Inorg. Chem.* **2010**, *49*, 8310-8322.

BIOGRAPHICAL SKETCH

The author was born on February 8, 1984 in Saigon, Vietnam. He and his family immigrated to the United States in 1990. Loi received his undergraduate degree in chemistry from the University of California, San Diego where he conducted research with Prof. Seth M. Cohen in supramolecular chemistry. He then pursued graduate studies at the Massachusetts Institute of Technology under the tutelage of Prof. Stephen J. Lippard. He will continue his scientific training as a postdoctoral fellow in the laboratory of Prof. John E. Bercaw at the California Institute of Technology starting in the summer of 2011.

CURRICULUM VITAE

Education

- 2002-2006 B.S., Biochemistry/Chemistry, University of California-San Diego
Overall GPA: 3.8 (*magna cum laude*)
Major GPA: 3.9 (with highest department honors)
- 2006-2011 Ph.D. in Inorganic Chemistry, Massachusetts Institute of Technology
Thesis advisor: Prof. Stephen J. Lippard

Teaching Experience

- 2005 (Fall) Undergraduate Teaching Assistant, UCSD
CHEM 140A (Organic Chemistry I)
- 2006-2007 Graduate Teaching Assistant, MIT
5.112 (Introduction to Chemical Principles)
5.03 (Inorganic Chemistry I)
- 2008 (Fall) Graduate Teaching Assistant, MIT
5.062 (Principles of Bioinorganic Chemistry)

Research Experience

- 2004-2006 Undergraduate Research Assistant, UCSD
Laboratory of Prof. Seth M. Cohen
Project Title: "Assembly of supramolecular motifs utilizing transition metal dipyrin complexes as molecular building blocks."
- 2005 (summer) Undergraduate Research Assistant, MIT
Laboratory of Prof. Stephen J. Lippard
Project Title: "Water-soluble conjugated metallopolymers for fluorescence detection of reactive nitrogen species."
- 2006-2011 Graduate Research Assistant, MIT
Laboratory of Prof. Stephen J. Lippard
Project Title: "Biomimetic studies of carboxylate-bridged diiron protein active sites using synthetic models."

Honors and Awards

- 2002-2006 University of California Regents Scholarship:
For demonstration of high academic potential and achievement.

- 2004 UCSD Physical Science Dean's Undergraduate Award for Excellence:
For excellence in undergraduate research and academic performance.
- 2005 American Chemical Society Student Affiliate Summer Undergraduate
Research Fellowship:
Award for undergraduate summer research.
- 2006 Joseph E. Mayer Award, UCSD
For most outstanding research among graduating chemistry students.
- 2006-2011 Robert T. Haslam Presidential Graduate Fellowship, MIT:
Awarded in recognition of outstanding undergraduate record,
exceptional background, and promising future.

Publications

Loi Do, Sara H. Halper, and Seth M. Cohen. "Helical Coordination Polymers and Cyclic Dimers Formed from Heteroleptic Thioether-Dipyrinato Copper(II) Complexes." *Chem. Commun.*, **2004**, 2662–2663.

Loi Do, Rhett C. Smith, Andrew G. Tennyson, Stephen J. Lippard. "Luminescent Properties of Water-Soluble Conjugated Metallopolymers and their Application to Fluorescent Nitric Oxide Detection." *Inorg. Chem.* **2006**, 45(22), 8998–9005.

Sara R. Halper, Loi Do, Jay R. Stork, Seth M. Cohen. "Topological Control in Heterometallic Metal-Organic Frameworks by Anion Templating and Metalloligand Design." *J. Am. Chem. Soc.*, **2006**, 128(47), 15255–15268.

Andrew G. Tennyson, Loi Do, Rhett C. Smith, Stephen J. Lippard. "Selective Fluorescence Detection of Nitroxyl over Nitric Oxide in Buffered Aqueous Solution using a Conjugated Metallopolymer." *Polyhedron*, **2007**, 26, 4625–4630.

Zachery J. Tonzetich, Loi H. Do, Stephen J. Lippard. "Dinitrosyl Iron Complexes Relevant to Rieske Nitrosylation." *J. Am. Chem. Soc.*, **2009**, 131(23), 7964–7965.

Loi H. Do, Stephen J. Lippard. "2-Phenoxypyridyl Dinucleating Ligands for Assembly of Diiron(II) Complexes; Efficient Reactivity with O₂ to Form μ -Oxodiiron(III) Units." *Inorg. Chem.*, **2009**, 48(22), 10708–10719.

Loi H. Do, Takahiro Hayashi, Pierre Moënne-Loccoz, Stephen J. Lippard. "Carboxylate as the Protonation Site in (Peroxo)diiron(III) Model Complexes of Soluble Methane Monooxygenase and Related Diiron Proteins." *J. Am. Chem. Soc.*, **2010**, 132(4), 1273–1275.

Zachary J. Tonzetich, Hongxin Wang, Devrani Mehta, Christine E. Tinberg, Loi H. Do, Francis Jenney, Stephen P. Cramer, Stephen J. Lippard. "Identification of Protein-Bound Dinitrosyl Iron Complexes by Nuclear Resonance Vibrational Spectroscopy." *J. Am. Chem. Soc.*, **2010**, 132(20), 6914-6916.

Christine E. Tinberg, Zachary J. Tonzetich, Hongxin Wang, Loi H. Do, Yoshitaka Yoda, Stephen P. Cramer, Stephen J. Lippard. "Characterization of Iron Dinitrosyl Species Formed in the Reaction of Nitric Oxide with a Biological Rieske Center." *J. Am. Chem. Soc.*, **2010**, 132(51), 18168-18176.

Zachary J. Tonzetich, Florent Héroguel, Loi H. Do, Stephen J. Lippard. "Chemistry of Nitrosyl Iron Complexes Supported by a β -Diketiminato Ligand." *Inorg. Chem.*, **2011**, 50(4), 1570-1579.

Glen E. Alliger, Peter Müller, Loi H. Do, Christopher C. Cummins, and Daniel G. Nocera. "A Family of Cofacial Bimetallic Complexes of Hexaanionic Carboxamide Cryptands." *Inorg. Chem.*, **2011**, 50(9), 4107-4115.

Loi H. Do, Stephen J. Lippard. "Toward Functional Carboxylate-Bridged Diiron Protein Mimics: Achieving Structural Stability and Conformational Flexibility Using a Macrocyclic Ligand Framework." *J. Am. Chem. Soc.*, **2011**, *Submitted*.

Loi H. Do, Stephen J. Lippard. "Rationally Designed Synthetic Mimics of Diiron Protein Active Sites: A Chronological Perspective." *J. Inorg. Biochem.*, **2011**, *Invited review in preparation*.

Presentations

Loi Do, Sara R. Halper, and Seth M. Cohen. "Supramolecular Assemblies Based on Thioether-Dipyrrinato Transition Metal Complexes," Undergraduate Poster Presentation, 229th ACS National Meeting, San Diego, CA, March **2005**.

Loi H. Do, Stephen J. Lippard, "New Synthetic Platforms that Mimic the Structure and Function of Diiron Monooxygenases," MIT Inorganic Seminar Series, Cambridge, MA, June **2010**.

Loi H. Do, Stephen J. Lippard. "New synthetic platforms that mimic the structure and function of diiron monooxygenases," Inorganic Chemistry Session, 240th ACS National Meeting, Boston, MA, August **2010**.

Loi H. Do, Takahiro Hayashi, Pierre Moënné-Loccoz, and Stephen J. Lippard. "Investigating the Effect of Protons on the Reactivity of (μ -1,2-Peroxo)diiron(III) Model Complexes of Bacterial Multi-Component Monooxygenases." *Frontiers in Metallobiochemistry: 29th Summer Symposium*; Pennsylvania State University, PA, June **2010**.

ACKNOWLEDGEMENTS

As I am nearing the completion of my Ph.D. studies, I can proudly say that my time at MIT has been an intellectually and personally enriching experience. Arriving at this destination, however, was not devoid of a few bumps and hurdles along the way, but most of what I will remember is the thrill of making new discoveries and the privilege of working besides some amazing people. I was fortunate to have the unconditional support of numerous mentors, colleagues, friends, and family during the course of these five years, and for that, I am forever grateful.

I would like to thank my thesis advisor, Steve Lippard, for his constant reminder that we should strive for the absolute best in our work and in our scientific presentations. I am amazed by his ability to manage a highly diverse research group, in terms of science as well as personnel, with such efficiency and poise. It is not difficult to see why Steve has been such an influential figure for many fledgling scientists, such as myself. I am grateful to him for allowing me to take charge of my Ph.D. project and for supporting my professional endeavors.

My decision to pursue an advance degree in chemistry was largely due to the encouragement of my undergraduate mentors. I am extremely grateful to Seth Cohen for taking me under his wings when I was a student at UCSD. Despite my inexperience, Seth gave me my own project and got me excited about doing research. I thank him for all his guidance and support over the years. I also thank Sarah Halper for being my lab mentor and Jana Lewis and David Puerta for being good role models. I was fortunate to work with Rhett Smith during my stint in the Lippard lab as a summer undergraduate student. He introduced me to Schlenck chemistry and has an infectious enthusiasm for science.

During my time at MIT, I have had the privilege to work with some of the most talented people I know. I would like to especially thank the following three people for directly contributing to my work at MIT. Zach Tonzetich and I were bench neighbors and glovebox co-inhabitants for several years. He is a deeply insightful scientist and was always eager to discuss our latest research results. I thank him for his generosity and “keepin’ it fresh.” Mike Pluth resided next door in the sensing bay and was always a reliable source of knowledge. I appreciated his advice regarding postdoc and fellowship applications, as well as his expert proofreading of my manuscripts. Daniela Buccella was an invaluable addition to our research group. She taught me a tremendous amount about X-ray structure refinement and I thank her for her patience in walking me through each painful step. Daniela and I have also had many enjoyable philosophical discussions about life and science.

I would like to thank several of the BMM members for being great friends. Woon Ju Song and I are classmates and we will hopefully defend our dissertations successfully in the same week. I greatly admire her tenacity and strong work ethic. We’ve had a lot of fun exploring boston and going through all the trials and tribulations of graduate school. Christy Tinberg is a year ahead of me. She was a great travel companion and confidant; we’ve had epic journeys to the U.S. Open as well as Japan. Rachel Behan was a postdoc in the group whom I admire for her no-nonsense attitude. I thank her for convincing me to train and complete my first full marathon, an experience that I won’t forget.

I thank all of my coworkers in the diiron modeling subgroup for keeping the synthetic side of the lab just as vibrant as the others. Simone Friedle was the graduate student before me who trained me on using many of the instruments. Yang Li and Nakédia Carvalho are postdocs who sat through many subgroup meetings with me. Ali Liang worked with me during my last

summer in the lab. Mik Minier is the most recent addition to the subgroup and I hope, will take the diiron modeling project to the next level.

There are a few more Lippard members whom I would like to acknowledge for making my lab experience a positive one. Elisa Tomat was an incredibly generous and considerate labmate. Lindsey McQuade was a fellow runner and sports enthusiast. Wee Han Ang was a hard worker, but always cheerful. Nora Graf was always willing to lend a hand. Other current group members that have also been helpful in some way: Justin Wilson, Eric Victor, and Ulf-Peter Apfel.

I want to thank some classmates who have been great friends throughout these five years. Alex Lichtscheidl is a free spirit and is always honest and caring. We've had many great times together, especially the summer BBQs and movie nights. Maggie Flook is a very grounded individual. She has an unwavering positive outlook on life that is inspiring. Her house parties are also a hoot. I want to acknowledge a few other MIT chemistry friends: Jeewoo Lim, Joey Cotruvo, and Anthony Colombo.

Finally, I would like to dedicate this thesis to my family: mom, dad, and brother. They are the backbone of my life and have taught me that there are no substitutes for kindness and hard work.